APPLIED COMPUTATIONAL ELECTROMAGNETICS SOCIETY JOURNAL

February 2021
Vol. 36 No. 2
ISSN 1054-4887

The ACES Journal is abstracted in INSPEC, in Engineering Index, DTIC, Science Citation Index Expanded, the Research Alert, and to Current Contents/Engineering, Computing & Technology.

The illustrations on the front cover have been obtained from the research groups at the Department of Electrical Engineering, The University of Mississippi.

FEBRUARY 2021 REVIEWERS

Hamza Ahmad
Safia Akram
Ravi Kumar Arya
Arunsundar B.
Nozhan Bayat
Behrokh Beiranvand
Aysu Belen
Toni Björninen
Nenad Cvetkovic
Mona Elhelbawy
Piotr Gas
Nan Hu
Khalid Ibrahim
Rahul Kaushik
Naoki Kobayashi
Sandeep Kohar
Yingsong Li
Yong Li
Peyman Naderi
Amir Nazeri
Mohammad Mehdi Nezamabadi
Antonio Orlandi
Mirjana Peric
Alain Reineix
Sivaprakash S.C.
Guo Shuai
Tomasz Stefanski
Christopher Trueman
Denchai Worasawate
Peiyu Wu
Yuancheng Xu
Abubakar Yakubu
Huanhuan Yang
Tuba Yilmaz
Peize Zhang

THE APPLIED COMPUTATIONAL ELECTROMAGNETICS SOCIETY JOURNAL

Vol. 36 No. 2 February 2021

TABLE OF CONTENTS

In Memory of Gerald “Jerry” Burke

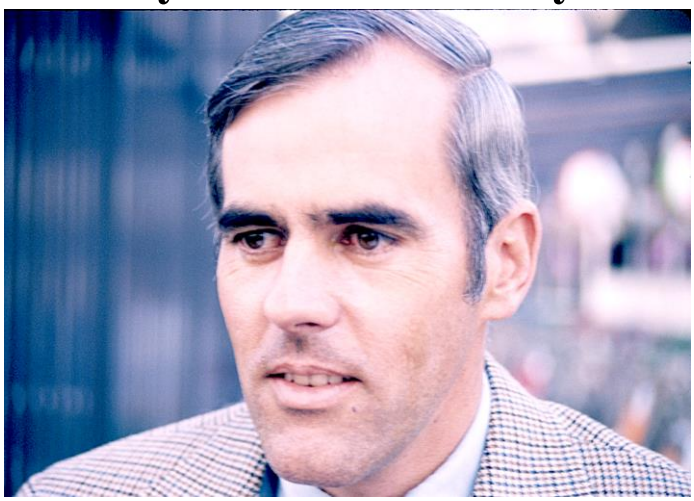

By: Edmund K. Miller and Andrew J. Poggio

Jerry Burke died on February 14, 2021 from esophageal cancer. He had earned a B.S. and M.S. in Electrical Engineering from the University of California, Berkeley in 1965 and 1968 respectively. Ed Miller first met Jerry in 1968 at MBAssociates in San Ramon, CA, where he had worked since 1966. Andy Poggio joined our group at MBA in 1969. We, and with others at MBA at the time, continued development of one of the first general-purpose computer codes for modeling wires. This code, originally called BRACT (don’t ask) transitioned to ANTBRACT, AMP (Antenna Modeling Program) and NEC (Numerical Electromagnetics Code, the latter a name suggested by Carl Baum).

Jerry had become a mainstay in the MBA/LLNL EM modeling activities. During his years at MBA he was instrumental in transforming BRACT into an effective tool for modeling antennas near an interface. After hearing for the first time about time-domain, integral-equation modeling at a 1968 APS meeting in Boston, from Edward Sayre and C. L. Bennett, Ed returned to MBA and suggested that this technology be pursued. Jerry was given some time to explore this possibility and in about 2 weeks had written the first version of what eventually came to be called TWTD (Thin-Wire Time-Domain). This code later became instrumental in designing an RIFD tag for cattle after modification by Jeremy Landt, initially at LLNL and further at Los Alamos National Laboratory. Jerry also developed a technique for interpolating frequency-domain antenna and RCS data with something he termed FDI (Frequency-Derivative Interpolation). This was the forerunner of what eventually became MBPE (Model-Based Parameter Estimation).

Andy and Jerry later joined Ed in the Wave Theory and Applications Group at Lawrence Livermore National Laboratory in 1973 and 1975 respectively. Subsequently, with support from Army, Navy, and Air Force sources including Naval Ocean Systems Center in San Diego, they produced a popular 3-volume document for NEC [G. J. Burke and A. J. Poggio, “Numerical electromagnetics code (NEC)-method of moments, Part I: Theory, Part II: Code, Part III: User’s manual,” NOSC TD-116, Naval Ocean Syst. Center, San Diego, CA, July 18, 1977 (NEC-1). revised Jan. 2, 1980 (NEC-2)]. Versions NEC-3 and NEC-4 followed over the next 15 or so years [G. J. Burke, E. K. Miller, and A. J. Poggio (2004) “The numerical electromagnetics code (NEC)—A brief history,” *2004 IEEE Int. Antennas Propagat. Symposium Digest*, vol. 42, pp. 2871-2874, June]. Just before he died, Jerry had completed rewriting the basis of NEC-4, renamed the modified code, NEC-5, and had begun to distribute it through LLNL. Over the years after he left LLNL in 1985 and until just the past year, Ed felt fortunate to be able to maintain a continuing collaborative working relationship with Jerry. This mostly involved Jerry’s responding the Ed’s request for changes or additions to be made to NEC and TWTD in order to explore various topics of special interest for which he is very grateful. Jerry’s accommodation of these requests led to several joint publications in model-based parameter estimation, electromagnetic radiation physics, and chiral media.

Although a quiet and unassuming person, Jerry was gifted analytically, an outstanding programmer and talented numerical analyst. He was a valued colleague and friend that we were privileged to know and work with for over 50 years. Our records show that one or both of us (and others at times) were coauthors of more than 80 journal articles and conference presentations. Jerry also lectured at short courses and workshops in a variety of locales in the US and South Africa, Italy, Japan, Australia and Sweden. The EM modeling community will miss him.

By: Jim Breakall

It is with great sadness that I inform the ACES community and others of the passing of Jerry Burke on February 14th, 2021. Jerry received his B.S. and M.S. degrees in Electrical Engineering from the University of California – Berkeley, Berkeley, CA, in 1965 and 1968, respectively. In the mid-60s after graduation he joined a small company, MBA Associates that was working on chaff for radar cross section (RCS) decoys. A method was needed to predict the RCS of the chaff, and Jerry and others developed the first version of an antenna modeling program called BRACT in 1967. Jerry implemented the three-term basis function (constant – sine – cosine) from Prof. Ken Mei at Berkeley that became the main type of basis function for all future versions. This basis function was a huge improvement over pulse and triangle type functions used up to then resulting in very fast convergence of results, and therefore, a smaller number of segments needed. Jerry and others then added a voltage generator and reflection coefficient approximation ground to allow the code to model the transmitting situation over earth since it was only used for RCS up to that time. This version was called ANTBRACT, and the year was 1968. MBA Associates was fortunate to win a large contract in 1971 from the government (Navy, Army, and Air Force) to extensively upgrade ANTBRACT to a version named AMP (Antenna Modeling Program). Ed Miller, Andy Poggio, and Jerry then joined the Lawrence Livermore National Laboratory (LLNL), Livermore, CA in 1971, 1973, and 1975, respectively, and that was the start of what became the code most know today as the Numerical Electromagnetics Code (NEC). AMP incorporated the electric field integral equation (EFIE) for thin wires and the magnetic field integral equation (MFIE) for voluminous surfaces that was added later becoming AMP2 in 1975. The capability of AMP2 was demonstrated by the accurate modeling of a Navy frigate in 1975. Throughout this early development, it was mainly Jerry Burke who was the master of Fortran programming and algorithmic implementation in all of these codes.

In 1977, the interest was on Electromagnetic Pulse (EMP) effects on aircraft from the Air Force Weapons Lab (Carl Baum) and shipboard communications from the Naval Ocean Systems Center (Jay Rockway). They both suggested that AMP should be improved, and Carl Baum came up with the name of the Numerical Electromagnetics Code (NEC). They actually wanted a suite of NEC family codes and also funded the development of the NEC Basic Scattering Code (NEC-BSC) at Ohio State (Ron Marhefka). The hybridization of both NEC and NEC-BSC allowed the method of moments (MoM) analysis and the uniform (geometric) theory of diffraction (UTD-GTD) to be used to solve problems over a very wide frequency range. Again, Jerry Burke was instrumental in making all of this happen.

Continual improvements were being incorporated into now NEC at LLNL and the need for accurate modeling near the earth was needed. Jerry and others came up with a very clever interpolation scheme named Model-Based Parameter Estimation (MBPE) for the complex Sommerfeld integrals needed. This became NEC2 in 1980 and is now released in the public domain. Jerry again was the person who made this happen with his extensive analytical skills in the complex plane of Sommerfeld integrals and his ability to produce very efficient and fast Fortran code. I remember contacting Jerry around this time as a graduate student at Case Western Reserve University, and that was our first time to meet on the phone. Jerry was very excited to hear a student was so interested in antenna modeling, and he sent me all the huge manuals and a computer tape with the code on it. I never paid a cent and was so grateful. I had used AMP back at Penn State in the late 1970s for modeling a large HF heating array at Arecibo Observatory that consisted of many log periodic antennas. NEC was even more advanced, and it could do so much I thought as a young Ph.D. student at the time. Jerry said to call him if I ever had any questions, and I must admit that I kept his phone busy. Bob Collin, Professor at Case and fellow Ph.D. student, Georg Karawas, and I at that time used to have many conversations about NEC, MoM, Jerry Burke, Ed Miller, and LLNL. Bob was writing another book at the time Antennas and Radiowave Propagation that discussed MoM. I remember those conversations fondly with Jerry, Bob, and Georg.

Fortune would have it that my dream came true to get an offer from LLNL in 1983 to work with Jerry and Ed and others there on NEC and other projects. I remember that my hotel reservations got messed up when I got there, and there was no room available with some big conference at LLNL. I called Ed, and he said come over to his house and stay. I will never forget that night with Ed and I staying up to the wee hours of the night talking about antennas and Jerry and my conversations with him while a graduate student. What a thrill it was I remember for the first time to meet Jerry in person on that interview and hear all the things he was doing to NEC at the time.

During 1983, we released NEC3, and I was involved in the releases for the DEC VAX and similar computers. NEC3 could model wires buried in the ground and had many other improvements mainly put in by Jerry. I remember many times I would try things with NEC and other methods and tell Jerry that something was not quite correct, for example it would give errors when trying to model stepped-diameter wires. Jerry would come back some days, or weeks later at the most, and say he put in some mini-FDTD method for the step in the diameter, and it was fixed. It seemed Jerry knew the inside of that code so well, that he could fix anything we would tell him. All of these things eventually created the final version that was funded by the Army and Navy, NEC4. I remember once that some of us were working on monopole ground systems with maybe some 120 radial wires. Jerry put together a highly efficient version of NEC3 called NEC Ground Screen (NECGS) that was extremely fast for this specialized problem. I also was involved with making helicopter measurements of HF antennas in irregular terrain and using NEC-BSC type of methods to model this scenario. The results were very close, and I remember Jerry writing some custom code to do the same thing with high accuracy and efficiency and reporting on that in a LLNL technical document. LLNL still has the licensing of NEC4, and fortunately, NEC2 is now in the public domain, and there are many versions of it available for free online (4NEC2, CocoaNEC, etc.) or commercially (EZNEC, NEC-WIN), etc.). Before Jerry's death, on his own time, he wrote a new version, NEC5, that can model wires and surfaces. I have not tried it yet myself as of this writing, but plan to get a copy and do so. I am sure it will be right up there with anything that Jerry has ever created.

Jerry was a very humble person and was not outwardly social. Jerry was the person who was quiet in a crowd and would never be forward or take credit for things. He would go on weekends from Livermore to San Mateo where he grew up and take care of his mother there. When she died and he retired from Livermore, he moved into the house he grew up in. Jerry was a confirmed bachelor for most of his life but finally found the love of his life and got married several years ago. I know he was really happy and did a lot of traveling. He still was active in antenna modeling and still would go into LLNL monthly on his own time I heard. I know that Jerry liked to ski and would go with other workers at LLNL on ski trips to the Sierras. I always enjoyed being with Jerry on trips to sponsors or to conferences. We would hang out together, and Jerry liked good restaurants and food.

It is hard to believe he is not with us anymore. I had just found some new results about that same stepped-diameter wire problem, that I discussed before, and was going to send my results for his comments. That will not happen now, but I will never forget all of the great times and just what a pleasure and honor it was to know Jerry. His legacy with NEC will live on for sure. I would like to speak for all of his friends at LLNL and the antenna community to pass on our sincere condolences to Jerry's wife and family. We all will really miss him so much. Rest in peace Jerry.

Non-uniform Feeding Network for a Dual Circularly Polarized 16×16 Ku-Band Antenna Array for On-Move Satellite Communication

W. M. Hassan [1], Khalid M. Ibrahim [1], E. A. Abdallah [2], and A. M. Attiya [1]

[1] Microwave Engineering Department
Electronics Research Institute (ERI), El-Nozha El-Gadidah, Cairo, 11843 Egypt
walaa81hassan@yahoo.com, khaledmus@gmail.com, attiya@eri.sci.eg

[2] Microstrip Department
Electronics Research Institute (ERI), El-Nozha El-Gadidah, Cairo, 11843 Egypt
esmataa2@hotmail.com

Abstract **–** This paper presents analysis and design of a dual circularly polarized 16×16 Ku band antenna array with emphasis on its feeding network. The proposed antenna is designed for on-move satellite communication system where the radiation pattern and the side-lobe level should meet the ITU standards to avoid interference with other satellite systems. This requirement is obtained by using non-uniform feeding distribution network. In addition, dual circular polarization operation requires sequential feeding networks with appropriate phase shift sequences. The proposed antenna is divided into 16 sub-cells of 4×4 radiating elements. The elements inside the sub-cell are fed by uniform dual sequential feeding networks. These sub-cells are connected together via two non-uniform feeding networks on a single layer in the shape of two interlaced fork configurations. In addition, cascaded power dividers are used to achieve the required low power division ratios between some of the sub-cells according to the required feeding distribution. These modifications simplify the fabrication process of the proposed antenna structure and reduce the required layers while satisfying the required radiation parameters.

Index Terms **–** Antenna array, circular polarized antenna, feeding network, Ku-band antenna, satellite antenna.

I. INTRODUCTION

On-move Ku-band satellite communication systems have a significant importance in different military and civilian applications where it may not be available other wired or wireless communication systems. This situation can usually be found in rural areas, in disserts, in ships away from shores and other similar situations. Parabolic reflector antennas with horn feeding are good candidate for fixed transceiver systems. However, for the case of moving situations like cars, trains and ships, the size and the aerodynamics of reflector antennas may not be suitable for these applications. In these cases, a planar antennas inside a radom represent a better choice for antenna structure than reflector antenna. The suitable planar antenna for such application usually has the configuration of an antenna array. Different planar antenna arrays for satellite communication systems were developed in X band and Ku band. The type of the radiating element and the feeding networks of such antenna arrays represent the main design parameters. On the other hand, the operating bandwidth, the radiation pattern, and the polarization represent some of the main specifications which should be included in the proposed antenna design. In addition, the weight, the manufacturing process and the number of layers represent important aspects in developing these antenna arrays.

In this paper we present a dually circular polarized antenna array operating in Ku band in the frequency range from 10.5 to 14.5 GHz. The proposed antenna array is composed of 4×4 sub-cells where each sub-cell is composed of 4×4 radiating elements. Each radiating element is fed by wideband branch-line coupler to introduce dually circular polarization. Each 2×2 radiating elements are connected by dual sequential feeding networks for both circular polarizations [1]. These 2×2 sequential fed elements are connected by uniform feeding networks to compose the sub-cells composed of 4×4 radiating elements. To develop a total radiation pattern compatible with the required ITU standards for satellite communication systems [2], these sub-cells are connected by dual non-uniform feeding networks for both polarizations [3]. The distributions of these feeding networks have a significant effect on the error function between the obtained radiation pattern and the standard ITU Mask. On the other hand, developing such distribution function may require developing complicated power dividers with quite small power division ratios. In addition, integrating the dual non-uniform feeding networks on a single layer to reduce the number of layers in the designed antenna represents another critical aspect

Submitted On: July 22, 2020
Accepted On: January 18, 2021
https://doi.org/10.47037/2020.ACES.J.360201

in the proposed design.

Similar antenna configurations can be found in literature. However, not all the previously mentioned specifications are found in these configurations. In [4] a LH circularly polarized slot antenna array is presented in the frequency range from 12.01 to 12.14 GHz with a uniform SIW feeding network. Another configuration is presented in [5] based on sequentially fed microstrip patches fed by a SIW feeding network to operate in the frequency range from 11.55 to 12.25 GHz with LH circular polarization. A dual band dual circularly polarized array is presented in [6] based on two layers of different polarization rotation artificial magnetic conductor operating at different frequency bands. The two bands in this case are 8.15 to 8.35 GHz for RH circular polarization and 14.2 to 14.8 GHz for LH circular polarization. Uniform feeding distribution function is used to feed the exciting double sided dipole array. On the other hand, other similar configurations are discussed in other frequency bands. A ridge gap waveguide feeding network is discussed to feed a RH circularly polarized array in mm-wave range [7]. A dual circularly polarized antenna based on slotted SIW is presented in [8] with a bandwidth extends from 11.6 to 13 GHz. Other configurations based on dual linearly polarized antenna arrays in Ku band are also discussed in [9 – 11]. In these configurations waveguide feeding networks with complicated manufacturing process were used.

On the other hand, similar antenna structures are studied in X-band [12 – 14]. In [12] the main feeding networks is implemented by using corporate feeding networks on two different layers separated by a ground plane to implement the dual circular polarizations. However, in [13] these feeding networks are implemented on the same layer, but for smaller antenna array. Based on the results shown in [3], the feeding distribution function used in [12 – 13] are not the optimum to reduce the error with respect to the ITU mask. However, better distribution functions would require less power division ratios which are more complicated in physical implementation. This is the motivation here to introduce a new non-uniform feeding network which can be interlaced with another similar one on the same layer to feed dual polarized 4×4 sub-cells in Ku-band. This dual non-uniform feeding network is used to develop 16×16 dual circularly polarized antenna array in Ku band in the frequency range from 10.5 to 14.5 GHz.

The organization of the present paper is as follows: In Sec. II we present in detail the geometry of the radiating element with its feeding network to introduce dual circular polarization. Then we introduce the designed dual sequential feeding networks for the sub-cell. The main properties for the sub-cell is given. In Sec. III, we present the analysis and design of the proposed non-uniform feeding network which connect these sub-cells to compose the proposed 16×16 antenna array. In this section the main limits on implementing this non-uniform feeding networks and how it can be implemented by using cascaded power divider are given. In addition, we present in this section how to integrate the two feeding networks for the two polarizations on the same layer. Section IV presents the experimental results for the designed antenna array. Finally, Sec. V gives the conclusion.

II. SEQUENTIAL FEEDING NETWORK FOR DUAL CIRCUALR POLARIZED 4×4 ANTENNA ARRAY

The proposed antenna array is composed of 4×4 sub-cells. Each sub-cell is composed of a 4×4 antenna array. Different configurations for radiating elements can be used of this application [15 – 17]. However, in the present case, it is required to develop a wideband antenna element with dual circular polarization. The appropriate configuration in this case is a stacked symmetric microstrip patch fed by a wideband branch-line coupler [13], [18], and [22].

The used radiating element in the present case is a stacked circular patch microstrip antenna as shown in Fig. 1. The lower fed element is printed on a substrate RT/ duroid 5880 with substrate thickness $L_2 = 0.787$ mm. The dielectric constant of RT/duroid 5880 is 2.2 and loss tangent is 0.0009. On the other hand, the upper parasitic element is printed on a substrate RO3003 with substrate thickness $L_1 = 0.25$ mm. The dielectric constant of RO3003 is 3 and loss tangent is 0.001. The parasitic element is separated from the fed element by a foam layer of thickness $L_F = 2$ mm. The radius of the lower patch is 8.2 mm and the radius of the upper patch is 8.8 mm. This stacked configuration is designed to verify the required wideband operation of the proposed antenna in the frequency range from 10.5 to 14.5 GHz. This antenna element is fed by two feeding probes through vias which are connected in a separate layer by a wideband branch line-coupler (BLC) to introduce the required dual circular polarizations. The dimensions of the BLC are $L_4 = 4.95$ mm, $L_6 = 1.2$ mm, $T_2 = 0.3$ mm, $T_3 = 0.6$ mm, and $T = 0.9$ mm as shown in Fig.1(c). The feeding BLC is printed on a substrate RO3003 with thickness $L_3 = 0.25$ mm. These radiating elements are arranged in 2×2 configurations. The separation between the elements is 18 mm which is nearly $0.75\lambda_0$ at the center frequency. This 2×2 antenna array is fed by two interlaced sequential feeding networks with two opposite sequences to compose dual circularly polarized 2×2 antenna array.

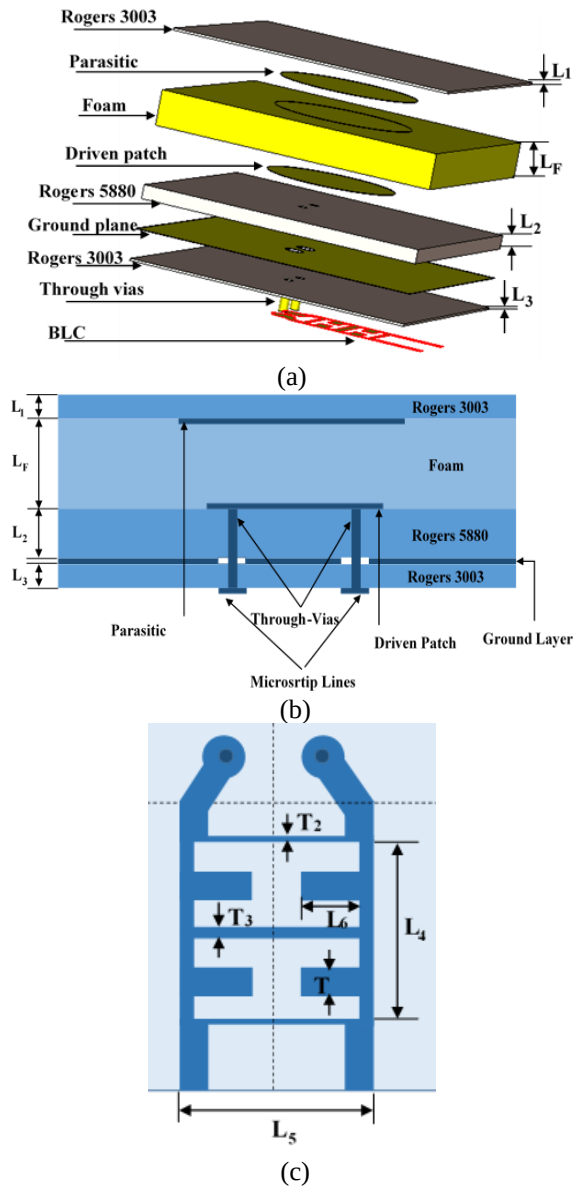

Fig. 1. Geometry of the radiating element of the antenna array: (a) 3-D view, (b) side view, and (c) BLC.

This sequential feeding networks include successive phase shifts of -90^0 in clockwise and counter clockwise directions to assets right hand and left hand circular polarizations, respectively. These successive phase shifts are obtained by increasing the feeding line sections by $\lambda_g/4$ in a successive form where λ_g is the guided wavelength of the feeding microstrip line on the feeding substrate. These $\lambda_g/4$ increments cannot be added directly in the form of straight lines due to the limited space between the radiating elements. Thus, multiple bends, U-shapes and meander shapes are used as shown in Fig. 2.

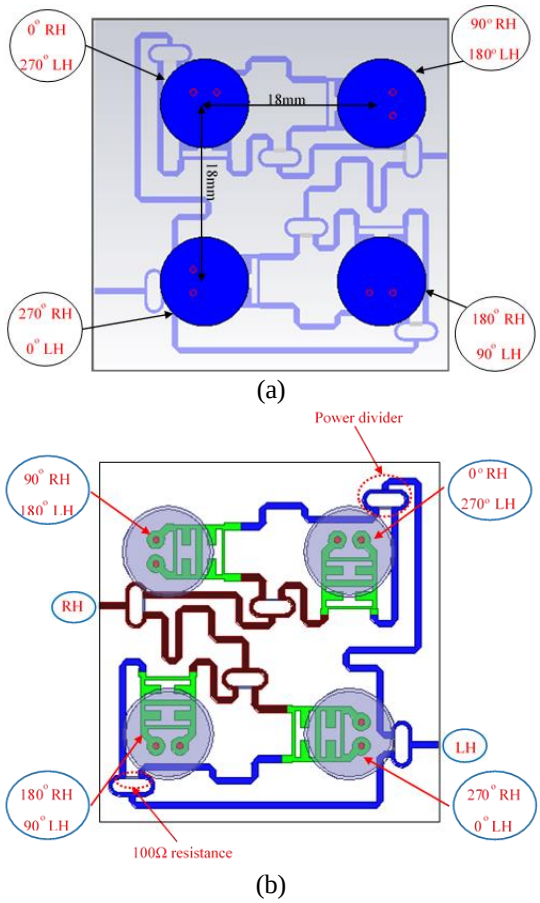

Fig. 2. Sequential feeding network for dual circularly polarized 2×2 radiating elements: (a) front view and (b) bottom view.

These configurations have additional effects in the total matching and phase sequence. In addition the coupling between the nearby sections of these feeding lines has additional effects. Thus, a preliminarily design of these two interlaced sequential feeding networks is obtained by using Keysight Advanced Design System (ADS2019). Then, this design is simulated by using full wave analysis Ansoft HFSS to include the effects of these parameters. This full wave analysis is optimized to introduce reflection coefficients below -10 dB and axial ratios below 3dB for the two circular polarizations in the operating band from 10.5 to 14.5 GHz [19]. Then, these 2×2 antenna arrays are arranged to compose the 4×4 sub-cell as shown in Fig. 3. In this case, the 2×2 arrays are connected together by two uniform interlaced feeding networks with equal amplitude and phase distribution. The total dimension of the sub-cell is 72×72 mm^2. To develop these uniform feeding networks in the available space, similar effects like bending and coupling should also be treated as in the case of the sequential feeding

networks of the 2×2 antenna array. In addition, to compensate the effects of mutual coupling between the nearby transmission line sections two matching stubs are added as shown in Fig. 3. The lengths of these matching stubs are optimized for both matching and axial ratio [19]. Figure 4 shows the fabricated 4×4 sub-cell.

Figure 5 shows the simulated and measured reflection coefficients of the two feeding ports of this sub-cell. It can be noted that the obtained reflection coefficients is below -10dB in almost all the entire operating bandwidth. On the other hand, Fig. 6 shows the corresponding axial ratios and gain for both RH and LH circular polarizations. It can be noted that the condition of axial ratio below 3 dB is verified in most of the operating bandwidth. The normalized radiation pattern of the sub-cell for both RH and LH circular polarization at 12.7 GHz is shown in Fig. 7. This sub-cell is the building block of the proposed 16×16 antenna array.

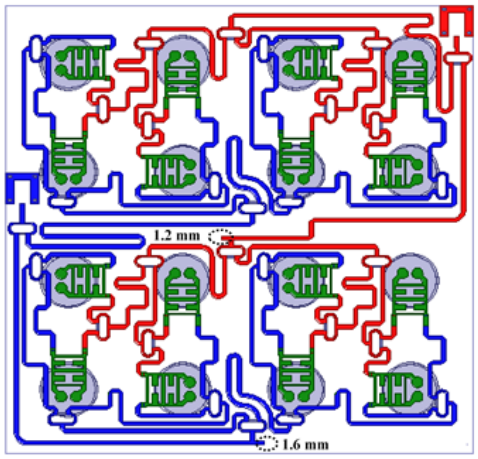

Fig. 3. Sequential feeding network with adjusting stubs for dual circularly polarized 4×4 radiating elements.

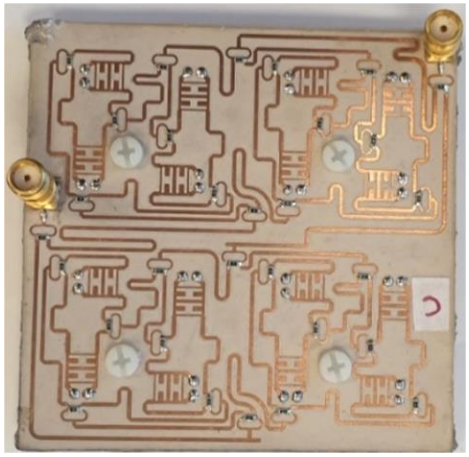

Fig. 4. Fabricated 4×4 sequential fed antenna (bottom side).

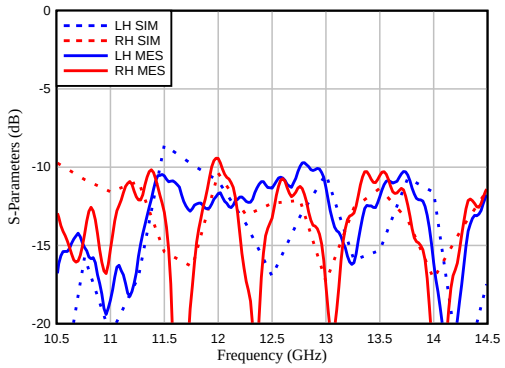

Fig. 5. Measured and simulated reflection coefficients of the 4×4 sequential fed antenna for LH and RH circular polarizations.

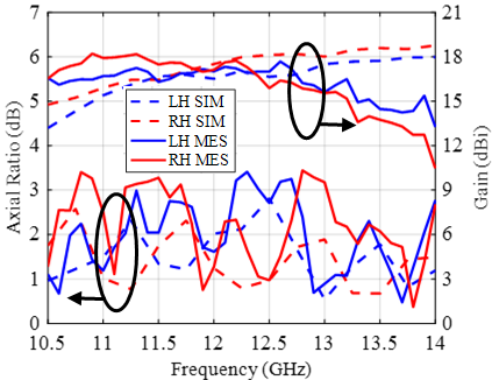

Fig. 6. Measured and simulated axial ratios and gain for RH and LH circular polarizations at broadside direction.

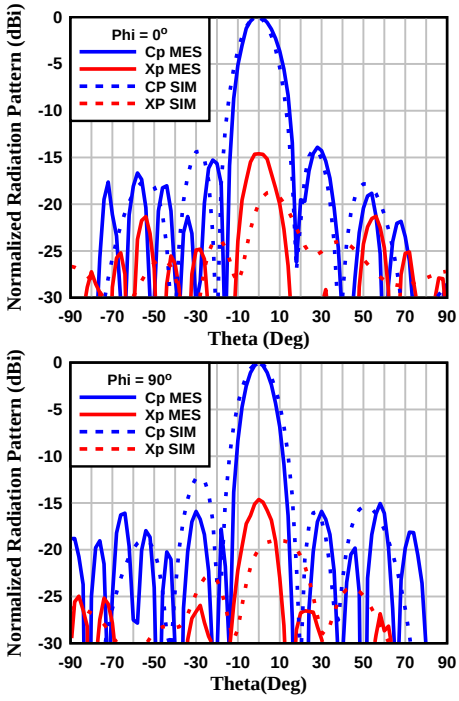

(a)

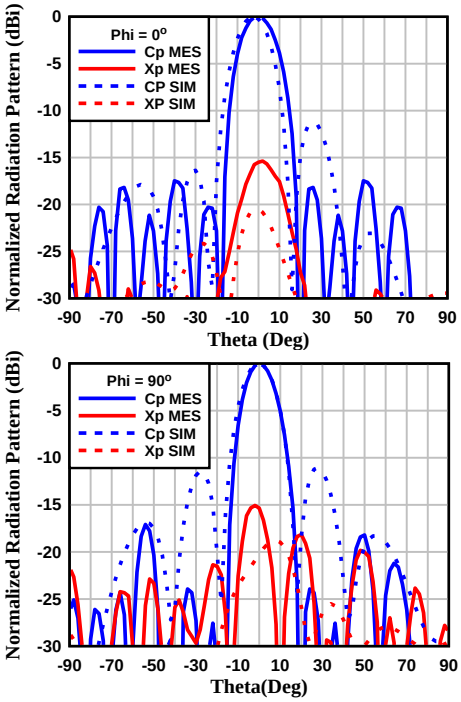

(b)

Fig. 7. Measured and simulation normalized radiation patterns for circular polarizations at 12.7 GHz (a) RH and (b) LH.

III. DESIGN AND ANALYSIS OF NON-UNIFORM FEEDING NETWORK FOR SUB-CELLS

The following step is to design a non-uniform feeding network to connect these sub-cells to form a 16×16 antenna array. Since the required radiation pattern is symmetric, the feeding distribution network should be symmetric as shown in Fig. 8, where A, B and C represent the amplitudes of the feeding current excitations at the different subcells. The amplitude A is normalized to be unity while B and C is less than unity. The total radiation pattern is a function of this distribution function and the radiation pattern of the sub-cell. The error function between the total radiation pattern and the required ITU Mask is defined as [3]:

$$\zeta = \frac{1}{N}\sum_{\mathrm{i}} \frac{1+\mathrm{sgn}(P_r(\theta_i)_{dBi}-\mathrm{Mask}(\theta_i)_{\mathrm{dBi}})}{2}[P_r(\theta_i)_{dBi} - \mathrm{Mask}(\theta_i)_{\mathrm{dBi}}]. \quad (1)$$

For the case of a uniform distribution function along the array elements the error function is nearly 2 dBi.

Different configurations for distribution networks were discussed in [3] including continuous amplitude distributions, continuous phase distribution, complex distribution and complex distribution with discrete amplitudes. In the present case, continues amplitude distribution is used to implement the required non-uniform feeding network. Thus, all the sub-cells have the same phase. The error function between the ITU Mask and the total radiation pattern as a function of the amplitude distribution is shown in Fig. 9, assuming that the amplitude of the central sub-cells $A = 1$. It can be noted that the minimum error between the ITU Mask and the total radiation pattern can be obtained when $C \approx 0.6$ and $B < 0.4$. Previous implementations of similar feeding networks were based on distribution values $B = 0.8$ and $C = 0.6$. However, these values correspond to an error value much greater than the minimum value as shown in Fig. 9, where the error function in this case is around 1.53 dBi.

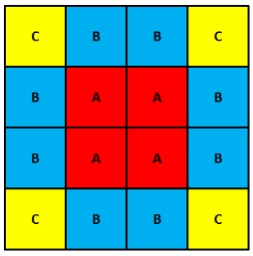

Fig. 8. Symmetric distribution function of a 16x16 array (Each square consists of 4x4 sub-cell).

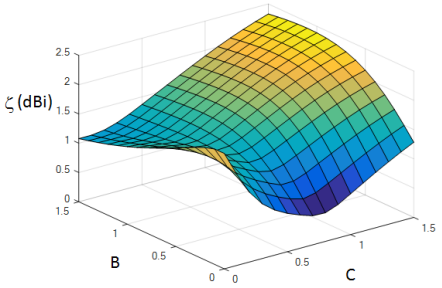

Fig. 9. Error w.r.t the ITU Mask as a function of B and C. The value of A is fixed to unity.

The key point in implementing these feeding distribution networks is the dimensions of the power dividers. These dimensions depend on the required characteristic impedances of the different transmission line sections of these power divider. For the case of a Wilkinson power divider with a non-equal power division ratio $P_3/P_2 = |V_3/V_2|^2 = K$, the required transmission line section of the power divider would have characteristic impedances of [20]:

$$Z_{03} = Z_0\sqrt{\frac{1+K}{K^{3/2}}}, \quad (2\text{-a})$$

$$Z_{02} = Z_0\sqrt{K^{0.5}(1+K)}. \quad (2\text{-b})$$

while the matching resistance between the two arms of the Wilkinson power divider is given by:

$$R = Z_0\left(\sqrt{K} + 1/\sqrt{K}\right). \quad (2\text{-c})$$

In this case, the output ports 2 and 3 of the Wilkinson power divider are matched to impedances $Z_0\sqrt{K}$ and $Z_0/\sqrt{K}$, respectively. Thus, it would be required to add $\lambda_g/4$ transformer sections of impedances $Z_0K^{1/4}$ and $Z_0K^{-1/4}$, respectively to match the non-equal Wilkinson power divider to Z_0 load. For the case of a power ratio $K = 0.43$, the required impedance of Z_{03} would be nearly $2.25Z_0$. The feeding substrate is RO3003 with a dielectric constant $\varepsilon_r = 3$ and substrate thickness $h = 0.25$ mm. The matching impedance $Z_0 = 50\Omega$. Thus, the required characteristic impedance of Z_{03} in this case is 113Ω. The width of this transmission line section in this case would be about 120 µm. This corresponds to the limiting value for fabrication process. Thus, lower power division ratios could not be directly implemented. This explains why previously published feeding networks used large values of B in the distribution network to avoid small power division ratios.

In addition, the feeding network in [12] is based on corporate feeding configuration. This configuration cannot be implemented for dual polarizations on the same layer. Thus, this corporate feeding network was implemented on multi-layered strip line configuration which increases the cost and the complexity of the fabrication process.

The proposed feeding network in this paper is based on fork type feeding network configuration as shown in Fig. 10. In this case the two networks of the dual polarizations are interlaced on the same layer. Thus, this feeding network structure is composed on a single layer. The values of the distribution functions in the present case would be $B = 0.4$ and $C = 0.6$ which introduce an error function around 1.23 dBi which is less than the error function of previous feeding networks [3], [12 – 13].

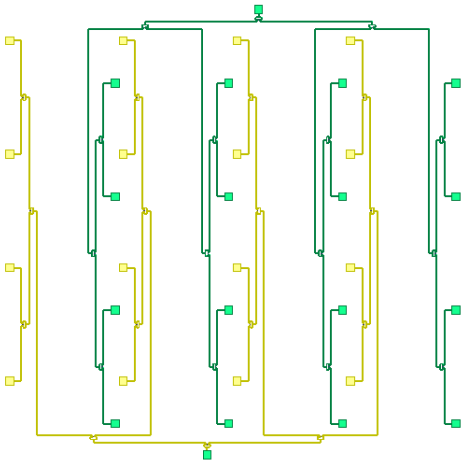

Fig. 10. Fork type dual polarized array feeding network based on Wilkinson power dividers.

Figure 11 shows the proposed distribution function for both amplitude and power ratios. The feeding network consists of four branches. Each two branches are connected by a power divider and these two power dividers are connected by an equal division power divider. On the other hand, each branch consists of four feeding points. Each two feeding points are connected by a power divider and the resulting two power dividers are connected by an equal division power divider. The assumed power division ratio in the first branch is $K_1 = B^2/C^2 = 0.444$, and in the second branch is $K_2 = B^2/A^2 = 0.16$ as shown in Fig. 11. The total normalized power in the first branch is 1.04 and in the second branch is 2.32. Thus, the power division ratio between the first and the second branches is $K_3 = (2B^2 + 2C^2)/(2A^2 + 2B^2) = 0.448$. The first and the third power dividers, K_1 and K_3, can be fabricated directly with their ratios. However, the second power divider K_2 cannot be fabricated with the present ratio. To implement the power division of K_2, cascaded power division can be implemented as shown in Fig. 12. In this case, the power between the first and the second feeding points in the second branch is divided by a ratio $K_2 = (B^2 + 0.36)/A^2 = 0.52$. Then this power is divided again between the first feeding point and a matched load by a power division ratio $K_2' = B^2/0.36 = 0.444$ as shown in Fig. 12. In this case, both power dividers K_2 and K_2' can be fabricated. However, this additional power divider increases the total normalized power of the second branch to be 3.02. Thus, the power division ratio between the second and the third branch is reduced to be $K_3 = (2B^2 + 2C^2) / (2A^2 + 2B^2 + 0.72) = 0.344$ which cannot be fabricated directly. Thus, the power divider between the two branches should be implemented by cascading two power dividers as in the case of K_2. This can be done as shown in Fig. 13 where the power divider $K_3 = (2B^2 + 2C^2 + 0.5)/(2A^2 + 2B^2 + 0.72) = 0.51$ is followed by power divider $K_3' = (2B^2 + 2C^2)/0.5 = 0.48$.

Thus, the final required power dividers have power division ratios $K_1 = K_2' = 0.444$, $K_2 = 0.52$, $K_3 = 0.51$ and $K_3' = 0.48$, in addition to equal power dividers. These power dividers are designed by using Keysight ADS2019 and the corresponding designs are verified by using full wave analysis by using Ansoft HFSS. Then, these power dividers are integrated together according to the distribution shown in Fig. 13. Figure 14 shows the geometry of a single arm of the designed fork type feeding network. The ports are arranged from 1 to 17, while the inner numbers in Fig. 14 correspond to the values of the required resistances in Ohms between the arms of the different power dividers. The feeding network shown in Fig. 14 is simulated by using Keysight ADS2019.

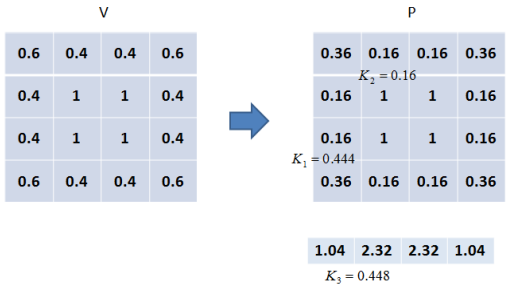

Fig. 11. Proposed feeding distribution: (a) amplitude ratios and (b) power ratios.

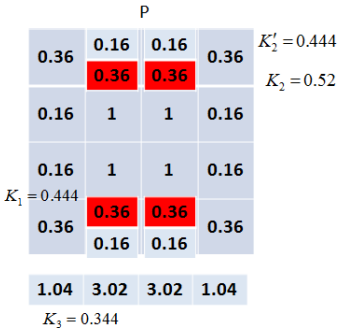

Fig. 12. Power distribution function with cascaded $\boldsymbol{K_2}$ power division. The red highlighted branches are terminated with matched loads.

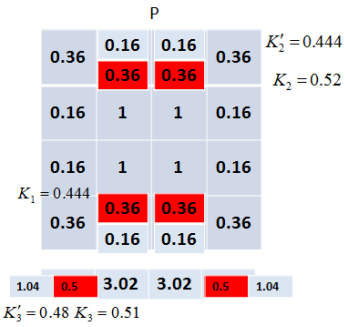

Fig. 13. Power distribution function with cascaded $\boldsymbol{K_2}$ and $\boldsymbol{K_3}$ power division. The red highlighted branches are terminated with matched loads.

Figure 15 shows the simulated reflection coefficient of the input port 17. It can be noted that the designed feeding network is good matched below -10 dB reflection coefficient in the operating frequency band from 10.5 to 14.5 GHz.

Figure 16 shows the amplitude ratios of the different output ports with respect to the inner output ports 1-4. It can be noted that the obtained amplitude ratios coincide with the proposed designed values $B = 0.4$ and $C = 0.6$.

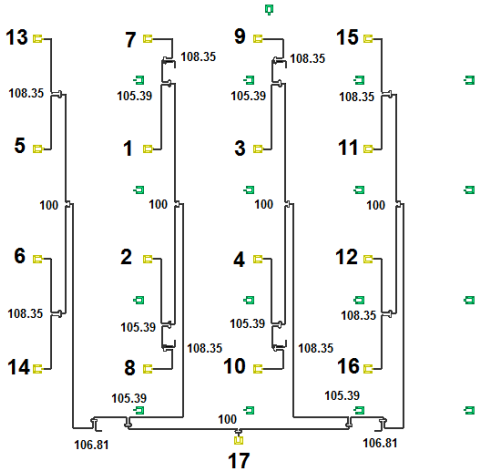

Fig. 14. Geometry of a single arm of the designed fork type dual polarized array feeding network.

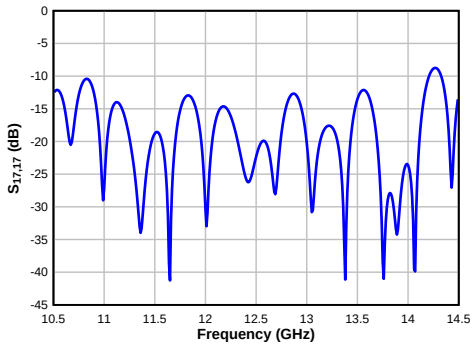

Fig. 15. Simulated reflection coefficient of the input port of the designed fork type feeding network.

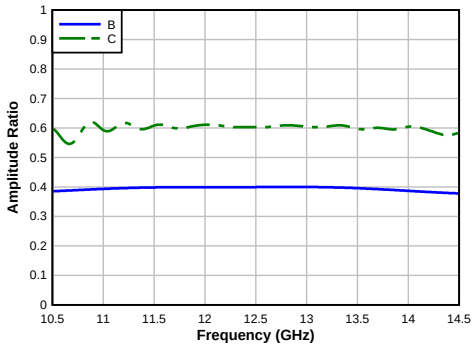

Fig. 16. Simulated amplitude ratios B and C of the designed feeding network.

IV. EXPERIMENTAL RESULTS AND DISCUSSIONS

Figure 17 shows the complete fabricated 16×16 antenna array structure including the non-uniform feeding network and the measurement setup inside the anechoic

chamber. The measurements are obtained by using the antenna measurement system Starlab 18 © [21] with a dynamic range of 60dB in the frequency range from 6 to 18 GHz. The antenna is supported by a foam layer with a dielectric constant of about 1.07 which does not have a significant effect on the measured parameters of the fabricated antenna array. The sub-cells are fabricated and assembled separately and the connecting feeding network is fabricated on a separate RO3003 substrate. The sub-cells are connected to the feeding network by using SMP miniaturized push-on connectors on both the sub-cells and the feeding network.

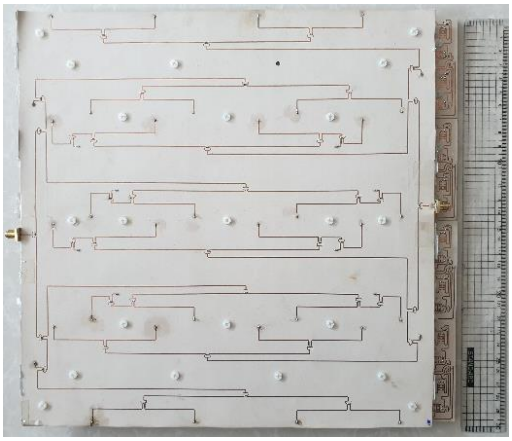

(a)

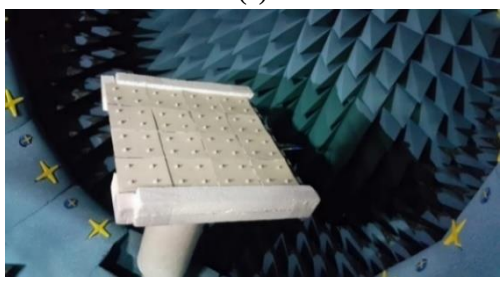

(b)

Fig. 17. Fabricated 16×16 antenna array structure: (a) non-uniform feeding network, and (b) antenna inside the antenna measurement chamber.

Figure 18 (a) shows the measured reflection coefficients of the two feeding ports of the main feeding networks. Port 1 corresponds to the feeding point of LH circular polarization while port 2 corresponds to the feeding point of the RH. It can be noted that good matching is obtained along the required operating bandwidth for both polarizations. On the other hand, Fig. 18 (b) shows the isolation between the two feeding ports. It can be noted that the obtained isolation is less than -30dB over the entire operating bandwidth which is sufficient for the proposed application.

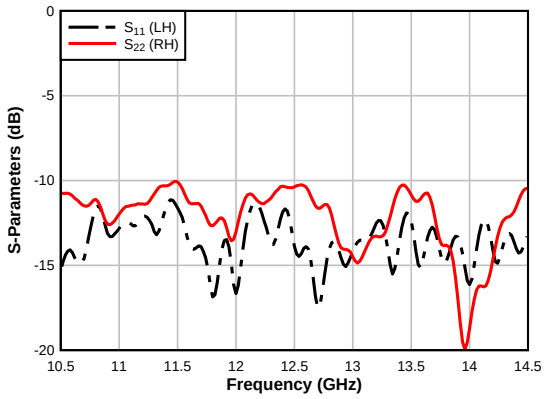

(a)

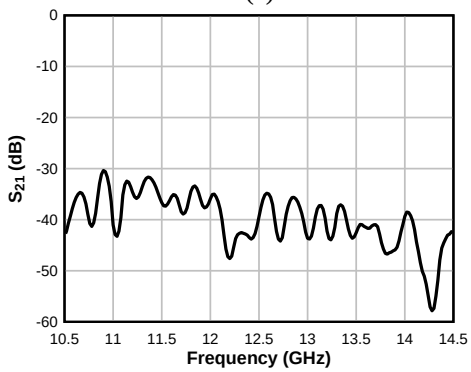

(b)

Fig. 18. Measured S-parameters of the complete antenna structure: (a) measured reflection coefficients of the complete antenna structure for the two feeding ports, and (b) measured isolation between the two feeding ports.

On the other hand, Fig. 19 shows the measured radiation patterns for both LH and RH polarizations compared to the ITU Mask at 12.7 GHz. It can be noted that the obtained radiation patterns are satisfying the ITU Mask except at few separated angles. These are expected results because the proposed feeding distribution does not completely have zero the error function of the simulated radiation pattern with respect to the ITU Mask. In a similar way, Fig. 20 shows the radiation patterns at 11 GHz near the low frequency limit and Fig. 21 shows the radiations patterns at 14 GHz near the upper frequency limit. It can be noted that these radiation patterns also satisfy the required ITU Mask except at few separated angles.

Figure 22 shows the measured peak antenna gain for the two feeding ports while Fig. 23 shows the corresponding axial ratios in the broadside direction. It can be noted that the axial ratio is almost less than 3dB in the required frequency band. Based on the measurement results it can be concluded that the designed non-uniform feeding network for the sub-cells introduces the required radiation parameters for the proposed antenna for on-

move satellite communication system in Ku-band from 10.5 to 14.5 GHz.

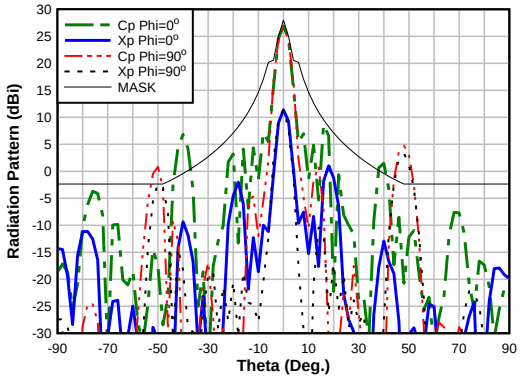

(a)

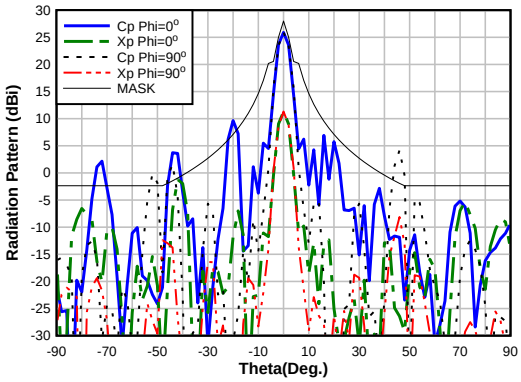

(b)

Fig. 19. Measured radiation patterns compared to the ITU Mask at the planes $\boldsymbol{\phi = 0^o}$ and $\boldsymbol{\phi = 90^o}$; at 12.7GHz: (a) (Port 1) LH excitation, and (b) (Port 2) RH excitation.

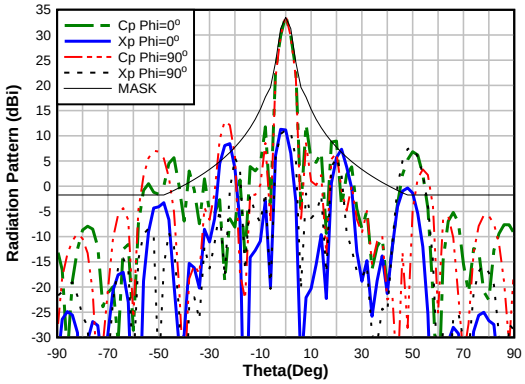

(a)

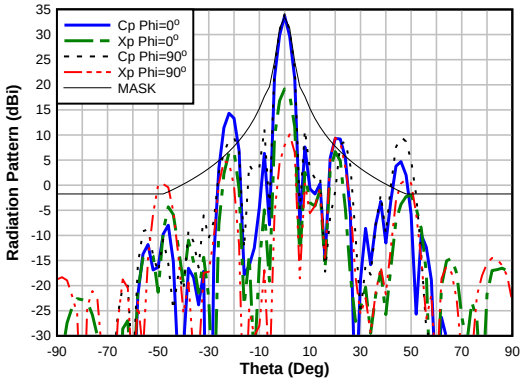

(b)

Fig. 20. Measured radiation patterns compared to the ITU Mask at the planes $\boldsymbol{\phi = 0^o}$ and $\boldsymbol{\phi = 90^o}$; at 11GHz: (a) (Port 1) LH excitation, and (b) (Port 2) RH excitation.

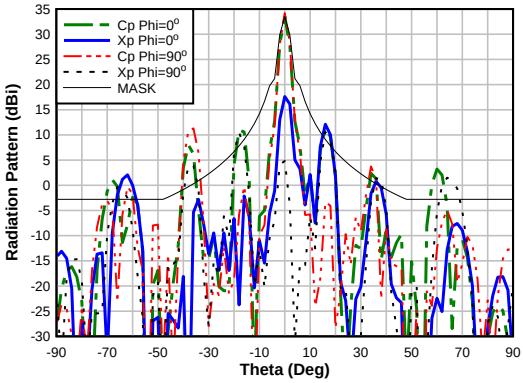

(a)

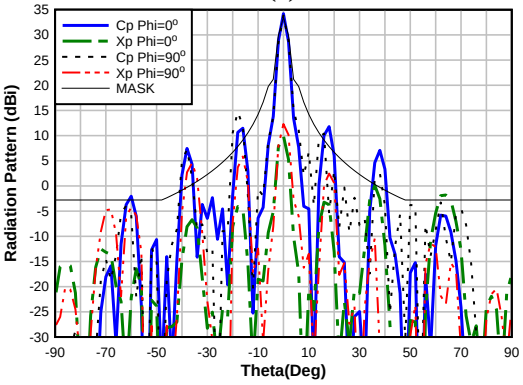

(b)

Fig. 21. Measured radiation patterns compared to the ITU Mask at the planes $\phi = 0^o$ and $\phi = 90^o$; at 14GHz: (a) (Port 1) LH excitation, and (b) (Port 2) RH excitation.

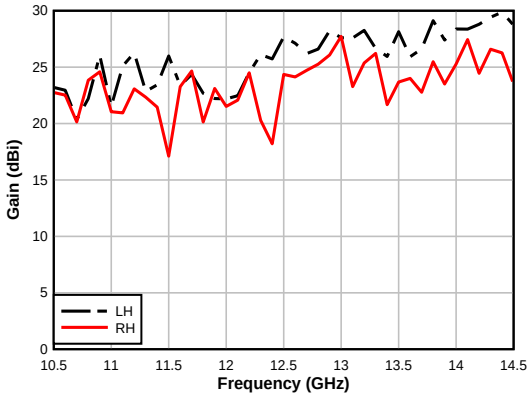

Fig. 22. Measured peak antenna gains for the two feeding ports.

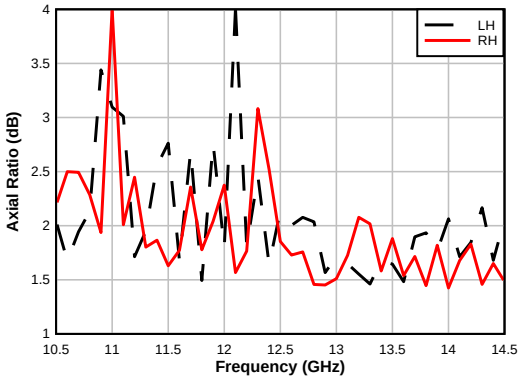

Fig. 23. Measured axial ratios for the two feeding ports.

V. CONCLUSION

Analysis and design of a single layer dual feeding networks for 16×16 Ku band dual circularly polarized antenna array is presented. The antenna array is divided into sub-cells composed of 4×4 radiating elements and connected by a dual sequential feeding network. These sub-cells are connected by a dual non-uniform interlaced fork type feeding networks. New feeding distribution is used to minimize the error between the obtained radiation pattern and the required ITU Mask. The feeding distribution function is verified by using cascaded power dividers to obtain the required small power division ratios. The obtained experimental results satisfy the required properties for a Ku band antenna array for on-move satellite communication system.

REFERENCES

[1] S. K. Lin and Y.-C. Lin, "A compact sequential-phase feed using uniform transmission lines for circularly polarized sequential-rotation arrays," *IEEE Trans. on Antennas Propag.*, vol. 59, no. 7, pp. 2721-2724, July 2011.

[2] "Methods for the determination of the coordination area around an earth station in frequency bands between 100 MHz and 105 GHz," *2016 Edition of ITU Radio Regulations*, vol. 2, Appendix 7, 2016.

[3] T. Sallam and A. M. Attiya, "Different array synthesis techniques for planar antenna array," *J. Applied Computational Electromagnetics Society*, vol. 34, no. 5, pp. 716-723, May 2019.

[4] J. Huang, F. Qiu, W. Lin, Z. Tang, D. Lei, M. Yao, Q.-X. Chu, and Y. J. Guo, "A new compact and high gain circularly-polarized slot antenna array for Ku-band mobile satellite TV reception," *IEEE Access*, vol. 5, pp. 6707-6714, 2017.

[5] J. Huang, W. Lin, F. Qiu, C. Jiang, D. Lei, and Y. J. Guo, "A low profile, ultra-lightweight, high efficient circularly-polarized antenna array for Ku band satellite applications," *IEEE Access*, vol. 5, pp. 18356-18365, 2017.

[6] J. Zhu, Y. Yang, S. Li, S. Liao, and Q. Xue, "Dual-band dual circularly polarized antenna array using FSS-integrated AMC ground for vehicle satellite communications," *IEEE Trans. Veh. Technol.*, 2019.

[7] M. Akbari, A. Farahbakhsh, and A.-R. Sebak, "Ridge gap waveguide multilevel sequential feeding network for high-gain circularly polarized array antenna," *IEEE Trans. on Antennas Propag.*, vol. 67, no. 10, pp. 251-259, Jan. 2019.

[8] R. Kazemi, S. Yang, S. H. Suleiman, and A. E. Fathy, "Design procedure for compact dual-circularly polarized slotted substrate integrated waveguide antenna arrays," *IEEE Trans. on Antennas Propag.*, vol. 67, no. 6, pp. 3839-3852, June 2019.

[9] H.-T. Zhang, W. Wang, M.-P. Jin, and X.-P. Lu, "A dual-polarized array antenna for on-the-move applications in Ku-band," *IEEE-APS Topical Conference on Antennas and Propagation in Wireless Communications (APWC)*, pp. 5-8, 2016.

[10] H.-T. Zhang, W. Wang, M.-P. Jin, Y.-Q. Zou, and X. Liang, "A novel dual-polarized waveguide array antenna for ku band satellite communications," *IEEE International Symposium on Antennas and Propagation & USNC/URSI National Radio Science Meeting*, pp. 633-634, 2017.

[11] M. M. Bilgic and K. Yegin, "Low profile wideband antenna array with hybrid microstrip and waveguide feed network for Ku band satellite reception systems," *IEEE Trans. on Antennas Propag.*, vol. 62, no. 4, pp. 2258-2263, Apr. 2014.

[12] A. García-Aguilar, J. M. Inclán-Alonso, L. Vigil-Herrero, J. M. Fernández-González, and M. Sierra-Pérez, "Printed antenna for satellite communications," *IEEE International Symposium on Phased Array Systems and Technology*, pp. 529-535, 2010.

[13] A. Garcia-Aguilar, J.-M. Inclán-Alonso, L. Vigil-Herrero, J.-M. Fernández-González, and M. Sierra-Pérez, "Low-profile dual circularly polarized

antenna array for satellite communications in the X band," *IEEE Trans. on Antennas Propag*., vol. 60, no. 5, pp. 2276-2284, May 2012.
[14] Y. Q. Zou, H.-T. Zhang, W. Wang, and M.-P. Jin, "Dual circularly polarized waveguide antenna array for satellite communications in the X band," *IEEE International Symposium on Antennas and Propagation (ISAP)*, pp. 1-3, 2015.
[15] M. H. Awida and A. E. Fathy, "Substrate-integrated waveguide Ku-band cavity-backed 2×2 microstrip patch array antenna," *IEEE Antennas and Wireless Propagation Letters*, vol. 8, pp. 1054-1056, 2009.
[16] A. Harrabi, T. Razban, Y. Mahe, L. Osman, and A. Gharsallah, "Theoretical approach for the design of a new wideband Ku-band printed antenna," *J. Applied Computational Electromagnetics Society*, vol. 30, no. 11 pp. 1200-1208, 2015.
[17] S. Trinh-Van, H. B. Kim, G. Kwon, and K. C. Hwang, "Circularly polarized spidron fractal slot antenna arrays for broadband satellite communications in Ku-band," *Progress in Electromagnetics Research*, vol. 137, pp. 203-218, 2013.
[18] M. Qu, L. Deng, M. Li, L. Yao, and S. Li, "Compact sequential feeding network with quadruple output ports and its application for wideband circularly polarized antenna," *IEEE Access*, vol. 6, pp. 31891-31898, Apr. 2018.
[19] S. Sun, Y. Lv, J. Zhang, Z. Zhao, and F. Ruan, "Optimization based on genetic algorithm and HFSS and its application to the semiautomatic design of antenna," *IEEE International Conference on Microwave and Millimeter Wave Technology*, pp. 892-894, 2010.
[20] D. M. Pozar, *Microwave Engineering*. Wiley, 2012.
[21] https://www.mvg-world.com/en/system/files/starlab_2014.pdf
[22] K. M. Ibrahim, W. M. Hassan, E. A. Abdallah, and A. M. Attiya, "Wideband sequential feeding network for Ku-band dual circularly polarized 4 × 4 antenna array," *Int. J. RF Microw. Comput. Aided Eng*., 2020; e22283. https://doi.org/10.1002/mmce.22283

Walaa M. Hassan B.Sc., M.Sc., and Ph.D. degrees from Menoufia University in 2002, 2010 and 2016. She is currently a Researcher at Electronics Research Institute (ERI), Microwave Department, Egypt. Her research interest at, FDFD, breast cancer detection, optimization techniques, scattering problems, DRA, transmitarray, reflectarray, solar cell, textile antenna, graphene, and RFID.

Khalid M. Ibrahim B.Sc., M.Sc., and Ph.D. Electronics and Electrical Communications, Faculty of Engineering, Al-Azhar University at 2000, 2007, and 2014 respectively. He joined Electronics Research Institute as a Researcher Assistant in 2001. His research interests include antennas, electromagnetic waves, antennas and wave propagations, ground penetrating radars, antenna and microwave measurement techniques, numerical techniques in electromagnetics.

Esmat A. Abdallah graduated from the Faculty of Engineering and received the M.Sc. and Ph.D. degrees from Cairo University, Giza, Egypt, in 1968, 1972, and 1975, respectively. She was nominated as Assistant Professor, Associate Professor and Professor in 1975, 1980, and 1985, respectively. She has focused her research on microwave circuit designs, planar antenna systems, and recently on EBG structures, UWB components, and antenna and RFID systems. She has authored and coauthored more than 250 research papers in highly cited international journals and in proceedings of international conferences in her field, such as IEEE Transactions on Antenna and Propagation and IEEE Transactions on Microwave Theory Techniques, etc. She supervised more than 70 Ph.D. and M.Sc. thesis. She has been the President of the Electronics Research Institute in Egypt for more than ten years.

Ahmed M. Attiya M.Sc. and Ph.D. Electronics and Electrical Communications, Faculty of Engineering, Cairo University at 1996 and 2001 respectively. He joined Electronics Research Institute as a Researcher Assistant in 1991. In the period from 2002 to 2004 he was a Postdoc in Bradley Department of Electrical and Computer Engineering at Virginia Tech. In the period from 2004 to 2005 he was a Visiting Scholar in Electrical Engineering Dept. in University of Mississippi. In the period from 2008 to 2012 he was a Visiting Teaching Member in King Saud University. He is currently Full Professor and the Head of Microwave Engineering Dept. in Electronics Research Institute. He is also the Founder of Nanotechnology Lab. in Electronics Research Institute.

Compact 5G Hairpin Bandpass Filter Using Non-Uniform Transmission Lines Theory

Sahar Saleh [1], Widad Ismail [1], Intan S. Zainal Abidin [1], and Moh'd H. Jamaluddin [2]

[1] School of Electrical and Electronic Engineering
Universiti Sains Malaysia, Penang, 14300, Malaysia
sahar_saleh@student.usm.my, eewidad@usm.my, intan.sorfina@usm.my

[2] Wireless Communication Centre
Universiti Teknologi Malaysia, Johor Bahru, Johor, 81310, Malaysia
haizal@utm.my

Abstract ─ A compact three order 5G low frequency band Hairpin Bandpass Filter (HPBF) is analyzed, designed and fabricated in this paper. The designed filter operates at 5G frequency range (5.975-7.125 GHz). 17.76% compactness in each λ/2 uniform transmission line (UTL) resonator of the filter is achieved by applying Non-Uniform Transmission Lines (NTLs) theory. This compactness will make modern wireless transmitter and receiver designs more compatible. Study on the best reduction size percentage and suitable constraints to design the required NTL resonator is highlighted in this paper. Six samples with different size reductions percentage are fabricated and measured. The simulation is carried out in this study uses High Frequency Structure Simulator (HFSS) software and Computer Simulation Technology (CST) software. The simulated results for UTL HPBF and NTL HPBF with the six cases are verified with measurement. For the best size reduction percentage design, the measured results demonstrated that the 6.55 GHz NTL and UTL HPBF show good impedance matching within the unsilenced 5G frequency band.

Index Terms ─ 5G, hairpin bandpass filter, HFSS and CST, non-uniform transmission lines theory, uniform transmission line.

I. INTRODUCTION

Filters play an important role in many RF/ Microwave applications which it is used to control the frequency responses (bandpass, bandstop, lowpass, and highpass). HPBF is a compact structure bandpass filter and simply constructed by folding the λ/2 resonators of the parallel coupled line filter, to get the U shape that eases its fabrication process where no grounding via holes are needed [1]. By controlling the filter resonators' parameters (length, width and space between them), the required pass band can be obtained [2]. At different frequencies of interest, HPBFs were used in many applications such as Ku-band satellite communication [3, 4], X-band radar navigation [5], (2 – 4 GHz) satellite application [6], 5th generation mobile communication system [7], narrow band communication (uplink frequency in the band -3 eNodeB LTE) [8], millimeter-wave applications [9, 10], 923 MHz RFID application [11] and WiMAX application [12, 13]. Hairpin units are used in [14] to get a wide stop band of 3.36 – 21.5 GHz with a sharp roll off skirt for 3.1 GHz lowpass filter. Defected Ground Structures (DGS) and Microstrip Structures (DMS) are used in HPBF design for performance enhancement and size reduction [15-19]. One of the major concerns in any RF front ends wireless communication system, is to miniaturize its devices. Many techniques were developed to reduce the size of HPBF such as using ground holes [11], high dielectric substrate [20], multilayers structure [3, 21, 22], Nonuniform Coupled Lines (NCLs) resonators [10], metamaterial complimentary split ring resonators [13], Inkjet Printing (IP) [23] and Integrated Passive Device Technologies (IPDT) [9]. In this paper, in order to reduce high cost and the difficulties of the previous methods with the aim to reduce HPBF size, NTLs theory [24-29] is applied for the first time to compact the HPBF size at 5G low frequency band of 5.975 – 7.12 GHz, available for unlicensed operations [30] without effecting its primary performance. Furthermore, a study to achieve the best size reduction percentage with the suitable constraints of NTL HPBF is highlighted.

II. NON-UNIFORM TRANSMISSION LINES (NTLs) THEORY

Higher performance, lower cost and compact size passive microwave components are important devices in the modern wireless communication system to be compatible with the recent industrial requirements. There are many approaches to achieve the required

Submitted On: July 4, 2020
Accepted On: November 29, 2020

https://doi.org/10.47037/2020.ACES.J.360202

compactness by reducing the devices transmission lines size such as using NTLs. NTLs theory [24-29] has been applied to many microwave circuits in order to reduce their sizes. The idea behind this theory is to make the performance of NTL with reduced length (d), varying characteristics impedance Z(z) and propagation constant β(z), equivalent to UTL of length (d_0), constant characteristics impedance Z and propagation constant β over the desired frequency range. Both NTL and UTL are shown in Fig. 1. Z(z) can be expanded in a truncated Fourier series as:

$$\ln(Z(z)/Z_0) = \sum_{n=0}^{N} C_n \cos\left(\frac{2\pi n z}{d}\right), \quad (1)$$

where Z_0 is the characteristics impedance of UTL and N is chosen to be 10. NTL and UTL will have equivalent performance if their ABCD matrix parameters are equal. Figure 1 (b) shows how to get the ABCD parameters of NTL by dividing it into K UTL sections then finding the ABCD parameters of those UTLs, so the total ABCD matrix will be:

$$\begin{bmatrix} A & B \\ C & D \end{bmatrix} = \prod_{i=1}^{K} \begin{bmatrix} A_K & B_K \\ C_K & D_K \end{bmatrix}, \quad (2)$$

where $A_i = D_i = \cos(\Delta\theta)$, (2.1)

$B_i = j\, Z(z)\, ((i - 0.5)\Delta z)\sin(\Delta\theta)$, (2.2)

$C_i = \frac{j\sin(\Delta\theta)}{Z((i-0.5)\Delta z)}$, i = 1, 2,….K , Δz = d/K, (2.3)

and $\Delta\theta = \frac{2\pi}{\lambda}\Delta z = \frac{2\pi f}{c}\sqrt{\varepsilon_{eff}}\ \Delta z$, (2.4)

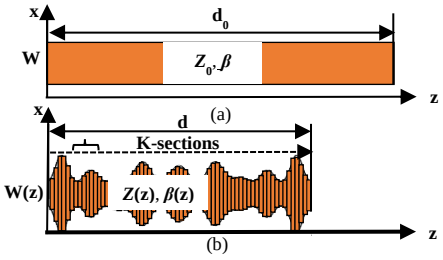

Fig. 1. (a) UTL and (b) NTL with its subdivision into K uniform sections.

The Z(z) coefficients C_ns are optimized using built in MATLAB function "fmincon" to minimize the following error function through the frequency band of 5.975 – 7.125 GHz:

$$\text{Error} = \sqrt{\frac{1}{M}\sum_{m=1}^{M}\frac{1}{4}\left(|A - A_0|^2 + Z_0^{-2}|B - B_0|^2 + Z_0^2|C - C_0|^2 + |D - D_0|^2\right)}, \quad (3)$$

where M is the number of the frequencies f_m (m = 1, 2, . . . M) within the desired band with frequency increment Δf and A_0, B_0, C_0 and D_0 are the ABCD matrix parameters of UTL. To restrict the error function in (3), two constraints should be considered: The resulting NTL should have the same width of UTL at the two ends to guarantee physical matching and it should be easy to fabricate. In this work, NTLs theory is applied to reduce the resonators' length of UTL HPBF without effecting its performance in terms of matching and transmission coefficients as will be explained in the next sections.

III. DESIGN OF THE PROPOSED 6.55 GHz UTL AND NTL HPBF

A. UTL HPBF design

Based on the design equations in [1], 6.55 GHz HPBF is deigned. In this study, the chosen substrate material is Rogers RO4003C (ε_r= 3.55 and h = 0.813 mm). Table 1 indicates all the calculated and optimized parameters of the filter, where Q_{ext}, M_{12}, L_{res}, W_{res}, S, L_t, L_{p1}, L_{p2} and W_p are external quality factor, coupling coefficient, the length of the resonator, width of the resonator, the space between two adjacent resonators, tapping length, length of the first and second port and width of the ports, respectively. Based on equations in [1], the relation between S and M_{12} and between L_t and Q_{ext} as shown in Fig. 2 is extracted using Full Wave Electromagnetic simulations such as HFSS. The optimized parameters in Table 1 are obtained via parametric studies to get better filter matching response as indicated in Fig. 3. The proposed UTL HPBF is shown in Fig.4.

Table 1: Calculated and optimized parameters for 6.55 GHz UTL HPBF

Parameters	Calculated	Optimized
Q_{ext}	7.84	-
$M_{12} = M_{21}$	0.162	-
L_{res} (mm)	14.324	15.524
W_{res} (mm)	0.5	0.6
S (mm)	0.65	0.3
L_t (mm)	1.3	2.9
$L_{p1} = L_{p2}$ (mm)	-	4
W_p (mm)	1.819	1.819

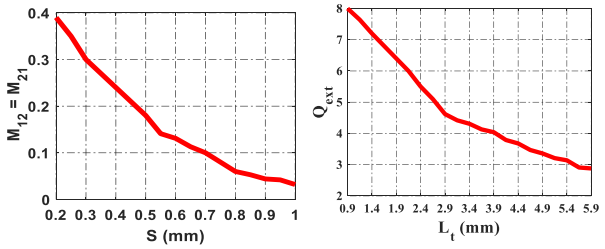

(a) (b)

Fig. 2. Relation between (a) M_{12} and S and (b) Q_{ext} and L_t.

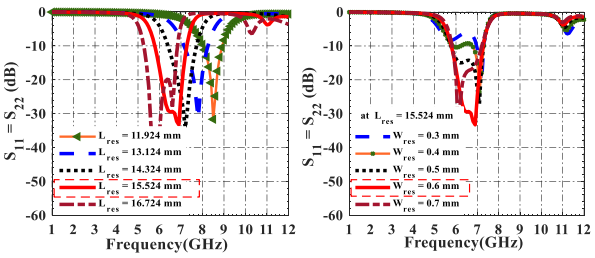

(a) (b)

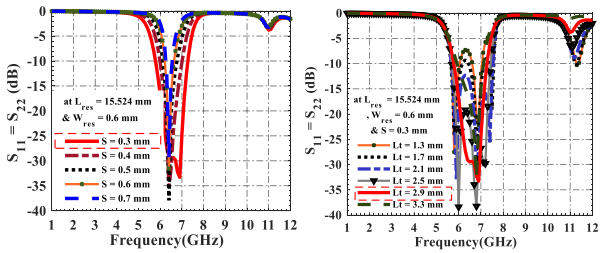

(c) (d)

Fig. 3. Parametric studies of the proposed 6.55 GHz UTL HPBF on (a) L_{res}, (b) W_{res}, (c) S, and (d) L_t.

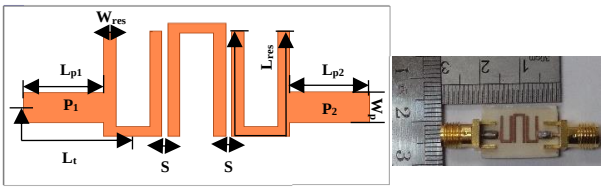

(a) (b)

Fig. 4. (a) Layout of the proposed 6.55 GHz UTL HPBF, and (b) Fabricated prototype.

B. NTL HPBF design

Since modern 5G wireless system applications require compact microwave components, NTLs theory is applied to 6.55 GHz UTL HPBF resonators to reduce their sizes. Since W_{res} of UTL is 0.6 mm, so the width of NTL (W_{NTL}) should be between W_{res} and the minimum allowable width for fabrication, W_{min}= 0.3 mm. To test many cases with different size reduction percentages, in the MATLAB optimization code, the operation frequency band (5.975 –7.125 GHz) is relaxed to (5.5 –7.5 GHz) and different Δfs are used. As a result, six different samples of NTL HPBF are designed, fabricated and measured to test the best obtained size reduction percentage. Details on these cases and the required constraints are found in [29]. The measurement in this work is carried out uses N5245A network analyzer. The best achieved size reduction of 17.79% (i.e., the length of NTL resonator L_{resNTL} is equal to 12.766 mm) is obtained at Δf = 0.5 GHz. The optimized C_ns coefficients for this case is shown in Table 2. The six NTL HPBF porotypes as they are compared to UTL HPBF are illustrated in Fig. 5.

Table 2: Optimized Fourier coefficients for λ/2 6.55 GHz NTL HBPF's resonator

Constraints: $1.305 \le \bar{Z}(z) \le 1$					
C_0	C_1	C_2	C_3	C_4	C_5
-0.5196	-0.1508	0.2651	0.0146	0.0841	0.0978
C_6	C_7	C_8	C_9	C_{10}	
0.0362	0.0515	0.0718	-0.0111	0.0604	

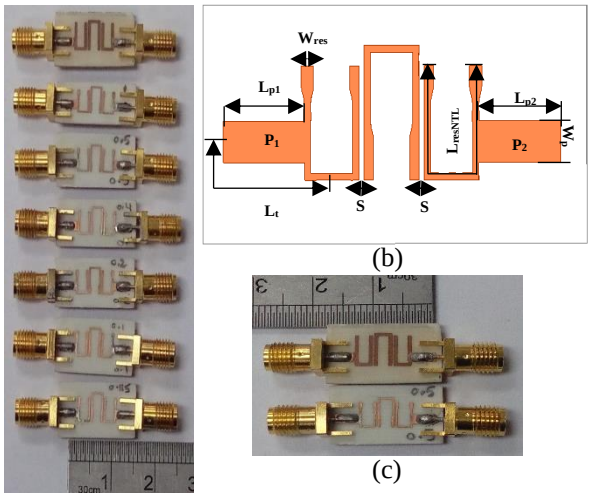

(a) (b) (c)

Fig. 5. (a) Fabricated prototypes of 6.55 GHz NTL HPBF at six different Δfs, (b) configuration of the proposed 6.55 GHz NTL HPBF at Δf = 0.5, and (c) fabricated prototypes of 6.55 GHz UTL and NTL HPBF.

IV. RESULTS AND DISCUSSION

The simulated and measured reflection and transmission coefficients of the six samples are shown in Figs. 6 and 7, respectively. As it is clear all the samples give good impedance matching and transmission response through 5.975 GHz - 7.125 GHz.

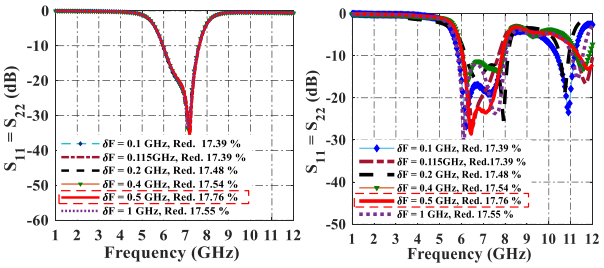

(a) (b)

Fig. 6. (a) Simulated and (b) measured return loss of the proposed 6.55 GHz NTL HPBF for six different Δfs.

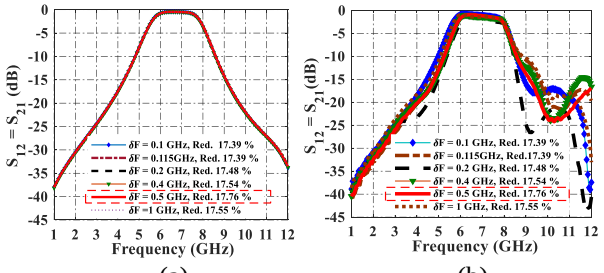

(a) (b)

Fig. 7. (a) Simulated and (b) Measured insertion loss of the proposed 6.55 GHz NTL HPBF for six different Δfs.

NTL HPBF results of the best obtained size reduction (17.79%) at Δf = 0.5 GHz is compared with UTL HPBF as shown in Fig. 8. Both filters provide good reflection and transmission coefficients. The comparison between the simulated and the realized results of 6.55 GHz UTL and NTL HPBF is given in Table 3. The slight difference between the simulated and measured results is due to the fabrication and measurement tolerances. Finally, as indicated in Fig. 8 (c), due to NTL and UTL resonators' lengths difference there is a slight difference in phase between the 6.55 GHz NTL and NTL HPBF. This difference has no big effect on the filter obtained matching and transmission performance which in turn indicates the effectiveness of applying NTLs theory to reduce the filter size.

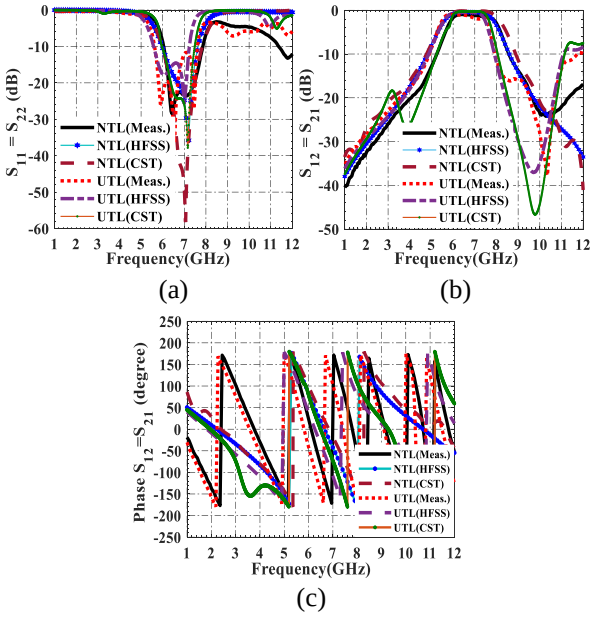

Fig. 8. (a) Return loss, (b) insertion loss, and (c) phase of 6.55 GHz UTL and NTL HPBF.

Table 3: Comparison between simulated and measured results for the designed UTL and NTL 6.55 GHz HPBFs

Parameters	Sim. (HFSS)	Sim. (CST)	Meas.
$S_{11} = S_{22}$ (NTL)	-22.7 dB at (5.99 - 7.34) GHz	-43 dB at (5.97 - 7.83) GHz	-22.52 dB at (6 - 7.86) GHz
$S_{11} = S_{22}$ (UTL)	-19.1 dB at (5.87 - 7.35) GHz	-25 dB at (5.96 - 7.48) GHz	-11.66 dB at (5.62- 7.6) GHz
$S_{12} = S_{21}$ (NTL)	-0.46 dB at Fc = 6.67 GHz	-0.29 dB at Fc = 6.9 GHz	-1.15dB at Fc = 6.93 GHz
$S_{12} = S_{21}$ (UTL)	-0.5dB at Fc = 6.61 GHz	-0.28 dB at Fc = 6.72 GHz	-1.17dB at Fc = 6.61 GHz

A comparison to other HPBFs in the literature at different frequency ranges in terms of techniques used for miniaturization, obtained size reduction percentage in λ/2 of the filter resonator's length, BW, filter response and circuit area is shown in Table 4, indicating that although the proposed filter uses simple miniaturization technique (NTLs theory) as compared to others, it provides low cost, better S_{11} and S_{12} and wider bandwidth. In addition, it provides better compactness in the resonator's length as compared to [10], [18] and [31].

Table 4: Comparison to other works in literature

Ref.	Technique Used	h (mm)/ε_r	Reduction % in λ/2 L_{res}	3 dB FBW, Freq. Band GHz	S_{11}= S_{22} (dB)<	S_{12}= S_{21} (dB)	Circuit Area λg x λg
This work	NTLs	0.813/3.55	17.76	26.95% 6 – 7.86	< -22.5	-1.15	0.64 × 0.23
[9]	UTLs using IPT on LCP	0.1/3.2	NA	15% 28.12 – 32.68	-18.9	2.41-	0.50 × 0.48
[10]	NCLs	0.127/2.94	9.2	3.45% 31.02 – 32.11	< - 9	-3.5	2.16 × 0.25
[18]	UTLs with Square DGS	1.58/2.2	1.69	30.11% 9.11 – 9.39	−19.2	- 3.7	1.81 × 0.35
[23]	UTLs using IPDT	different/different	NA	0.83% 91.9 – 99.9	-10	-5	0.95 × 0.4 mm^2
[31]	UTLs with Square DGS	0.348/1.524	11.31	97.33% 2.82 – 3.02	-19.5	-1.6	0.87 × 0.29

* LCP-Liquid Crystal Polymer, NA-Not Available.

VI. CONCLUSION

Three order 5G Hairpin Band Pass Filter (HPBF) with compact size λ/2 resonators at frequency range (5.975 – 7.125 GHz) is analyzed, designed and fabricated. Nonuniform Transmission Lines (NTLs) theory is used effectively in this study to get simple compactness in the filter resonators' lengths without additional components for matching or bandwidth enhancement. A study on the best size reduction percentage and the suitable constraints to design NTL HPBF is highlighted in this paper. 17.76% size reduction is achieved in each λ/2 resonator's length of HPBF. The designed NTL 6.55 GHz HPBF provides good impedance matching, enhanced bandwidth and good rejection out of band up to 11 GHz. The realized slight difference between simulation and hardware measurement is due to fabrication and measurement processes errors. As a future work, many techniques can be applied to the proposed filter to get further harmonics suppressions.

ACKNOWLEDGMENT

This work was supported by the University of Science Malaysia through the RUI Grant (1001/PELECT/ 8014058).

REFERENCES

[1] J.-S. G. Hong and M. J. Lancaster, *Microstrip Filters for RF/Microwave Applications*. vol. 167, John Wiley & Sons, 2011.

[2] C. Benar, I. A. Tafida, M. P. Kündüz, and T. Imeci, "Changing passband on microstrip hairpin band-pass filter," *Int. Conf. on Wireless Information Technology and Systems and Applied Computational Electromagnetics*, Honolulu, HI, USA, pp. 1-2, Mar. 2016.

[3] Q. Abdullah, N. S. M. Shah, N. Farah, W. A.

Jabbar, N. Abdullah, A. Salh, and J. A. A. Mukred, "A compact size microstrip five poles hairpin band-pass filter using three-layers structure for Ku-band satellites application," *Telkomnika*, vol. 18, pp. 80-89, Feb. 2020.

[4] K. K. Sethi, A. Dutta, G. Palai, and P. Sarkar, "Hairpin structure band-pass filter for IoT band application," *New Paradigm in Decision Science and Management, ed: Springer*, pp. 399-405, 2020.

[5] B. Adli, R. Mardiati, and Y. Y. Maulana, "Design of microstrip hairpin bandpass filter for X-band radar navigation," *4th Int. Conf. on Wireless and Telematics*, Nusa Dua, Bali, Indonesia, pp. 1-6, July 2018.

[6] K. Kavitha and M. Jayakumar, "Design and performance analysis of hairpin bandpass filter for satellite applications," *Procedia Computer Science*, vol. 143, pp. 886-891, Nov. 2018.

[7] S. Ono and K. Wada, "Design and fabrication of 3-pole BPF configured by hairpin resonators and different types of coupling and feed types at 20 GHz," *Asia-Pacific Microwave Conf.*, Kyoto, Japan, pp. 1363-1365, Nov. 2018.

[8] M. Fadhil, H. Wijanto, and Y. Wahyu, "Hairpin line bandpass filter for 1.8 GHz FDD-LTE eNodeB receiver," Radar, *Int. Conf. on Antenna, Microwave, Electronics, and Telecommunications*, Jakarta, Indonesia, pp. 134-136, Oct. 2017.

[9] H.-L. Kao, C.-L. Cho, X. Dai, C.-S. Yeh, X.-Y. Zhang, L.-C. Chang, and H.-C. Chiu, "Hairpin bandpass filter on liquid crystal polymer substrate using inkjet printing technology," *IEEE MTT-S Int. Microwave Symp. Dig.*, Seattle, WA, USA, pp. 1-4, June 2013.

[10] H. Shaman, S. Almorqi, O. Haraz, and S. Alshebeili, "Hairpin microstrip bandpass filter for millimeter-wave applications," *Mediterranean Microwave Symp.*, Marrakech, Morocco, pp. 1-4, Dec. 2014.

[11] F. Y. Zulkifli, R. Saputra, and E. T. Rahardjo, "Microstrip hairpin bandpass filter using via ground holes for 923 MHz RFID application," *Int. Symp. on Antennas and Propagation*, Jeju, Korea pp. 1-4, Oct. 2011.

[12] N. A. Wahab, W. N. W. Muhamad, M. M. A. M. Hamzah, S. S. Sarnin, and N. F. Naim, "Design a microstrip hairpin band-pass filter for 5 GHZ unlicensed WiMAX," *Int. Conf. on Networking and Information Technology*, Manila, Philippines, pp. 183-186, June 2010.

[13] M. F. M. Yusoff, M. A. M. Sobri, F. Zubir, and Z. Johari, "Multiband hairpin-line bandpass filters by using metamaterial complimentary split ring resonator," *Indonesian Journal of Electrical Engineering and Informatics*, vol. 7, pp. 289-294, June 2019.

[14] M. Hayati and H. S. Vaziri, "Wide stop-band microstrip lowpass filter with sharp roll-off using hairpin resonators," *Applied Computational Electromagnetics Society Journal (ACES)*, vol. 28, pp. 968-975, Oct. 2013.

[15] N. Ismail, S. M. Ulfah, I. Lindra, A. S. Awalluddin, I. Nuraida, and M. A. Ramdhani, "Microstrip hairpin bandpass filter for radar S-band with dumbbell-DGS," *IEEE 5th Int. Conf. on Wireless and Telematics*, Yogyakarta, Indonesia, pp. 1-4, July 2019.

[16] M. Naser-Moghadasi, M. Alamolhoda, and B. Rahmati, "Spurious response suppression in hairpin filter using DMS integrated in filter structure," *Progress In Electromagnetics Research*, vol. 18, pp. 221-229, 2011.

[17] M. Othman, N. M. Zaid, M. A. Aziz, and H. Sulaiman, "3GHz hairpin filter with defected ground structure (DGS) for microwave imaging application," *Int. Conf. on Computer, Communications, and Control Technology*, Langkawi, Malaysia, pp. 411-414, Sep. 2014.

[18] B. Adli, R. Mardiati, and Y. Y. Maulana, "Design of microstrip hairpin bandpass filter for X-band radar navigation," *4th Int. Conf. on Wireless and Telematics*, Nusa Dua, Indonesia, pp. 1-6, July 2018.

[19] K. Vidhya and T. Jayanthy, "Design of microstrip hairpin band pass filter using defected ground structure and open stubs," *Int. Conf. on Information and Electronics Engineering*, Singapore, pp. 268-272, Oct. 2011.

[20] M. Tan, Y. Xuan, Y. Ma, L. Li, and Y. Zhuang, "Design of C-band interdigital filter and compact C-band hairpin bandpass film filter on thin film substrate," *RF and Microwave Microelectronics Packaging II, ed: Springer*, pp. 63-73, Mar. 2017.

[21] N. Chami, D. Saigaa, A. Djaiz, R. AlThomali, and M. Nedil, "A new miniature microstrip two-layer bandpass filter using aperture-coupled hairpin resonators," *International Journal of Advanced and Applied Sciences*, vol. 4, pp. 10-14, 2017.

[22] J. Ni, "*Development of Tunable and Miniature Microwave Filters for Modern Wireless Communications*," Heriot-Watt University, Mar. 2014.

[23] B. Chen, Y. Tang, H. Zhu, H. Yue, Z. Wen, and X. Deng, "Design of W band hairpin filter with IPD technology," *IEEE MTT-S International Wireless Symp.*, Guangzhou, China, pp. 1-3, Aug. 2019.

[24] D. Hawatmeh, K. A. Shamaileh, and N. Dib, "Design and analysis of multi-frequency unequal-split Wilkinson power divider using non-uniform transmission lines," *Applied Computational Electromagnetics Society Journal (ACES)*, vol. 27, pp. 248-255, Mar. 2012.

[25] F. Hosseini, M. Khalaj-Amir Hosseini, and M.

Yazdani, "A miniaturized Wilkinson power divider using nonuniform transmission line," *Journal of Electromagnetic Waves and Applications*, vol. 23, pp. 917-924, 2009.

[26] M. Khalaj-Amirhosseini, "Wideband or multiband complex impedance matching using microstrip nonuniform transmission lines," *Progress In Electromagnetics Research*, vol. 66, pp. 15-25, 2006.

[27] S. Saleh, A. Alzoubi, and M. H. Bataineh, "Compact UWB unequal split Wilkinson power divider using nonuniform transmission lines," *Int. Conf. on Computer, Control, Electrical, and Electronics Engineering*, Khartoum, Sudan, pp. 1-5, Aug. 2018.

[28] S. Saleh, W. Ismail, I. S. Zainal Abidin, M. H. Jamaluddin, S. A. Al-Gailani, A. S. Alzoubi, and M. H. Bataineh, "Nonuniform compact Ultra-Wide Band Wilkinson power divider with different unequal split ratios," *Journal of Electromagnetic Waves and Applications*, vol. 34, pp. 154-167, 2020.

[29] S. Saleh, W. Ismail, I. S. Z. Abidin, S. A. Al-Gailani, M. H. Bataineh, and A. S. Alzoubi, "Size reduction percentage study of 5G hairpin bandpass filter nonuniform transmission line resonator," *IEEE Asia-Pacific Conf. on Applied Electromagnetics*, Malacca, Malaysia, pp. 1-5, Nov. 2019.

[30] "5G Spectrum Vision," p. 50, Feb. 2019.

[31] N. Ismail, T. S. Gunawan, T. Praludi, and E. A. Hamidi, "Design of microstrip hairpin bandpass filter for 2.9 GHz–3.1 GHz S-band radar with defected ground structure," *Malaysian Journal of Fundamental and Applied Sciences*, vol. 14, pp. 448-455, July 2018.

Sahar Saleh received her bachelor's degree in Electronics and Communication Engineering and M.Sc. degree in Wireless Communications Engineering from Aden University, Yemen, and Yarmouk University, Jordan in 2010 and 2016, respectively. Her research work is mainly on Microwaves Engineering and Numerical Techniques in Electromagnetics. She worked as a Junior Lecturer at Faculty of Engineering at Aden University, Yemen in 2012. Currently, she is pursuing her Ph.D. study at Universisti Sains Malaysia in the field of microwave and satellite systems.

Widad Ismail (M'04) received the bachelor's (Hons.) degree in Electronics and Communication Engineering from the University of Huddersfield, U.K., in 1999, and the Ph.D. degree (Active Integrated Antenna with Image Rejection) in Electronics and Communication Engineering from the University of Birmingham, U.K., in 2004. She is currently a Professor and a Project Coordinator with the AutoID Laboratory, Universiti Sains Malaysia. Her main areas of research are wireless system design, RFID, active integrated antennas, and RF and microwave systems engineering. She is a member of the Wireless World Research Forum.

Intan Sorfina Zainal Abidin received her M.Eng. in Electronics Engineering from University of Surrey, Guildford, UK in 2008. She then worked with Motorola Solutions, Penang, Malaysia as an Electrical Engineer for 2 years before moving to Celestica, Kulim, Malaysia to work as a Product Engineer. In 2017, She received her Ph.D. from University of Surrey for her Ph.D. under the 5G Innovation Centre in Institute of Communication System and proceed to work as a Senior Lecturer at School of Electrical and Electronic Engineering, Universiti Sains Malaysia, specializing in Electronics Communication System, Antenna, Channel Propagation, RF, Microwave Engineering and MIMO system. Abidin is a member of IEEE.

Mohd Haizal Jamaluddin received bachelor's and master's degrees in Electrical Engineering from Universiti Teknologi Malaysia, Malaysia, in 2003 and 2006, respectively, and the Ph.D. degree in Signal Processing and Telecommunications from the Université de Rennes 1, France, in 2009, with a focus on microwave communication systems and specially antennas such as dielectric resonator and reflectarray and dielectric dome antennas. He is currently an Associate Professor with the Wireless Communication Centre, Faculty of Electrical Engineering, Universiti Teknologi Malaysia. His research interests include dielectric resonator antennas, printed microstrip antennas, MIMO antennas and DRA reflect array antenna.

Gain Enhancement of a Traditional Horn Antenna using 3D Printed Square-Shaped Multi-layer Dielectric Lens for X-band Applications

Aysu Belen [1], Peyman Mahouti[*2], Filiz Güneş [3], and Özlem Tari [4]

[1] Hybrid and Electric Vehicles Technology, Iskenderun Vocational School of Higher Education
Iskenderun Technical University, Hatay, TURKEY
aysu.belen@iste.edu.tr

[2] Department of Electronic and Automation, Istanbul University-Cerrahpaşa, Istanbul/TURKEY
pmahouti@iuc.edu.tr

[3] Department of Electronics and Communication, University of Yıldız Technical, İstanbul, TURKEY
gunes@yildiz.edu.tr

[4] Department of Mathematics and Computer Science, Istanbul Arel University, Büyükçekmece, Istanbul-TURKEY
ozlemilgin@arel.edu.tr

Abstract ─ In this work, gain of a traditional horn antenna is enhanced up to 2.9 dB over X-band using 3D printed square-shaped multi-layer lens. For this purpose, firstly the multi-layer lenses are designed using Invasive Weed Optimization (IWO) and simulated in 3-D CST Microwave Studio (MWS) environment as consisting of square-shaped five layers with variable dielectric constants and heights. Thus, optimum values of the dielectric constants and heights are resulted limiting from 1.15 to 2.1 and 9.2 mm to 10 mm, respectively compatible for Fused Deposition Modeling (FDM) based 3D-printing process. Finally, the optimum lens is realized by 3D printer via FDM evaluating infill rate of cheap Polylactic Acid (PLA) material for each layer. The simulated and measured performance of the multi-layer dielectric structures are hand to hand. The horn antenna equipped by our proposed dielectric lens achieves gain enhancement of the traditional antenna up to 2.9 dB over the operation band. Furthermore, the proposed design is compared with the counterpart designs in literature and based on the comparison results it can be said that the proposed design achieves the better performance in the smaller in size as equipped a traditional X-band horn antenna.

Index Terms ─ 3D printer, dielectric lens, fused deposition modeling, gain enhancement.

I. INTRODUCTION

The X-band is the designation for a band of frequencies. In radar engineering, the frequency range is specified by the Institute of Electrical and Electronics Engineers (IEEE) at 8.0–12.0 GHz. X-band have a wide range of applications of civil, military, weather monitoring, air traffic control, maritime vessel traffic control, defense tracking, and vehicle speed detection etc. each of the mentioned applications requires high performance sub-system stages such as bandpass filter [1], microwave absorber [2], high isolated MIMO Array [3], which are a thought-provoking topic for microwave engineers.

One of the most important elements in wireless communication systems is antenna with high gain characteristics. Although antenna arrays are a common solution since gain increase can be obtained with the increase of array element alongside high level of loss in feeding network which causes decrease in efficient, complexity of design. Another solution for high gain performance is usage of dielectric lens structures. Dielectric lens have been used for gain enhancements of microwave antennas due to their ability of focusing the incoming electromagnetic waves. Also, the dielectric lens antenna has advantages of low loss and wide operation band. These designs have been used in many applications such as millimeter wave, automotive radar, satellite or indoor communication applications [4-11], or are used to beam forming for generation of multiple beams [12-13]. However, widespread dielectric lenses like Luneburg, Einstein, dielectric rod, Fresnel lens are commonly optical or quasi-optical devices, which have 3D design structures that make them hard to fabricate with dielectric materials. However, with the advances in 3D printing technology, applications of these devices are increasing.

One of the most recent applications of 3D printing technology is prototyping of microwave designs such as

Submitted On: August 27, 2020
Accepted On: December 3, 2020

https://doi.org/10.47037/2020.ACES.J.360203

antennas [14-16]. Due to their high accurate, fast printing ability even for the most complex structures whose prototyping by traditional methods becomes either impractical or costly, the interest to usage of 3D printing technology for microwave design prototyping become widespread [17-23].

Herein, it is aimed at designing and realizing a square shaped multi-layer lens for gain enhancement of a X-band traditional horn antenna using 3D printing technology. For this purpose, in the next section, firstly design procedure of the proposed multi-layer lens structure will be presented alongside of its simulated results. Then in Section 3, the antenna design will be prototyped via the use of 3D printing technology and its experimental results are compared with its simulated results and performance results of the counterpart designs in literature. Finally, the paper will end conclusion.

II. DESIGN AND SIMULATION

Horn antenna is one of the most commonly used antenna types in wireless communication systems such as astronomy, satellite tracking and high power RF systems [24]. Although they have a relatively good gain characteristics, they are limited by their dimension limitation where they should have a certain size with respect to their operation frequencies wavelengths, otherwise they would have efficiency problems. For the last decades many methods have been presented for performance improvement of horn antennas. Commonly hybrid designs had been presented to improve performance measures such as side lobe level, cross polarization [25-26], Corrugated horns [27–29], dielectric core horns [30], and strip-loaded horns [31] are the typical examples. Placement of dielectric lens structures to the aperture of antenna designs is one of the commonly used methods for performance improvement, where by placing the carefully selected materials and geometrical designs [32-35].

Herein, a squared shaped multi-layer dielectric lens (Fig. 1) is proposed as consisting of layers having variable heights and dielectric constants. In the design it should be noted that (i) the gain may be increased/ decreased by increasing/decreasing the dielectric width of the square layers; (ii) Operation frequency can be shifted via the width of layers; (iii) the dielectric constant of the lens material is also an important design parameter for focusing the EM waves [35-36].

In Table 1, geometrical values of the proposed designs are given. These values have been obtained by using a novel meta-heuristic optimization algorithm Invasive Weed Optimization (IWO). IWO is a population-based method inspired from the behavior of weed colonies that they search for an optimal environment to live [37]. IWO had shown great potential in application of; aperiodic planar thinned array antennas [38], the Shape of Non-Planar Electronically Scanned Arrays [39], directivity maximization of Uniform Linear Array of Half-wavelength Dipoles [40], Low Pass Elliptic Filter [41], Reflector Antenna [42] and design of a compact step impedance transmission line low pass filter [43]. Here similar to [44], an IWO algorithm coded in MATLAB environment has been used alongside of CST 3D EM simulator to obtain optimal performance criteria's based on the following cost function:

$$\text{Cost} = \sum_{f_{\min}}^{f_{\max}} \frac{C_1}{D_i(f)} + \frac{C_2}{\left|S_{11_i}(f)\right|}, \qquad (1)$$

where C values have been found as C_1=0.9, C_2= 0.3 by trial and error [44]. Here the goal is to maximize both of the performance measures within the given operation band between $f_{\min}$=8 GHz and $f_{\max}$=12 GHz. Thus, both S_{11} and directivity D are optimized along the X-band using the cost function given by (1). In Fig. 2, a flow chart of the proposed design optimization process is presented.

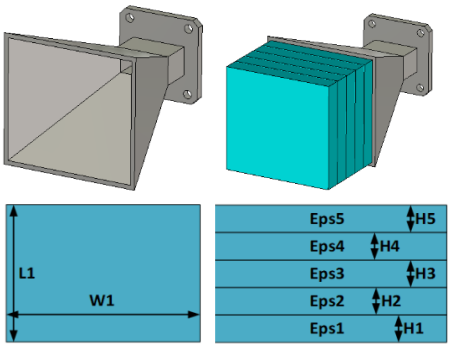

Fig. 1. Schematics of the proposed multi-layer squared lens antenna.

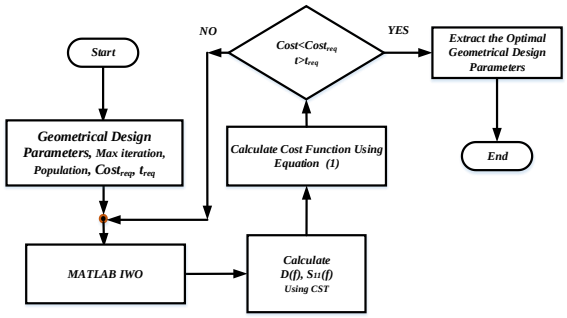

Fig. 2. Flow chart of the SIW antenna design optimization.

Table 1: Optimally selected design values

Eps1	1.66	**H1**	9.2 mm
Eps2	1.45	**H2**	10 mm
Eps3	1.15	**H3**	9.8 mm
Eps4	1.38	**H4**	9.9 mm
Eps5	2.1	**H5**	10 mm
L1	60mm	**W1**	60mm

In Fig. 3, the simulated performance of horn antenna with and without the multi-layer dielectric lens structure are presented. As it can be seen from the Fig. 2, not only the proposed design improves the overall radiation performance of the horn antenna over the operation band but also it has a low level of deteriorating on the performance of the return loss. A more detailed performance comparison of both antenna designs are presented in Table 2, where it can be clearly seen that the proposed dielectric lens antenna improves the realized gain characteristics up to 2.9dB over the aimed operation frequency.

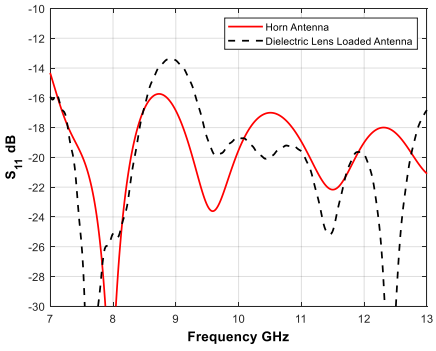

(a)

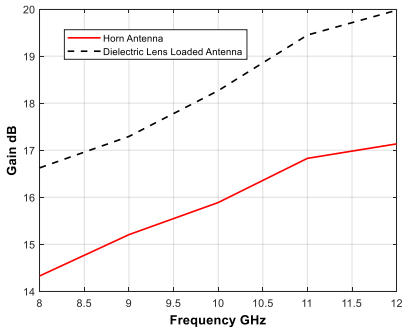

(b)

Fig. 3. Simulated (a) return loss and (b) gain of horn antenna with and without dielectric lens structure.

Table 2: Simulated performances of horn/horn antenna equipped with multi-layer dielectric lens

f (GHz)	Realized Gain (dB)	Enhanced (dB)	3dB (Angle)	Side lobe level (dB)
8	14.4 / 16.6	2.2	32.1 / 25.5	-15.2 / -16.3
9	15.2 / 17.3	2.1	27.9 / 21.2	-12.5 / -12.6
10	15.9 / 18.3	2.4	26.4 / 19.7	-12.7 / -16.6
11	16.9 / 19.4	2.5	22.4 / 17.6	-11.3 / -14.7
12	17.1 / 20	2.9	22.3 / 16.6	-10.8 / -15.2

III. EXPERIMENT RESULTS

3D printing technology is one of the recent innovation that is being used for fast, accurate and low cost manufacturing of microwave devices [45]. Recently 3D printing technology has been applied for manufacturing of Multi-layered Cylindrical Dielectric Lens Antenna [36], Non-Uniform Reflectarrays [45], Quasi Yagi Antenna for indoor application [14], or prototyping of Horn Antennas for X-band applications [15], Electrically Small Spherical Wire Antennas [46].

In this section, the proposed multi-layer lens antenna has been prototyped via the use of a commercial 3D printer, CEL Robox® Micro manufacturing platform [47]. The 3D printer uses PLA material "PLA Filament - Polar White RBX-PLA-WH002" [48]. Thanks to the unique ability of 3D printer's infill rate adjustment, not only it allows to the lower weight of the designs but also it is possible to create dielectric materials with variable dielectric constant values [49-50]. Some cases of the PLA material with the different dielectric constants are presented in Table 3. The analytical expression in Eq. (2) between infill rate and dielectric constant is obtained via regression method using the experimental data given in Table 3:

$$\varepsilon_r = -1.3x10^{-6}x^3 + 0.0374x + \frac{6.42}{x} + 0.217, \quad (2)$$

where, x indicates the infill rate in %.

Table 3: Dielectric constant value of PLA with respect to the variant infill rate [49]

Infill Rate %	Dielectric Constant ε_r	Loss Tangent
18	1.24	0.002
33	1.6	0.004
73	2.53	0.006
100	2.72	0.008

The 3D printed multi-layer dielectric antenna and its measurement setup are presented in Fig. 4. A network analyzer with a measurement bandwidth of 9 KHz - 13.5GHz and a horn antenna [51] is used for the measuring the experimental results of the antenna.

Fig. 4. 3D printed antenna design.

The measured S_{11}, and radiation patterns of the 3D printed multi-layer dielectric lens antenna are given in Figs. 5-6 and Table 4. As it can be seen form Fig. 5, similar to the simulated results, placement of the 3D lens structure to the aperture of the antenna does not have any concerning distortive effect on the return loss performance. The design achieves a return loss characteristics of less than -10 dB over the operation band of 8-12 GHz. The measured radiation patterns of the proposed antenna with and without lens structure are

presented in Fig. 6, and Table 4. From the measurement results it can be concluded that, just it was expected form the simulated results, the 3D printed lens structure increases the radiation performance of the antenna design 2.9 dB over the operation band of 8-12 GHz.

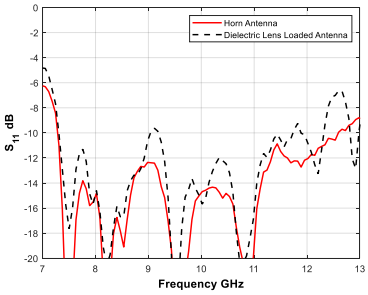

Fig. 5. Measured return loss.

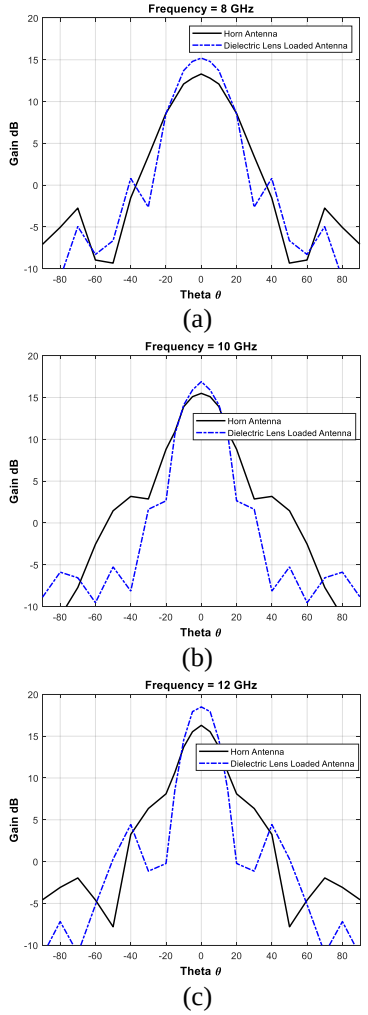

Fig. 6. Measured radiation patterns of the prototyped antenna at: (a) 8 GHz, (b) 10 GHz, and (c) 12 GHz.

Table 4: Maximum gain (dB) comparison between simulation and measurement

Frequency (GHz)	Simulated	Measured
8	16.2	15.2
9	17.3	16.4
10	18.3	16.9
11	19.5	18.1
12	19.9	18.6

Table 5: Comparison of gain (dB) of typical dielectric loaded antenna modules

	Size (mm)	Operation Band (GHz)				
		8	9	10	11	12
Here	68x65x149	15.2	16.5	16.9	18.1	18.5
[52]	279x244x159	16	18	14.8	17	15
[53]	85.1x30.8x15.9	8.5	9	9	9	10
[54]	90.7x210x210	---	---	17	---	---
[55]	87.4x59.3x80	14	15.5	16.5	15	17

Furthermore a comparison of gain (dB) performance of the horn antenna equipped with multi-layer dielectric lens antenna with the counterpart designs in literature [42-55] has been presented in Table 5. From the comparisons, it can be concluded that the proposed dielectric lens structure can be used to model a high performance antenna that achieves better gain vs. size performance within the requested operation frequency compared to its counterpart designs.

VI. CONCLUSION

In this work, design and realization of a squared shaped multi-layer dielectric lens antenna via the use of 3D printing technology has been achieved. By using the unique features of 3D printing technology a dielectric lens structures with multiple layers that each has different values of substrate height and dielectric constant values are prototyped. By placing the proposed multi-layer dielectric lens stricter to the aperture of a traditionally horn antenna the gain performance of the antenna has been enhanced without deteriorating the return loss characteristics of the antenna over the selected operation up to 2.9dBi. Furthermore the experimental results of the prototyped antenna is compared with the counterpart dielectric loaded lens antenna designs in literature and found to be a better solution both in means of size and gain enhancement performance for the selected operation band.

ACKNOWLEDGMENT

We would like to express our special thanks of gratitude to the Research Fund of the Yıldız Technical University for founding our research under project number of FAP-2018-3427, TÜBİTAK 2211/A, YÖK 100/2000, microwave and antenna laboratories of Yıldız

Technical University, and Aktif Neser Elektronik for providing their support for our researches.

REFERENCES

[1] B. Zheng, S. Wong, Y. Wu, and Q. Chu, "A novel stack PCB structure for X-band cavity bandpass filter implementation," *2017 International Applied Computational Electromagnetics Society Symposium (ACES)*, Suzhou, pp. 1-2, 2017.

[2] S. Vinayasree, M. A. Soloman, V. Sunny, P. Mohanan, P. Kurian, and M. R. Anantharaman, "A microwave absorber based on strontium ferrite–carbon black–nitrile rubber for S and X-band applications," *Composites Science and Technology*, vol. 82, pp. 69-75, 2013.

[3] J. Jiang, Y. Xia, and Y. Li, "High isolated X-band MIMO array using novel wheel-like metamaterial decoupling structure," *Applied Computational Electromagnetics Society Journal*, vol. 34, no. 12, 2019.

[4] J. R. Risser, *Microwave Antenna Theory and Design*. New York, NY, USA: McGraw-Hill, 1949.

[5] B. Chantraine-Bares, R. Sauleau, L. L. Coq, and K. Mahdjoubi, "A new accurate design method for millimeter-wave homogeneous dielectric substrate lens antennas of arbitrary shape," *IEEE Trans. Antennas Propag*., vol. 53, no. 3, pp. 1069-1082, Mar. 2005.

[6] W. E. Kock, "Metallic delay lens," *Bell System Tech. J*., vol. 27, pp. 58-82, Jan. 1948.

[7] W. E. Kock, "Metal lens antennas," *Proc. IRC*, vol. 34, no. 11, pp. 826-836, Nov. 1946.

[8] B. Schoenlinner, X. Wu, J. P. Ebling, G. V. Eleftheriades, and G. M. Rebeiz, "Wide-scan spherical-lens antennas for automotive radars," *IEEE Trans. Microwave Theory Tech*., vol. 50, pp. 2166-2175, 2002.

[9] B. Fuchs, O. Lafond, S. Rondineau, M. Himdi, and L. Le Coq, "Off-axis performances of half Maxwell fish-eye lens antennas at 77GHz," *IEEE Trans. Antennas Propag*., vol. 55, pp. 479-482, 2007.

[10] J. R. Costa, C. A. Fernandes, G. Godi, R. Sauleau, L. Le Coq, and H. Legay, "Compact Ka-band lens antennas for LEO satellites," *IEEE Trans. Antennas Propag*., vol. 56, pp. 1251-1258, 2008.

[11] C. A. Fernandes, "Shaped dielectric lenses for wireless millimeter-wave communications," *IEEE Antennas Propag. Mag*., vol. 41, pp. 141-150, 1999.

[12] O. Lafond, M. Caillet, B. Fuchs, S. Palud, M. Himdi, S. Rondineau, and L. Le Coq, "Millimeter wave reconfigurable antenna based on active printed array and inhomogeneous lens," *Eur. Microwave Conf*., Amsterdam, Holland, pp. 147-150, 2008.

[13] B. Fuchs, S. Palud, O. Lafond, M. Himdi, and S. Rondineau, "Système antennaire dont le diagramme de rayonnement est reconfigurable parmi des diagrammes de rayonnement sectoriels et directifs, etdispositifs émetteur et/ou récepteur correspondant," *French Patent 0756664*, July 20, 2007.

[14] M. A. Belen and P. Mahouti, "Design and realization of quasi Yagi antenna for indoor application with 3D printing technology," *Microw. Opt. Technol. Lett*., vol. 60, no. 9, pp. 2177-2181, 2018. https://doi.org/10.1002/mop.31319

[15] P. Mahouti, F. Güneş, M. A. Belen, and A. Çalışkan, "A novel design of non-uniform reflectarrays with symbolic regression and its realization using 3-D printer," *Applied Computational Electromagnetics Society Journal*, vol. 34, no. 2, 2019.

[16] J. J. Adams, E. J. Duoss, T. Malkowski, M. Motala, B. Y. Ahn, R. G. Nuzzo, J. T. Bernhard, and J. A. Lewis, "Conformal printing of electrically small antennas on three-dimensional surfaces," *Advanced Materials*, vol. 23, no. 11, pp. 1304-1413, 2011.

[17] G. Shaker, L. Ho-Seon, S. Safavi-Naeini, and M. Tentzeris, "Printed electronics for next generation wireless devices," *IEEE Antenna and Propagation Conference (LAPC)*, pp. 1-5, Nov. 2011.

[18] J. Mei, M. Lovell, and M. Mickle, "Formulation and processing of novel conductive solution inks in continuous inkjet printing of 3-D electric circuits," *IEEE Transactions on Electronics Packaging Manufacturing*, vol. 28, no. 3, pp. 265-273, July 2005.

[19] G. Shaker, S. Safavi-Naeini, N. Sangary, and M. Tentzeris, "Inkjet printing of ultrawideband (UWB) antennas on paper based substrates," *Antennas and Wireless Propagation Letters, IEEE*, vol. 10, pp. 111-114, 2011.

[20] J. Hester, S. Kim, J. Bito, T. Le, J. Kimionis, D. Revier, C. Saintsing, W. Su, B. Tehrani, A. Traille, B. S. Cook, and M. M. Tentzeris, "Additively manufactured nanotechnology and origami-enabled flexible microwave electronics," *Proc. IEEE*, vol. 103, no. 4, pp. 583-606, pr. 2015.

[21] J. Kimionis, A. Georgiadis, M. Isakov, H. J. Qi, and M. M. Tentzeris, "3D/inkjet-printed origami antennas for multi-direction RF harvesting," in *IEEE MTT-S Int. Microw. Symp. (IMS)*, Phoenix, AZ, USA, pp. 1-4, May 2015.

[22] R. Martinez, et al., "Planar monopole antennas on substrates fabricated through an additive manufacturing process," *in 9th Eur. Conf. Antennas and Propag. (EuCAP)*, Lisbon, Portugal, Apr. 2015.

[23] B. Tehrani, B. S. Cook, and M. M. Tentzeris, "Post-process fabrication of multi-layer mm-wave on-package antennas with inkjet printing," in *2015 IEEE Int. Symp. Antennas and Propag. (APSURSI)*, Vancouver, BC, Canada, July 2015.

[24] F. Karshenas, A. R. Mallahzadeh, and A. Imani,

"Modified TEM horn antenna for wideband applications," in *2009 13th International Symposium on Antenna Technology and Applied Electromagnetics and the Canadian Radio Science Meeting, IEEE*, pp. 1-5, Feb. 2009.

[25] E. Lier and P. S. Kildal, "Soft and hard horn antennas," *IEEE Trans. Antennas Propag*., vol. 36, no. 8, pp. 1152-1157, 1988.

[26] E. Lier, "Review of soft and hard horn antennas, including metamaterial based hybrid-mode horns," *IEEE Trans. Antennas Propag. Mag*., vol. 52, no. 2, pp. 31-39, 2010.

[27] A. J. Simmons and A. F. Kay, "The scalar feed – A high performance feed for large paraboloid reflectors," in *Design and Construction of Large Steerable Aerials*, vol. 21, pp. 213-217, 1966.

[28] H. Minnett and B. Thomas, "A method of synthesizing radiation patterns with axial symmetry," *IEEE Trans. Antennas Propag*., vol. 14, no. 5, pp. 654-656, 1966.

[29] V. Rumsey, "Horn antennas with uniform power patterns around their axes," *IEEE Trans. Antennas Propag*., vol. 14, no. 5, pp. 656-658, 1966.

[30] P. J. B. Clarricoats, A.D. Olver, and M. S. A. S. Rizk, "A dielectric loaded conical feed with low cross-polar radiation," *Proc. URSI Symp. Electromagnetic Theory*, Santiago, Spain, pp. 351-354, Aug. 1983.

[31] E. Lier and T. Schaug-Pettersen, "The strip-loaded hybrid-mode feed horn," *IEEE Trans. Antennas Propag*., vol. 35, no. 9, pp. 1086-1089, 1987.

[32] M. A. Belen, P. Mahouti, and M. Palandöken, "Design and realization of novel frequency selective surface loaded dielectric resonator antenna via 3D printing technology," *Microwave and Optical Technology Letters*, vol. 62, no. 5, pp. 2004-2013, 2020.

[33] M. A. Belen and P. Mahouti, "Design of nonuniform substrate dielectric lens antennas using 3D printing technology," *Microwave and Optical Technology Letters*, vol. 62, no. 2, pp. 756-762, 2020.

[34] A. Belen, F. Güneş, P. Mahouti, and M. Palandöken, "A novel design of high performance multi-layered cylindrical dielectric lens antenna using 3D printing technology," *International Journal of RF and Microwave Computer-Aided Engineering*, vol. 30, no. 1, e21988, 2020.

[35] M. A. Belen and P. Mahouti, "Realization of dielectric sheets for gain improvement of ultra-wideband horn antennas using 3D printer technology," *Applied Computational Electromagnetics Society Journal*, vol. 34, no. 5, 2019.

[36] P. Mahouti, M. A. Belen, F. Güneş, and R. Yurt, "Design and realization of multi-layered cylindrical dielectric lens antenna using 3D printing technology," *Microwave and Optical Technology Letters*, vol. 61, no. 5, pp. 1400-1403, 2019.

[37] M. Misaghi and M. Yaghoobi, "Improved invasive weed optimization algorithm (IWO) based on chaos theory for optimal design of PID controller," *Journal of Computational Design and Engineering*, vol. 6, no. 3, pp. 284-295, 2019.

[38] S. Karimkashi and A. A. Kishk, "Invasive weed optimization and its features in electromagnetics," *IEEE Transactions on Antennas and Propagation*, vol. 58, no. 4, pp. 1269-1278, 2010.

[39] S. Maddio, G. Pelosi, M. Righini, S. Selleri, and I. Vecchi, "Optimization of the shape of non-planar electronically scanned arrays for IFF applications via multi-objective invasive weed optimization algorithm," *Applied Computational Electromagnetics Society Journal*, 2020.

[40] A. R. R. Mallahzadeh, H. Oraizi, and Z. Davoodi-Rad, "Application of the invasive weed optimization technique for antenna configurations," *Progress in Electromagnetics Research*, vol. 79, pp. 137-150, 2008.

[41] M. Hayati, M. Amiri, and S. H. Sedighy, "Design of compact and wideband suppression low pass elliptic filter by n-segment step impedance transmission line," *Applied Computational Electromagnetics Society Journal*, vol. 30, no. 5, 2015.

[42] A. R. Mallahzadeh and P. Taghikhani, "Cosecant squared pattern synthesis for reflector antenna using a stochastic method," *Applied Computational Electromagnetics Society Journal*, vol. 26, no. 10, pp. 823, 2011.

[43] H. R. Khakzad, S. H. Sedighy, and M. K. Amirhosseini, "Design of compact SITLs low pass filter by using invasive weed optimization (IWO) technique," *Applied Computational Electromagnetics Society Journal*, vol. 28, no. 3, pp. 228-233, 2013.

[44] A. Belen, F. Güneş, and P. Mahouti, "Design optimization of a dual-band microstrip SIW antenna using differential evolutionary algorithm for X and K-band radar applications," 2020.

[45] A. Belen, F. Güneş, M. A. Belen, and P. Mahouti, "3D printed wideband flat gain multi-layer nonuniform reflectarray antenna for X-band applications," *International Journal of Numerical Modelling: Electronic Networks, Devices and Fields*, e2753, 2020.

[46] O. S. Kim, "Rapid prototyping of electrically small spherical wire antennas," *Antennas and Propagation, IEEE Transactions*, vol. 62, no. 7, pp. 3839-3842, 2014.

[47] Available on 19.6.2018. http://cel-uk.com/3d-printer/rbx01-480.html

[48] Available on 21.11.2018. http://cel-uk.com/3d-printer/filament/pla/rbx-pla-wh002.html

[49] S. Zhang, C. C. Njoku, W. G. Whittow, and J. C.

Vardaxoglou, "Novel 3D printed synthetic dielectric substrates," *Microw. Opt. Technol. Lett.*, vol. 57, pp. 2344-2346, 2015. doi:10.1002/mop.29324.

[50] P. Mahouti, "Boyutlu Yazıcı Teknolojisi ile Bir Mikroşerit Yama Antenin Maliyet Etkin Üretimi," *Journal of Engineering Sciences and Design*, Kabul Edildi, 2019. (in Turkish).

[51] LB8180, "0.8-18 GHz broadband horn antenna," Aug. 14 2017. Available at: http://www.ainfoinc.com/en/p_ant_h_brd.asp

[52] A. S. Türk, A. K. Keskin, and M. D. Şentürk, "Dielectric loaded TEM horn-fed ridged horn antenna design for ultrawideband ground-Penetrating impulse radar," *Turkish J. Elec. Eng. & Comp. Sci*., vol. 23, pp. 1479-1488, 2015.

[53] R. J. Bauerle, R. Schrimpf, E. Gyorko, and J. Henderson, "The use of a dielectric lens to improve the efficiency of a dual-polarized quad-ridge horn from 5 to 15 GHz," *IEEE Transactions on Antennas and Propagation*, vol. 57, no. 6, June 2009.

[54] J. Tak, D.-G. Kang, and J. Choi, "A lightweight waveguide horn antenna made via 3d printing and conductive spray coating," *Microwave and Optical Technology Letters*, vol. 59, no. 3, Mar. 2017.

[55] M. F. Ain, A. Othman, and Z. A. Ahmad, "Hybrid dielectric resonator integrated pyramidal horn antenna," *Microwave and Optical Technology Letters*, vol. 55, no. 6, June 2013.

Aysu Belen received her Ph.D. degree in Electronics and Communication Engineering from the Yıldız Technical University in 2021. Currently, she is a Lecturer in İskenderun Technical University. Her main research areas are optimization of microwave circuits, circuits, device modeling, and computer aided circuit design and microwave amplifiers.

Peyman Mahouti received his M.Sc. and Ph.D. degree in Electronics and Communication Engineering from the Yıldız Technical University, Turkey, in 2013 and 2016, respectively. He is currently an Associated Professor with the Department of Electronic and Communication, Istanbul University - Cerrahpasa, Turkey. The main research areas are analytical and numerical modelling of microwave devices, optimization techniques for microwave stages, and application of artificial intelligence-based algorithms. His research interests include analytical and numerical modelling of microwave and antenna structures, surrogate-based optimization, and application of artificial intelligence algorithms.

Filiz Güneş received her M.Sc. degree in Electronics and Communication Engineering from the Istanbul Technical University. She attained her Ph.D. degree in Communication Engineering from the Bradford University in 1979. Her current research interests are in the areas of multivariable network theory, device modeling, computer-aided microwave circuit design, monolithic microwave integrated circuits, and antenna designs.

Özlem Tari received her B.Sc., M.Sc. and Ph.D. in Physics Engineering from the Istanbul Technical University (ITU). She was the recipient of the Universidad Carlos III de Madrid Research Fellowship award before accepting her position at Istanbul Arel University in 2010. Her research areas are the phase transitions and phase diagram of some physical systems, Multi-Objective Optimization problems and development of Meta-Heuristic Optimization Algorithms.

A New Metasurface Structure for Bandwidth Improvement of Antenna Array

Lan Ngoc Nguyen

Faculty of Electronics and Telecommunications
Saigon University, Vietnam
nnlan@moet.edu.vn

Abstract ─ In this paper, the design of an antenna array with enhanced bandwidth is presented. The antenna array includes 16 elements (4 x 4) based on RT5880 with height of 1.575 mm, dielectric constant of 2.2 and loss tangent of 0.0009 and it is yielded at the central frequency of 5.8 GHz for Wireless Local Area Network (WLAN) applications. In addition, in order to enhance bandwidth for antenna, the paper proposes a new metasurface. The metasurface, which is a lattice of 3 x 3 cells, is printed on a substrate of FR4 (h = 1.6 mm, ε_r = 4.4, and tanδ = 0.02) and it acts as an artificial magnetic conductor reflector. The final prototype with an overall dimension of 123 x 120 x 3.315 mm^3 was fabricated and measured. The antenna witnesses an impedance bandwidth of 5.1-7.5 GHz at -10 dB (41%) and a peak gain of 17.65 dBi for measurement. The simulation results are confirmed by measurement ones to verify the performance of the proposed antenna.

Index Terms ─ Array antenna, bandwidth enhancement, metasurface.

I. INTRODUCTION

The antenna plays an important role in wireless systems and a good design of the antenna can satisfy system requirements and improve overall system performance. However, due to limitation of space for antenna in modern communication systems, microstrip antennas [1] are preferred thanks to their advantages such as small size, low cost and profile, easy fabrication and integration. Besides the above advantages, there are some limitations in microstrip antennas that narrow bandwidth, low gain and efficiency are their main drawbacks.

Moreover, Wireless Local Area Network (WLAN) is one of the most popular applications in the wireless communication field. In these applications, antennas with high gain are always required in order to satisfy the demand for long distance communication. Therefore, the improvement for parameters including gain and bandwidth of WLAN antenna is very necessary.

Besides, metasurface can be considered a new version of metamaterial [2]. Compared to metamaterial, metasurface has some advantages including less losses, planar structure and easy for fabrication while they consist of the same characteristics. Currently, thanks to its flexible features is listed in [3], metasurface is becoming more and more popular in a lot of different applications such as cloak [4], imaging [5], absorber [6], beamforming [7] and so on [7] - [8]. For antenna, using metasurface can divide into two types: the first type, the antennas are placed above metasurface [10]. In this case, metasurface includes a metallic lattice and it acts as an artificial reflector. Meanwhile, for the second type, the antennas are located under metasurface [11]. The operation principle of these two types is found in [12]. Recently, many papers have been published to improve performance for antennas [13]–[16]. In [13], a broadband multi-feed tightly coupled patch array antenna is proposed with the bandwidth percentage of 41.3%; however, the peak gain of antenna is only 11.2 dBi. In [14], although a substrate-integrated-waveguide antenna array is designed at frequency of 28 GHz, the bandwidth percentage is only 8.2%. In addition, the peak gain of the fabricated antenna is 13.97 dBi. In other paper [15], a wideband tightly-coupled compact array of dipole antennas arranged in triangular lattice has achieved the bandwidth percentage at -5 dB of 96.3%, but the peak gain is only 16.4 dBi. With paper [16], a hybrid array antenna for millmeter-wave applications at frequency of 30 GHz; however, the percentage of bandwidth is only 13.3%.

For the above reason, an antenna array of 4 x 4 with enhanced bandwidth by using metasurface is presented in this paper. Metasurface composes a new metamaterial structure arranged into a lattice of 3 x 3 based on a substrate layer of FR4. The dimension of the proposed antenna is 120 x 123 x 3.315 mm^3 with a 10dB impedance bandwidth of 41% (respect to the frequency of 5.8 GHz) and a peak gain of 17.65 dBi for measurement. In addition, the antenna remains a high radiation efficiency of 71% at the central frequency. The antenna has been modeled numerically by the software of Computer Simulation Technology Microwave Studio (CST MS) and verified through measurement results to confirm the performance of the proposed antenna.

Submitted On: July 6, 2020
Accepted On: January 18, 2021

https://doi.org/10.47037/2020.ACES.J.360204

II. ANTENNA DESIGN AND CHARACTERISTICS

A. The proposed metasurface

First of all, the model of a cell in the proposed metasurface and its equivalent circuit are shown in Fig 1. The proposed model includes a square and a quadrangle, in which the square is outside and the quadrangle is inside. Moreover, to make parasitic capacitors, these shapes are truncated in the middle while the microstrip lines are placed inside of the quadrangle to make inductors. Meanwhile, the proposed metasurface is a lattice of 3 x 3 cells as illustrated in Fig. 2 (a). The metasurface is located on a FR4 substrate with parameters: h = 1.6 mm, ε_r = 4.4, and tanδ = 0.02. The total size of the metasurface is 123 x 120 x 3.315 mm^3 whereas the one of cell is 26.5 x 26.5 x 0.035 mm^3 (0.035 is the thickness of copper layer). The distance between cells is 41 mm. Table 1 shows some parameters of the proposed metasurface whereas the reflection phase of the metasurface is given in Fig. 2 (b). It is observed that the reflection phase is 0^o at the central frequency of 5.8 GHz.

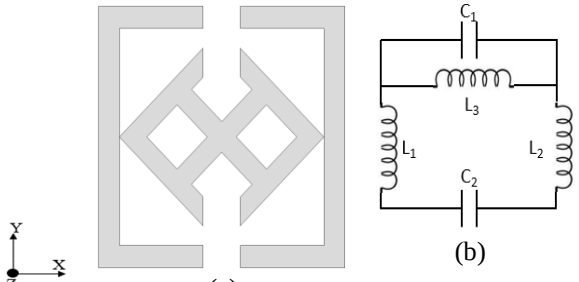

Fig. 1. The model of the proposed metasurface (a); equivalent circuit (b) (dark colour for metal and light colour for substrate).

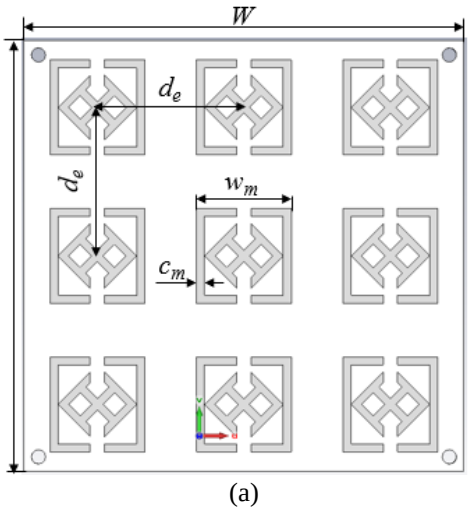

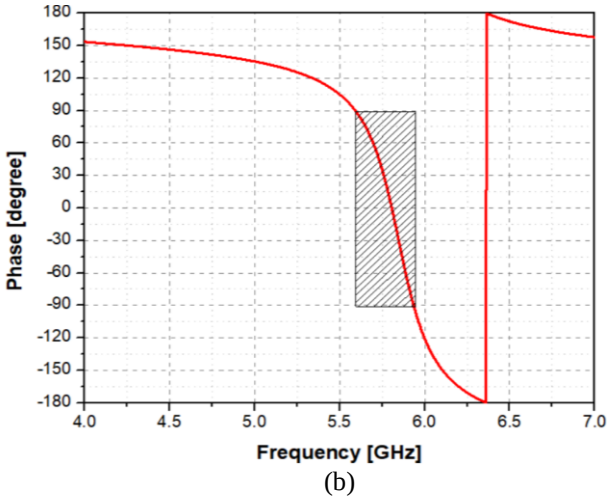

Fig. 2. Geometry of the proposed metasurface (a); the reflection phase (b).

Table 1: Optimized parameters of the proposed metasurface (mm)

W	L	d_e	w_m	c_m	r	w_c
123	120	41	26.5	4.5	11	4

B. Antenna geometry

Figure 3 depicts the geometry of the proposed antenna array. The antenna consists of 16 microstrip elements (4 x 4), a feeding network, two dielectric layers, the ground plane and a connector of 50 Ohm. The elements, feeding network and the cells of the metasurface are printed on the top side of the first and the second substrate, respectively. Each single element is composed of a truncated corner square patch with the size of w_c while the distance between elements is about 30.5 mm. The two selected dielectric substrates in this paper are Roger RT/Duroid^{TM} 5880 substrate (h = 1.575 mm, ε_r = 2.2, and tanδ = 0.0009) and FR4 (h = 1.6 mm, ε_r = 4.4, and tanδ = 0.02). The feeding network includes 14 equal power dividers to distribute power to elements. The dimension of array is 120 x 123 x 3.315 mm^3. The antenna is implemented for WLAN applications at the frequency of 5.8 GHz. Table 2 shows some parameters of the proposed antenna.

Table 2: The parameters of the proposed antenna (mm)

W	L	d	w_p	l_p	w_s	l_s
123	120	30.5	19	13	0.5	2.75
l_{s1}	w_{s1}	w_c	w_f			
4	0.6	5.2	1.45			

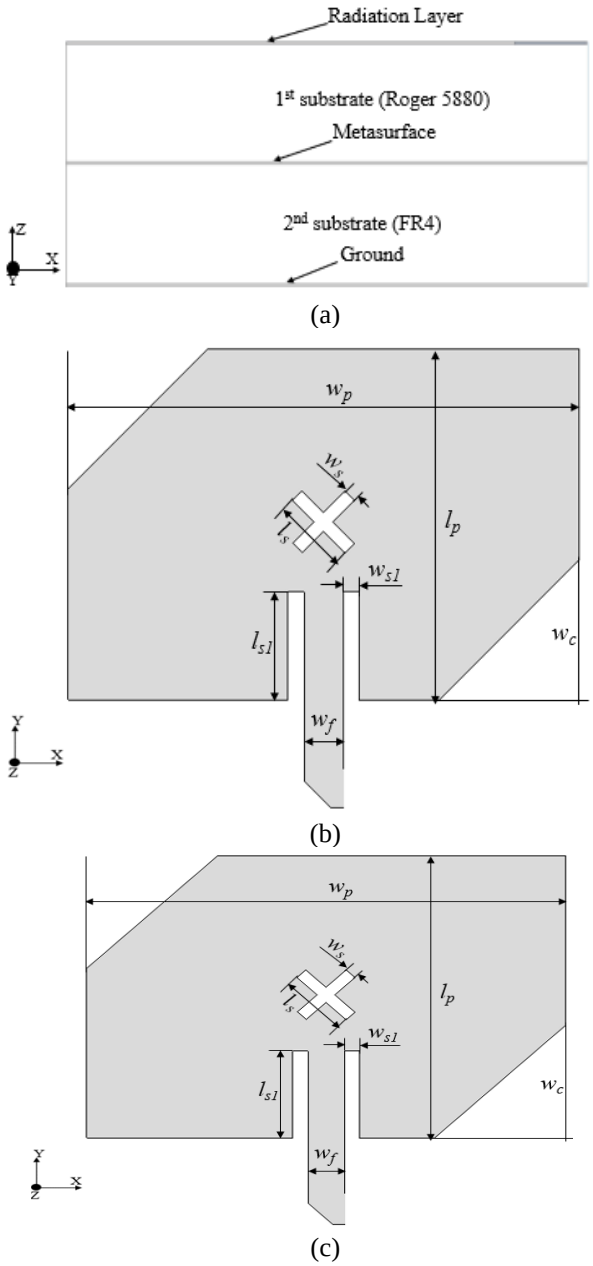

Fig. 3. The model of the proposed antenna: side view (a); the model of array (b); the geometry of an element (c).

III. ANTENNA OTIMIZATION

As mentioned above, the goal of using metasurface in this paper is to enhance bandwidth by generating extra-resonances. Therefore, this section will concentrate to investigate the effect of metasurface to reflection coefficient. To clarity these mechanisms, some key parameters of the proposed antenna are studied and illustrated in Fig. 4.

Figure 4 (a) shows two values of reflection coefficient in two case with and without metasurface of the antenna array. It is observed that the presence of metasurface generated consecutive extra-resonances [17] and as a result, the bandwidth is significantly expanded. This can see that with the presence of metasurface, the number of resonances is four while this value is only one without metasurface. Therefore, the bandwidth percentages with and without metasurface are 29% and 2.5%, respectively.

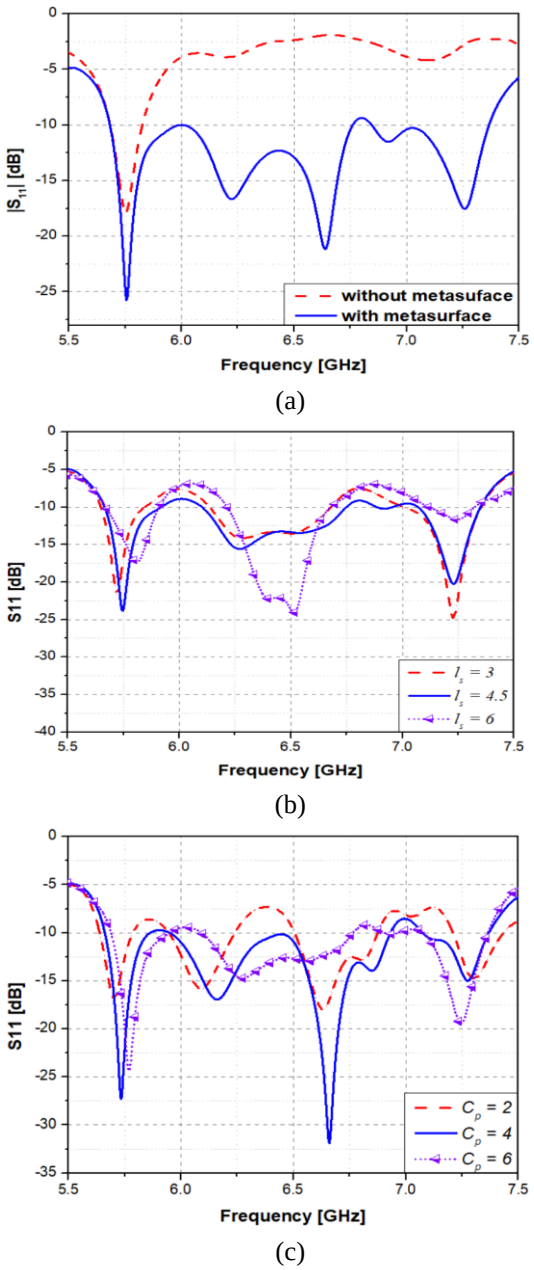

Fig. 4. The simulated result of reflection coefficient versus the change of parameters: (a) with and without metasurface; (b) different slot lengths; (c) cutting at four corners of patch with different dimensions.

Figure 4 (b) displays the simulated S11 for different slot length of the patch. There are many various types of impedance matching including microstrip line feed, probe feed, aperture-coupled feed, and proximity-coupled feed [18]. For microstrip line feed type, the principle for impedance matching is to find point where the impedance is 50 Ohm. Therefore, the reflection coefficient will achieve the best value when it finds the closest value to 50 Ohm. As shown in Fig. 4 (b), by increasing ls, the slot length (ls) from 3 to 4.5, there is an improvement in impedance matching whereas the slot length is 6, the impedance is not as good as the two above cases.

To achieve broadband impedance bandwidth, the cut at four corners of patch is implemented. Figure 4 (c) shows the effect of the cut at four corners of patch with different dimensions. Like as the effect of patch length, with increasing the cut dimension at four corners of patch (C_p), the impedance matching shifted toward the higher frequency. However, while the value of C_p is 4 and this is the best for impedance matching.

IV. RESULTS AND DISCUSSION

To confirm the performance of the proposed antenna, the prototype of the antenna was fabricated and shown in Fig. 5. The size of antenna is 123 x 120 x 3.315 mm^3. The antenna is fabricated on Roger5880 (h =1.575 mm, ε_r = 2.2, and tanδ = 0.0009) while metasurface is based on FR4 (h =1.6 mm, ε_r = 4.4, and tanδ = 0.02). Fig. 6 illustrates the simulated results of the proposed antenna. Observe Fig. 6 (a), we can see that the bandwidth of the proposed antenna at -10 dB covers from 5.68 to 7.36 GHz for simulation while this value is from 5.1 to 7.5 GHz for measurement and it corresponds to 29% and 41.3%, respectively. Here, there is a difference between simulation and measurement results. The reason of this tolerance can be contributed from the instability of the FR4 substrate, an undesired air between two substrate layers and the tolerance in fabrication. However, there is a similarity between the shape of measurement and simulation results and the operating frequency range is ensured. Therefore, this tolerance is acceptable.

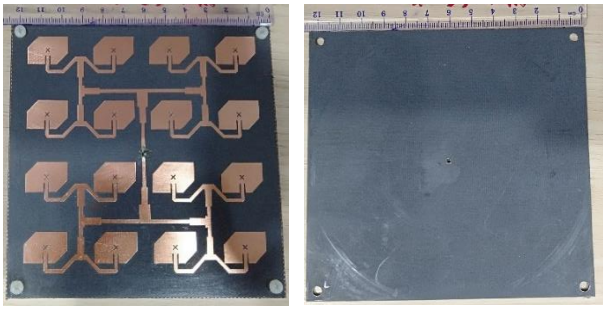

(a)

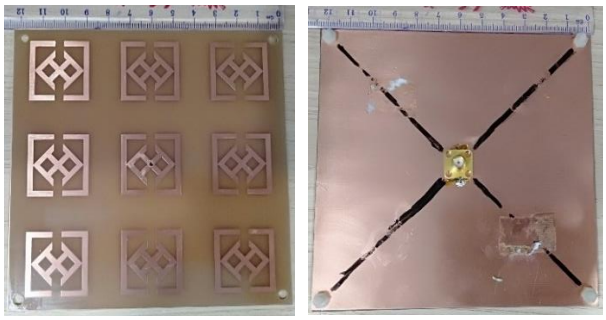

(b)

Fig. 5. The model of the fabricated antenna: (a) antenna array and (b) metasurface.

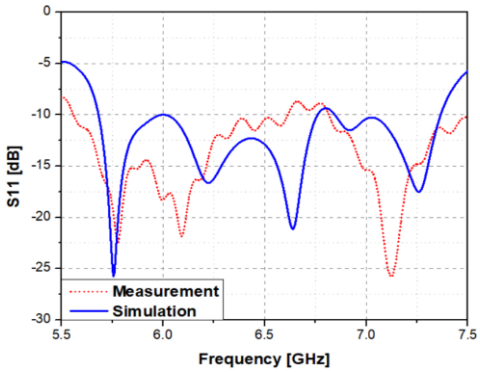

(a)

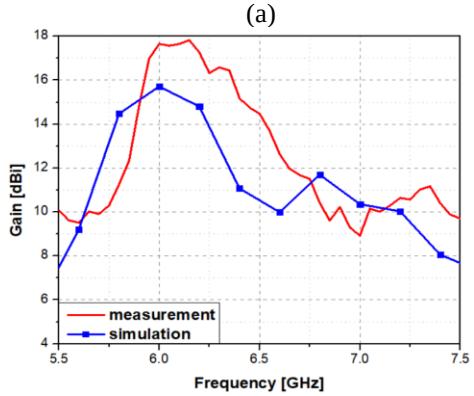

(b)

Fig. 6. The reflection coefficient (a); and gain of the proposed antenna (b).

Switch to Fig. 6 (b), we can see that the peak gain of antenna for measurement is 17.65 dBi at frequency of 6 GHz while this figure for simulation is 15.7 dBi. In this case, the measurement result is better that simulation one. This can be explained due to the effect of multipath signal. When there are many in-phased multipath signals, then the total signal is the sum of all signals. As a result, the measurement gain is better simulation one. Therefore, this difference is acceptable.

Figure 7 shows measured and simulated results in xz and yz planes. Observe Fig. 7, we can see that the measurement in yz plane is better and close to simulation result. Although there are differences between simulated and measured results in xz and yz planes, the direction of main lobe in two cases is not changed.

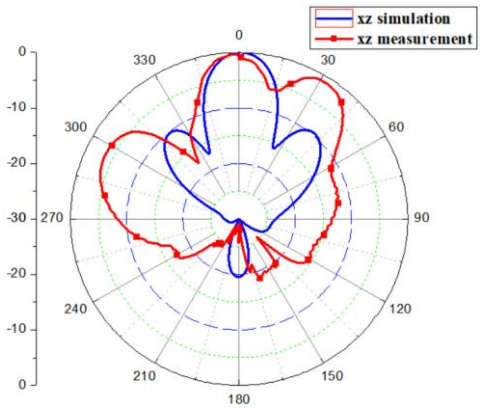

(a)

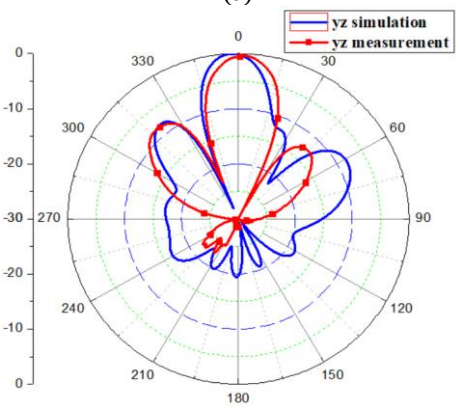

(b)

Fig. 7. The simulation and measurement results of radiation pattern: (a) xz plane and (b) yz plane.

Table 3: The comparison between the performance of the proposed antenna with recent antennas

References	[18]	[19]	[20]	[21]	**My work**
Number of elements	16	17	32	10	**16**
Frequency [GHz]	5.3	12	84.25	10	**5.8**
Bandwidth [%]	17	52.2	13.89	< 3	**41.3**
Efficiency [%]	x	64	82	x	**71**
Gain [dBi]	15	20.3	19.6	11.8	**17.65**
Size (λ)	2.33 x 2.33	1200 x 9200 x 440	x	2.5 x 1.06 x 0.027	**2.378 x 2.32 x 0.006**

Table 3 compares the performance of the proposed antenna with recent antennas. From Table 3, we can see that an antenna array including 16 elements is yielded at 5.3 GHz; however, the impedance bandwidth and gain are not high (17% and 15 dBi) [18]. Similarly, the percentage of bandwidth and gain in the antenna in [21] are not high (3% and 11.8 dBi) although antenna consists of 10 elements and is implemented at 10 GHz. In another proposal [19], although the antenna has a large bandwidth percentage and high gain (52.2% and 20.3 dBi) when the antenna is designed at 12 GHz (17 elements), the efficiency of antenna is not good (64%). In addition, an antenna of 32 elements operates at the center frequency of 84.25 GHz; however, the bandwidth percentage is only 13.89% [20].

V. CONCLUSION

A method for enhancing the bandwidth for antenna array by using metasurface is presented in this paper. The antenna comprises 16 elements placed RT5880 (h = 1.575 mm, εr = 2.2, and tanδ = 0.0009) and metasurface is implemented FR4 (h = 1.6 mm, εr = 4.4, and tanδ = 0.02). The final prototype with overall dimension of 123 x 120 x 3.315 mm3 accomplished a bandwidth percentage of 41% and a gain of 17.65 dBi (for measurement). Moreover, the efficiency of antenna achieves 71%. With benefits including simple configuration, ease for fabrication, integration and low cost, the proposed antenna can be widely used in WLAN applications.

ACKNOWLEDGEMENTS

Thanks to Mr. Nguyen Minh Thien and Laboratory of Monolithic Microwave Integrated Circuit (MMIC) & Applications for Embedded Systems - International University, VNU HoChiMinh City, Vietnam supported us in antenna measurement.

REFERENCES

[1] K. F. Lee and K. F. Tong, "Microstrip patch antennas basic characteristics and some recent advances," *Proceedings of the IEEE*, vol. 100, no. 7, pp. 2169-2180, 2012.

[2] N. Rajak and N. Chattoraj, "A bandwidth enhanced metasurface antenna for wireless applications," *Microwave and Optical Technology Letters*, vol. 59, no. 10, pp. 2575-2580, 2017.

[3] C. L. Holloway, E. F. Kuester, J. A. Gordon, J. O'Hara, J. Booth, and D. R. Smith, "An overview of the theory and applications of metasurfaces: The two-dimensional equivalents of metamaterials," *IEEE Antennas and Propagation Magazine*, vol. 54, no. 2, pp. 10-35, 2012.

[4] P. Y. Chen, J. Soric, Y. R. Padooru, H. M. Bernety, A. B. Yakovlev, and A. Alù, "Nanostructured graphene metasurface for tunable terahertz

cloaking," *New Journal of Physics*, vol. 15, p. 123029, 2013.

[5] J. A. Goldstein and D. R. Englund, "Imaging Metasurfaces based on Graphene-Loaded Slot Antennas," *arXiv preprint arXiv:2004.06777*, 2020.

[6] T. Badloe, J. Mun, and J. Rho, "Metasurfaces-based absorption and reflection control: Perfect absorbers and reflectors," *Journal of Nanomaterials*, vol. 2017, 2017.

[7] L. Bao, R. Y. Wu, X. Fu, Q. Ma, G. D. Bai, J. Mu, R. Jiang, and T. J. Cui, "Multi-beam forming and controls by metasurface with phase and amplitude modulations," *IEEE Transactions on Antennas and Propagation*, vol. 67, no. 10, pp. 6680-6685, 2019.

[8] Í. Ederra Urzainqui, A. Tellechea Pereda, F. Caminita, E. Martini, J. C. Iriarte Galarregui, R. Gonzalo García, and S. Maci, "Dual circularly polarized broadside beam metasurface antenna," *IEEE Transactions on Antennas and Propagation*, vol. 64, no. 7, pp. 2944-2953. 2016.

[9] M. Yan, S. Qu, J. Wang, J. Zhang, A. Zhang, S. Xia, and W. Wang, "A novel miniaturized frequency selective surface with stable resonance," *IEEE Antennas and Wireless Propagation Letters*, vol. 13, no. c, pp. 639-641, 2014.

[10] J. Li, T. A. Khan, J. Chen, M. U. Raza, and A. Zhang, "Design of low RCS circularly polarized patch antenna array using metasurface for CNSS adaptive antenna applications," *Materials*, vol. 12, no. 12, 2019.

[11] S. X. Ta and I. Park, "Compact wideband circularly polarized patch antenna array using metasurface," *IEEE Antennas and Wireless Propagation Letters*, vol. 16, no. c, pp. 1932-1936, 2017.

[12] S. X. Ta, Q. S. Ho, K. K. Nguyen, and C. Dao-Ngoc, "Single-dipole antenna on a metasurface for broadband circularly polarized radiation," *Journal of Electromagnetic Waves and Applications*, vol. 32, no. 4, pp. 413-427, 2018.

[13] X. Yang, P. Y. Qin, Y. Liu, Y. Z. Yin, and Y. J. Guo, "Analysis and design of a broadband multifeed tightly coupled patch array antenna," *IEEE Antennas and Wireless Propagation Letters*, vol. 17, no. 2, pp. 217-220, 2018.

[14] S. J. Park, D. H. Shin, and S. O. Park, "Low side-lobe substrate-integrated-waveguide antenna array using broadband unequal feeding network for millimeter-wave handset device," *IEEE Transactions on Antennas and Propagation*, vol. 64, no. 3, pp. 923-932, 2016.

[15] A. K. Awasthi and A. R. Harish, "Wideband tightly-coupled compact array of dipole antennas arranged in triangular lattice," *International Journal of Microwave and Wireless Technologies*, vol. 11, no. 4, pp. 382-389, 2019.

[16] S. Costanzo, I. Venneri, G. Di Massa, and G. Arriendola, "Hybrid array antenna for broadband millimeter-wave applications," *Progress in Electromagnetics Research*, vol. 83, pp. 173-183, 2008.

[17] S. X. Ta, V. Du Le, K. K. Nguyen, and C. Dao-Ngoc, "Planar circularly polarized X-band array antenna with low sidelobe and high aperture efficiency for small satellites," *International Journal of RF and Microwave Computer-Aided Engineering*, vol. 29, no. 11, pp. 1-9, 2019.

[18] C. E. Santosa, J. T. Sri Sumantyo, C. M. Yam, K. Urata, K. Ito, and S. Gao, "Subarray design for C-band circularly-polarized synthetic aperture radar antenna onboard airborne," *Progress in Electromagnetics Research*, vol. 163, no. August, pp. 107-117, 2018.

[19] S. Kim and S. Nam, "A compact and wideband linear array antenna with low mutual coupling," *IEEE Transactions on Antennas and Propagation*, vol. 67, no. 8, pp. 5695-5699, 2019.

[20] Z. C. Hao, Q. Yuan, B. W. Li, and G. Q. Luo, "Wideband W-band substrate-integrated waveguide magnetoelectric (ME) dipole array antenna," *IEEE Transactions on Antennas and Propagation*, vol. 66, no. 6, pp. 3195-3200, 2018.

[21] B. Singh, N. Sarwade, and K. P. Ray, "Compact series FED tapered antenna array using unequal rectangular microstrip antenna elements," *Microwave and Optical Technology Letters*, vol. 59, no. 8, pp. 1856-1861, 2017.

Lan Ngoc Nguyen received Ph.D. degree from School of Electronics and Telecommunications, Hanoi University of Science and Technology in 2019. Currently, she is a Lecturer at Faculty of Electronics and Telecommunications, Saigon University. Her research interests are microstrip antenna, mutual coupling, MIMO antennas, array antennas, reconfigurable antennas, polarization antennas, metamaterial, metasurface. ORCID: https://orcid.org/0000-0001-8506-9979.

A Compact CPW-Fed UWB Antenna with Dual-Band Notched Characteristics for WiMAX/WLAN Applications

Rabah W. Aldhaheri [1], Ibrahim S. Alruhaili [1], Kamili J. Babu [2], and Muntasir M. Sheikh [1]

[1] Department of Electrical and Computer Engineering
King Abdulaziz University, Jeddah 21589, Saudi Arabia
raldhaheri@kau.edu.sa, ibra.s.s@hotmail.com, mshaikh@kau.edu.sa

[2] Department of Electronics & Communication Engineering
St. Ann's College of Engineering & Technology, Chirala, India
jagan_ec@yahoo.com

Abstract ─ A dual-notched bands ultra-wideband (UWB) antenna with coplanar waveguide (CPW) fed is presented in the paper. The two notched bands are selected at 3.5 and 5.8 GHz frequencies to overcome the interference from WiMAX and WLAN bands. The overall size of the antenna is 17.5×17.5 mm^2, which can be considered as one of the smallest UWB antennas in the literature. The developed antenna has an impedance band width ranging from 2.9 to 13 GHz. The measured radiation patterns on E and H planes are nearly omni-directional and stable with acceptable gain over the entire band. The dual-band notched at WiMAX and WLAN is created by embedding I-shaped and C-shaped stubs in the radiation patch of the antenna. Due to the compactness, good radiation patterns and the reasonable stable gain, this antenna is well suited for integration into portable wireless communications devices for UWB applications.

Index Terms ─ CPW fed antenna, dual-band-notched characteristics, Ultra-Wideband (UWB), C-shaped stub.

I. INTRODUCTION

The federal communications commission (FCC) permitted 3.1 GHz to 10.6 GHz band for unlicensed civil applications with a good radiation power [1]. Since then, ultra-wideband (UWB) technology is one of the most promising wireless technologies owing to its high data rate, low power consumption, and increased flexibility to multipath interference. Microstrip feeding with full or partial ground and CPW-fed antenna are widely used for designing UWB Antennas of bandwidth ranging from 3.1 to 10.6 GHz. Over this band, there are several narrow band wireless communication systems, such as WiMAX (3.3–3.7 GHz) and WLAN (5.15–5.875 GHz), and the downlink of X-band satellite system (7.25-7.85 GHz), etc. [2, 3]. So, in order to overcome the interference with these narrow bands, a new UWB antennas design with band-notched characteristics were presented to filter out the interferences caused by the narrow bands wireless systems [2-17]. Many of these techniques used various types of slots in the radiating patch or/and in the ground to create the notch band at certain frequency bands. Some of these designs fail to achieve the desired notched bands and some designs have complex structures to generate notched band at certain bands. In [2], a comprehensive review for achieving band notch characteristics in UWB using different techniques such as etching slots, parasitic element, metamaterials and electromagnetic band gap (EBG) are discussed. In [3 – 6], a single band notched is created by etching certain shapes in the radiating patch or in the ground.

In [7 – 14], dual-band notched UWB antennas were presented where E-shaped, L-shaped, C-shaped or inverted C-shaped, split rings are employed to create notches in in the WiMAX and WLAN bands. In these examples the structures are more complicated and with bigger size. In [9], the overall size is 29 X 20.5 mm^2, but the structure is more complicated than our structure and controlling the notched bands needs more than one factor and it might require a major change in the antenna structure. The antenna proposed in [10] covers the WLAN 2.4/5.8 GHz and the WiMAX band at 3.5 GHz, but the size is 38 X 20 mm^2. In [11], an octagonal-shaped UWB with Minkowski fractal notch and dual C-shaped notch at the either side of the feed line for rejection of the WLAN band is presented and the size of this antenna is 26 X 16.5 mm^2. In [12-14], triangular patch and double rectangular ring-shaped were suggested, but the dimensions are still big and the structures are more complex.

In [15 - 17], triple notch band characteristics are achieved by adding two modified S-shaped cells on either side of Microstrip line as in [15], or etching open-ended L-shaped slot in the ground plane for notching the downlink of the X-band [7.25-7.85 GHz] as in [16], or by adding two separated quarter-wavelength strips in the

Submitted On: October 18, 2020
Accepted On: December 5, 2020

https://doi.org/10.47037/2020.ACES.J.360205

patch and etching a half wavelength hook-shaped slot on the ground as in [17].

In this paper, a very compact, simple and low cost CPW-fed UWB antenna design is presented and analyzed. The characteristic of this antenna is investigated numerically and experimentally. A dual-band notched at WiMAX and WLAN is created by embedding I-shaped and C-shaped stubs in the radiation patch of the antenna. The center frequency and the band of the WLAN is controlled by the length and width of the I-shaped stub, while the center frequency and the band of the WiMAX is controlled and adjusted by the minor and the major radii of the elliptic C-shaped stub. The overall size of this antenna is 17.5 × 17.5 × 1.5 mm^3, which is very compact to be integrated in hand-held high-speed wireless devices.

II. ANTENNA STRUCTURE

The schematic view of the proposed antenna is shown in Fig. 1. The design and optimization of the proposed antenna dimensions are carried out using ANSOFT HFSS electromagnetic simulator [18]. An FR4 substrate with a relative permittivity of 4.4 having a substrate thickness of 1.5 mm and a loss tangent of 0.02 is used for the antenna design. A coplanar waveguide CPW-fed of a trapezoidal shape of width, F_w and P_{L3} with a gap distance of g_1 and g_2 are used to feed the antenna in order to achieve a 50 Ω input impedance matching. The antenna consists of trapezoid ground planes symmetrically around the CPW feed line. The bottom plane dimensions are taken with a width of G_W, a lower length of G_{LL} mm and an upper length of G_{UL} as shown in Fig. 1. The dimensions of the two trapezoids are *C1* and *C2* respectively, and the lengths of the bottom and top parallel sides are P_{L1}, P_{L2} and P_{L3}.

The elliptic slot of major and minor radii of *A* and *B* is etched from the radiating area to insert the C-shaped and the I-shaped resonators which are using for controlling the band notched characteristics for the WiMAX and WLAN, respectively.

III. DESIGN PROCEDURE

Three antennas are presented in Fig. 2 to analyze the evolution process of the final designed antenna. As in traditional antenna design procedures, design starts by initial theoretical calculation to estimate dimensions of Antenna 1 as illustrated in Fig. 2. The first antenna has two trapezoid shapes fed by a 50-Ω CPW-line surrounded by symmetrical ground planes in both sides with optimized dimensions as given in Table 1. The current distribution of Antenna 1 at 3.5 GHz is shown in Fig. 3, where it can be seen that the current distribution is minimum at the middle portion of the patch at this particular frequency. Hence, this portion is removed and an elliptic slot is etched at the middle portion as shown in Antenna 2 and this elliptical slot is responsible in achieving the wideband with notch characteristics as explained below. In the next step, an I-shaped monopole resonator is incorporated with length L_I as shown in Fig. 2 to achieve band-notched characteristic at WLAN.

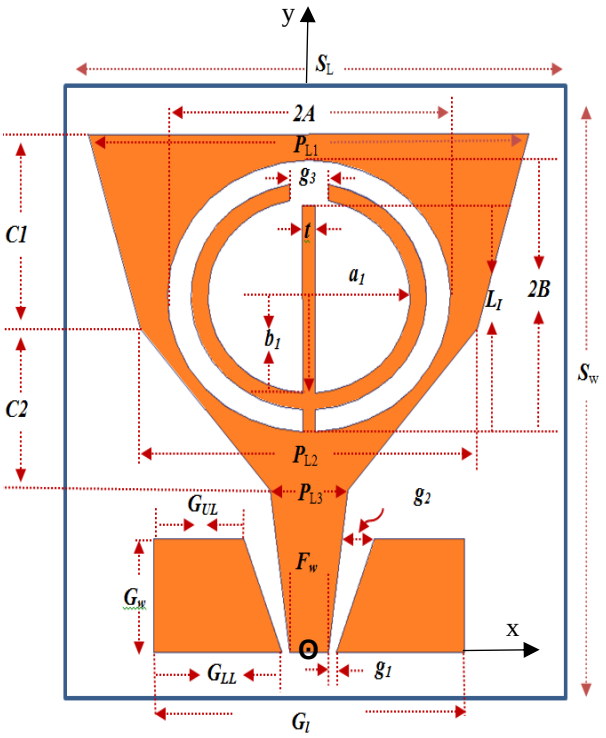

Fig. 1. Geometry of proposed antenna.

Another notch band rejecting WiMAX band is realized by embedding a C-shaped stub at the center of the ellipse resulting the final antenna structure as indicated in Fig. 2, Antenna 3.

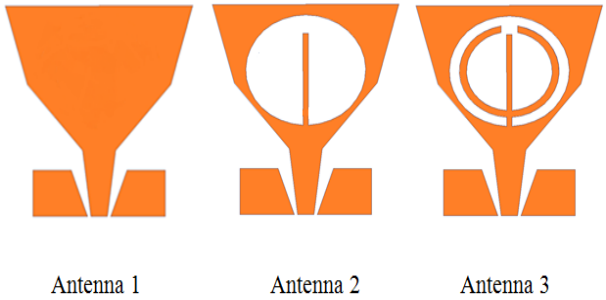

Fig. 2. Evolution of the Proposed Antenna.

The numerical reflection coefficients of the three designed antennas without, with one-notch at 5.8 GHz and with 2 notches at 3.5 GHz and 5.8 GHz are shown in Fig. 4.

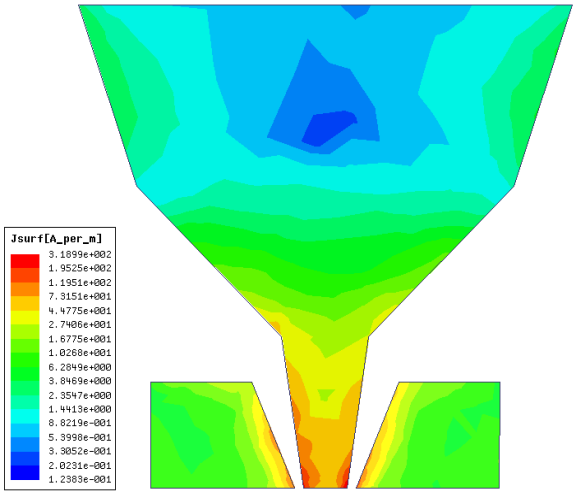

Fig. 3. Current distribution of Antenna 1 at 3.5 GHz.

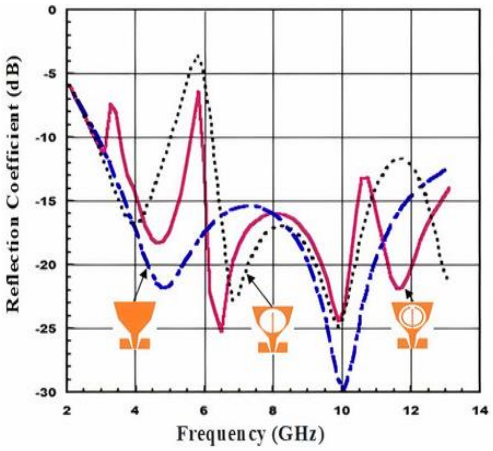

Fig. 4. Simulated reflection coefficient of Antenna 1, Antenna 2 and Antenna 3.

IV. DUAL-BAND NOTCH DESIGN PARAMETERS

Antenna 1 covers the entire UWB band. For obtaining band-notch for WLAN frequency (5.8 GHz), a monopole I-shaped quarter-wavelength stub, L_I is inserted on radiating part as shown in Antenna 2. The length of I-shaped slot is given approximately by Eq. (1), [3, 6]:

$$L_I = \frac{c}{4f_{5.8}\sqrt{(\varepsilon_r+1)/2}}, \quad (1)$$

where L_I is the length of the I-shaped stub for WLAN band, c represents light speed, $\mathcal{E}_r$ is dielectric permittivity constant 4.4 and $f_{5.8}$ represents center frequency of WLAN band (5.8 GHz). After exhaustive simulation studies, it is found that the practical length of L_I is 7.55 mm compared with 7.87 mm obtained by Eq. (1). The value of L_I is critical in determining the center frequency of rejected band of WLAN. By inserting C-shaped stub, we can generate the second notched band at 3.5 GHz to reject WiMAX band. The length of C-shaped stub acting as a half-wavelength resonator [6, 10] as given by Eq. (2):

$$L_c = \frac{c}{2f_{3.5}\sqrt{(\varepsilon_r+1)/2}}, \quad (2)$$

where L_C represents C-shaped stub length, and $f_{3.5}$ is center frequency of WiMAX band (3.5 GHz). L_C is approximately equal to the perimeter of the ellipse of major radius $a = (a_1+t)$ mm and minor radius, $b = (b_1+t)$ mm. The approximate perimeter equation is given by Eq. (3), [6]:

$$\boldsymbol{P} \approx 2\pi\sqrt{\frac{a^2+b^2}{2}}. \quad (3)$$

Equation (3) gives $\boldsymbol{P} \approx 24.98$ mm while the optimized L_C = 26.06 mm is obtained using Equation (2). By introducing the strip with length of L_C, the desired dual-band notched characteristics with UWB operating band is obtained. Hence, the etched gap (g_3) in the C-shaped stub is to adjust and control the middle frequency of lower notch band of the WiMAX, a compromise result of g_3 = 1.0 mm is obtained.

The surface current distributions of the final antenna structure at both the notch frequencies are shown in Fig. 5. From Fig. 5 (a), it is clear that surface current distribution on the C-shaped of the patch at WiMAX frequency is maximum. Similarly, the current distribution presented on I-shaped stub at WLAN frequency is maximum as shown in Fig. 5 (b).

V. PARAMETRIC STUDY

Parametric analyses of the antenna is carried out to compute the optimal parameters of the desired antenna using Ansoft HFSS electromagnetic simulator [18]. The final optimized parameters are listed in Table 1.

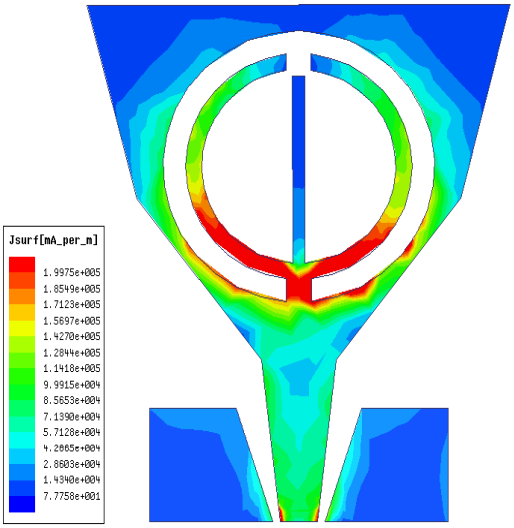

(a)

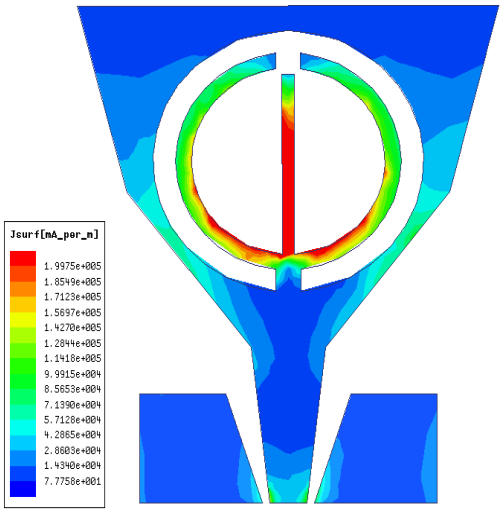

(b)

Fig. 5. Current distribution of Antenna 3 at: (a) 3.5 GHz and (b) 5.8 GHz.

Table 1: Optimized parameters of proposed antenna

Parameters	Unit (mm)
S_L	17.5
S_w	17.5
P_{L1}	17.0
P_{L2}	13.0
P_{L3}	3.0
G_l	12.0
G_w	3.5
G_{LL}	5.85
G_{UL}	3.47
g_1	0.15
g_2	1.23
g_3	1.0
F_w	1.5
a_1	3.9
b_1	3.0
t	0.5
$C1$	6.0
$C2$	5.0
A	5.46
B	4.2

The parametric study of all the parameters is conducted and in the figures below we present some of these studies. Figures 6 and 7 show the reflection coefficients as a function of the ground width and length, G_W and G_l. In Fig. 6, it is observed that as the parameter G_W increases, the center frequency of the WiMAX band increases while the center frequency of the WLAN notch frequency is slightly changed. However, increasing the length, G_l of ground will slightly shift the WLAN and WiMAX notched bands as shown in Fig. 7. Figure 8 illustrates the effect of the minor radius of the inner ellipse of C-shaped, b_1 which mainly controls the center frequency of WiMAX band. The other parameters are studied and the final results are listed in Table 1.

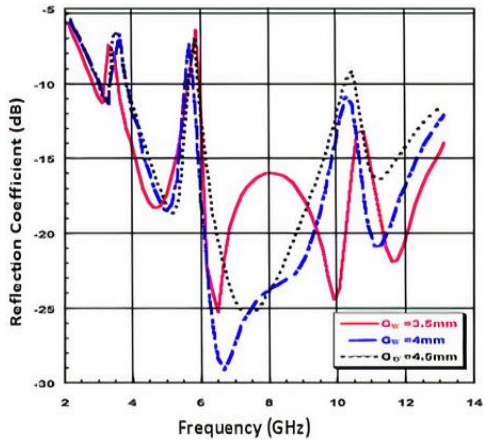

Fig. 6. Parametric analysis w.r.t G_w.

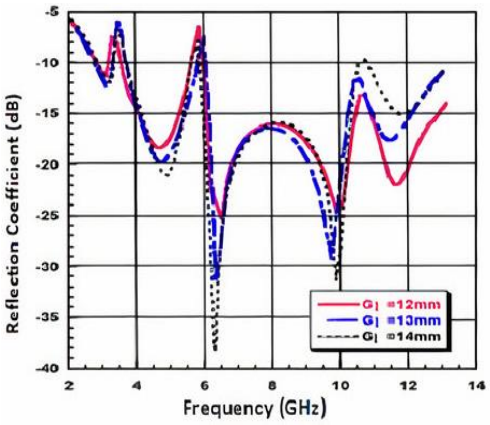

Fig. 7. Parametric analysis w.r.t *Gl*.

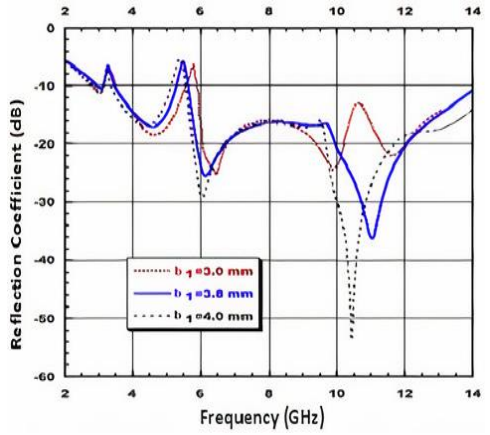

Fig. 8. Parametric analysis w.r.t b_1.

VI. RESULTS AND DISCUSSION

To evaluate the performance of the optimized antenna, the proposed antenna is fabricated and tested. The photograph of the final version of the fabricated antenna is shown in Fig. 9. Vector Network Analyzer (VNA) N5225A is used to carry out the measurements of the reflection coefficient, gain and radiation patterns of the designed antenna. Figure 10 gives the simulated and measured results of the reflection coefficients. As shown from the figure, a good agreement between the measured and simulated reflection coefficients is observed. The slight variation between the results is due to the fabrication tolerances and the SMA connector soldering to the feeder, which is included in the measurements but not taken into account in the simulated results. As seen, the developed antennas rejects both the WiMAX and WLAN bands, while covering the entire UWB band.

Fig. 9. Fabricated antenna.

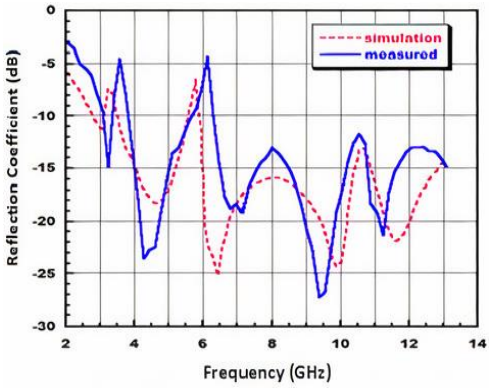

Fig. 10. Comparison of simulated and measured results.

At different frequencies like 4.5 GHz, 7.0 GHz, and 10.0 GHz the measured radiation patterns in the E and H planes are displayed in Fig. 11. From this figure, it is observed that the radiation patterns in the H-plane (x-z plane) are nearly omni-directional for the three frequencies. In the E-plane (y-z plane), they are approximately omnidirectional at 7 GHz and bidirectional at the other two frequencies. Hence, the developed compact antenna has a good radiation patterns over the operating bands. The measured gain of the antenna is given in Fig. 12. It is clearly seen that the proposed antenna exhibits a moderate gain response with gain variation between 2.4 dBi and 5.2 dBi throughout the desired UWB frequency band and except at the notched bands, a sharp reduction of the gain to -1.1 and -2.3 dBi, respectively is observed at WiMAX and WLAN notched bands which shows that the antenna performed well in these bands.

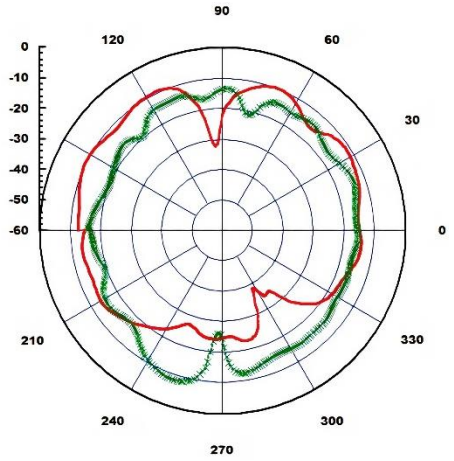

(a) At 4.5 GHz

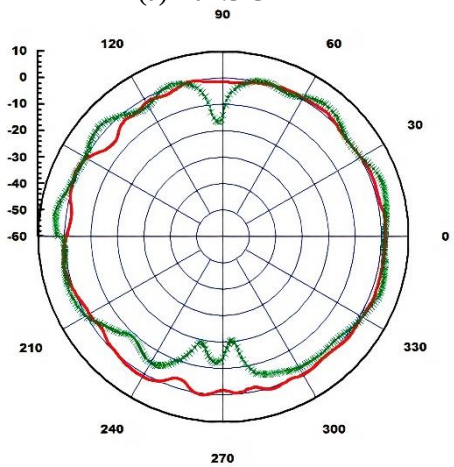

(b) At 7 GHz

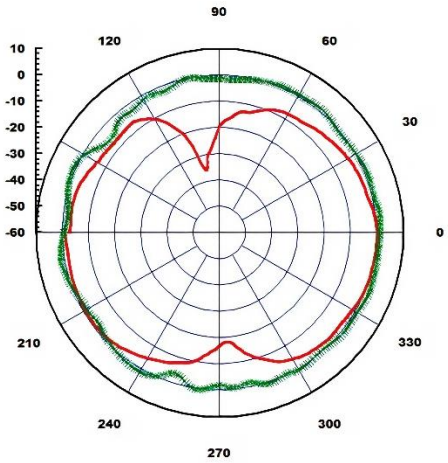

(c) At 10 GHz

Fig. 11. Measured E-plane (red) and H-plane (green) of the proposed antenna at: (a) 4.5 GHz, (b) 7.0 GHz, and (c) 10 GHz.

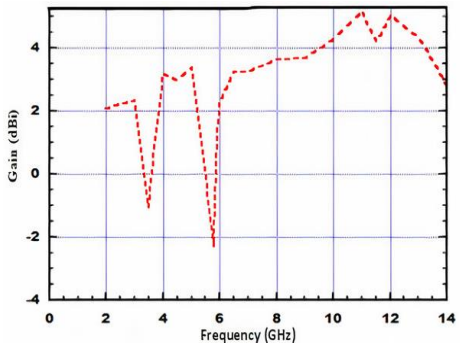

Fig. 12. Measured gain of the proposed antenna.

VII. CONCLUSION

In the proposed work, a very compact with a size of 17.5 mm × 17.5 mm UWB antenna with dual band-notch characteristics is designed and studied. The dual-notch characteristics are obtained by simply inserting C-shaped and I-shaped stubs on the antenna to attain dual-notch properties for rejecting the interference of signals at WiMAX and WLAN applications with a wide bandwidth from 2.9 to 13 GHz. The desired notch frequencies can be adjusted and tuned by properly choosing the I-shaped length, L_I, for the WLAN and the major and minor radii of the elliptic C-shaped for the WiMAX. Also, good radiation patterns and stable gain are achieved in the entire operating band. The operation of the antenna with dual-notch band is justified using reflection coefficient and gain values over the UWB except at the two notched bands. The compact size and the good radiation performance of this presented antenna make it appropriate for UWB system applications.

REFERENCES

[1] Federal Communication Commission, "First report and order Revision of part 15 of the Commission's rules regarding ultra-wideband transmission system," Tech. Rep., ET 98-153, FCC Washington, DC, USA, 2002.

[2] K. Gurupreet and K. Rajeev, "A survey on planar ultra-wideband antennas with band notch characteristics: Principle, design, and applications," *AEU International Journal of Electronics and Communications*, vol. 109, pp. 76-98, 2019.

[3] R. W. Aldhaheri, K. J. Babu, A. Syed, and M. M Sheikh, "A novel UWB rectangular slot disk monopole antenna with band-notch characteristics," *Microwave and Optical Technology Letters*, vol. 57, no. 10, pp. 2405-2410, 2015.

[4] R. Azim, A. T. Mobashsher, and M. T. Islam, "UWB antenna with notched band at 5.5 GHz," *Electronics Letters*, vol. 49, no. 15, 2013.

[5] K. J. Babu, B. K. Kumar, B. S. Rao, and A. M. Varaprasad, "Design of a compact elliptical slot printed UWB antenna with band-notched characteristic," *International Journal of Electronics Letters*, vol. 7, no. 4, pp. 448-457, 2020.

[6] R. W. Aldhaheri and I. S. Alruhaili, "A simple and compact CPW-fed UWB antenna with WLAN band rejection," *In: Proceedings of IEEE 19th Mediterranean Microwave Symposium (MMS)*, Hammamet, Tunisia, pp. 1-4, 2019.

[7] L. Chen, Y. Liu, and P. Wu, "Design of compact asymmetric coplanar strip-fed UWB antenna with dual band-notched characteristics," *Progress In Electromagnetics Research Letters*, vol. 47, pp. 103-109, 2014.

[8] C. Liu, T. Jiang, Y. Li, and J. Zhang, "A compact wide slot antenna with dual band-notch characteristic for ultra-wideband applications," *Journal of Microwaves Optoelectronics and Electronics*, vol. 10, no.1, pp. 55-64, 2011.

[9] R. Azim and M. T. Islam, "Ultra-wideband antenna with notched bands at 3.5/5.5 GHz," *Applied Computational Electromagnetics Society Journal*, vol. 31, no. 4, pp. 388-395, 2016.

[10] X. Ren, S. Gao, and Y. Yin, "Compact tri-band monopole antenna with hybrid strips for WLAN/ WIMAX applications," *Microwave and Optical Technology Letters*, vol. 57, no. 1, pp. 94-99, 2015.

[11] S. Tripathi, A. Mohan, and S. Yadav, "A compact UWB antenna with dual 3.5/5.5 GHZ band-notched characteristics," *Microwave and Optical Technology Letters*, vol. 57, no. 3, pp. 551-556, 2015.

[12] S. Hoseyni, J. Nourinia, C. Ghobadi, S. Masumina, and B. Mohammadi, "A compact design and new structure of monopole antenna with dual bad notch

characteristic for UWB applications," *Applied Computational Electromagnetics Society Journal*, vol. 31, no. 7, pp. 797-805, 2016.
[13] S. Jo, H. Choi, J. Lim, B. Shin, S. Oh, and J. Lee, "A CPW-fed monopole antenna with double rectangular rings and vertical slots in the ground plane for WLAN/WiMAX applications," *International Journal of Antenna and Propagation*, vol. 2015, pp. 1-7, 2015.
[14] R. Shi, X. Xu, J. Dong, and Q. Luo, "Design and analysis of a novel dual band-notched UWB antenna," *International Journal of Antennas and Propagation*, vol. 2014, pp. 1-10, 2014.
[15] Z. Ma, F. Dong, Z. Han, S. Han, and Q. Xue, "Compact UWB antenna with triple band – Notches using C-shaped and S-shaped structures," *Applied Computational Electromagnetics Society Journal*, vol. 31, no. 4, pp. 348-354, 2016.
[16] A. Syed and R. W. Aldhaheri, "A new inset-feed UWB printed antenna with triple 3.5/5.5/7.5 GHz band-notched characteristics," *Turkish Journal of Electrical Engineering & Computer Sciences*, vol. 26, no. 3, pp. 1190-1201, 2018.
[17] L. Cui, H. Liu, C. Hao, and X. Sun, "A novel UWB antenna with triple band-notches for WiMAX and WLAN," *Progress in Electromagnetics Research Letters*, vol. 82, pp. 101-106, 2019.
[18] Ansoft High Frequency Structure Simulation (HFSS), ver. 15, Ansoft Corporation, Pittsburgh, PA, 2013.

Rabah W. Aldhaheri received his Ph.D. degree from Michigan State University in 1988, in Electrical and Computer Engineering. He is currently a Full Professor in the Department of Electrical and Computer Engineering, King Abdulaziz University (KAU), Jeddah, Saudi Arabia. He served as the Head of the Department of Electrical and Computer Engineering at KAU from May 2005 till May 2011. He is currently serving as the Founder and Director of the Microelectronics and RF Circuits Laboratory, FSS and Metamaterial Research Laboratory and the Head of the Communication Systems and Networks Research Group.

Aldhaheri has held Visiting Research Scholar positions with Michigan State University during 1994-1995, and Queensland University of Technology (QUT) in Brisbane, Australia in 2000. His research interests include digital signal processing with application to filter design, and biometric recognition, microelectronics devices; and wireless communications, particularly, antennas design for UWB communication, medical imaging, RFID readers and Frequency Selective Surfaces (FSS).

Ibrahim S. Alruhaili was born in Madinah, KSA 1973. He received his B.Sc. in Electrical and Telecommunication Engineering from King Fahad University for Petroleum and Minerals (KFUPM) Dhahran, KSA, in 1998 and M.Sc. degrees in Electronics and Communication, from King Abdulaziz University, Jeddah, KSA in 2016. His primary research interests are in high speed design, printed circuits boards, signal integrity, RF and antenna design.

Jagadeesh Babu Kamili was born in Chirala, Andhra Pradesh, India in 1978. He received B.Tech. degree from SVH College of Engineering, Machilipatnam in the year 1999, M.Tech. and Ph.D. degrees from Jawaharlal Nehru Technological University, Hyderabad, India in 2006 and 2013 respectively. Presently working as Professor and Head of the Department at St. Ann's College of Engineering & Technology, Chirala, India. Also, he is a Postdoctoral Researcher under Certificate of Excellence in Research program from Indian Institute of Technology Kharagpur, India.

He received Travel Grant from SERB, Department of Science and Technology (DST), India to attend International Conference PIERS-2017 in Singapore. He received Best Researcher Award from JNTUK University in 2018. He is senior member of IEEE and life member of IE and ISTE, India. His research areas include printed antennas, meta-materials, Ground penetrating Radar and Characteristic Mode Analysis.

Muntasir M. Sheikh received his B.Sc. from King Abdulaziz University, Saudi Arabia, in Electronics and Communications Engineering, M.Sc. in RF Communications Engineering from the University of Bradford, U.K., and Ph.D. from the University of Arizona, U.S.A. Since then, he has been teaching in the Electrical and Computer Engineering Dept. in KAU. His research interests are Antenna Theory and Design, Radar applications, and electromagnetic metamaterials.

A Frequency and Polarization Reconfigurable Dual-Patch Microstrip Antenna for Wireless ISM Band

Cong Danh Bui [1,2], Thanh Cuong Dang [2], Minh Thuan Doan [3], and Truong Khang Nguyen [1,2,*]

[1] Division of Computational Physics, Institute of Computational Science, Ton Duc Thang University
Ho Chi Minh City, Vietnam

[2] Faculty of Electrical and Electronics Engineering, Ton Duc Thang University
Ho Chi Minh City, Vietnam

[3] Faculty of Electrical and Electronics Engineering, Bach Khoa University, Ho Chi Minh City, Vietnam
*nguyentruongkhang@tdtu.edu.vn

***Abstract* —** This paper proposes a reconfigurable microstrip patch antenna design for wireless ISM band applications. The antenna simultaneously uses PIN Diodes to switch between linear and circular polarization at 2.45 GHz and uses Varactor Diode to continuously tune the operating frequency from 1.73 GHz to 2.45 GHz. The antenna performance is characterized as a combination of ON/OFF state of PIN Diode and a bias voltage of Varactor Diode varying from 0.8V to 10V. A good agreement between simulation and measurement is obtained which validates the proposed method. The proposed frequency/polarization reconfigurable antenna is promising for various applications in wireless ISM band such as DCS (1710 – 1880 MHz), PCS (1850 – 1990 MHz), GSM 1800, GSM 1900, UMTS (1920 – 2170 MHz) and WiFi/Bluetooth (2.4 – 2.5 GHz).

***Index Terms* —** Frequency reconfigurable, patch antenna, polarization reconfigurable.

I. INTRODUCTION

Reconfigurable antenna (RA) is mainly classified based on its reconfigurability which can offer single or multiple reconfiguration features such as frequency (F), bandwidth (B), polarization (P), radiation pattern (R), and a combination of them, i.e., F/B, F/R, R/P, and F/R/P [1]. Among them, F/P RAs are particularly useful in various wireless applications due to their numerous advantages such as efficient spectrum utilization, improved system capacity and flexibility, increased communication security [2]. Therefore, in the last decade, F/P RAs have attracted much attention by employing several different techniques, such as circular cavity [3], metasurface [4, 5], magnetized ferrite substrate [6], bow-tie dipole [7], liquid metal [8], etc. However, their disadvantages are complexity profile and high cost that could be unsuitable in the emergence of modern smart systems.

As a sequence, there has been increasing attention and efforts placed on designing RAs using microstrip technology, especially microstrip patch configuration [9-17]. In [11], frequency reconfiguration was realized by switching two groups of diodes placed across the slots while another two PIN diodes were added between the input port and the 3dB hybrid coupler to achieve LHCP/ RHCP reconfigurability. In [12], by using eight PIN diodes and six conductive pads, the antenna obtained the frequency reconfigurability between two WLAN bands (5.2 GHz and 5.8 GHz) and was capable of switching between linear polarization (LP) and left-hand/right-hand circular polarization (LHCP/RHCP) at each frequency. In [13], by superimposing a square ring slot into the corner truncated square patch and incorporating four PIN diodes into the square ring slot, frequency reconfigurability was obtained at two WLAN bands (5.15 - 5.35GHz and 5.75 - 5.85GHz) and polarization reconfigurability of dual-senses LP (horizontal/vertical) and CP (LHCP/RHCP) was generated at dual frequencies. In [14], by properly using a combination between PIN diodes and shorting pins, eight discrete operating frequency bands and three polarization states (LHCP/ RHCP/LP) can be realized simultaneously. In [15], two switchable frequency bands were achieved by connecting an additional small patch to the main patch through a PIN diode while were also capable of operating in three polarization states (LP/LHCP/RHCP). However, the main disadvantage of these designs was that they were only able to switch between LP/CP and/or between RHCP/ LHCP in a specific frequency band. Although the antenna in [9] provided a continuous and wide frequency tuning range, CP has not been reported or considered. In [10], by using 12 Varactor Diodes, frequency reconfigurability is achieved in a continuously tuned fractional bandwidth while allowing selection between CP (both rotating senses) and LP. In [16], frequency reconfigurability with continuously tunable range and polarization reconfigurability with either LP or CP (RHCP or LHCP) was achieved by using four pairs of Varactor diodes. Therefore, it can be seen that a simple

Submitted On: September 16, 2020
Accepted On: January 18, 2021

https://doi.org/10.47037/2020.ACES.J.360206

profile microstrip patch RAs that can be reconfigured in both frequency and polarization (LP and RHCP/LHCP) in a continuous frequency range is very challenging to obtain.

This paper proposes a planar microstrip dual-patch F/P RA. Two PIN Diodes work as a switch between LP and CP at 2.45 GHz while one Varactor Diode is used to tune the operating frequency from 1.73 GHz to 2.5 GHz which is able to cover many wireless applications in ISM band such as DCS (1710 – 1880 MHz), PCS (1850 – 1990 MHz), GSM 1800, GSM 1900, UMTS (1920 – 2170 MHz) and WiFi/Bluetooth (2.4 – 2.5 GHz). The paper will start by describing the antenna design including the bias circuit in Section 2. Then, the detailed antenna characteristics will be presented in Section 3. Finally, simulation and measurement results of the fabricated antenna at various frequencies and different polarizations will be presented and discussed in Section 4.

II. ANTENNA AND BIAS CIRCUIT DESIGN

The antenna geometry is illustrated in Fig. 1. The radiator is comprised of primary and secondary patches that are connected together by a microstrip line. The primary patch is fed by a standard 50Ω coaxial cable and has its corners separated by PIN Diodes to create CP. The secondary patch is connected to the primary one by a transmission line that has a Varactor Diode in between functioning as a tuning element. Both patches are placed on a 1.6 mm FR-4 substrate (ε = 4.4, tan δ = 0.02) with a ground plane underneath.

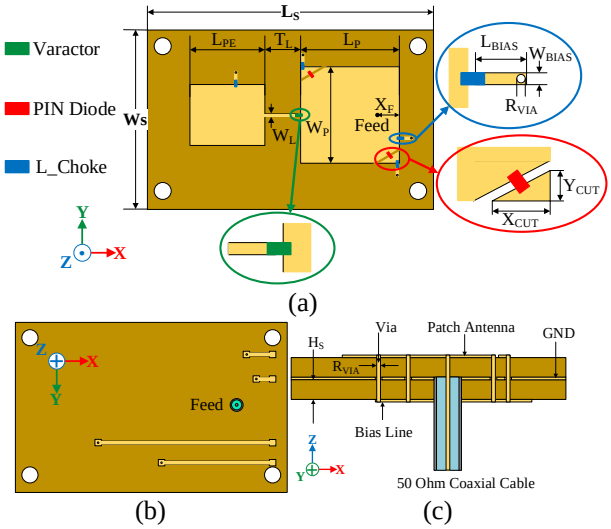

Fig. 1. Antenna geometry: (a) top view of the radiator, (b) bottom view, and (c) side view.

Another 1.6 mm FR-4 substrate is stacked underneath to support the bias circuits for PIN Diodes and Varactor Diode. A simplified bias circuit is illustrated in Fig. 2. V_{DC}, R and *rheostat* are the components of external DC circuits that are used to supply DC voltage for PIN Diodes and Varactor Diodes. To supply a variable voltage source, a variable resistor *rheostat* is used to change the bias voltage of Varactor Diode while a defined resistor R is used to supply a constant one for PIN Diode. A manual switch *SW* is also placed at PIN Diode bias line to alter the ON/OFF operating mode. L_{choke} = 90 nH (LQW04CA90NK00D) is used both at each branch of active components and in front of DC source (V_{DC} = 12V) to efficiently block RF power from the antenna.

The equivalent circuit model of PIN Diode (MADP-042305-13060) and Varactor Diode (MA46H120), found in their respective datasheets as illustrated in Fig. 3, have been used in simulation by CST Microwave Studio [18]. PIN Diode has two operating modes and each has its equivalent circuit. While mode OFF can be represented as a series circuit of L and parallel of R_p and C_T, mode ON is represented by a series circuit of L and R_s. On the other hand, Varactor Diode can be characterized by a parallel circuit of C_p and series of L_S, C_J and R_S whereas C_J value can be varied within the component's range of [C_{Jmin}-C_{Jmax}] = [0.14pF – 1.1pF]. Their respective equivalent electric models are illustrated in Fig. 3 and optimized parameters' values for the final design are listed in Table 1.

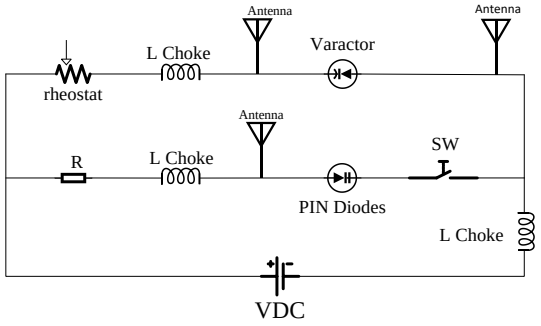

Fig. 2. Simplified bias circuit of the proposed F/P RA.

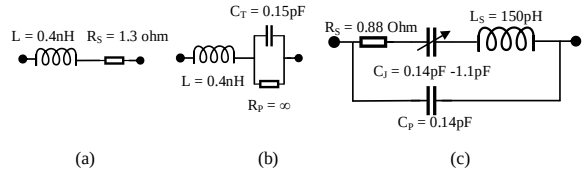

Fig. 3. Equivalent circuit of: (a) PIN Diode in ON state; (b) PIN Diode in OFF state; (c) Varactor Diode.

Table 1: Optimized values of the proposed antenna (unit: mm)

W_S	L_S	W_P	L_P	X_F	T_L	W_L
53	84	29	28.5	8	9.5	0.8
L_{PE}	W_{PE}	X_{CUT}	Y_{CUT}	L_{BIAS}	W_{BIAS}	R_{VIA}
22	18	6.4	3.7	3	0.5	0.25

III. ANTENNA CHARACTERISTICS

A. Frequency reconfigurable by using varactor diode

The Varactor Diode can change the impedance and power distribution of the antenna; therefore, its resonance frequency can be shifted. Particularly, when the value of Varactor Diode reaches its greatest limit (C_{JMAX}), the RF power transferred from the primary patch to the secondary patch is maximized. As a result, the electrical length of the antenna is then extended to its maximum possible value and has its resonance frequency the lowest. The opposite result can be concluded for the case of the minimal value of Varactor Diode (C_{JMIN}). In short, the proposed F/P RA can have its resonance frequency highest when C_{JMIN} and lowest when C_{JMAX}. Consequently, the bandwidth tuning range can be determined within this range.

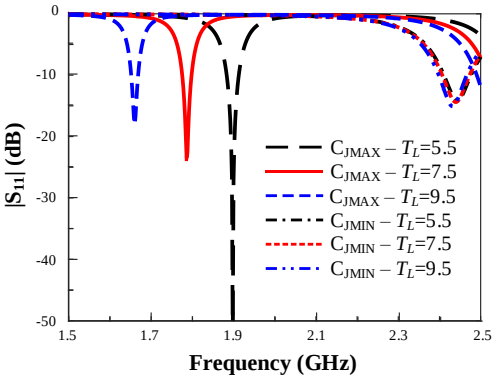

Fig. 4. T_L parameter sweep when PIN Diode is ON.

In the simulation and optimization process, it is observed that the tuning fractional bandwidth (FBW) is greatly affected by parameter T_L which is the length of the transmission line. A parameter sweep of 3 values 5.5, 7.5 and 9.5 mm when Varactor Diode's values are C_{JMIN} and C_{JMAX} was performed. As shown in Fig. 4, the lower operating frequency is shifted while the upper one remains unchanged leading to a conclusion that tuning bandwidth is affected by this transmission line length significantly. It can be seen that the resonance frequencies of the antenna at these three lengths are 1.936 GHz and 2.44 GHz, 1.786 GHz and 2.44 GHz, and 1.66 GHz and 2.43 GHz when Varactor Diode's value is C_{JMAX} and C_{JMIN}, respectively. Maximum E-field distributions at their low operating frequencies are illustrated in Fig. 5. In all 3 cases, E-field distribution is emphasized at the patch's edges in the x-direction, which is the characteristic of patch antenna [19], Moreover, the fields are strongest at the Varactor Diode as it serves as a tunable power supply line for the secondary patch. However, the main difference can be seen in the gap between the primary and secondary patch. The edges of the two patches act as two parallel metal plates with distance T_L and form a coupling capacitor ($C_{coupling}$). While performing the change of the transmission line length, $C_{coupling}$ has its value smallest when T_L = 9.5 mm and highest when T_L = 5.5 mm. This behavior has led to variation in RF power coupled between 2 patches and an abrupt difference in bandwidth tuning range. It can be found in the simulation that T_L of 9.5 mm has been chosen to have a bandwidth tuning range entirely covering DCS, PCS, UMTS and WiFi/Bluetooth applications while maintaining good gain characteristics.

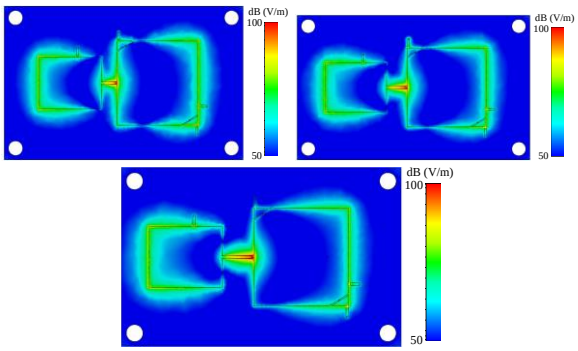

Fig. 5. Maximum E-field distribution of the proposed F/P RA: (a) at 1.918 GHz (T_L = 5.5 mm); (b) at 1.778 GHz (T_L = 7.5 mm); (c) at 1.66 GHz (T_L = 9.5 mm).

B. Polarization reconfigurable by using PIN diode

As mentioned, the polarization reconfigurability of the antenna is based on the operating mode of PIN Diode. Two PIN Diodes, implemented on the gap separating the primary patch and its corners, serve as switches to create the polarization reconfigurability by connecting/disconnecting the primary patch to its corners. Since the polarization reconfigurability is created on the primary patch, Varactor Diode's value is set on C_{JMIN} to choke the RF power transferring to the secondary patch. Therefore, the switch between linear and circular polarization only occurs at the upper operating frequency, WiFi/Bluetooth application. A parameter sweep of X_{cut} from 5.5 mm to 6.1 mm and 6.7 mm, while switching PIN Diode mode ON/OFF, was performed and illustrated in Fig. 6. In Fig. 6 (a), $|S_{11}|$ results indicate that there is little change in operating frequency between these three values when PIN Diode is OFF and ON. The Axial Ratio (AR) performance of the antenna is shown in Fig. 6 (b). It is observed clearly that polarization reconfigurability can be switched between circular and linear polarization when PIN Diode mode is OFF and ON, respectively. There is a slight change in AR resonant frequency with respect to the variation of X_{cut}. Finally, X_{cut} = 6.1 mm has been chosen as the optimized value for the best AR performance.

To further verify the polarization reconfigurability of the design, the current distributions of the proposed F/P RA at 2.46 GHz when PIN Diode is OFF and ON at C_{JMIN} value of Varactor Diode are shown in Fig. 7. As shown in Fig. 7 (a) and Fig. 7 (b) with 90° phase

difference, not only the magnitude is similar but also the direction of the current is rotated 90° counterclockwise. Therefore, it can be concluded that the antenna exhibits right – hand CP when PIN Diode is OFF. A summary of antenna operating cases can be found in Table 2.

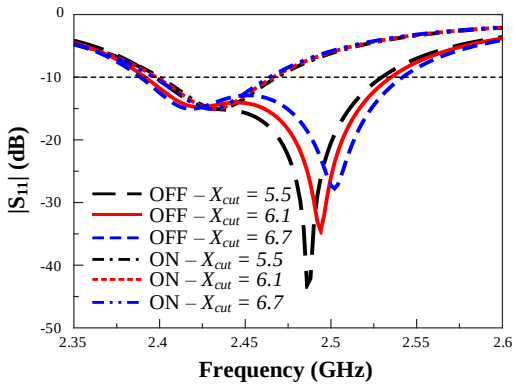

(a)

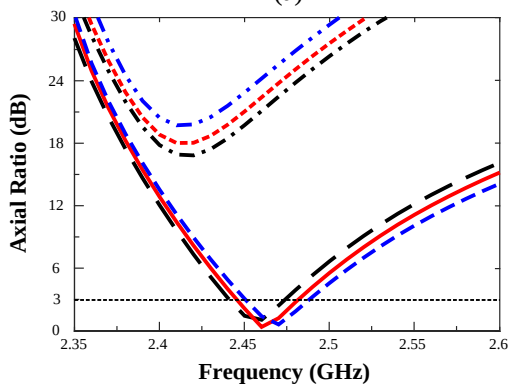

(b)

Fig. 6. X_{cut} parameter sweep while Varactor Diode's value is C_{JMIN}. (a) S_{11}; (b) axial ratio.

Table 2: Summary of operating cases of the proposed F/P RA

Case	PIN Diode	Varactor Diode	Antenna Performance
1	OFF	C_{JMIN}	- 2.4 GHz – 2.5 GHz - Polarization: Circular - WiFi/Bluetooth
2	ON	C_{JMIN}	- 2.4 GHz – 2.5 GHz - Polarization: Linear - WiFi/Bluetooth
3	ON	C_{JMIN} - C_{JMAX}	- 1.73 GHz – 2.45 GHz - Polarization: Linear - DCS, PCS, GSM, UMTS, WiFi/Bluetooth

Based on the observed results, a design procedure is provided as follows:

- Design a linear polarization patch antenna at WiFi/Bluetooth application, its initial dimension can be calculated using (1) [19]:

$$W_p = L_p \approx \frac{c_0}{2 f_0 \sqrt{\varepsilon_r}}. \quad (1)$$

Where c_0 is the velocity of light in free-space, f_0 is the desired operating frequency and ε_r is the permittivity of the substrate.

- Detach two opposite corners from the patch by a small gap which will be used to place PIN Diode to achieve polarization reconfigurability.
- Design and connect the secondary patch to the primary one by a Transmission Line and a Varactor Diode. Note that parameter TL should be chosen carefully to acquire the desired tuning range and antenna gain characteristics.
- Add the bias circuit for both Varactor diode and PIN diode and finalize the antenna design performance.

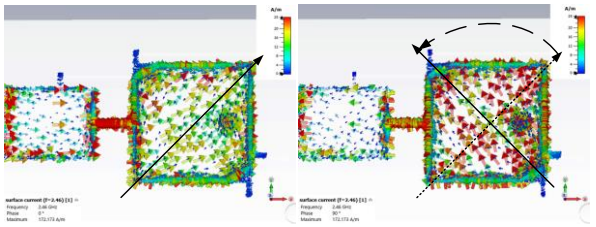

(a) (b)

Fig. 7. E-field distribution to prove CP of the proposed F/P RA at 2.46 GHz when PIN Diode's state is OFF and Varactor Diode's value is C_{JMIN}: (a) 0° and (b) 90°.

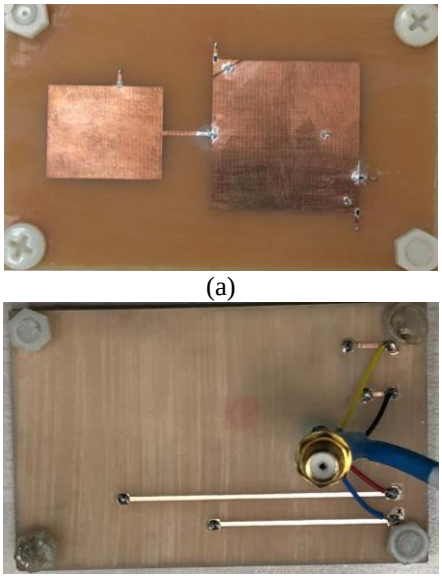

(a)

(b)

Fig. 8. Fabricated antenna design: (a) top view; (b) bottom view.

IV. SIMULATION AND MEASUREMENT RESULTS

The proposed F/P RA is fabricated as shown in Fig. 8 and its performance in a comparison between measurement and simulation at various active component states are illustrated in Fig. 9 and Fig. 10. Generally, when the bias voltage is tuned from 10V to 0.8V, which corresponds to the change of Varactor Diode's capacitor from C_{JMIN} (10V) to C_{JMAX} (0.8V), the frequency is tuned from upper band to lower band continuously. The highest and lowest resonant frequencies of measurement and simulation in that range are 2.4 GHz and 2.39 GHz at 10V and 1.75 GHz and 1.76 GHz at 0.8V, respectively. It can be concluded that in this voltage range, all resonant frequencies at their respective bias voltage in measurement and simulation are in good agreement. As seen in Fig. 9 (b), the antenna is found to have CP (Axial Ratio, AR<3dB) within the range of 2.45 – 2.486 GHz and 2.445 – 2.48 GHz in measurement and simulation, respectively, when PIN Diode state is OFF and a bias voltage of Varactor Diode is 10V. Particularly, the proposed antenna presents a small variation of measured gains (0.02 dBi – 2.56 dBi) among reconfigurable modes within the whole operating frequency band. The maximum gains of measurement and simulation are 2.56 dBi and 3.03 dBi (PIN Diode ON – 6V) whereas the minimum gains are -0.5 dBi and 0.02 dBi (PIN Diode ON – 0.8V), respectively. The simulated gains are slightly lower than the measured ones which could be contributed by the effects of active components and FR-4 substrate. A detailed comparison between simulation and measurement results in terms of resonance frequency, S_{11}, and broadside gain is summarized in Table 3.

The simulated and measured radiation patterns at multiple operating states are presented and compared in Fig. 10. It can be seen that PIN Diode states and the bias voltage of Varactor Diode do not change the patch-like radiation pattern characteristic of the proposed F/P RA. The main radiation beam of the antenna is maintained at broadside direction while almost completely suppressed in *xy* – plane, the plane of the antenna. The simulated and measured radiation patterns are in good agreement within the whole frequency range of interest.

Table 3: Comparison between simulation and measurement results of the proposed F/P antenna

V_{Bias}	Frequency (GHz)		S_{11} (dB)		Gain (dBi)	
	Sim.	Mea.	Sim.	Mea.	Sim.	Mea.
10 V	2.40	2.39	-30	-15	3.0	2.05
8 V	2.37	2.36	-25	-17	2.95	2.1
6 V	2.34	2.33	-42	-19	3.03	2.56
4 V	2.22	2.22	-31	-17	2.8	2.2
2 V	1.88	1.88	-20	-11	0.9	-0.1
0.8 V	1.76	1.75	-17	-10	0.02	-0.5

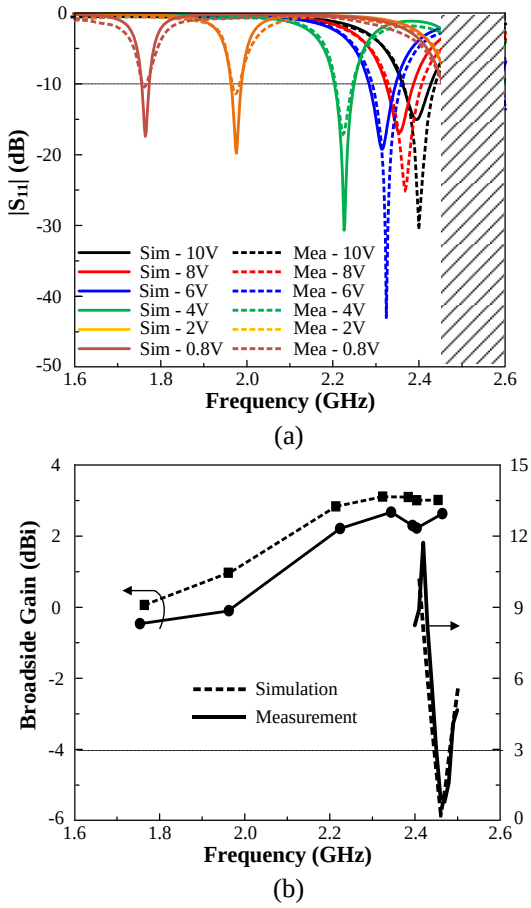

Fig. 9. Simulation and measurement results. (a) S-parameter (PIN Diode ON); (b) Gain (PIN Diode ON) and AR for CP at 2.45 GHz (PIN Diode OFF).

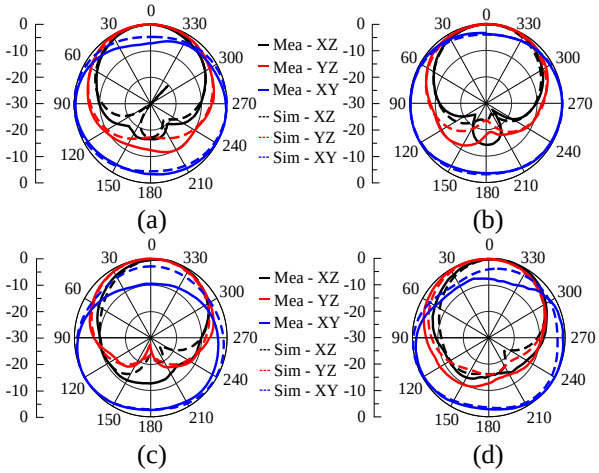

Fig. 10. Radiation patterns of the proposed F/P RA. (a) ON - 0.8 V; Mea. at 1.75 GHz, Sim. at 1.76 GHz; (b) ON - 4 V; Mea. at 2.21 GHz, Sim. at 2.22 GHz; (c) ON - 10 V; Mea. at 2.40 GHz, Sim. at 2.39 GHz; (d) OFF - 10 V; Mea. at 2.46 GHz, Sim. at 2.45 GHz.

Table 4 presents a comparative summary of the proposed RA antenna with other RAs having frequency and polarization reconfigurability. Though having dual-polarization, reconfigurable antennas in [12] and [14] using PIN Diode has a disadvantage of discrete frequency selection. On the contrary, despite having a wider band and continuous frequency tuning by using Varactor Diode, [9] and [10] only have either linear or circular polarization. The proposed antenna has shown to have both linear and circular polarization and also continuous frequency tuning within decent bandwidth while still having a simple profile.

Table 4. Comparison of proposed F/P RA with other frequency and polarization reconfigurable antenna (λ_0 is the wavelength at the lowest operating frequency)

Ref.	Active Devices	Size (λ^2_0)	Frequency (GHz)	Polarization
[9]	PIN & Varactor Diode	0.3 x 0.3	1.35 – 2.25 (50%)	LP-V/ LP-H/ LP-45^0
[10]	Varactor Diode	0.5 x 0.5	2.4 – 3.6 (40%)	LHCP/ RHCP
[12]	PIN Diode	0.6 x 0.3	5.2/5.8	LP/CP
[14]	PIN Diode	0.6 x 0.3	1.85/1.95/ 2.15/2.2/ 2.35/2.45/ 2.55/2.6	LHCP/ RHCP/ LP
Proposed	**PIN & Varactor Diode**	**0.5 x 0.3**	**1.73 – 2.45 (~34.4%)**	**LP/CP**

V. CONCLUSION

This paper has presented a F/P microstrip dual-patch RA by using both reconfiguration means of PIN and Varactor Diodes. Despite suffering from power loss on active components and having higher cost than a conventional passive antenna, the proposed antenna can produce frequency reconfigurability with a continuously tunable range of 1.73 GHz – 2.45 GHz (~34.4%) and polarization reconfigurability with either LP and CP while having a simple profile, using fewer reconfiguration means, and achieving good/stable gain characteristics. As a result, the proposed antenna is applicable for various wireless applications in the ISM band such as DCS, PCS, GSM 1800/1900, UMTS and WiFi/Bluetooth.

ACKNOWLEDMENT

This research is funded by National Foundation for Science and Technology Development (NAFOSTED) under Grant No. 102.04-2019.04. The first two authors contributed equally to this work.

REFERENCE

[1] N. Ojaroudi Parchin, H. Jahanbakhsh Basherlou, Y. I. Al-Yasir, R. A. Abd-Alhameed, A. M. Abdulkhaleq, and J. M. Noras, "Recent developments of reconfigurable antennas for current and future wireless communication systems," *Electronics*, vol. 8, no. 2, p. 128, 2019.

[2] C. G. Christodoulou, Y. Tawk, S. A. Lane, and S. R. Erwin, "Reconfigurable antennas for wireless and space applications," *Proceedings of the IEEE*, vol. 100, no. 7, pp. 2250-2261, 2012.

[3] N. Nguyen-Trong, A. Piotrowski, L. Hall, and C. Fumeaux, "A frequency-and polarization-reconfigurable circular cavity antenna," *IEEE Antennas and Wireless Propagation Letters*, vol. 16, pp. 999-1002, 2016

[4] C. Ni, M. S. Chen, Z. X. Zhang, and X. L. Wu, "Design of frequency-and polarization-reconfigurable antenna based on the polarization conversion metasurface," *IEEE Antennas and Wireless Propagation Letters*, vol. 17, no. 1, pp. 78-81, 2017.

[5] G. Liu, J. Han, X. Gao, H. Liu, and L. Li, "A novel frequency reconfigurable polarization converter based on active metasurface," *Applied Computational Electromagnetics Society Journal*, vol. 34, no. 7, pp. 1058-1063, 2019.

[6] F. A. Ghaffar, M. Vaseem, L. Roy, and A. Shamim, "Design and fabrication of a frequency and polarization reconfigurable microwave antenna on a printed partially magnetized ferrite substrate," *IEEE Transactions on Antennas and Propagation*, vol. 66, no. 9, pp. 4866-4871, 2018.

[7] J. Liu, J.-Y. Li, R. Xu, and S.-G. Zhou, "A reconfigurable printed antenna with frequency and polarization diversity based on bow-tie dipole structure," *IEEE Transactions on Antennas and Propagation*, vol. 67, no. 12, pp. 7628-7632, 2019.

[8] Y. Liu, Q. Wang, Y. Jia, and P. Zhu, "A frequency-and polarization reconfigurable slot antenna using liquid metal," *IEEE Transactions on Antennas and Propagation*, 2020.

[9] P.-Y. Qin, Y. J. Guo, Y. Cai, E. Dutkiewicz, and C.-H. Liang, "A reconfigurable antenna with frequency and polarization agility," *IEEE Antennas and Wireless Propagation Letters*, vol. 10, pp. 1373-1376, 2011.

[10] N. Nguyen-Trong, L. Hall, and C. Fumeaux, "A frequency-and polarization-reconfigurable stub-loaded microstrip patch antenna," *IEEE Transactions on Antennas and Propagation*, vol. 63, no. 11, pp. 5235-5240, 2015.

[11] P. Zhang, S. Liu, R. Chen, and X. Huang, "A reconfigurable microstrip patch antenna with frequency and circular polarization diversities," *Chinese Journal of Electronics*, vol. 25, no. 2, pp. 379-383, 2016.

[12] B. Anantha, L. Merugu, and P. S. Rao, "A novel single feed frequency and polarization reconfig-

urable microstrip patch antenna," *AEU-International Journal of Electronics and Communications*, vol. 72, pp. 8-16, 2017.

[13] A. Bharathi, M. Lakshminarayana, and P. S. Rao, "A quad-polarization and frequency reconfigurable square ring slot loaded microstrip patch antenna for wlan applications," *AEU-International Journal of Electronics and Communications*, vol. 78, pp. 15-23, 2017.

[14] J. Hu and Z.-C. Hao, "Design of a frequency and polarization reconfigurable patch antenna with a stable gain," *IEEE Access*, vol. 6, pp. 68, 169-68, 175, 2018.

[15] R. K. Singh, A. Basu, and S. K. Koul, "A novel reconfigurable microstrip patch antenna with polarization agility in two switchable frequency bands," *IEEE Transactions on Antennas and Propagation*, vol. 66, no. 10, pp. 5608-5613, 2018.

[16] H. Gu, J. Wang, L. Ge, and L. Xu, "A reconfigurable patch antenna with independent frequency and polarization agility," *Journal of Electromagnetic Waves and Applications*, vol. 33, no. 1, pp. 31-40, 2019.

[17] R. K. Singh, A. Basu, and S. K. Koul, "Reconfigurable microstrip patch antenna with polarization switching in three switchable frequency bands," *IEEE Access*, vol. 8, pp. 119, 376-119, 386, 2020.

[18] CST Microwave Studio, CST GmbH, 2016. http://www.cst.com

[19] C. A. Balanis, *Antenna Theory: Analysis and Design*. 4th ed., John Wiley & Sons, ch. 14, July 2016.

Efficient Electromagnetic Analysis of a Dispersive Head Model Due to Smart Glasses Embedded Antennas at Wi-Fi and 5G Frequencies

Fatih Kaburcuk [1] and Atef Z. Elsherbeni [2]

[1] Department of Electrical-Electronics Engineering
Sivas Cumhuriyet University, Sivas 58140, Turkey
fkaburcuk@cumhuriyet.edu.tr – fkaburcu@syr.edu

[2] Department of Electrical Engineering
Colorado School of Mines, Golden, CO 80401, United States
aelsherb@mines.edu

Abstract ─ Numerical study of electromagnetic interaction between an adjacent antenna and a human head model requires long computation time and large computer memory. In this paper, two speeding up techniques for a dispersive algorithm based on finite-difference time-domain method are used to reduce the required computation time and computer memory. In order to evaluate the validity of these two speeding up techniques, specific absorption rate (SAR) and temperature rise distributions in a dispersive human head model due to radiation from an antenna integrated into a pair of smart glasses are investigated. The antenna integrated into the pair of smart glasses have wireless connectivity at 2.4 GHz and 5th generation (5G) cellular connectivity at 4.9 GHz. Two different positions for the antenna integrated into the frame are considered in this investigation. These techniques provide remarkable reduction in computation time and computer memory.

Index Terms ─ 5G, dispersive head, FDTD method, SAR, smart glasses, temperature rise, Wi-Fi.

I. INTRODUCTION

Due to recent increase of wireless and mobile communication capabilities with the 5th generation (5G) technology and the use of higher frequencies for smart communication devices, there is a great need to assessment of electromagnetic (EM) wave penetration and related temperature rise in the human head.

With the recent introduction of 5G technology, the use of smart wearable devices such as smart watches and smart glasses has increased in popularity. Currently, smart glasses, manufactured by different companies [1-3], utilize wireless connectivity based on Bluetooth and Wi-Fi around the 2.4 GHz band. Future smart glasses would include antennas operating for Wi-Fi and 5G cellular connectivity. It is universally recognized that the EM fields radiated from the adjacent antennas to a human head may be harmful to human health. As a consequence, it is important to assess the effects of EM fields on the human head and report the corresponding SAR and temperature rise distributions.

The numerical calculation of EM interaction between an antenna and a three dimensional (3D) human head model has been performed in [4-9] using the finite-difference time-domain (FDTD) method. It requires long computation time and large computer memory because the number of cell in the computational domain is more than several millions, especially for high frequencies with proper resolution. This makes such calculations impossible on ordinary desktop computers. A dispersive algorithm proposed in [9] provides remarkable reduction in the computation time to analyze a dispersive head model at multiple frequencies of interest in a single simulation. However, as the frequencies get higher, this reduction is not sufficient to simulate the entire human head model with the ordinary desktop computers.

The effect of EM radiation produced by a cellular phone on a human head with regular glasses made of metallic frames was investigated using an EM commercial software [10-12] and the traditional FDTD method [13-14]. By using an EM commercial software, the effects of an antenna integrated into the pair of smart glasses for Wi-Fi connectivity [15-18] and 4G cellular connectivity [19-23] on the human head have been studied to investigate the radiation pattern and SAR distribution in the head. In the previous studies [15-23], analysis of SAR in the human head due to the smart glasses was performed at only one frequency of interest using a single simulation while ignoring the dispersive characteristics of the biological tissues of the head. The temperature rise in the head due to an integrated antenna into the pair of smart glasses has not been considered yet.

In this paper, the algorithm proposed in [9] is used to obtain radiation pattern, SAR and temperature rise distributions in the dispersive head at multiple

Submitted On: December 16, 2020
Accepted On: February 8, 2021

https://doi.org/10.47037/2020.ACES.J.360207

frequencies of interest in a single simulation. This algorithm, which will be referred to as a dispersive algorithm, is based on the Debye model of the head tissue parameters to be used in auxiliary differential equation (ADE) formulation of the FDTD method [24]. Then the calculations of SAR and temperature rise with the help of Pennes bioheat equation [25] are performed. In the Debye model, the three-term Debye coefficients calculated and tabulated in [26] are used as the dispersive EM properties of the human head tissues to obtain solutions at a wide range of frequencies (500 MHz to 20 GHz). The work presented here is an extension of the preliminary work presented in [27].

The effect of the integrated antenna into the pair of smart glasses on a realistic head model is investigated to evaluate the validity of two speeding up techniques for the dispersive algorithm. The integrated antenna is designed to operate at two frequency bands for Wi-Fi at 2.4 GHz and 5G cellular at 4.9 GHz. In order to show the effect of the position of the integrated antenna on the pair of smart glasses on the human head, the antennas integrated into the frame have been placed in two different positions closest to the eye, the most sensitive organ. The spatial-peak SAR over any 1 gram of tissue (SAR_{1g}), 10 gram of tissue (SAR_{10g}) in the head, and temperature rise distributions in the head at 2.4 and 4.9 GHz are computed for each antenna position. Numerical results show that the speeding up techniques would be efficient for analyzing the head model due to EM waves of higher frequencies.

Two speeding up techniques are used here and the electromagnetic effects of smart glasses on the human head are investigated using the dispersive algorithm with these techniques. The speeding up technique proposed in [28] for anisotropic materials is applied to the dispersive algorithm and based on dividing the computation domain into two regions: one is the dispersive region analyzed using the dispersive formulation [24] and the other is non-dispersive region analyzed using the non-dispersive formulation [24]. The other speeding up technique is to use a half head model instead of the full head model in the FDTD simulations. These speeding up techniques provides more than 50% reduction in computation time and computer memory.

II. COMPUTATION METHODS AND MODELS

A. 3D human head model with dispersive tissues

A human head model generated in [29] and used in this work consists of eight tissues (skin, muscle, bone, blood, fat, lens, and white and grey matter). Figure 1 shows a sample of a horizontal slice of the human head model which consists of 172 (width) × 218 (depth) × 240 (height) cubic cells.

The EM parameters of all tissues in the human body are frequency dependent. Therefore, with a traditional FDTD solution one can obtain results due to only one frequency in a single simulation. The numerical technique proposed provides the three-term Debye coefficients tabulated in [26] for the biological tissues in the frequency range between 500 MHz and 20 GHz. The complex relative permittivity $\left(\epsilon_r^*(\omega)\right)$ for the three-term Debye coefficients is defined [26] as:

$$\epsilon_r^*(\omega) = \epsilon_\infty + \sum_{k=1}^{3} \frac{\Delta\epsilon_k}{1+j\omega\tau_k};\ \Delta\epsilon_k = A_k(\epsilon_s - \epsilon_\infty), \quad (1)$$

where ϵ_∞ is permittivity at high frequencies, $\Delta\epsilon_k$ is pole weight, and τ_k is relaxation time.

In order to ensure the numerical stability in the FDTD method, the cell size (Δ) should be less than $\lambda_{min}/10$ [6-7] and expressed as:

$$\Delta = \frac{\lambda_{min}}{10} = \frac{c}{10 f_{max}\sqrt{real(\epsilon_r^*)}}, \quad (2)$$

where λ_{min} is the wavelength of the highest frequency (f_{max}) in the head model and c is the speed of light in free space. The head model is rescaled to have a cell size of Δ=0.9 mm (about $\lambda_{min}/10$ in the head model exposed to EM waves at 4.9 GHz) in all directions to ensure the numerical stability.

B. Speeding up techniques

In the dispersive algorithm, the electric and magnetic field components, and additional field terms due to Debye dispersive tissues [24] are calculated for every FDTD time-step in the entire computational domain. It has been realized that additional field terms do not need to be calculated in every cell of the computational domain. Therefore, a speeding up technique proposed similarly in [28] is used to reduce the computation time and computer memory. This technique called as domain division technique (DDT) is based on dividing the computation domain into two regions: one is called dispersive region which contains a dispersive head and the other is called non-dispersive region which contains air layer, convolution perfect matching layer (CPML) [24], and non-dispersive materials, as shown in Fig. 2. In the dispersive region, the dispersive formulation is performed to calculate the field components, whereas, in the non-dispersive region, the regular FDTD formulation in [24] is performed to update the field components.

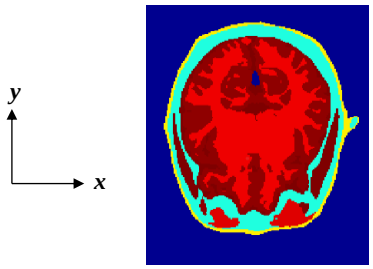

Fig. 1. Horizontal slice of the 3D realistic head model.

The penetration depth is a function of frequency and a measure of how deep the electromagnetic wave is affecting the biological tissues. In [30], the penetration depth of the electromagnetic wave for one-dimensional human head model has been extensively studied from 500 MHz to 100 GHz. According to [30] and the best of our knowledge, the penetration depth in the human head model is less than 100 mm at 500 MHz and becomes smaller as the frequency increases. It can be said that the electromagnetic waves radiated by the antenna placed on one side of the human head cannot send a significant amount of waves to the other half of the head. Therefore, it is not necessary to simulate the full head model. As the other speeding up technique, a half head model instead of full head model is used in the simulation to reduce the computation time and computer memory. In this technique, it is assumed that the cut side of half head model is terminated by 10 cell layers of CPML [24] extending to inside of the head tissues and other sides of the head model is terminated by 10 cell layers of CPML with 10 cell air layers. The number of cells for the half head model, shown in Fig. 3, cut in the *x*- and *y*-directions is 7,657,440. However, the number of cell is 15,314,880 for the entire computational domain including the full head model, 10 cell air layers and 10 cell layers of CPML. These two techniques used in this work provide more than 50% reduction in the computation time and computer memory.

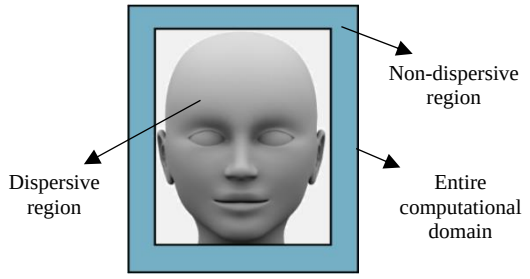

Fig. 2. Entire FDTD computational domain divided into the dispersive and non-dispersive regions.

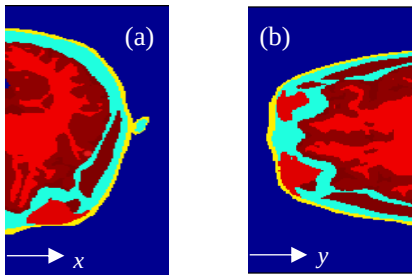

Fig. 3. Horizontal slice of the half head model cut in the (a) *x*- and (b) *y*-directions.

C. Smart glasses model and antenna

The smart glasses includes non-dispersive materials which are plastic frames, metallic hinges, lens, and antenna. The relative permittivity of lens and frame of the smart glasses is 4.82 and 3.5, respectively, and the wires of antenna are made of PEC. The configuration of the smart glasses is shown in Fig. 4 with all dimensions. In order to obtain solutions at multiple frequencies in a single simulation, the antenna integrated into the frame of the smart glasses requires to operate at least two frequency bands which will be Wi-Fi and 5G cellular connectivity for this work. The antenna, as shown in Fig. 5, consists of a dipole with two passive wires which create double resonances. The length and radius of the dipole antenna and passive wires are given in Fig. 5. Two passive wires are placed at a distance of 2.7 mm at the two sides of the dipole antenna. Two different positions for the antenna in the frame are considered: left arm of the frame and bridge of the frame as shown in Fig. 4. The combination of the dipole antenna and the two passive wires were simulated using the thin-wire formulation [24] based on the FDTD method. The input reflection coefficients (S_{11}) at the terminals of the integrated antenna placed into the frame with and without the head model are shown in Fig. 6. The resonance frequencies of the antenna have been slightly affected by the presence of the human head and a third resonance frequency appeared.

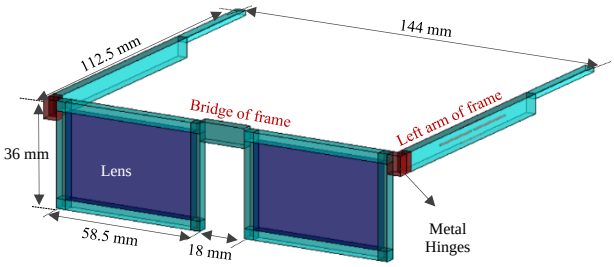

Fig. 4. Geometry of the smart glasses included lens, frame, and antenna.

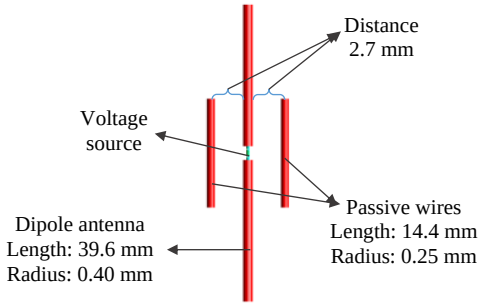

Fig. 5. Integrated dipole antenna with two passive wires.

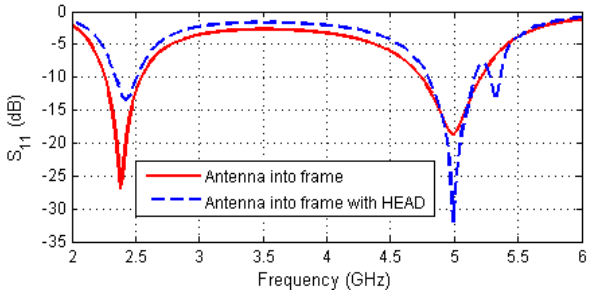

Fig. 6. S_{11} of the integrated antenna into the frame with and without the human head model.

D. SAR calculation

SAR is the ratio of absorbed RF energy per unit mass of biological tissues. The SAR values in the biological tissues are computed by using the FDTD method. The electric fields in time-domain are calculated on the edges of each cell during each FDTD time-step. The twelve-field component approach proposed in [31] is used to obtain the averaged electric field components in the center of each cell. Then, these averaged electric field components are transformed to frequency domain by using the discrete Fourier transform (DFT). After EM simulation is completed, the electric field components are obtained for the calculation of the steady-state SAR distribution in the human head model at each frequency of interest. In order to make a comparison with existing studies in [19-22], all calculated SAR values are normalized to the antenna input power of 0.25 W for each frequency of interest. For calculating SAR_{1g} and SAR_{10g} in the head model, the IEEE standard in [32] is used. The obtained SAR_{1g} values are considered as RF heat source in the temperature rise calculation.

E. Temperature rise calculation

After performing the EM simulation and SAR calculation for the head, the temperature rise calculation using the Pennes bioheat equation [25] is carried out in two parts for each frequency of interest. In the first part, the steady-state temperature distribution in the head is calculated by solving the bioheat equation with no RF heat source (SAR_{1g}=0). In the second part, the temperature distribution due to RF heat source is calculated by substituting the SAR_{1g} distribution into the bioheat equation. By taking the difference between the temperature distributions obtained in the two parts, the temperature rise distribution in the head is obtained. The bioheat equation computes the temperature distribution based on the tissues mass density, heat capacity, thermal conductivity, blood perfusion rate, and blood temperature. All these parameters for the tissues along with the convective boundary condition for the bioheat equation applied to the skin-air and internal cavity-air interface are presented in [4] and [9].

III. NUMERICAL RESULTS

To verify the validity of the dispersive algorithm for the smart glasses application, the SAR_{1g} values in the head using the dispersive algorithm are compared with those reported in [17] at 2.4 GHz and with those reported in [20-21] at 1.9 GHz when the antenna is placed into the left arm of the frame. The maximum SAR_{1g} value in the head at 2.4 GHz obtained using the dispersive algorithm is 0.548 W/kg, whereas that obtained in [17] using an EM commercial software is 0.557 W/kg when the input power was set to 63.095 mW. The obtained maximum SAR_{1g} value in the head at 1.9 GHz using the dispersive algorithm is 1.75 W/kg, whereas that obtained in [20-21] using an EM commercial software is 1.64 W/kg when the input power was set to 0.25 W. The compared results are in good agreement with acceptable differences. The reason for these differences in the compared results would come from the use of different head model and head resolution, and from different types of antennas used in the studies.

In order to show the performance of applying DDT and using a half head model, and the effects of the antenna positions into the frame of the smart glasses on the SAR_{1g}, SAR_{10g}, and temperature rise distributions, two different antenna positions in the frame of the glasses are evaluated at 2.4 and 4.9 GHz using the dispersive algorithm. The specification of the computer used in this work is Intel® Core™ i7-8700 CPU and 16 GB RAM. The FDTD program is developed on the 64-bit MATLAB version 8.2.0.701 (R2013a).

A. SAR and temperature rise due to the antenna integrated into the left arm of the smart glasses

The maximum SAR_{1g}, SAR_{10g}, and temperature rise values in the full head model without DDT and half head with DDT at 2.4 GHz and 4.9 GHz are obtained and tabulated in Table 1. It can be seen that applying DDT and using half head model do not affect the results. The distributions of SAR_{1g} and temperature rise obtained in the full head model without DDT and in the half head model with DDT are evaluated at 2.4 and 4.9 GHz and shown in Figs. 7 and 8, respectively. It can be realized from these figures that there are no difference in the obtained distributions and the maximum SAR_{1g} and temperature rise occur at the left side of the head because the antenna is placed into the left arm of the smart glasses. It can be also realized that the temperature rise distributions depend on the SAR distributions. In order to show the effect of the human head on the antenna radiation patterns, the radiation patterns of the antenna in the left arm of the frame with and without the human head at the resonance frequencies are calculated and shown in Fig. 9. It can be seen from the radiation patterns on the *xy* and *xz* plane cuts that the presence of the human head model greatly attenuates the radiation of the antenna

towards the head and increases in the other direction.

In Table 2, the computation time and computer memory for the EM analysis of the full human head without DDT and half human head with DDT using the dispersive algorithm are tabulated. It can be seen from Table 2 that applying DDT and using half head model in the simulations provides more than 60% reduction in computation time and 50% reduction in computer memory.

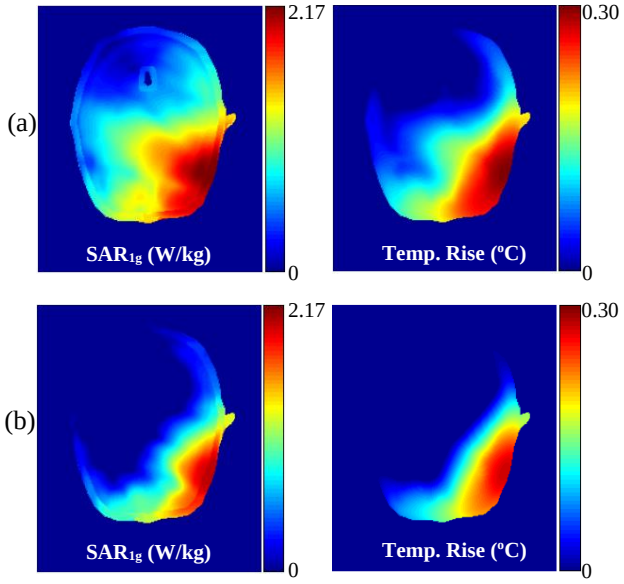

Fig. 7. SAR_{1g} and temperature rise distributions in the full head model at (a) 2.4 and (b) 4.9 GHz.

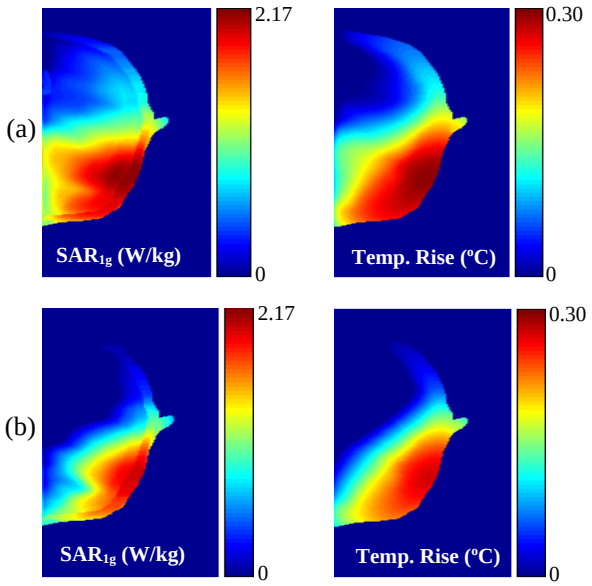

Fig. 8. SAR_{1g} and temperature rise distributions in the half head model at (a) 2.4 and (b) 4.9 GHz.

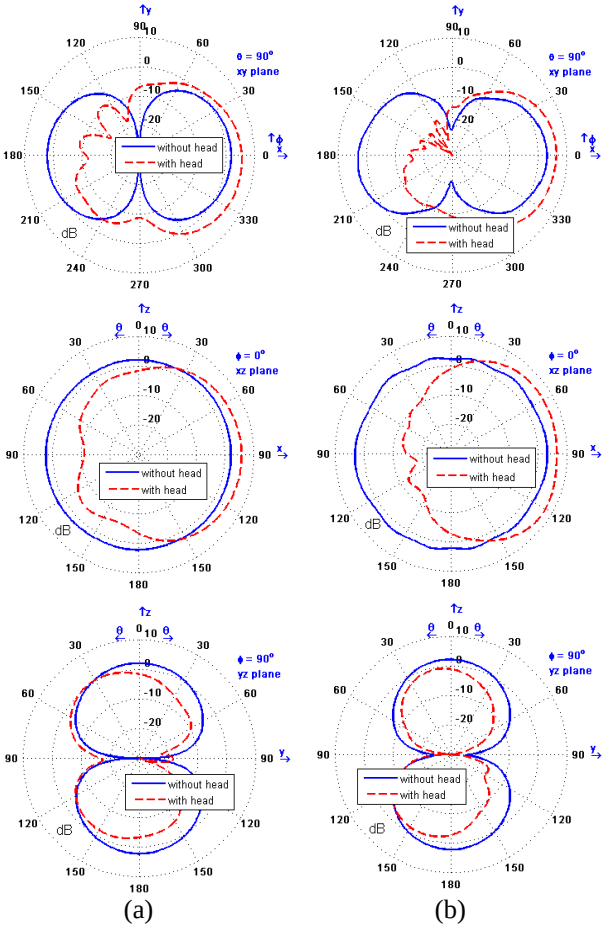

Fig. 9. Radiation patterns at (a) 2.4 and (b) 4.9 GHz with and without the head in the *xy*, *xz*, and *yz* plane cuts.

Table 1: Max. SAR and temperature rise values obtained for the full head without DDT and half head with DDT

Freq. (GHz)	Head Model	SAR_{1g} (W/kg)	SAR_{10g} (W/kg)	Max. Temp. Rise (°C)
2.4	Full Head	2.1696	1.1467	0.2990
	Half Head	2.1541	1.1409	0.2971
4.9	Full Head	1.1379	0.4676	0.1538
	Half Head	1.1375	0.4674	0.1534

Table 2: Computation time and computer memory of full and half head model

	Model	Computation Time (min.)	Computer Memory (MB)
Without DDT	Full Head	2178	8870
With DDT	Half Head	871	4380

B. SAR and temperature rise due to the antenna integrated into the bridge of the smart glasses

The maximum SAR_{1g}, SAR_{10g}, and temperature rise values in the full head model without DDT and half head with DDT at 2.4 GHz and 4.9 GHz are obtained and

tabulated in Table 3. It can be seen that applying DDT and using the half head model do not affect the results. The distributions of SAR_{1g} and temperature rise obtained in the full head model without DDT and in the half head model with DDT are evaluated at 2.4 and 4.9 GHz and shown in Figs. 10 and 11, respectively. It can be realized from these figures that there are no difference in the obtained distributions and the maximum SAR_{1g} and temperature rise occur at the front side of the head because the antenna is placed into the bridge of the smart glasses. The radiation patterns of the antenna in the bridge of the frame with and without the human head at resonance frequencies are shown in Fig. 12. It can be seen from the radiation patterns on the *xy* and *yz* plane cuts that the presence of the human head model greatly attenuates the radiation of the antenna towards the head and increases in the other direction.

In Table 4, the computation time and computer memory for the EM analysis of full human head without DDT and half human head with DDT using the dispersive algorithm are tabulated. It can be seen from Table 4 that applying DDT and using half head model in the simulations provides more than 60% reduction in computation time and 50% reduction in computer memory.

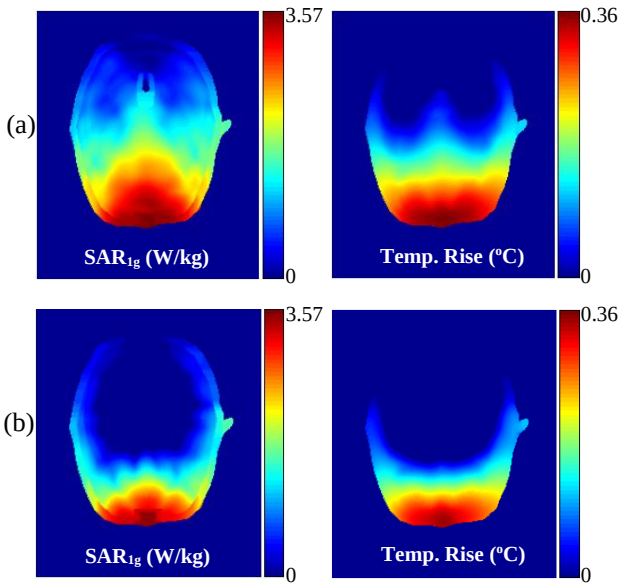

Fig. 10. SAR_{1g} and temperature rise distributions in the full head model at (a) 2.4 and (b) 4.9 GHz.

Table 3: Max. SAR and temperature rise values obtained for the full head without DDT and half head with DDT

Freq. (GHz)	Head Model	SAR_{1g} (W/kg)	SAR_{10g} (W/kg)	Max. Temp. Rise (°C)
2.4	Full Head	3.5735	1.2419	0.3606
	Half Head	3.5730	1.2415	0.3607
4.9	Full Head	2.8160	0.2670	0.2456
	Half Head	2.8171	0.2672	0.2501

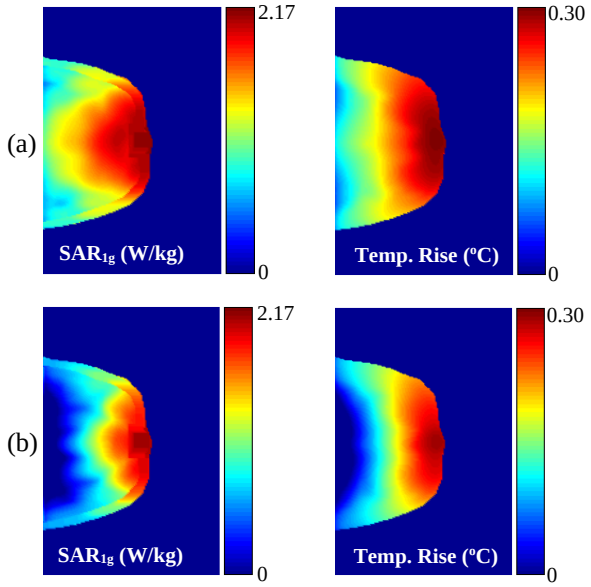

Fig. 11. SAR_{1g} and temperature rise distributions in the half head model at (a) 2.4 and (b) 4.9 GHz.

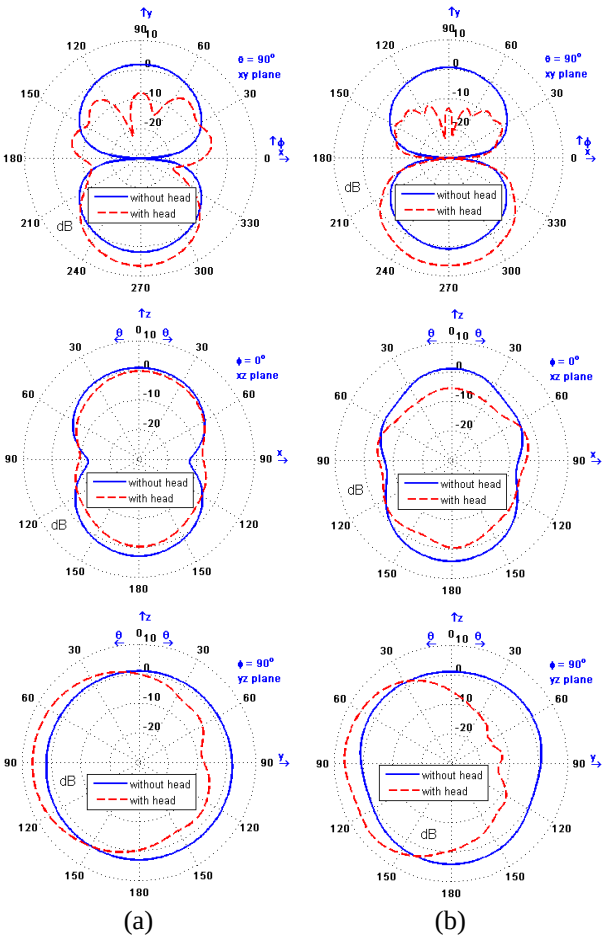

Fig. 12. Radiation patterns at (a) 2.4 and (b) 4.9 GHz with and without the head in the *xy*, *xz*, and *yz* plane cuts.

Table 4: Computation time and computer memory of full and half head model

	Model	Computation Time (min.)	Computer Memory (MB)
Without DDT	Full Head	2165	8820
With DDT	Half Head	837	4320

C. Comparison of results obtained due to the antenna into two different positions

The maximum SAR_{1g}, SAR_{10g}, and temperature rise values in the head at 2.4 GHz and 4.9 GHz are tabulated in Tables 1 and 3 when the antenna is placed into two different positions in the smart glasses. The electric conductivities of the tissues become larger as the frequency is increased, hence the magnitude of EM waves penetration in the head decreases significantly. Therefore, the SAR_{1g}, SAR_{10g}, and resulting temperature rise values in the head decrease at higher frequencies. It is well known that the SAR values are dependent on the frequency, the type of antenna, the input power of the antenna, the EM parameters of tissues, antenna polarization, the distance between the human head and the antenna, etc.

The limits of maximum SAR_{1g} and SAR_{10g} values are determined by the RF exposure guidelines and standards in [33-34]. The SAR_{1g} values reported in Tables 1 and 3 are generally above the limit of 1.6 W/kg, whereas the SAR_{10g} values reported in these tables are always less than the limit of 2 W/kg when the antenna input power is set to 0.25 W. These high values above the limit would require this power to be reduced to comply with the RF exposure guidelines and standards.

It must be noted that the distance between the antenna and human head is 13.5 mm and 7.2 mm for left arm and bridge of the frame, respectively. These distances are closer than those reported in [4-9]. The SAR and resulting temperature rise values obtained due the antenna in the bridge of the frame are higher than those obtained due to the antenna in the left arm of the frame because the integrated antenna in the bridge of the frame is closer to the head and eye which is one of the most sensitive organs in the human head for EM field exposure.

The maximum temperature rises reported in Tables 1 and 3 are less than the temperature rise limit of 4.5 °C [35] for tissue health injury, but they are not negligible. The maximum temperature variations at 2.4 and 4.9 GHz due to the antenna placed into two different positions in the glasses frame as a function of time are shown in Fig. 13. It can be seen that the maximum temperature rises increases exponentially over the first 6 minutes, then they slow down, and the maximum temperature rises are reached after 30 minutes of exposure.

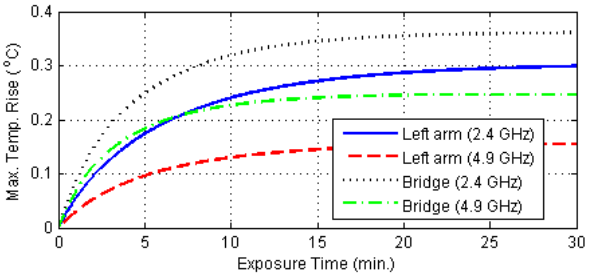

Fig. 13. Maximum temperature rise at 2.4 and 4.9 GHz due to the antenna placed into position-1 and position-2.

VI. CONCLUSION

The electromagnetic interactions between a 3D dispersive human head model and electromagnetic fields radiated by an antenna integrated into a pair of smart glasses at 2.4 and 4.9 GHz are investigated using a dispersive FDTD algorithm. Additionally, in order to show the effect of the position of the integrated antenna on the SAR and temperature rise distributions in the head, two possible positions for the antenna into the frame of the smart glasses are considered. In order to reduce to computation time and computer memory of the simulations, two speeding up techniques used in this work are based on dividing the computational domain into two sub-regions and using a half head model instead of a full head model. Applying these techniques provides more than 50% in the computation time and computer memory. These techniques would be efficient for analyzing the human head due to electromagnetic waves of higher frequencies.

REFERENCES

[1] https://www.vuzix.com/Products/m100-smart-glasses [Online website 2021].

[2] https://x.company/glass/ [Online website 2021].

[3] https://www.theverge.com/2015/4/16/8422111/recon-jet-smart-glasses-sports-google-glass [Online website 2021].

[4] J. Wang and O. Fujiwara, "FDTD computation of temperature rise in the human head for portable telephones," in *IEEE Transactions on Microwave Theory and Techniques*, vol. 47, no. 8, pp. 1528-1534, Aug. 1999.

[5] P. Bernardi, M. Cavagnaro, S. Pisa, and E. Piuzzi, "Power absorption and temperature elevations induced in the human head by a dual-band monopole-helix antenna phone," in *IEEE Transactions on Microwave Theory and Techniques*, vol. 49, no. 12, pp. 2539-2546, Dec. 2001.

[6] A. Hirata and T. Shiozawa, "Correlation of maximum temperature increase and peak SAR in

the human head due to handset antennas," in *IEEE Transactions on Microwave Theory and Techniques*, vol. 51, no. 7, pp. 1834-1841, July 2003.

[7] A. Hirata, M. Morita, and T. Shiozawa, "Temperature increase in the human head due to a dipole antenna at microwave frequencies," in *IEEE Transactions on Electromagnetic Compatibility*, vol. 45, no. 1, pp. 109-116, Feb. 2003.

[8] M. Fujimoto, A. Hirata, J. Q. Wang, O. Fujiwara, and T. Shiozawa, "FDTD-derived correlation of maximum temperature increase and peak SAR in child and adult head models due to dipole antenna," in *IEEE Transactions on Electromagnetic Compatibility*, vol. 48, no. 1, pp. 240-247, Feb. 2006.

[9] F. Kaburcuk and A. Z. Elsherbeni, "Temperature rise and SAR distribution at wide range of frequencies in a human head due to an antenna radiation," *Applied Computational Electromagnetics Society Journal*, vol. 33, no. 4, pp. 367- 372, Apr. 2018.

[10] M. Zhang and X. Wang, "Influence on SAR due to metallic frame of glasses based on high-resolution Chinese electromagnetic human model," *Asia-Pacific International Symposium on Electromagnetic Compatibility*, Beijing, pp. 48-51, 2010.

[11] M. H. Mat, M. F. B. A. Malek, W. G. Whittow, S. H. Ronald, M. S. Zulkefli, N. Saudin, and L. Mohamed, "The influence of human head model wearing metal-frame spectacles to the changes of SAR and antenna gain: Simulation of frontal face exposure," *Progress In Electromagnetics Research*, vol. 137, pp. 453-473, 2013.

[12] G. Bellanca, G. Caniato, A. Giovannelli, P. Olivo, and S. Trillo, "Effect of field enhancement due to the coupling between a cellular phone and metallic eyeglasses," *Microw. Opt. Technol. Lett.*, vol. 48, no. 1, pp. 63-65, Jan. 2006.

[13] K. Stergiou, C. Panagamuwa, W. Whittow, and R. Edwards, "Effects of metallic semi-rimmed spectacles on SAR in the head from a 900MHz frontal dipole source," *Loughborough Antennas & Propagation Conference*, Loughborough, pp. 721-724, 2009.

[14] J. Q. Lan and K. M. Huang, "Evaluation of SAR in a human head with glasses exposed to radiation of a mobile phone," *Journal of Electromagnetic Waves and Applications*, vol. 27, no. 15, pp. 1919-1930, 2013.

[15] M. Ferreira, C. Oliveira, F. Cardoso, and L. M. Correia, "SAR assessment of google glasses at cellular wireless frequency bands," *10th European Conference on Antennas and Propagation (EuCAP)*, Davos, pp. 1-4, 2016.

[16] Y. F. Zheng, G. H. Sun, Q. K. Huang, S. W. Wong, and L. S. Zheng, "Wearable PIFA antenna for smart glasses application," *IEEE International Conference on Computational Electromagnetics*, Guangzhou, pp. 370-372, 2016.

[17] S. Choi and J. Choi, "Miniaturized MIMO antenna with a high isolation for smart glasses," *IEEE-APS Topical Conference on Antennas and Propagation in Wireless Communications*, Verona, pp. 61-63, 2017.

[18] Y. A. A. Pizarro, A. A. de Salles, S. Severo, J. L. T. Garzon, and S. M. R. Bueno, "Specific absorption rate (SAR) in the head of Google glasses and Bluetooth user's," *IEEE Latin-America Conference on Communications*, Cartagena de Indias, pp. 1-6, 2014.

[19] A. Cihangir, C. Luxey, G. Jacquemod, R. Pilard, F. Gianesello, W. G. Whittow, and C. J. Panagamuwa, "Investigation of the effect of metallic frames on 4G eyewear antennas," *Loughborough Antennas and Propagation Conference*, Loughborough, pp. 60-63, 2014.

[20] A. Cihangir, W. G. Whittow, C. J. Panagamuwa, F. Ferrero, G. Jacquemod, F. Gianesello, and C. Luxey, "Feasibility study of 4G cellular antennas for eyewear communicating devices," in *IEEE Antennas and Wireless Propagation Letters*, vol. 12, pp. 1704-1707, Oct. 2013.

[21] A. Cihangir, W. Whittow, C. Panagamuwa, G. Jacquemod, F. Gianesello, and C. Luxey, "4G antennas for wireless eyewear devices and related SAR," *Comptes Rendus Physique*, vol. 16, no. 9, pp. 836-850, Nov. 2015.

[22] A. Cihangir, C. J. Panagamuwa, W. G. Whittow, F. Gianesello, and C. Luxey, "Ultrabroadband antenna with robustness to body detuning for 4G eyewear devices," in *IEEE Antennas and Wireless Propagation Letters*, vol. 16, pp. 1225-1228, Nov. 2017.

[23] J. Lan and G. Du, "Evaluation of remperature elevation in human ocular tissues due to wireless eyewear devices," *Applied Computational Electromagnetics Society Journal*, vol. 34, no. 1, pp. 17-24, Jan. 2019.

[24] A. Z. Elsherbeni and V. Demir, *The Finite-Difference Time-Domain Method for Electromagnetics with MATLAB Simulations*, second edition, ACES Series on Computational Electromagnetics and Engineering, SciTech Publishing, an Imprint of IET, Edison, NJ, 2016.

[25] H. H. Pennes, "Analysis of tissue and arterial blood temperature in resting forearm," *J. Appl. Physiol*., vol. 1, pp. 93-122, 1948.

[26] M. A. Eleiwa and A. Z. Elsherbeni, "Debye constants for biological tissues from 30 Hz to 20 GHz," *Applied Computational Electromagnetics Society Journal*, vol. 16, no. 3, pp. 202-213, Nov. 2001.

[27] F. Kaburcuk and A. Z. Elsherbeni, "Smart glasses radiation effects on a human head model at Wi-Fi and 5G cellular frequencies," *2018 International Applied Computational Electromagnetics Society Symposium - China (ACES)*, Beijing, China, pp. 1-2, 2018.
[28] F. Kaburcuk and A. Z. Elsherbeni, "A speeding up technique for lossy anisotropic algorithm in FDTD method," *Applied Computational Electromagnetics Society Journal*, vol. 31, no. 12, pp. 1377-1381, 2016.
[29] I. G. Zubal, C. R. Harrell, E. O. Smith, Z. Rattner, G. R. Gindi, and P. B. Hoffer, "Computerized three-dimensional segmented human anatomy," *Medical Physics*, vol. 21, no. 2, pp. 299-302, Feb. 1994.
[30] F. Kaburcuk, A. Z. Elsherbeni, R. Lumnitzer, and A. Tanner, "Electromagnetic waves interaction with a human head model for frequencies up to 100 GHz," *Applied Computational Electromagnetics Society Journal*, vol. 35, no. 6, pp. 613-621, 2020.
[31] K. Caputa, M. Okoniewski, and M. A. Stuchly, "An algorithm for computations of the power deposition in human tissue," in *IEEE Antennas and Propagation Magazine*, vol. 41, no. 4, pp. 102-107, Aug. 1999.
[32] IEEE Recommended Practice for Measurements and Computations of Radio Frequency Electromagnetic Fields with Respect to Human Exposure to Such Fields, 100 kHz-300 GHz, IEEE Standard C95.3-2002, Annex E, 2002.
[33] Federal Communications Commission, "Evaluating compliance with FCC guidelines for human exposure to radio frequency electromagnetic fields," Rep., Washington, DC, Tech. Rep. OET Bull. 65, 1997.
[34] IEEE Standard for Safety Levels with Respect to Human Exposure to Radio Frequency Electromagnetic Fields, 3 kHz to 300 GHz, IEEE Standard C95.1, 1999.
[35] A. C. Guyton and J. E. Hall, *Textbook of Medical Physiology*. Philadelphia, PA: W. B. Saunders, chap. 73, 1996.

Fatih Kaburcuk received both the M.Sc. and Ph.D. degrees from Syracuse University, Syracuse, NY, USA, in 2011 and 2014, respectively, all in Electrical eEgineering. During his graduate studies, he worked as a Research Assistant with Syracuse University and PPC-Belden Inc. in Liverpool, NY, USA. He worked as a Visiting Research Scholar at the Department of Electrical Engineering, Colorado School of Mines, Golden, CO, USA in 2014. He joined the Erzurum Technical University in 2015 and served as an Assistant Professor until 2019. Since 2020, he has been serving as an Associate Professor with the Department of Electrical-Electronics Engineering, Sivas Cumhuriyet University, Turkey. His research interest includes numerical methods in electromagnetics, biological effect of electromagnetic radiation.

Atef Z. Elsherbeni received an honor B.Sc. degree in Electronics and Communications, an honor B.Sc. degree in Applied Physics, and a M.Eng. degree in Electrical Engineering, all from Cairo University, Cairo, Egypt, in 1976, 1979, and 1982, respectively, and a Ph.D. degree in Electrical Engineering from Manitoba University, Winnipeg, Manitoba, Canada, in 1987. He started his engineering career as a part time Software and System Design Engineer from March 1980 to December 1982 at the Automated Data System Center, Cairo, Egypt. From January to August 1987, he was a Post-Doctoral Fellow at Manitoba University. Elsherbeni joined the faculty at the University of Mississippi in August 1987 as an Assistant Professor of Electrical Engineering. He advanced to the rank of Associate Professor in July 1991, and to the rank of Professor in July 1997. He was the Associate Dean of the college of Engineering for Research and Graduate Programs from July 2009 to July 2013 at the University of Mississippi. He then joined the Electrical Engineering and Computer Science (EECS) Department at Colorado School of Mines in August 2013 as the Dobelman Distinguished Chair Professor. He was appointed the Interim Department Head for (EECS) from 2015 to 2016 and from 2016 to 2018 he was the Electrical Engineering Department head. In 2009 he was selected as Finland Distinguished Professor by the Academy of Finland and TEKES. Elsherbeni is a Fellow member of IEEE and ACES. He is the Editor-in-Chief for ACES Journal, and a past Associate Editor to the Radio Science Journal. He was the Chair of the Engineering and Physics Division of the Mississippi Academy of Science, the Chair of the Educational Activity Committee for IEEE Region 3 Section, the General Chair for the 2014 APS-URSI Symposium, the President of ACES Society from 2013 to 2015, and the IEEE Antennas and Propagation Society (APS) Distinguished Lecturer for 2020-2022.

Frequency Band Rejection Technique Based on the Operating Modes for a Wideband H-Shaped DRA

Feras Z. Abushakra and Nathan Jeong

Department of Electrical and Computer Engineering
University of Alabama, Tuscaloosa, 35487, USA
fabushakra@crimson.ua.edu, shjeong@eng.ua.edu

Abstract ─ In this paper, a new approach to create frequency band rejection is applied to a wideband H-shaped dielectric resonator antenna (DRA). In order to create a notch characteristic in the operating band of the $TE^{y}_{1\delta1}$ and $TE^{y}_{2\delta1}$ modes, and guided by their theoretical and simulated electric field distributions, a narrow conductive strip is incorporated around the mid-section of the H-shaped DRA. The orientation of the notching strip is determined based on the electric field distribution of the selected modes for the frequency rejection. Furthermore, the selected feeding method improves the radiation patterns for this DRA shape compared to its previous designs. The new design offers an operating frequency range that extends from 4.15 to 9.8 GHz, allowing 81% of fractional bandwidth. The first notch is created at 6.5 GHz, while the second one is at 8 GHz. Average radiation efficiency of 95% across the frequency of interest is achieved with overall dimensions of 40×30×11.4 mm^3. The proposed design is simulated using Ansys HFSS and validated by measurement.

Index Terms ─ Dielectric Resonator Antenna (DRA), H-shaped antenna, modes distribution, notch rejection.

I. INTRODUCTION

During the last few decades a great attention has been paid to the DRAs due to their capabilities to provide wide bandwidth, high gain, and high radiation efficiency compared to other types of antennas. Many shapes and feeding methods of DRAs were introduced for various applications such as 5G, WiMAX, radar, etc. [1]. Different feeding mechanisms to excite the DRA were also used such as microstrip transmission lines, coaxial probe and slot aperture [2]. The coaxial feeding method is the most commonly used method due to its matching flexibility by changing the probe position and height [3]. Various shapes of the DRA were presented (P, Z and T), where some of them were fed by microstrip line feeder, while others were fed by a probe [4-9]. In the last few years, many designs of the DRA showed that the single element DRA could achieve a bandwidth up to 120% [10-13]. This extremely wide band covers many applications where in some cases the interference becomes the main obstacle and needs to be suppressed. To overcome this problem, many designs suggested different methods to create notches in the operating band of wide band DRAs. In [10], an inverted conical shaped DRA fed directly by a circular ring patch antenna was presented. A notch rejection was created and shifted by changing the dimensions of the patch resonator. Also, several wide band DRA designs fed by a microstrip line feeder with notch characteristics were reported [11, 12]. For these designs, several modifications in the feeder or ground plane were done to create a stop band filtering in the operating bandwidth of the design. On the other hand, the DRA position was rotated with respect to the microstrip line feeder to create the notch characteristics [13]. In addition, a cross slot aperture was formed in a circular patch antenna placed directly underneath the DRA at the same side of the substrate. Two different etches in the microstrip patch antenna were conducted to create two frequency rejection bands [14]. These designs covered wide bandwidth up to 120%. Also, the DRA size is very small compared to the lower operating band in these designs. In such a hybrid method, the broadband response comes from both the microstrip feeder and DRA. Accordingly, such designs created the rejection band in the microstrip line feeder operating band while the DRA modes were not affected. On the other hand, UWB DRA was proposed with frequency rejection and fed using metallic strip with a probe on the side of the DRA with the presence of a shorting pin drilled inside the DRA [15]. A slot was created in the feeding vertical strip to create a notch in the operating band of the antenna. In this paper, a wide band H-shaped DRA with enhanced radiation pattern is presented. In order to create the notch frequency for the first two modes in the operating band, a narrow strip will be used to suppress part of the operating mode by wrapping it around the DRA in different directions. The antenna performance is discussed before and after applying the notching technique on this design.

Submitted On: August 22, 2020
Accepted On: December 6, 2020

https://doi.org/10.47037/2020.ACES.J.360208

II. ANTENNA DESIGN AND CONFIGURATION

The proposed H-shaped DRA is shown in Fig. 1. The excitation is realized with a U-shaped feeder which is directly connected to a coaxial probe. At the opposite side, another identical strip is placed and shorted to the ground. This feeding mechanism will be useful to create the $TE_{1\delta 1}$ and $TE_{2\delta 1}$ modes as the first two operating modes [16].

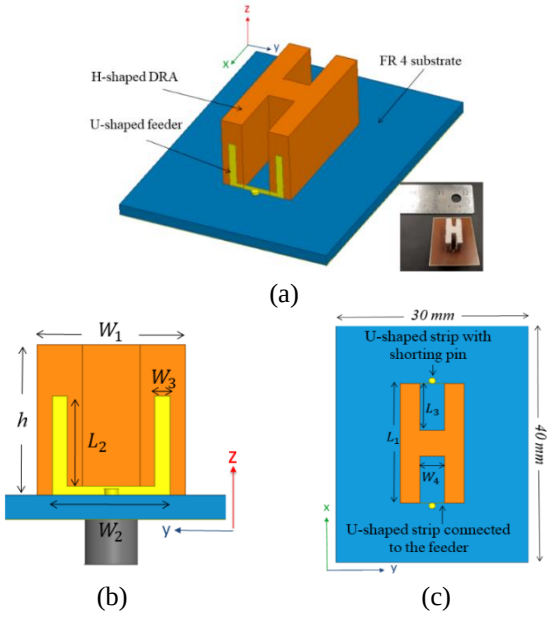

Fig. 1. The proposed H-shaped DRA: (a) 3D view with fabricated prototype, (b) *yz*-plane, and (c) *xy*-plane.

Among the different DRA shapes, the H-shape has the advantage of providing a symmetric geometry from the three principal axes. However, the radiation pattern of this shape has two problems. The cross polarization level is very high and the symmetry of the radiation pattern is poor at the perpendicular plane to the feeder. To address these issues, the proposed design is fed by two identical U-shaped strips. One for feeding the DRA while the other one is attached to the opposite side of the DRA and connected to the ground plane using via. This feeding method creates electric fields that allow the higher order modes to be more uniform and resulting in lower cross polarization level. In order for a better understanding of the second strip effects on the design, the electric field vector plots for the DRA with and without the second U-shaped strip are compared in Fig. 2. It could be seen that the electric field vectors at the mid-section show more uniform distribution in the DRA with the second U-strip at the 9 GHz. Also, the electric field shows better symmetry in its intensity at both sides of the design.

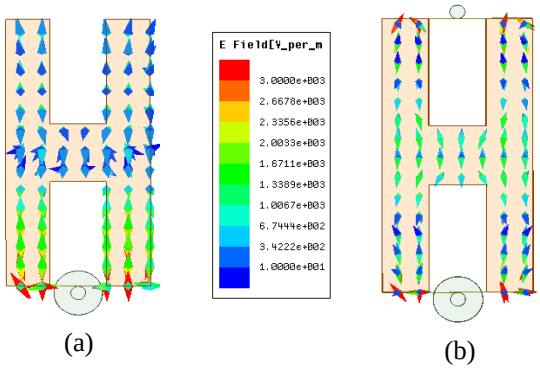

Fig. 2. Vector plot of the electric field at the *xy*-plane at 9 GHz. (a) DRA without the second U-shaped strip, and (b) DRA with the second U-shaped strip.

The DRA is placed directly at the top of 40×30×1.6 mm^3 FR-4 substrate with relative permittivity and dielectric loss tangent of (ϵ_r =4.4) and (tanδ=0.02), respectively. The ground plane is at the lower side of the substrate. For the DRA, Rogers RO 3010 material with a relative permittivity of 10.2 and dielectric loss tangent of 0.0035 is used. The design dimensions are W_1=10 mm, L_1=20 mm, L_3=7.85 mm, W_4=3.8 mm and h=11.4 mm. The feeder dimensions are L_2=6 mm, W_2=7.9 mm, and W_3=1 mm. The simulated and measured results of the design are shown in Fig. 3. The -10 dB impedance bandwidth is achieved from 4.85 to 9.8 GHz, 69% of the fractional bandwidth. The simulated peak realized gain is between 4.0 to 7.0 dBi. The measurement shows good agreement with the simulation. However, the slight difference between the measured and simulated performance is expected as there are many different substrate layers glued to fabricate the design.

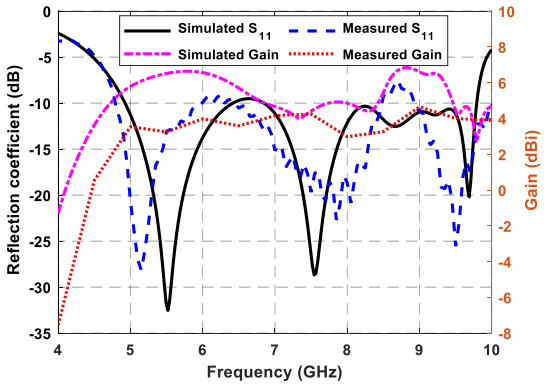

Fig. 3. Reflection coefficient and peak realized gain of the H-shaped DRA.

The radiation patterns of this design are illustrated in Fig. 4. The cross-polarization level is around -20 dB at the *yz*-plane, while it is less than -50 dB at the *xz*-plane

which is not shown in the scale. It is also notable that even at the end of the band, the cross polarization level remains low. The radiation pattern at the *yz*-plane shows highly symmetric pattern, while it is less symmetric at the *xz*-plane. However, compared to the previously reported H-shaped DRA, this design has better radiation patterns in terms of cross polarization level and symmetry [17, 18]. The front to back ratio (F/B) is around 10 dB.

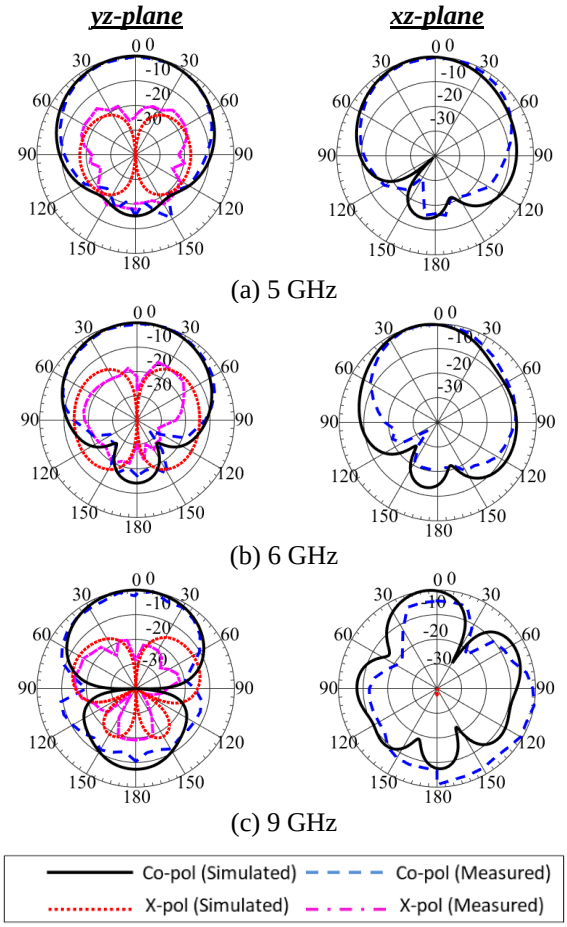

Fig.4. Radiation patterns of the H-shaped DRA at different frequencies.

For the operating modes in the DRA design, it could be seen at Fig. 3 that the first resonance is at 5.5 GHz, which is corresponds to the DRA dominant $TE_{1\delta1}$ mode. This mode has a uniform electric field distribution through the DRA geometry. For the second resonance at 7.6 GHz, it appears that the $TE_{2\delta1}$ mode starts to propagate [19]. The $TE_{2\delta1}$ mode has sinusoidal shape for the electric field vectors with a minimum electric field at the center of the DRA. This mode exists in this design as the DRA is placed on the substrate directly, while it will not propagate if it is placed on the ground plane [20]. The simulated electric field vector for the first and second resonances are plotted at the *xz*-plane in Fig. 5. It could be seen that the electric field distributions align well with the theory of these modes.

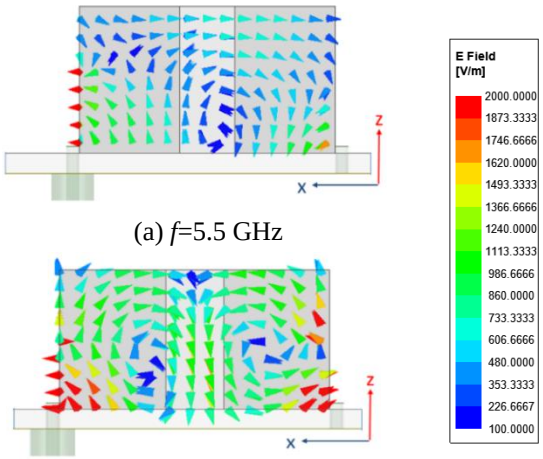

Fig. 5. Electric field vectors plot at the *xz*-plane at different frequencies.

III. FREQUENCY BAND REJECTION

In this section, a new method to create frequency rejection band for the first two operating modes for the DRA in general will be presented. Unlike previous literature where several modifications in the microstrip line feeder were made to create a stop band filtering in the bandwidth of the design, this design will create the frequency rejection in the operating modes of the DRA using open-circuited conductive strips. As shown in Fig. 6 (a), the $TE_{1\delta1}$ mode has uniform distribution across the *xz*-plane. This mode extends from the beginning of the operating band reaching just before the second mode that starts to propagate slightly before 7.6 GHz. In order to create the notch effectively in its operating band, it is essential to look at the electric field intensity of the DRA near the frequency where the notch needs to be created. It could be clearly seen that the electric field is minimum at the mid-section parallel to the x-axis. Therefore, a narrow conductive strip with 1 mm width is employed in parallel to the long sides of the H-shaped DRA to create the notch at the middle of the dominant mode. The strip is wrapped around the DRA and reaches to the substrate, as shown in Fig. 6 (b). The VSWR for this design is plotted in Fig. 7. Through the band from 4.5 to 9.8 GHz, the VSWR value is under 2 except at the middle of the operating band of the first mode, where the VSWR value increases. The center of the rejection band is controlled by adjusting the value of the DRA height (*h*). As expected, larger size of the DRA, (i.e., higher *h*), will shift the notch center to the lower frequency band [21].

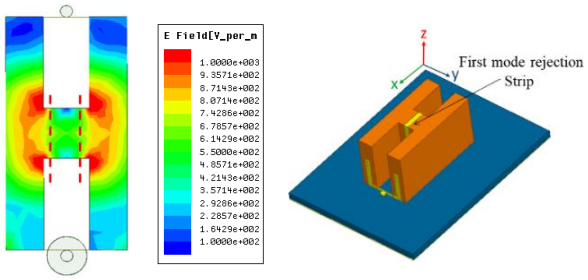

(a) (b)

Fig. 6. Notch rejection at the first mode at 6.5 GHz: (a) electric field magnitude at *xy*-plane, and (b) conducting strip applied at the mid-section of the DRA.

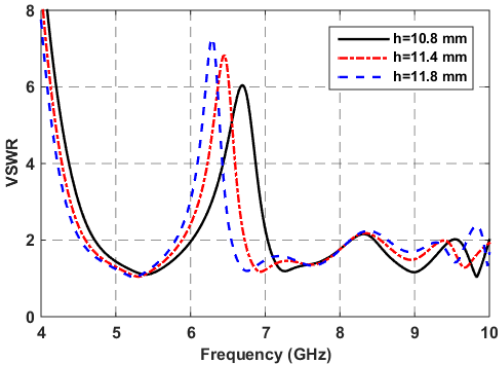

Fig. 7. VSWR curves for the first notch design with different values of (*h*).

On the other hand, for the $TE_{2\delta 1}$ mode, the electric field magnitude has a null at the mid-section parallel to the y-axis as shown in Fig. 8 (a). This region where the electric field vectors of the two sinusoidal waves are cancelling each other in Fig. 5 (b). To create the notch within this mode a conductive strip parallel to the y-axis is wrapped on the DRA, as shown in Fig. 8(b).

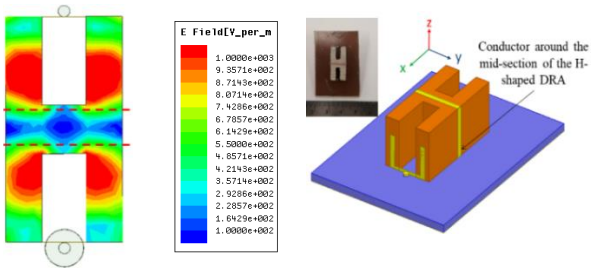

(a) (b)

Fig. 8. Notch rejection at the second mode at 8 GHz: (a) electric field magnitude at *xy*-plane, and (b) conducting strip for the second notch rejection with fabrication.

Figure 9 shows the VSWR for the band rejection for the $TE_{2\delta 1}$ mode with different values of (*h*). The overall operating band extends from 4.15 to 9.8 GHz, achieving 81% fractional bandwidth. The comparison between the simulated and measured VSWR at *h*=10.8 mm is plotted in Fig. 10 where they are in good agreement with slight frequency shift which may be caused by the fabrication tolerance. At 8 GHz, where the stop band occurs, the peak gain falls to less than -6 dBi and the radiation efficiency is less than 30%, while achieving around 95% through the band of interest as shown in Fig. 11.

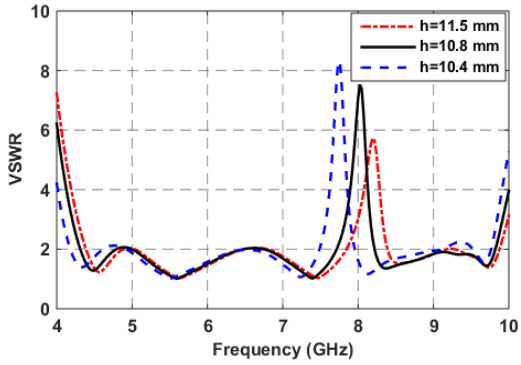

Fig. 9. VSWR curves for the second notch with different values of (*h*).

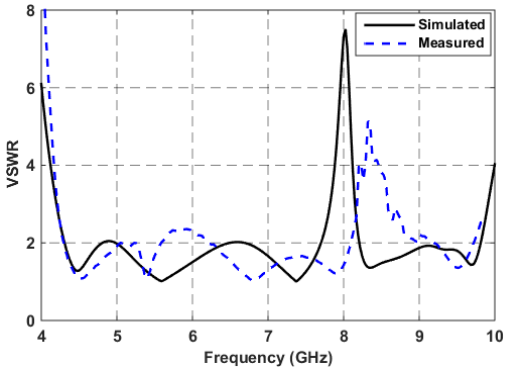

Fig. 10. Measured VSWR for the second notch design (*h*=10.8 mm).

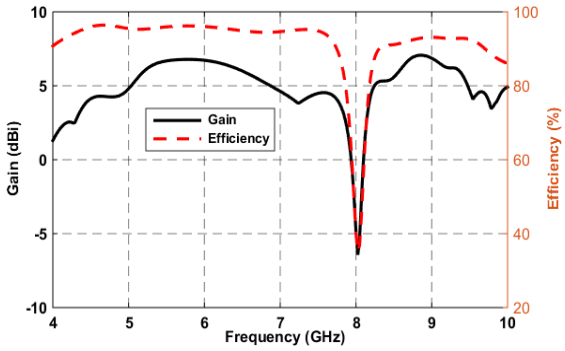

Fig. 11. Peak gain and efficiency for the second notch design (*h*=10.8 mm).

To investigate the effects of adding the notching strip on the radiation patterns of the design, the radiation patterns after adding the strip is plotted as shown in Fig. 12. It could be seen that the radiation patterns are still almost the same with the strip.

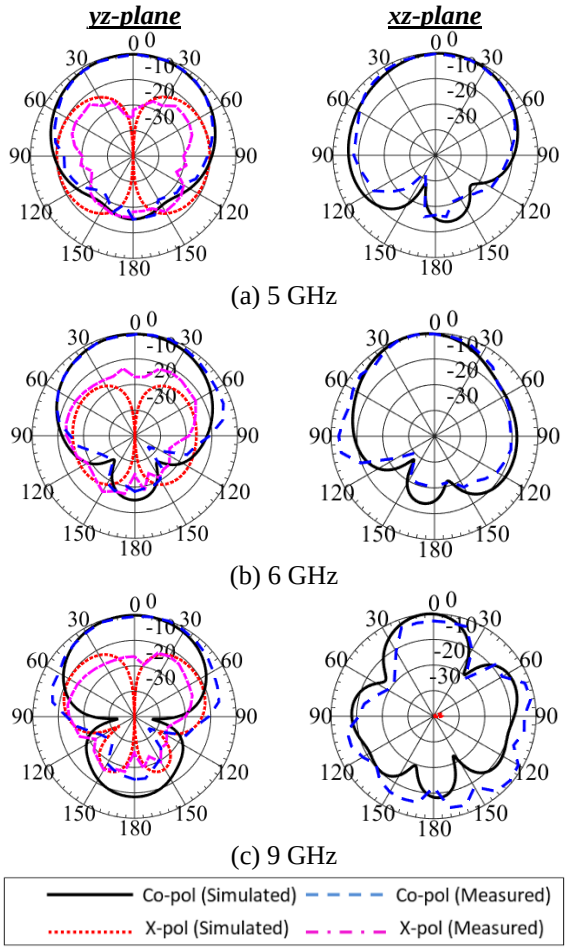

Fig. 12. Radiation patterns of the H-shaped DRA with the second notch rejection at 8 GHz (h=10.8 mm).

IV. CONCLUSIONS

A new method to create frequency band rejection was proposed in this paper. The new method depends on the electric field distribution of the operating modes to create the notch using a strip around the DRA. The first notch was created at the $TE^{y}_{1\delta1}$ mode band while the second notch was created within the $TE^{y}_{2\delta1}$ mode frequency region. The design covers a wideband up to 81% of fractional bandwidth, with 95% radiation efficiency and stable gain throughout the operating band. Furthermore, the radiation patterns of this design showed better characteristics compared to the previous literature for the same shape. The presence of the strip has minimal effect on the radiation patterns of the design.

REFERENCES

[1] D. Soren, R. Ghatak, R. K. Mishra, and D. R. Poddar, "Dielectric resonator antennas: Designs and advances," *Progress in Electromagnetics Research B*, vol. 60, pp. 195-213, 2014.

[2] F. Z. Abushakra, A. S. Al-Zoubi, and D. F. Hawatmeh, "Design and measurements of rectangular dielectric resonator antenna linear arrays," *Applied Computational Electromagnetics Society Journal (ACES)*, vol. 33, no. 4, pp. 380-387, 2018.

[3] I. A. Eshrah, A. A. Kishk, A. B. Yakovlev, and A. W. Glisson, "Excitation of dielectric resonator antennas by a waveguide probe: Modeling technique and wide-band design," *IEEE Trans. on Antennas and Propagation*, vol. 53, no. 3, pp. 1028-1037, 2005.

[4] M. Khalily, M. K. A. Rahim, A. A. Kishk, and S. Danesh, "Wideband P-shaped dielectric resonator antenna," *Radioengineering*, vol. 22, no. 1, 2013.

[5] A. Sharma and R. K. Gangwar, "Circularly polarised hybrid Z-shaped cylindrical dielectric resonator antenna for multiband applications," *IET Microwaves, Antennas & Propagation*, vol. 10, no. 12, pp. 1259-1267, 2016.

[6] R. Cicchetti, A. Faraone, E. Miozzi, R. Ravanelli, and O. Testa, "A high-gain mushroom-shaped dielectric resonator antenna for wideband wireless applications," *IEEE Trans. on Antennas and Propagation*, vol. 64, no. 7, pp. 2848-2861, 2016.

[7] J. Kumar, B. Mukherjee, and N. Gupta, "A novel tetraskelion dielectric resonator antenna for wideband applications," *Microwave and Optical Technology Letters*, Wiley, vol. 57, no. 12, pp. 2781-2786, 2015.

[8] F. Z. Abushakra, A. S. Al-Zoubi, I. Uluer, and D. F. Hawatmeh, "Ultra-wideband E-shaped dielectric resonator antennas fed by coaxial probe and trapezoidal conductor," *International Journal of Electronics Letters-Taylor and Francis*, pp. 1-10, doi: 10.1080/21681724.2020.1726475, 2020.

[9] F. Abushakra and A. Al-Zoubi, "Wideband vertical T-shaped dielectric resonator antennas fed by coaxial probe," *Jordan Journal of Electrical Engineering (JJEE)*, vol. 3, no. 4, pp. 250-258, 2017.

[10] M. Niroo-Jazi and T. A. Denidni, "Experimental investigations of a novel ultrawideband dielectric resonator antenna with rejection band using hybrid techniques," *IEEE Antennas and Wireless Propagation Letters*, vol. 11, pp. 492-495, 2012.

[11] M. Abedian, S. K. A. Rahim, S. Danesh, M. Khalily, and S. M. Noghabaei, "Ultrawideband dielectric resonator antenna with WLAN band rejection at 5.8 GHz," *IEEE Antennas and Wireless Propagation Letters*, vol. 12, pp. 1523-1526, 2013.

[12] M. Abedian, S. K. A. Rahim, S. Danesh, S. Hakimi, L. Y. Cheong, and M. H. Jamaluddin, "Novel design of compact UWB dielectric resonator antenna with dual-band-rejection characteristics for WiMAX/ WLAN bands," *IEEE Antennas and Wireless Propagation Letters*, vol. 14, pp. 245-248, 2015.
[13] M. Y. A. Shahine, M. Al-Husseini, K. Y. Kabalan, and A. El-Hajj, "Dielectric resonator antennas with band rejection and frequency configurability," *Progress in Electromagnetics Research C*, vol. 46, pp. 101-108, 2014.
[14] U. A. Dash and S. Sahu, "UWB dual-band notched conical dielectric resonator antenna with improved gain," *IETE Journal of Research-Taylor and Francis*, 2018.
[15] Y. F. Wang, T. A. Denidni, Q. S. Zeng, and G. Wei, "Band-notched UWB rectangular dielectric resonator antenna," *Electronics Letters*, vol. 50, no. 7, pp. 483-484, 2014.
[16] A. Guptaa and R. K. Gangwar, "New excitation scheme to excite higher-order radiating modes in rectangular dielectric resonator antenna for microwave applications," *Journal of Microwave Power and Electromagnetic Energy*, vol. 52, no. 3, pp. 240-251, 2018.
[17] X. Liang and T. A. Denidni, "H-shaped dielectric resonator antenna for wideband applications," *IEEE Antennas and Wireless Propagation Letters*, vol. 7, pp. 163-166, 2008.
[18] N. A. Jaafar, M. H. Jamaluddin, J. Nasir, and N. M. Noor, "H-shaped dielectric resonator antenna for future 5G application," *2015 IEEE International RF and Microwave Conference (RFM)*, pp. 115-117, 2015.
[19] R. S. Yaduvanshi and H. Parthasarathy, *Rectangular Dielectric Resonator Antennas*. Springer India, 2016.
[20] A. Petosa, *Dielectric Resonator Antenna Handbook*. Artech House Publishers, 2007.
[21] A. A. Kishk and W. Huang, "Size-reduction method for dielectric-resonator antennas," *IEEE Antennas and Propagation Magazine*, vol. 53, no. 2, pp. 26-38, 2011.

Feras Abushakra received his B.Sc. degree in Electrical Engineering majoring in Communications and Electronics from the Jordan University of Science and Technology (JUST), Irbid, Jordan. He obtained his M.Sc. degree in Wireless Communication Engineering from Yarmouk University, Jordan, in 2017. He is currently working towards his Ph.D. in Electrical Engineering at the University of Alabama (UA), Tuscaloosa. His researches focus on dielectric resonator antennas, patch antennas, arrays and radar systems.

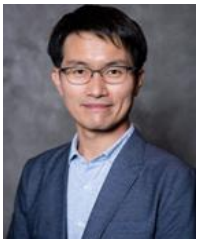

Nathan Jeong received his Ph.D. degree in Electrical and Computer Engineering from Purdue University, 2010. At 2018 he joined the University of Alabama as Assistant Professor. His current research interests include 5G millimeter-wave antenna and system, adaptive RF front-ends and electromagnetics. He has total of 12 years of industrial experience at Samsung Electronics, BlackBerry and Qualcomm. In addition, he holds more than 60 international patent and patent applications in the areas of wireless communication circuit, microwave and millimeter wave system, V2X (Vehicle to Everything), antennas, wireless power transfer and bioelectronics.

Uncertainty Quantification of the Crosstalk in Multiconductor Transmission Lines via Degree Adaptive Stochastic Response Surface Method

Quanyi Yu [1], Wei Liu [2], Kaiyu Yang [2], Xilai Ma [3], and Tianhao Wang [1*]

[1] College of Instrument Science and Electrical Engineering
Jilin University, Changchun, 130026, China
wangtianhao@jlu.edu.cn

[2] College of Automotive Engineering
Jilin University, Changchun, 130022, China

[3] Commercial Vehicle Development Institute Electric Department
FAW JIEFANG, Changchun, 130011, China

Abstract ─ The degree adaptive stochastic response surface method is applied to analyze statistically the crosstalk in multiconductor transmission lines (MTLs). The coefficient of polynomial chaos expansion (PCE) is obtained based on the least angle regression. The truncation degree of PCE is iterated using the degree adaptive truncation algorithm, and the optimal proxy model of the crosstalk of the original MTLs that satisfies the actual error requirements is calculated. The statistical properties of crosstalk in MTLs (such as mean, standard deviation, skewness, kurtosis, and probability density distribution) are obtained. The failure probability of the electromagnetic compatibility in the MTLs system is considered. The global sensitivity indices of crosstalk-related factors are analyzed. Finally, the proposed method is proved to be effective compared with the conventional Monte Carlo method. The uncertainty quantification of crosstalk in MTLs can be calculated efficiently and accurately.

Index Terms ─ Crosstalk, degree adaptive, multi-conductor transmission lines (MTLs), statistical property, stochastic response surface method.

I. INTRODUCTION

Crosstalk in multiconductor transmission lines (MTLs) is one of the main electromagnetic compatibility (EMC) problems in various electronic and electrical systems and devices. When predicting the crosstalk of systems or devices under actual conditions, the geometric parameters of MTLs and electrical parameters of load components related to crosstalk will be uncertain because of objective factors. This uncertainty increases considerably the difficulty of crosstalk prediction and causes the performance of crosstalk cancelling algorithms with certain parameters [1]–[2] to decrease. Therefore, to ensure EMC performance of a system or equipment, studying the statistical property of crosstalk in MTLs is very important. This problem has been explored extensively and some results have been obtained. The conventional Monte Carlo (MC) method can be used to analyze crosstalk models statistically with random input variables [3]–[5]. Although results obtained under a large number of samples are more accurate, MC is difficult to apply when using the crosstalk of large-scale systems or equipment because of its large consumption of computing resources and inefficiency. Therefore, classical reliability methods, such as first order reliability method, second order reliability method, stratified sampling, and importance sampling [6]–[7], and numerical integration methods, such as full factor numerical integration and coefficient grid numerical integration [8], have been proposed to analyze the uncertainty of crosstalk. Several other stochastic methods [9]–[11], have been applied for this analysis. The computational efficiency has been improved considerably compared with the MC method, but the statistical moments, EMC failure probability, and sensitivity analysis of crosstalk statistics have not been studied fully.

The polynomial chaos expansion (PCE) has been used widely in analyzing the uncertainty of the crosstalk in MTLs. The PCE has a solid mathematical foundation and can obtain a "cheap" proxy model of the original output response [12]. With this proxy model, the statistical moments of the crosstalk in MTLs, the failure probability of EMC, and the calculation of sensitivity analysis can be determined [13–15]. However, existing related studies only predict and verify the case where the model expansion degree is fixed within the full

Submitted On: July 5, 2020
Accepted On: January 18, 2021

https://doi.org/10.47037/2020.ACES.J.360209

frequency range of the simulation. The relationships among the model complexity, deployment degree, and calculation accuracy have not been discussed in depth. This paper will report an in-depth study on this problem.

Dr. Isukapalli of the New Jersey State University first proposed the stochastic response surface method (SRSM) [16], which belongs to the non-intrusive polynomial chaos method. The SRSM is highly similar to the deterministic response surface method. The difference between these methods is that the response surface of SRSM is constructed in the stochastic probability space. PCE coefficients are obtained based on linear regression and can be used to solve engineering uncertainty. Blatman *et al*. [17] proposed an adaptive PCE method based on linear regression to minimize the number of evaluations of the complex models. This method belongs to SRSM, but the degree of the model is obtained by the degree adaptive algorithm, and the least angle regression (LAR) algorithm is used when the model depends on numerous parameters to enable a better solution for the high-degree uncertainty [18]. This method has been applied successfully in many fields [19]–[20]. In this paper, the degree adaptive stochastic response surface (DA-SRSM) is proposed and used for the first time to solve the high-degree problem caused by the high complexity of the model of the uncertainty of crosstalk in MTLs. The proposed method provides an effective scheme for the uncertainty analysis of complex stochastic crosstalk model.

In this work, DA-SRSM is applied to analyze the uncertainty of crosstalk in MTLs. The statistical moment information can be directly calculated from the PCE coefficients, whereas the EMC failure probability of the system is calculated by using the PCE model obtained. Combined with the global sensitivity analysis via the Sobol method, the degree of influence of each random input variable on the crosstalk variation is obtained. In Part II, the analysis method of engineering uncertainty based on the DA-SRSM method is introduced and the three-conductor transmission lines model established in Part III is explored. In Part IV, the simulation results of the proposed method are compared with the MC method to verify the accuracy and validity of the proposed method. In Part V, relevant conclusions of this paper are provided.

II. DEGREE ADAPTIVE STOCHASTIC RESPONSE SURFACE METHOD

A. SRSM based on LAR

SRSM, as a non-intrusive approach, considers the complex response function as a black box when analyzing the engineering uncertainty problems and focuses only on the mapping relationship between the input and output. This method solves the PCE coefficient based on linear regression. By approximating the output of the stochastic system with the PCE model, the SRSM provides an efficient method for uncertainty propagation [21]. The LAR method is selected for linear regression. The flow chart of SRSM is shown in Fig. 1.

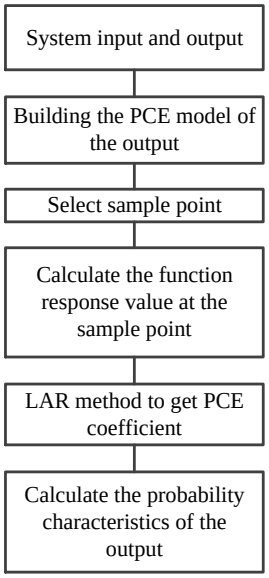

Fig. 1. SRSM flowchart.

First, a stochastic response surface is constructed. The output $Y(\theta)$ of the original model is represented as a general polynomial chaos model [22]:

$$\begin{aligned} Y(\theta) &= b_0 I_0 + \sum_{i_1=1}^{\infty} b_{i_1} I_1\left(\xi_{i_1}(\theta)\right) \\ &+ \sum_{i_1=1}^{\infty}\sum_{i_2=1}^{i_1} b_{i_1 i_2} I_2\left(\xi_{i_1}(\theta),\xi_{i_2}(\theta)\right) \\ &+ \sum_{i_1=1}^{\infty}\sum_{i_2=1}^{i_1}\sum_{i_3=1}^{i_2} b_{i_1 i_2 i_3} I_3\left(\xi_{i_1}(\theta),\xi_{i_2}(\theta),\xi_{i_3}(\theta)\right)+\cdots \\ &= \sum_{i=0}^{\infty} \hat{b}_i \Phi_i(\xi). \end{aligned} \tag{1}$$

In (1), $I_n\left(\xi_{i_1},\cdots,\xi_{i_n}\right)$ represents a mixed orthogonal polynomial of n degree. This equation is a function of multi-dimensional standard random variables $\left[\xi_{i_1},\cdots,\xi_{i_n}\right]$. $\hat{b}_i$ and Φ_i represents the PCE coefficients and orthogonal polynomials to be solved, which correspond to $b_{i_1 i_2 \ldots i_p}$ and $I_n\left(\xi_{i_1},\cdots,\xi_{i_n}\right)$ in (1). Combined with the actual problem for the calculation accuracy requirements, the PCE model in (1) is usually truncated to a certain degree p. The corresponding p-degree PCE approximation model is expressed as follows:

$$Y = \sum_{i=0}^{P} \hat{b}_i \Phi_i(\xi). \tag{2}$$

The number Q of the PCE coefficients $\hat{b}_i$ of the p-th degree truncation increases with the degree p and the dimension d of the random variable ξ. The Q value is as follows:

$$Q = \frac{(d+p)!}{d!\,p!}. \tag{3}$$

In (2), $\Phi_i(\xi)$ is the product of the one-dimensional orthogonal polynomial basis function corresponding to each dimension of the random variable $\xi_1,\ldots,\xi_d$, which satisfies the orthogonal relationship as follows:

$$\begin{aligned} \left\langle \Phi_i(\xi)\Phi_j(\xi) \right\rangle &= \int \Phi_i(\xi)\Phi_j(\xi) W(\xi) \mathrm{d}\xi \\ &= \left\langle \Phi_i(\xi)^2 \right\rangle \delta_{ij}, \end{aligned} \tag{4}$$

where δ_{ij} is the Kronecker function, $W(\xi)$ is the weight function, and the Askey scheme [23]–[24] provides the orthogonal polynomial basis functions corresponding to the random variables of different distribution types.

After the SRSM model is constructed, the sample points are selected by Latin Hypercube Sampling, which makes the sample exhibit simultaneously good spatial and projection uniformity [25]. Refer to [26], satisfactory results can be obtained by selecting sample size of twice the PCE coefficient, and the PCE coefficient $\hat{b}_i$ is estimated by the LAR method, which was proposed by Efron *et al*. [27] in 2004. The algorithm path is shown in Fig. 2.

Step 1: The initial value of all PCE coefficients $\hat{b}_i$ is set to 0. The correlation r between the regression variable $\Phi_i(\mathrm{x})$ and the current residual e_i is calculated. The input variable X_i with the highest correlation is obtained:

$$r = \frac{Cov(\Phi_i(\mathrm{x}), e_i)}{\sqrt{Var[\Phi_i(\mathrm{x})] Var[e_i]}}. \tag{5}$$

Step 2: Perform a least squares approximation on Y along the X_i direction until the next variable x_j appears, and the residuals e of $\hat{b}_{i1}\mathrm{x}_i$ and Y have the same correlation with x_i and x_j as follows:

$$\mathrm{r}_{\mathrm{x}_i \mathrm{e}} = \mathrm{r}_{\mathrm{x}_j \mathrm{e}}, \tag{6}$$

then, the third variable along the angle bisector X_i and X_j is found.

Step 3: By analogy, until the current residual is less than a given threshold, the iteration is terminated, and the final PCE coefficient $\hat{b}_j$ is obtained.

After $\hat{b}_j$ is obtained, the PCE model of the original output response is used to analyze the subsequent uncertainties. Compared with the ordinary least squares, the PCE coefficients are obtained by the LAR algorithm when calculating high-degree problems as follows:

$$\dim_{\mathrm{b}_j}^{\wedge} << \dim_{\mathrm{b}_i}^{\wedge}. \tag{7}$$

The automatic screening of regression variables is realized and the sparse PCE model is obtained, which is more efficient in solving high-degree problems.

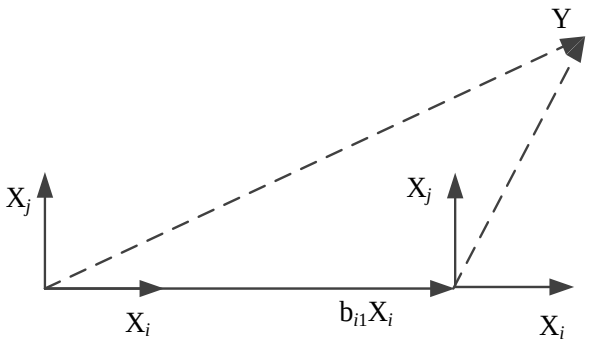

Fig. 2. LAR algorithm path.

After the PCE coefficient $\hat{b}_j$ is obtained, the first four statistical moments of the output response can be calculated. The expressions of mean μ, standard deviation σ, skewness δ, and kurtosis κ are calculated as follows:

$$\begin{cases} \mu = b_0 \\ \sigma = \sqrt{\sum_{i=1}^{p-1} \left[\mathrm{b}_i^2 \left\langle \Phi_i^2 \right\rangle \right]} \\ \delta = \dfrac{1}{\sigma^3} \sum_{i=1}^{p-1} \left[\mathrm{b}_i^3 \left\langle \Phi_i^3 \right\rangle \right] \\ \kappa = \dfrac{1}{\sigma^4} \sum_{i=1}^{p-1} \left[\mathrm{b}_i^4 \left\langle \Phi_i^4 \right\rangle \right] \end{cases}. \tag{8}$$

B. Degree adaptive truncation algorithm

The accuracy of the model determines directly the accuracy of the uncertainty analysis of the output response. In most cases, the higher the degree, the better the precision of the PCE model. The lower-degree model sometimes cannot fit the original output response well but a too high degree will lead to a waste of computing resources. Hence, to reduce the computational complexity and improve computational efficiency whereas satisfying the computational accuracy, the degree adaptive truncation algorithm [28]–[29] is used to construct the PCE model as follows:

Step 1: An initial truncation degree p_0 is set such that $p=p_0$;

Step 2: The coefficient of the p-degree PCE model and the leave-one-out (LOO) cross-validation error term e_{LOO} are calculated as follows:

$$e_{LOO} = \sum_{i=1}^{p-1} \left(\frac{Y_i - Y_i^{PC}}{1-h_i}\right)^2 / \sum_{i=1}^{p-1} (Y_i - \mu)^2, \quad (9)$$

where Y_i^{PC} is the ith PCE metamodel of the original output affecting Y_i, and h_i is the ith component of the vector h as follows:

$$A = \Phi_i(x), \quad (10)$$

$$h = \mathrm{diag}(A(A^T A)^{-1} A^T). \quad (11)$$

Step 3: e_{LOO} is compared with the threshold error e_T. If $e_{LOO} \le e_T$ or the number of defined iterations $N_{\max}$ is reached, the iteration is stopped. Otherwise, $p=p+1$ and step 2 is repeated.

Over-fitting can occur easily when the complexity of the PCE model is too high and the sample size is too small. LOO only leaves one sample as the verification set at a time, and the rest as the training set. The full use of sample data and numerous synthesis of error results can avoid over-fitting as much as possible. However, this training is time-consuming. In order to minimize the amount of calculation whereas ensuring the calculation accuracy and high computational efficiency, the earliest stopping strategy is adopted. The maximum number of iterations $N_{\max}$ is set. Whether e_{LOO} satisfies the given error criterion e_S is verified when at least two iterations e_{LOO} do not decrease or the number of iterations reaches $N_{\max}$. If this criterion is satisfied, p is accepted. Otherwise, $p=p+1$ and step 2 is repeated.

Thus, the optimal selection of the degree of the full-range PCE model under the required accuracy can be quickly realized. The complex output response can be quickly and accurately fitted.

C. Failure probability calculation of EMC performance via DA-SRSM

Usually, there are certain safety thresholds y_T for electronic and electrical systems that have EMC problems. When the input of the system is random, the output response has a small probability of exceeding y_T. When the failure probability exceeds the minimum standard in practical application, the designed electronic and electrical systems should be rectified. DA-SRSM can easily calculate the failure probability. To describe an uncertain system, a limit state function is defined as follows:

$$g(X) = y_T - Y(X), \quad (12)$$

where $Y(X)$ represents the output response of the system and y_T represents the security threshold of the system, which is generally given by numerous experimental data or empirical values. Figure 3 shows the limit state of a two-dimensional problem, and the failure probability is as follows:

$$P_f = P(g(X) < 0). \quad (13)$$

$g(X)$ is used directly as the original output response of the PCE model, and the corresponding PCE model is calculated by the DA-SRSM algorithm. The failure probability P_f of the system EMC performance is obtained by (12) combined with the PCE model.

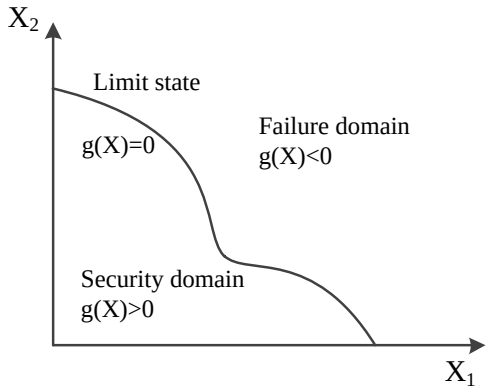

Fig. 3. Limit state concept.

D. Sensitivity analysis of Sobol via PCE

Another advantage of the proposed method is the feasibility of its combination with the Sobol method for global sensitivity analysis. The DA-SRSM is also more efficient than the conventional MC method for global sensitivity analysis. Sensitivity indices measure the influence of input variables on output response, including the first-order sensitivity and total sensitivity indices. Relevant parameters can be designed based on the sensitivity data to improve the EMC performance of the system.

Equation (2) is expanded into the Sobol decomposition form as follows:

$$\begin{aligned} Y(\xi) = b_0 &+ \sum_{i=1}^{n} \sum_{\alpha \in I_i} b_\alpha \Phi_\alpha(\xi_\alpha) + \\ &\sum_{1 \le i_1 < i_2 \le n} \sum_{\alpha \in I_{i_1,i_2}} b_\alpha \Phi_\alpha(\xi_{i_1}, \xi_{i_2}) + \cdots \\ &+ \sum_{1 \le i_1 < \cdots < n} \sum_{\alpha \in I_{i_1,\cdots,i_s}} b_\alpha \Phi_\alpha(\xi_{i_1}, \cdots, \xi_{i_s}) + \cdots \\ &+ \sum_{\alpha \in I_{1,\ldots,n}} b_\alpha \Phi_\alpha(\xi_1, \cdots, \xi_n) \end{aligned}, \quad (14)$$

where

$$I_{i_1,\ldots,i_s} = \begin{Bmatrix} \alpha \in (\alpha_1, \alpha_2, \cdots, \alpha_n) : \alpha_k = 0 \\ k \notin (i_1, \cdots, i_s), \forall k = 1, \cdots, n \end{Bmatrix}. \quad (15)$$

Calculated and sorted,

$$Y(\xi) = \sum_{\alpha \in I_{i_1,\cdots,i_s}} b_\alpha \Phi_\alpha(\xi_{i_1}, \ldots, \xi_{i_s}). \quad (16)$$

At the same time, the variance is obtained on both sides of (14) as follows:

$$Var\left[Y\left(\xi\right)\right] = D = \sum_{i=1}^{n} D_i + \sum_{1\le i<j\le n} D_{ij} + \cdots + D_{1,2,\ldots,n}. \quad (17)$$

Combined with the orthogonal relationship of (4),

$$D_{i_1,\ldots,i_s} = \sum_{\alpha\in I_{i_1,\cdots,i_s}} b_\alpha^2. \quad (18)$$

Thus, the Sobol first-order sensitivity index is as follows:

$$S_{i_1,\ldots,i_s} = \frac{D_{i_1,\ldots,i_s}}{D}, 1\le i_1<\ldots<i_s\le n; s=1,\ldots,n. \quad (19)$$

This equation represents the contribution of a single input to the output response variance.

The total sensitivity of Sobol is as follows:

$$S_i^T = S_i + \sum_{j<i} S_{j,k,i} + \cdots + S_{1,2,\cdots,n}, \quad (20)$$

which is the sum of the first-order sensitivity index of each input variable and the sensitivity indices of interaction between variables. Compared with the first-order sensitivity, this index also contains the influence of interaction among variables.

III. MULTICONDUCTOR TRANSMISSION LINES MODEL

The three-conductor transmission lines model with the infinite ground plane (IGP) as the reference conductor shown in Fig. 4 is used as the analysis object. It is the most general structure of MTLs and can be extended to any application scenario. The MTLs satisfies the assumption of uniformity, no conductor loss, and no surrounding dielectric loss. The cross-section of the transmission line is set as a small size, i.e., an electrically short transmission line. Only one transverse electromagnetic wave propagation mode is approximated on the transmission lines.

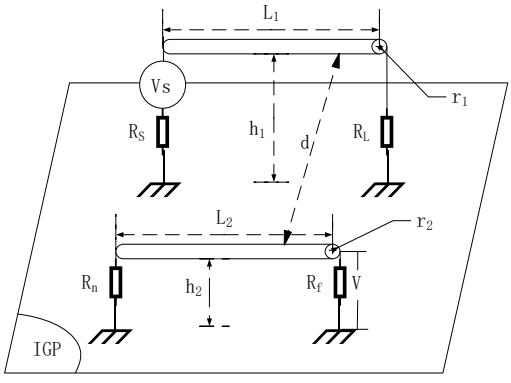

Fig. 4. Three-conductor transmission lines model.

The unit length inductance matrix and capacitance matrix of the three-conductor transmission lines can be obtained by the mirror analysis [30]. Then, the two-port transmission lines is described by the chain parameter matrix, and the current and voltage relationship at the port are characterized as follows:

$$\begin{bmatrix}\hat{V}(\ell)\\ \hat{I}(\ell)\end{bmatrix} = \psi\begin{bmatrix}\hat{V}(0)\\ \hat{I}(0)\end{bmatrix} = \begin{bmatrix}\hat{\phi}_{11} & \hat{\phi}_{12}\\ \hat{\phi}_{21} & \hat{\phi}_{22}\end{bmatrix}\begin{bmatrix}\hat{V}(0)\\ \hat{I}(0)\end{bmatrix}, \quad (21)$$

where $V(l)$, $I(l)$, $V(0)$, and $I(0)$ are the far-end crosstalk voltage, the far-end crosstalk current, the near-end crosstalk voltage, and the near-end crosstalk current, respectively, and ψ is the chain parameter matrix. For the transmission lines structure in Fig. 4, the generalized Thevenin theorem can be used to obtain the following:

$$\hat{V}(0) = \hat{V}_S - \hat{Z}_S\hat{I}(0), \quad (22)$$

$$\hat{V}(\ell) = \hat{Z}_L\hat{I}(\ell), \quad (23)$$

where $\hat{Z}_S$ and $\hat{Z}_L$ represent the near-end impedance matrix and far-end impedance matrix respectively and $\hat{V}_S$ represents the source voltage. Equations (22) and (23) are substituted in (21) to obtain the following:

$$I(0) = (\hat{\phi}_{12} - \hat{\phi}_{11} * Z_S - Z_L * \hat{\phi}_{22} + ZL * \hat{\phi}_{21} * Z_S)^{-1} * (Z_L * \hat{\phi}_{21} - \hat{\phi}_{11}) * V_S, \quad (24)$$

$$I(\ell) = \hat{\phi}_{21} * V_S + (\hat{\phi}_{22} - \hat{\phi}_{21} * Z_S) * I(0). \quad (25)$$

Equations (24) and (25) are substituted in (23) to obtain the far-end crosstalk voltage, and the correlation calculation of the chain parameter matrix is found in Ref. [31].

IV. NUMERICAL VERIFICATION AND DISCUSSION

The uncertainties of the crosstalk in the MTLs with random input parameters are analyzed using the transmission lines structure shown in Fig. 4. Assuming that the lengths of the two wires are equal $L=L_1=L_2$ and satisfy the uniform distribution [5.5 m, 6 m], the same radius $r=r_1=r_2$ obeys the normal distribution [0.7 mm, $(0.1\ \text{mm})^2$]. The equivalent height to ground $h=h_1=h_2$ obeys the uniform distribution [15 mm, 25 mm] and equivalent terminal impedance $R=R_L=R_f$ obeys the uniform distribution [45 Ω, 55 Ω]. The two wires are parallel and spacing d obeys the uniform distribution [5 mm, 10 mm]. The other parameters are set as constant: source voltage V_S=1 V, and source resistance $R_S=R_n$=50 Ω. The PCE model of the far-end crosstalk voltage in the frequency range of [1MHz, 100MHz] is established by using the equations in III and DA-SRSM.

Given the complex calculation of solving the crosstalk through the transmission lines equation, a high iteration degree upper limit p_{max}=20 is set. To ensure accuracy of the model, an error standard e_S=0.001 is set. Figure 5 shows the adaptive degree of each frequency band and the experimental error meets the requirements.

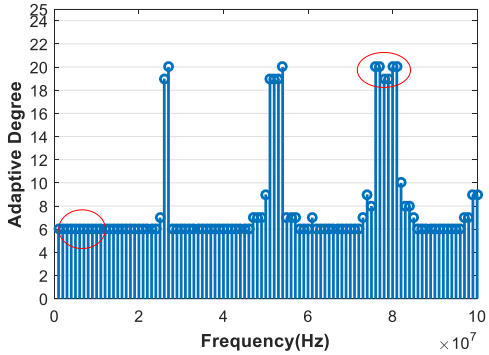

Fig. 5. Adaptive degree.

The adaptive degree varies at different frequencies. The adaptive degree is higher in [26 MHz, 27 MHz], [51 MHz, 54 MHz], and [76 MHz, 81 MHz], which indicates that the fitting model is more complex. The degree of other frequencies is relatively low, so the fitting model is simpler.

To verify the accuracy of the proposed model in the uncertainty analysis of crosstalk in MTLs, the first four statistical moments of the far-end crosstalk voltage V are calculated and compared with the results obtained by 10000-time MC methods as shown in Figs. 6 (a)–(d).

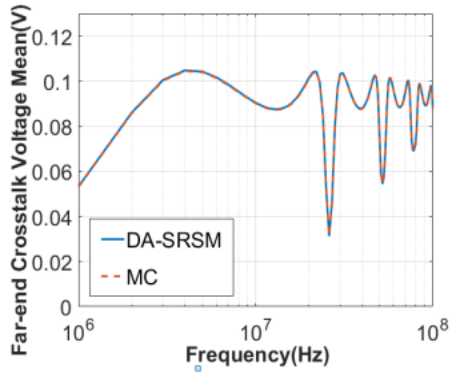

(a)

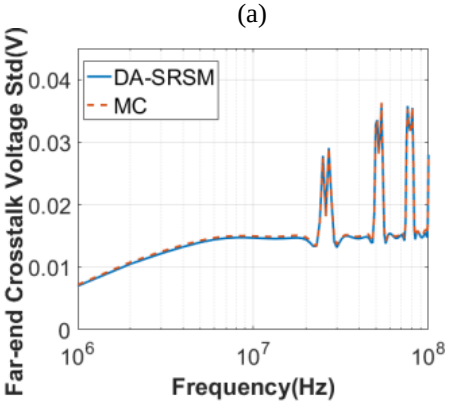

(b)

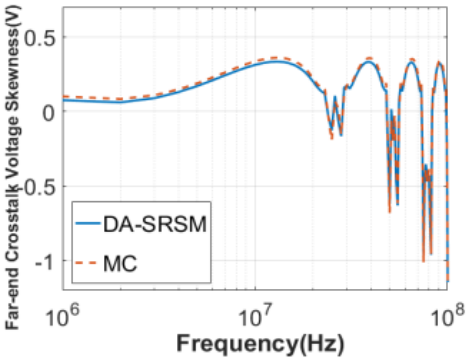

(c)

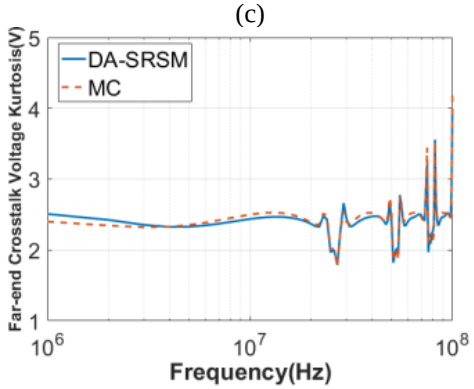

(d)

Fig. 6. Comparison of the results of the first four statistical moment of the far-end crosstalk voltage in the MTLs via DA-SRSM and the 10000-time MC method.

The first four statistical moments calculated by the proposed method have good consistency with the results calculated by 10000-time MC methods, which verifies the validity and accuracy of the proposed method. Figures 7 (a) and (b) further show the analysis of the error at the two frequency points of 40 MHz (p=6) and 80 MHz (p=20). The model error is the smallest at 6 degree and increases beyond 6 degree at 40 MHz. The model error decreases at 80 MHz, during which the p=20 model error is the smallest. The model meets the error standard at p=20. The accuracy and efficiency of the proposed method in full-band modeling are verified when the problem of crosstalk uncertainty of the complex MTLs is solved. The calculation times of the DA-SRSM and MC methods are shown in Table 1.

Table 1: Comparison of calculation times between DA-SRSM and MC methods

Calculation Method	Calculating Time (s)
DA-SRSM	537.3
MC	15012.4

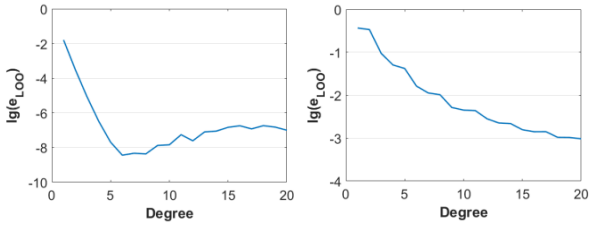

(a) (b)

Fig. 7. Model errors with iterative order at 40 MHz and 80 MHz via DA-SRSM.

Table 1 shows that to ensure accuracy of the model, the DA-SRSM greatly improves the computational efficiency compared with the MC method. The computer available for storage in this paper is 7.89 GB, the CPU clocked at 2.5 GHz, and no parallel operation is performed.

Next, the DA-SRSM is used to predict the failure probability of the EMC performance because of the crosstalk of the three-conductor transmission lines system shown in Fig. 4. The failure thresholds of the system in the [1 MHz, 10 MHz] and [75 MHz, 85 MHz] frequency intervals are all 0.12 V. Beyond the crosstalk voltage, the EMC performance of the system will be invalid. As shown in the red area in Fig. 5, the two sections represent the low-degree and high-degree models. The probability of the EMC performance failure of the MTLs system is calculated by DA-SRSM and compared with the 10000-time MC methods (Table 2).

Table 2: Comparison of EMC performance failure probability and calculated sample number in frequency ranges of [1 MHz, 10 MHz] and [75 MHz, 85 MHz]

Frequency	Method	Failure Probability	Number of Samples
[1MHz, 10 MHz]	DA-SRSM	0.0790	160
	MC	0.0806	10000
[75MHz, 85 MHz]	DA-SRSM	0.0540	210
	MC	0.0586	10000

Table 2 shows the failure probability obtained by DA-SRSM under the small sample calculation. The result is close to that obtained by the large sample calculation of the MC method. Compared with the MC method, DA-SRSM can considerably improve the calculation efficiency in two frequency intervals with certain calculation accuracy.

The two frequency points of 40 MHz and 80 MHz of the low-degree and high-degree models are selected based on Fig. 5. The probability density function of the far-end crosstalk voltage is calculated, and the results are compared with those of the 10000-time MC calculations, as shown in Figs. 8 (a) and (b).

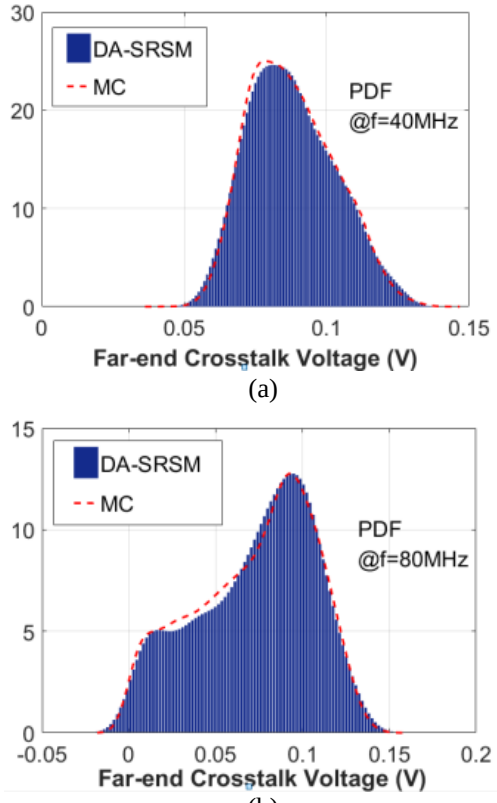

(a)

(b)

Fig. 8. Comparison of the far-end crosstalk voltage probability density function via DA-SRSM and MC method at 40 MHz and 80 MHz frequencies.

Figure 8 shows the probability density values obtained by DA-SRSM at both frequency points are consistent with those obtained by MC method. Thus, the accuracy of the proposed method is verified. The 40 MHz frequency has the highest probability density at 0.08 V, whereas the 80 MHz frequency has the highest probability density at 0.95 V. The probability density values of the same far-end crosstalk voltage response vary at different frequencies. The probability of failure at a certain frequency point can also be calculated by integrating the probability density curve.

The equations in Section II.D are combined to calculate the first-order and total sensitivities of each input variable at 40 MHz and 80 MHz. The result is compared with the results calculated by 10000-time MC, as shown in Figs. 9 (a)–(d).

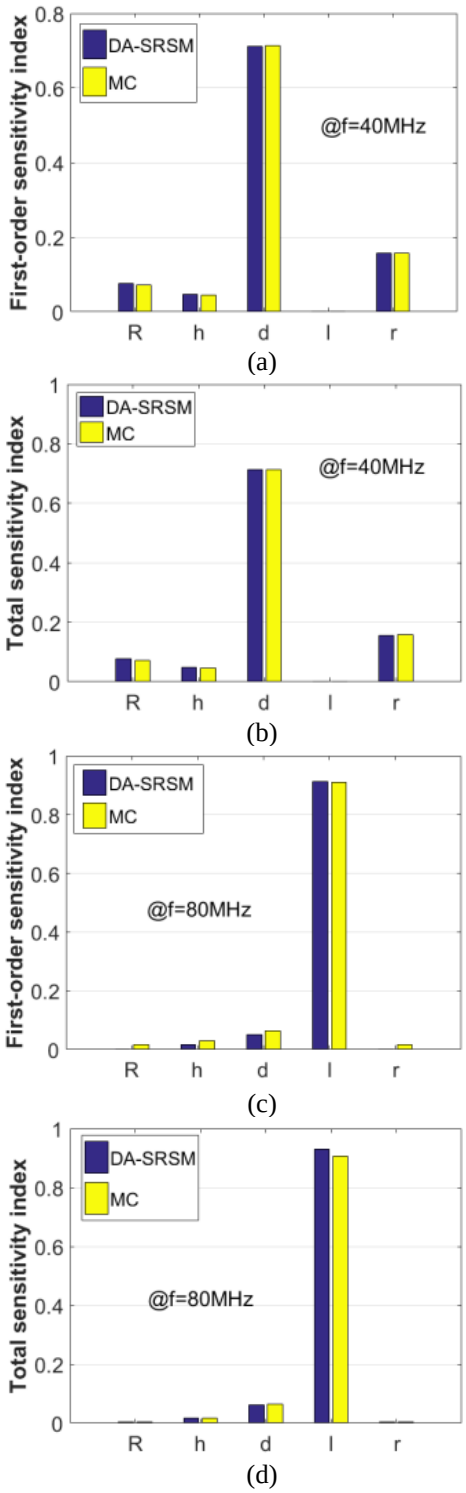

Fig. 9. Comparison of the first-order and total sensitivity indices of the input variables at 40 MHz and 80 MHz via DA-SRSM with the results calculated by the MC method.

Figure 9 shows the sensitivity results based on the DA-SRSM are consistent with those obtained by the MC method, which also verifies the accuracy of the proposed method. The first-order and total sensitivities at the same frequency point are the same, indicating that the interaction between input variables has little effect on the output response. At different frequencies, the results of the sensitivity indices vary greatly. The first-order and total sensitivities of lines spacing d are the highest at 40 MHz, which have the greatest effect on the change in the far-end crosstalk voltage. At 80 MHz, the first-order and total sensitivities of the conductor length L are the highest, whereas the sensitivity of d is very small. Thus, the influence of input variables on the far-end crosstalk voltage varies in the different frequency ranges. Comparisons of the above calculation time are shown in Table 3.

Table 3: Comparison of the program calculation time between DA-SRSM and MC method for calculating sensitivity

Frequency	Calculation Method	Calculating Time (s)
40MHz	DA-SRSM	4.3407
	MC	1604.3
80MHz	DA-SRSM	26.0113
	MC	1612.4

Table 3 shows that the calculation efficiency of Sobol sensitivity obtained by the DA-SRSM method is considerably higher than that of the MC method. To obtain the effects of the input variables in the [1 MHz, 100 MHz] frequency range on the variation of the far-end crosstalk voltage, the total sensitivity index at all frequency points is calculated (Fig. 10).

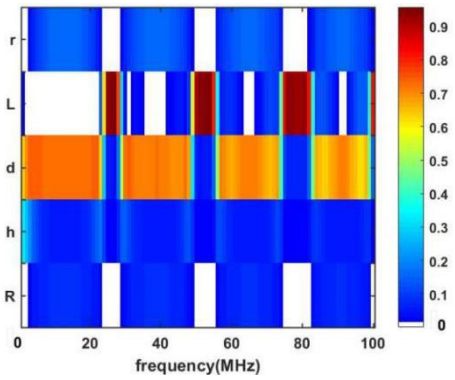

Fig. 10. Total sensitivity index of each input variable in [1 MHz, 100 MHz] interval via DA-SRSM.

Figure 10 shows the terminal impedance R, conductor height h, and wire radius r have a small effect on the output variation. The trend of the conductor spacing d and the wire length L is exactly the opposite. At [25

MHz, 27 MHz], [50 MHz, 54 MHz], [74 MHz, 83 MHz], L has considerable influence, d has a small degree of influence, and the other frequency bands is opposite. When designing the wiring of an electrical and electronic system or equipment where the above MTLs is located, if its main working frequency band is in the aforementioned three intervals, wire length L should be controlled strictly to ensure and the other parameters can be adjusted appropriately.

V. CONCLUSION

The DA-SRSM method is proposed for the statistical analysis of crosstalk in MTLs. The terminal impedance R, conductor-to-ground height h, conductor spacing d, conductor length L, and conductor radius R are set as random variables subject to certain distributions. The first four statistical moments and probability densities of the far-end crosstalk voltage are calculated and the model error is analyzed. The validity and accuracy of the proposed algorithm in the full frequency band are verified through a comparison with the MC method. DA-SRSM is also used to solve the problem of failure probability analysis of the EMC performance of an MTLs system. The failure probability of the EMC performance of the MTLs system is obtained quickly and accurately. The effects of random input variables at different frequencies on the variations of the far-end crosstalk voltage are also calculated by combining DA-SRSM with global sensitivity analysis of the Sobol method. This analysis is verified through the MC method. The proposed method is more accurate and efficient than the MC method in calculating the Sobol sensitivity indices. In conclusion, DA-SRSM can analyze the uncertainty of crosstalk in MTLs efficiently and accurately. Moreover, the proposed method can provide a theoretical basis and fast analysis for EMC problems, such as wire harness and cable crosstalk in electronic and electrical systems, which will have increasingly higher frequency and complexity in the future.

ACKNOWLEDGMENT

This work was supported in part by the National Natural Science Foundation of China under Grant 51707080, and in part by the Jilin Scientific and Technological Development Program under Grant 20180101032JC and Grant 20190103055JH.

REFERENCES

[1] V. Vulfin and R. Ianconescu, "Transmission of the maximum number of signals through a multi-conductor transmission line without crosstalk or return loss: Theory and simulation," *IET Microw. Antennas Propag.*, vol. 9, no. 13, pp. 1444-1452, 2015.

[2] R. Ianconescu and V. Vulfin, "Analysis of lossy multiconductor transmission lines and application of a crosstalk canceling algorithm," *IET Microw. Antennas Propag.*, vol. 11, no. 3, pp. 394-401, 2016.

[3] S. Shiran, B. Reiser, and H. Cory, "A probabilistic method for the evaluation of coupling between transmission lines," *IEEE Trans. Electromagn. Compat.*, vol. 35, no. 3, pp. 387-393, Aug. 1993.

[4] A. Ciccolella and F. G. Canavero, "Stochastic prediction of wire coupling interference," in *Proc. Int. Symp. Electromagn. Compat.*, Atlanta, GA, USA, pp. 51-56, Aug. 1995.

[5] B. Bellan, S. A. Pignari, and G. Spadacini, "Characterisation of crosstalk in terms of mean value and standard deviation," *IEE Proc.-Sci. Meas. Technol.*, vol. 150, no. 6, pp. 289-295, Nov. 2003.

[6] M. Larbi, P. Besnier, and B. Pecqueux, "Probability of extreme interference levels computed from reliability approaches: Application to transmission lines with uncertain parameters," *Int. Symp. Electromagn. Compa.*, Gothenburg, Sweden, pp. 648-655, 2014.

[7] M. Larbi, P. Besnier, and B. Pecqueux, "Probability of EMC failure and sensitivity analysis with regard to uncertain variables by reliability methods," *IEEE Trans. Electromagn. Compa.*, vol. 57, no. 2, pp. 274-282, 2015.

[8] L. Gao, Q. Yu, and D. C. Wu, "Probabilistic distribution modeling of crosstalk in multi-conductor transmission lines via maximum entropy method," *IEEE Access*, vol. 7, pp. 103650-103661, Aug. 2019.

[9] M. Wu, D. G. Beetner, T. H. Hubing, H. Ke, and S. Sun, "Statistical prediction of 'reasonable worst-case' crosstalk in cable bundles," *IEEE Trans. Electromagn. Compat.*, vol. 51, no. 3, pp. 842-851, Aug. 2009.

[10] M. S. Halligan and D. G. Beetner, "Maximum crosstalk estimation in lossless and homogeneous transmission lines," *IEEE Trans. Microw. Theory Techn.*, vol. 62, no. 9, pp. 1953-1961, Sep. 2014.

[11] A. C. Yücel, H. Bagci, and E. Michielssen, "An ME-PC enhanced HDMR method for effificient statistical analysis of multiconductor transmission lines networks," *IEEE Trans. Compon. Packag. Manuf. Technol.*, vol. 5, no. 5, pp. 685-696, May 2015.

[12] I. S. Stievano, P. Manfredi, and F. G. Canavero, "Parameters variability effects on multiconductor interconnects via Hermite polynomial chaos," *IEEE Trans. Compon., Packag., Manuf. Technol.*, vol. 1, no. 8, pp. 1234-1239, Aug. 2011.

[13] D. Xiu, *Numerical Methods for Stochastic Computations: A Spectral Method Approach*. Princeton, NJ, USA: Princeton Univ. Press, 2010.

[14] P. Manfredi, D. V. Ginste, I. S. Stievano, D. De Zutter, and F. G. Canavero, "Stochastic transmission lines analysis via polynomial chaos methods: An

overview," *IEEE Electromagn. Compat. Mag*., vol. 6, no. 3, pp. 77-84, 3rd Quart., 2017.

[15] I. S. Stievano, P. Manfredi, and F. G. Canavero, "Stochastic analysis of multiconductor cables and interconnects," *IEEE Trans. Electromagn. Compat*., vol. 53, no. 2, pp. 501-507, May 2011.

[16] S. Isukapalli, "Uncertainty analysis of transport-transformation models," *Ph.D. dissertation*, New Jersey, USA: Rutgers-The State University of New Jersey, 1999.

[17] G. Blatman, "Adaptive sparse polynomial chaos expansions for uncertainty propagation and sensitivity analysis," *Ph.D. dissertation*, Clermont Ferrand 2, 2009.

[18] G. Blatman and B. Sudret, "Adaptive sparse polynomial chaos expansion based on least angle regression," *J. Comput. Phys*., vol. 230, no. 6, pp. 2345-2367, 2011.

[19] S. Quicken, W. P. Donders, and E. M. J. V. Disseldorp, "Application of an adaptive polynomial chaos expansion on computationally expensive three-dimensional cardiovascular models for uncertainty quantification and sensitivity analysis," *J. Biomech. Eng*., vol. 138, no. 12, pp. 121010, 2016.

[20] F. Ni, P. Nguyen, and J. F. G. Cobben, "Basis-adaptive sparse polynomial chaos expansion for probabilistic power flow," *IEEE Trans. Power Syst*., vol. 32, no. 99, pp.1-1, Jan 2017.

[21] S. S. Isukapalli, A. Roy, and P. G. Georgopoulos, "Efficient sensitivity/uncertainty analysis using the combined stochastic response surface method and automated differentiation: Application to environmental and biological systems," *Risk Analysis*, vol. 20, no. 5, pp. 591-602, 2000.

[22] D. Xiu and G. E. Karniadakis, "Modeling uncertainty in flow simulations via generalized polynomial chaos," *J. Comput. Phys*., vol. 187, no. 1, pp. 137-167, 2003.

[23] W. Schoutens, *Stochastic Processes and Orthogonal Polynomials*. Springer Science & Business Media, vol. 146, 2012.

[24] M. Eldred, C. Webster, and P. Constantine, "Evaluation of non-intrusive approaches for wiener-askey generalized polynomial chaos," in *49th AIAA/ASME/ASCE/AHS/ASC Structures, Structural Dynamics, and Materials Conference*, pp. 1892, 2008.

[25] M. D. McKay, R. J. Beckman, and W. J. Conover, "A comparison of three methods for selecting values of input variables in the analysis of output from a computer code," *Technometrics*, vol. 42, no. 1, pp. 55-61, 2000.

[26] S. Hosder, R. Walters, and M. Balch, "Efficient sampling for non-intrusive polynomial chaos applications with multiple uncertain input variables," in *48th AIAA/ASME/ASCE/AHS/ASC Structures, Structural Dynamics, and Materials Conference*, pp.1939, 2007.

[27] B. Efron, T. Hastie, and I. Johnstone, "Least angle regression," *Ann. Stat*., vol. 32, no. 2, pp. 407-451, 2004.

[28] G. Blatman and B. Sudret, "An adaptive algorithm to build up sparse polynomial chaos expansions for stochastic finite element analysis," *Probab. Eng. Eng. Mech*., vol. 25, no. 2, pp. 183-197, 2010.

[29] M. Larbi, P. Besnier, and B. Pecqueux, "The adaptive controlled stratification method applied to the determination of extreme interference levels in EMC modeling with uncertain input variables," *IEEE Trans. Electromagn. Compat*., vol. 58, no. 2, pp. 543-552, Apr. 2016.

[30] C. R. Paul, *Introduction to Electromagnetic Compatibility*. John Wiley & Sons, 2006.

[31] C. R. Paul, *Analysis of Multiconductor Transmission Lines*. 2nd ed., New York, NY, USA: Wiley, 2008.

Evaluation of Power Receiving Signal of 5G Small Cells for Outdoor/Indoor Environment at Millimeterwave Bands

Nagham Hamid

University of Information Technology and Communications
College of Business Informatics, Baghdad, Iraq
nagham.finjan@uoitc.edu.iq

Abstract ─ This paper presents a simulation study of the outdoor and indoor propagation losses utilizing 5G small cells at suggested millimeter-wave frequencies of 26 GHz, 28 GHz, and 38 GHz. The environment of this study is conducted with penetration loss of new and old building characteristics. The simulation is performed with help of 3D ray tracing model NVIDIA OptiX engine and MATLAB. The targeted frequencies are 26 GHz, 28 GHz, and 38 GHz that specified by International Telecommunication Union ITU-R organization. The simulation routes are investigated in term of signal strength at multiple receiving points. The strength angular spectrum are represented for fixed points and the power receiving delay is presented by their attributes. The simulated responses showed an efficient and sufficient outdoor and indoor service might be provisioned at 26 GHz and 28 GHz. The received signals at 28 GHz and 38 GHz are found around 4.5 dB and 11 dB with comparison with signal received level at 26 GHz. However, at 38 GHz the indoor signal strength and power receiving delays demonstrate a weak signal reception which offers a poor solution to indoor user by outside fixed base station.

Index Terms ─ 5G small cell, millimeter-wave, NVIDIA OptiX, penetration loss, propagation loss.

I. INTRODUCTION

Currently, the fifth generation (5G) mobile networks are shifted toward standardization. The 5G mobile technology is delivered as a part of general 5G requirements with 3GPP Release [1]. Moreover, 5G technology is investigated in both academic and industry fields [2]. The recent researches cover 5G technology utilizing substantial multiple input multiple-output (MIMO) techniques, radio and air-interface access system (RAN), and beamforming networks [3-5]. The 5G technology requirements are higher capacity, huge bandwidth, high gain, directive antennas, compact antenna size, high receiving sensitivity, and high efficiency [6]. As such the frequency bands under 4 GHz suffer from overloaded users due to the latest mobile network technologies. Therefore, the main aim of 5G technology is to provide huge bandwidth by using millimeter-wave frequencies ranging from 3 GHz to 300 GHz.

In addition, it is estimated that the mobile information traffic will be rapidly increased by the mid of 2022 as a result of implementing smart technology in the internet of things (IoTs) technology [7]. Thus, to provide a wide bandwidth and coverage, the cellular network is shifted toward millimeter-wave frequencies such as 26 GHz, 28 GHz, 38 GHz, and 60 GHz [8]. In these proposed frequencies, the development of small or ultra-small cells is further investigated. Several issues and challenges are raised when it comes to small cells including the importance of handover (HO) factor. One of the challenges is related to the high path loss of millimeter-wave technology. As utilizing millimeter-wave wavelength increases the path loss [9]. As example, if an isotropic antenna is used as transmitter and receiver edge, the receive signal is around 20 dB at 3 GHz and 30 GHz respectively. This is due to the aperture antenna size based on the antenna wavelength. Hence, the aperture antenna size at 3 GHz will be repaired to utilize being an antenna array of 30 GHz. Hence, the difference between the power transmitted and received will be zero [10]. Therefore, several studies are done to increase the directivity of the antenna and reduces the path loss effects [11-13]. The other challenge is the multipath propagation at millimeter-wave frequencies. The traditional propagation prediction designs lack the attentiveness information about channel circumstances such as the model environment. The 3D ray tracing models providing these information such as reflections from walls, diffraction from building edges, scattering from small obstacles, and penetration models (concrete, glass) [14, 15]. Hence, the 3D ray tracing model is a potential tool to locate a multipath propagation characteristics between the transmitter and the receiver.

Therefore, this work aims to analyze and investigate the multipath propagation attributes of small cell for 5G cellular networks. The tested cell is chosen from Al Yarmouk Teaching Hospital locating in Baghdad, Iraq. The targeted frequencies are 26 GHz, 28 GHz, and 38 GHz frequency bands. A 3D ray tracing engine named

Submitted On: August 23, 2020
Accepted On: January 18, 2021

https://doi.org/10.47037/2020.ACES.J.360210

"NVIDIA OptiX" is used for simulation process with help of 3D ray tracing for indoor radio propagation code provided by MATLAB [16]. This paper also presents a genuine yard with old and new building model from Baghdad, Iraq.

II. PROFILE MODELLING OF THE STUDY

The simulations are done in this research follows the steps configuration provided in [17]. The obtained results of the 5G system configuration in [17] are found in [18]. The mentioned configuration are limited to 15 GHz. However, this analysis covers 26 GHz, 28 GHz along with 38 GHz. The realized 5G configuration have four contiguous carriers (CCs) providing a 100 MHz bandwidth and a carrier aggregation (CA) with bandwidth of 400 MHz. A 30.5 dBm power transmitted per CC is used, which leads to a total power of 35.3 dB of CC configuration. A transmitted directional antenna placed on the roof of the suggested building at 8 m height and tilted with 4° as shown in Fig. 1. The half power beamwidth in both direction (H and V directions) is selected to be 90° and 10.5° respectively. The chosen antenna gain for this study is configured to be 14.5 dBi.

Fig. 1. The google map of the targeted buildings.

Simulations are carried out by using a NVIDIA OptiX 3D ray tracing tool for outdoor and MATLAB code for indoor. Different than other quasi-3D ray tracing models, NVIDIA OptiX works full three dimensional ray tracing. In case of reflection paths, the reflection is provided by the reflection coefficients. The diffracted paths with its parameters are provided in this study. In such way, the scattering power is distributed in a broad range of directions. Moreover, the effect of scattering becomes substantial in higher frequencies. Thus, a concentric circle approach given at [19-21] is used to produce scattering areas on the walls of structures.

The NVIDIA OptiX 3D ray tracing simulation tool offers a various qualities of propagation of multipath plus supplies the outcomes resulting as form of standard crucial functionality signals (KPIs) including signal receiving strength. Similarly, the signal-to-noise-and-interference ratio (SINR) is also tested. The main aim is studying the signal receiving and propagation inside a small cell structure. Therefore a location of Al Yarmouk Teaching Hospital locating in Baghdad, Iraq is used for simulation. The Google chart perspective of the goal area is shown in Fig. 1. A representing model of two-dimensional graph of the proposed buildings area is represented in Fig. 2.

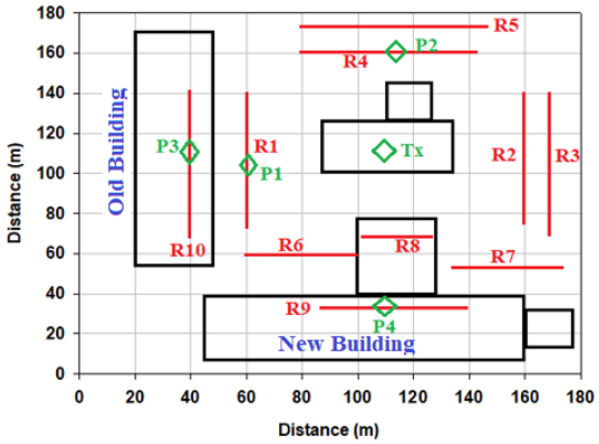

Fig. 2. A 2D representation of the Buildings.

In this proposed scenario, it has been assumed that the user carried a mobile with a height of 1.87 m for indoor and outdoor simulations. In the same time, it has been assumed that the user is always keep moving around and inside the tested area and buildings. A 7 outdoor routes denoted as (R1-R7) and 3 indoor routes denoted as (R8-R10) are marked with red lines as seen in Fig. 2. Four power receiving fixed points are placed in different locations as two outdoors (P1-P2) and two indoor points (P3-P4) for power angular spectrum (PAS) evaluation. At the front of the transmitter antenna, two paths are directly placed and two paths are placed at the back of the antenna transmission spot. The actual the transmitter (TX) antenna is marked with a green dot. Hence, the transmitter antenna is facing west direction towards first building. It's assumed that a directive antenna holding a receiver edge at a level of 1.87 m is turned by 360° within the azimuth with a step tilt of 4°. The parameters configuration of the simulation process are summarized in Table 1. Beside the path loss of LOS, the penetration loss comes from signal penetrated from the outdoor to the indoor environment. Building Penetration Loss (BPL) generally referred to the

penetration loss comes from the outdoor to the indoor environment. The BPL can be defined as a function of frequency. Moreover, the general building are consists of concrete and standard glass walls, while the new building are commonly equipped with newly Infrared Reflective (IRR) glass windows. Therefore, The BPL is depending on the material characteristics used in the concrete and glass walls. Several studies are conducted to investigate the BPL with different types of materials [19-21]. The authors successfully modelled a standard equations for BPL in outdoor and indoor environment. The concrete walls BPL and glass walls frequency dependent can be found by [22-26],

$$L_{concrete} = 4 \times Frequency_{GHz} + 5 \text{ dB}, \quad (1)$$

$$L_{singleglass} = 0.1 \times Frequency_{GHz} + 1 \text{ dB}, \quad (2)$$

$$L_{doubleglass} = 0.2 \times Frequency_{GHz} + 2 \text{ dB}, \quad (3)$$

$$L_{IRR} = 0.3 \times Frequency_{GHz} + 3 \text{ dB}. \quad (4)$$

Table 1: Configuration parameters for the simulation process

Parameters	Value
Frequency	26, 28, 38 GHz
Single carrier component (CC) bandwidth	100 MHz
Transmission power per CC	30.5 dBm
Total transmission power	35.3 dBm
System bandwidth (4 CCs)	400 MHz
Transmitter height	8
Antenna down tilt	4°
Diffractions	1
Reflections	3

Rx distance with respect to Tx (m)									
R1	R2	R3	R4	R5	R6	R7	R8	R9	R10
50	50	60	50	60	50	60	40	70	70

As the building is composed of concrete and glass walls, the BPL total loss for old and new building can be calculated as [20]. Therefore, Fig. 3 shows the BPL total loss of different new and old building and at the targeted frequencies (26 GHz, 28 GHz, and 38 GHz):

$$L_{oldbuilding} = -10 \log_{10}\left[0.3 \times 10^{\frac{-L_{doubleglass}}{10}} + 0.7 \times 10^{\frac{-L_{concrete}}{10}}\right], \quad (5)$$

$$L_{newbuilding} = -10 \log_{10}\left[0.7 \times 10^{\frac{-L_{IRR}}{10}} + 0.3 \times 10^{\frac{-L_{concrete}}{10}}\right]. \quad (6)$$

As indoor environment consists of penetration loss comes from different type of glass such as single, double, and IRR glass walls, Fig. 4 shows the penetration loss in the indoor environment at desired millimeter-wave frequencies.

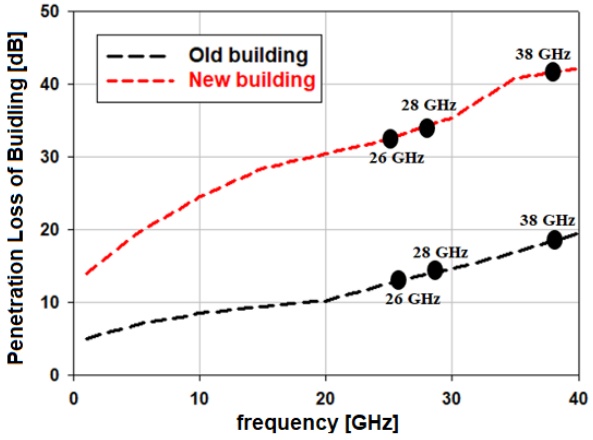

Fig. 3. The BPL of new and old building at desired frequencies.

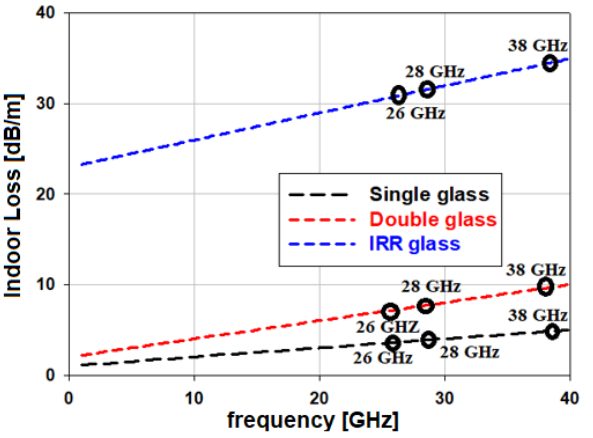

Fig. 4. Indoor loss for different type of glass at desired frequencies.

III. RESULTS AND DISCUSSIONS

Figures 5 (a), Fig. 5 (b), and Fig. 5 (c) display the received signal power in dBm for 7 outside routes and 3 indoor simulation routes at 26 GHz, 28 GHz, and 38 GHz respectively. It can be noticed that both R1 and R10 are in the main lobe of the transmitter antenna, while R2 and R3 are in the rear of the antenna. However, maximum signal amounts are achieved from simulation road at R1 with -42.54 dBm, whereas R2 is behind with the transmitter antenna and that's because of the low value of down tilt. The receive signal level of all paths at 26GHz, 28 GHz and 38 GHz are provided in Table 2. It is clearly seen that the signal level received at R1 route varies with the increasing of the frequency. The variance between 26 GHz and 28 GHz signal level at R1 is around 7.4 dBm, and 10 dBm between 28 GHz and 38 GHz. Most of the outdoor routes (R1-R7) have a signal receiving power ranging from -42.54 dBm to -80.27 dBm at different frequencies. Hence, the LOS path loss play a

key role when the frequency is increased. However, at 26 GHz and 28 GHz, the receiving power level is giving a promising solution utilizing the proposed 5G bands.

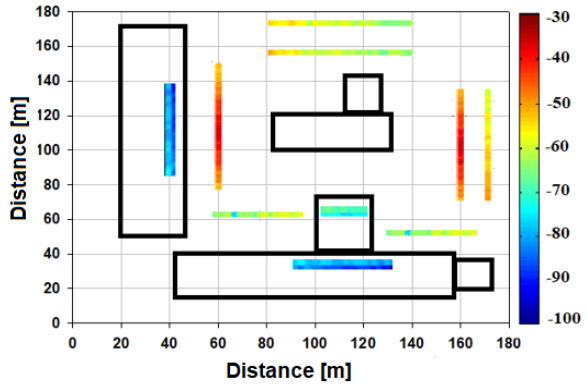

(a)

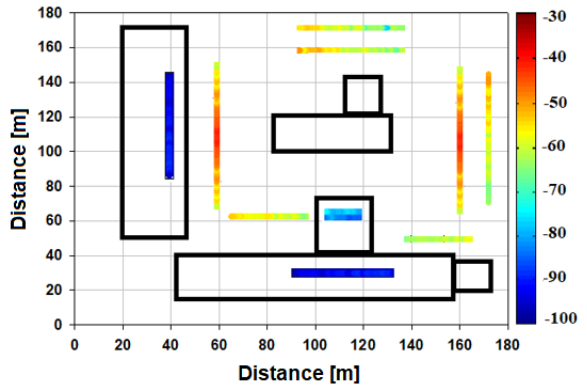

(b)

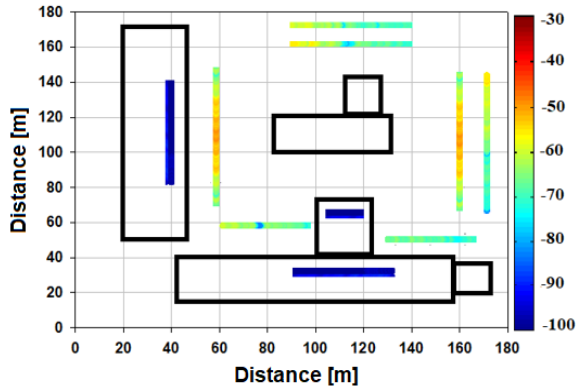

(c)

Fig. 5. The received signal map: (a) 26 GHz, (b) 28 GHz, and (c) 38 GHz.

In the indoor environment, the receiving power level is rapidly decreased. For instance, at 28 GHz and 38 GHz the signal level varies from -83.65 dBm to -125.02 dBm at (R8-R10) simulation routes. For example, the variance signal level between 26 GHz and 28 GHz at R9 route is around 10.7 dBm compared to the variance of 17 dBm between 28 GHz and 38 GHz. As mentioned earlier, the BPL in the building effects significantly when frequency is increased. Another effect of the BPL can be seen between R8 and R9 routes at 28 GHz. The variance between the two signal levels is around 16 dBm, while at 38 GHz is around 20 dB. That is caused by the losses come from the concrete and glass material beside the path loss of the LOS.

Table 2: Signal strength level at receiving points

Routes/ Frequency	26 GHz	28 GHz	38 GHz
R1	-42.54	-49.87	-59.66
R2	-45.36	-50.47	-60.24
R3	-56.21	-59.41	-70.87
R4	-59.47	-60.24	-72.57
R5	-62.35	-64.78	-73.87
R6	-66.89	-67.05	-79.87
R7	-70.25	-77.36	-80.27
R8	-82.47	-83.65	-96.87
R9	-88.98	-99.68	-125.05
R10	-92.45	-100.67	-110.2
Mean	-66.67	-70.31	-82.94
Standard deviations	16.25	18.02	20.29

Figure 6 shows the energy delay profile of P1-P4 at all desired frequencies. Both static areas are situated rather near one another therefore a nearly comparable PDP is obtained for equally areas. The multipath richness of environment is shown by a lot of multipath components. A comparable PDP is obtained for 28 GHz and 38 GHz. The mean delay for P1, P2, P3, and P4 are shown in Table 3. As can been noticed, the mean delays of P3 and P4 have similar values. This could be explained by the same distance of 70 m away from Tx at 38 GHz. The locations (R9 and R10) have similar multipath components as the height of the new building (R9) is same as the old building (R10). In such case, the height of location (R8) is lower with respect to the LOS and R9 height. A comparison is done in Table 4 between this work and other related works.

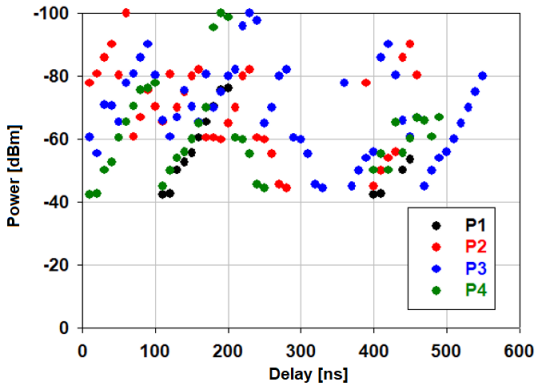

(a)

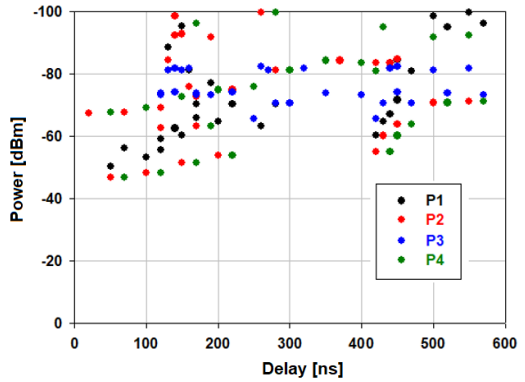

(b)

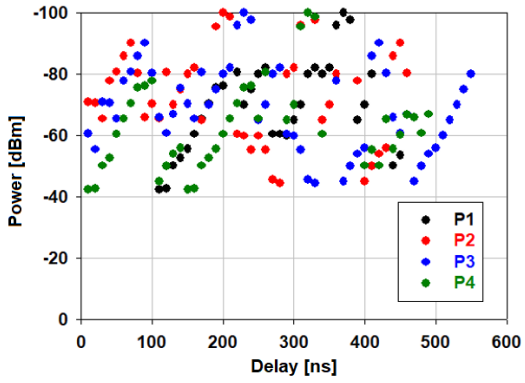

(c)

Fig. 6. Delay profile: (a) 26 GHz, (b) 28 GHz, and (c) 38 GHz.

Table 3: The mean delay (ns)

Power Received	26 GHz	28 GHz	38 GHz
P1	120	115	110
P2	124	119	115
P3	140	137	130
P4	150	140	130

Table 4: Comparison with other related works

Parameters	[24]	[26]	This work
Frequency (GHz)	15, 28, 60	0.8, 38	26, 28, 38
Max. received power (dBm)	-58	-45	-42.54
Min. received power (dBm)	-127	-80	-125.05
Mean delay (ns)	150	135	120
Outdoor routes	7	5	7
Indoor routes	4	2	3
Best scenario	15	0.8	26 GHz, 28 GHz
Location	Japan	Japan	Iraq
3D ray tracing model	SAGA	SAGA	NVIDIA OptiX

V. CONCLUSION

This paper presented an investigation for multipath propagation loss and model characteristics of power receiving levels for indoor and outdoor 5G small cell environment. The 5G small cell is conducted from genuine yard model from Baghdad, Iraq. The LOS and BPL are analysed with different receiving power points at targeted frequency of 26 GHz, 28 GHz, and 38GHz. The model consisted of seven outdoor routes and three indoor routes with one old building route and two new building routes. The maximum receiving power signal at LOS is around -42.54 dB at location R1 for 26 GHz, which is a LOS outdoor route while the minimum receiving power signal is around -80. 27 dBm at location R7 for 38 GHz. In the case of the indoor routes a poor receiving power signal achieved at routes R8-R10 with ranging of -82 dBm to -125 dB. This indicates that for outdoor 5G services it is a promising result for 26 GHz and 28 GHz bands. However, for services provided to indoor services, the receiving power signal suffers from BPL and diffraction losses. In such case, a directive and high gain antennas can be proposed as a solution for indoor services.

REFERENCES

[1] X. Wang, L. Kong, F. Kong, F. Qiu, M. Xia, S. Arnon, and G, Chen, "Millimeter wave communication: A comprehensive survey," *in IEEE Communications Surveys & Tutorials*, vol. 20, no. 3, pp. 1616-1653, 2018.

[2] J. Hirokawa, "Millimeter-wave antenna technologies for 5G mobile communication systems," *2016 IEEE International Workshop on Electromagnetics: Applications and Student Innovation Competition (iWEM)*, Nanjing, pp. 1-3, 2016.

[3] W. Hong, K.-H. Baek, Y. Lee, Y. Kim, and S.-T. Ko, "Study and prototyping of practically large-scale mmWave antenna systems for 5G cellular devices," *IEEE Commun. Mag.*, vol. 52, no. 9, pp. 63-69, 2014.

[4] J. Kim, M. Sung, S. Cho, Y. Won, B. Lim, S. Pyun, J. K. Lee, and J. Lee, 'MIMO-supporting radio-over-fiber system and its application in mmWave-based indoor 5G mobile network," *in Journal of Lightwave Technology*, vol. 38, no. 1, pp. 101-111, 2020.

[5] S. Buzzi, C. D'Andrea, A. Zappone, and C. D'Elia, "User-centric 5G cellular networks: Resource allocation and comparison with the cell-free massive MIMO approach," *in IEEE Transactions on Wireless Communications*, vol. 19, no. 2, pp. 1250-1264, 2020.

[6] N. Ojaroudiparchin, M. Shen, S. Zhang, and G. F. Pedersen, "A switchable 3-D-coverage-phased array antenna package for 5G mobile terminals," *in IEEE Antennas and Wireless Propagation Letters*,

vol. 15, pp. 1747-1750, 2016.

[7] D. Moongilan, "5G internet of things (IOT) near and far-fields and regulatory compliance intricacies," *2019 IEEE 5th World Forum on Internet of Things (WF-IoT)*, Limerick, Ireland, pp. 894-898, 2019.

[8] R. Q. Shaddad, F. Al-Kmali, M. Noman, N. Ahmed, E. Marish, A. Al-Duais, A. Al-Yafrsi, and F. Alsabri, "Planning of 5G millimeterwave wireless access network for dense urban area," *2019 First International Conference of Intelligent Computing and Engineering (ICOICE)*, Hadhramout, Yemen, pp. 1-4, 2019.

[9] L. Sevgi, "Electromagnetic diffraction modeling: High frequency asymptotics vs. numerical techniques," *Applied Computational Electromagnetics Society Journal*, vol. 32, no. 7, pp. 555-561, 2017.

[10] D. Shi, N. Lv, N. Wang, and Y. Gao, "An improved shooting and bouncing ray method for outdoor wave propagation prediction," *Applied Computational Electromagnetics Society Journal*, vol. 32, no. 7, pp. 581-585, 2017.

[11] T. A. Thomas, M. Rybakowski, S. Sun, T. Rappaport, H. Nguyen, I. Kovacs, and I. Rodriguez, "A prediction study of path loss models from 2–73.5 GHz in an urban-macro environment," *Proc. IEEE 83rd VTC Spring*, May 2016.

[12] S. Sun, G. R. MacCartney, and T. S. Rappaport, "Millimeter-wave distance-dependent large-scale propagation measurements and path loss models for outdoor and indoor 5G systems," *Proc. 10th EuCAP*, Apr. 2016.

[13] O. Ozgun, "Modeling of diffraction effects in urban radiowave propagation," *Applied Computational Electromagnetics Society Journal*, vol. 32, no. 7, pp. 593-599, 2017.

[14] D. Shi, N. Lv, and Y. Gao, "A diffraction ray tracing method based on curved surface ray tube for complex environment," *Applied Computational Electromagnetics Society Journal*, vol. 32, no. 7, pp. 608-613, 2017.

[15] L. Azpilicueta, M. Rawat, K. Rawat, F. Ghannouchi, and F. Falcone, "Convergence analysis in deterministic 3D ray launching radio channel estimation in complex environments," *Applied Computational Electromagnetics Society Journal*, vol. 29, no. 4, pp. 256-271, 2014.

[16] M. K. Samimi and T. S. Rappaport, "3-D statistical channel model for millimeter-wave outdoor mobile broadband communications," *2015 IEEE International Conference on Communications (ICC)*, London, pp. 2430-2436, 2015.

[17] F. Fuschini, H. El-Sallabi, V. Degli-Esposti, L. Vuokko, D. Guiducci, and P. Vainikainen, "Analysis of multipath propagation in urban environment through multidimensional measurements and advanced ray tracing simulation," *in IEEE Transactions on Antennas and Propagation*, vol. 56, no. 3, pp. 848-857, 2008.

[18] K. Tateishi, D. Kunta, A. Harada, Y. Kishryama, S. Parkvall, E. Dahlman, and J. Furuskg, "Field experiments on 5G radio access using 15-GHz band in outdoor small cell environment," *2015 IEEE 26th Annual International Symposium on Personal, Indoor, and Mobile Radio Communications (PIMRC)*, Hong Kong, pp. 851-855, 2015.

[19] D. N. Schettino, F. J. S. Moreira, and C. G. Rego, "Efficient ray tracing for radio channel characterization of urban scenarios," *in 12th Biennial IEEE Conference on Electromagnetic Field Computation*, Miami, FL, pp. 267-271, 2006.

[20] W. Tang, H. Cha, M. Wei, B. Tian, and Y. Li, "A study on the propagation characteristics of AIS signals in the evaporation duct environment," *2018 International Applied Computational Electromagnetics Society Symposium - China (ACES)*, Beijing, China, pp. 1-2, 2018.

[21] D. Shi, X. Tang, C. Wang, M. Zhao, and Y. Gao, "A GPU implementation of a shooting and bouncing ray tracing method for radio wave propagation," *Applied Computational Electromagnetics Society Journal*, vol. 32, no. 7, pp. 614-619, 2017.

[22] L. M. Frazier, "Radar surveillance through solid materials," *in Proceedings of the SPIE - The International Society for Optical Engineering*, vol. 2938, Hughes Missile Syst. Co., Rancho Cucamonga, CA, USA, pp. 139-146, 1997.

[23] R. Wilson, "Propagation losses through common building materials 2.4 GHz vs 5 GHz," *University of Southern California*, CA, Tech. Rep. E10589, Aug. 2002.

[24] M. U. Sheikh and J. Lempiainen, "Analysis of outdoor and indoor propagation at 15 GHz and millimeter wave frequencies in microcellular environment," *Advances in Science, Technology and Engineering Systems Journal*, vol. 3, no. 1, pp. 160-167, 2018.

[25] C. Bas, R. Wang, S. Sangodoyin, T. Choi, S. Hur, K. Whang, J. Park, C. Zhang, and A. Molisch, "Outdoor to indoor propagation channel measurements at 28 GHz," *in IEEE Transactions on Wireless Communications*, vol. 18, no. 3, pp. 1477-1489, 2019.

[26] T. Imai, K. Kitao, N. Tran, N. Omaki, Y. Okumura, and K. Nishimori, "Outdoor-to-Indoor path loss modeling for 0.8 to 37 GHz band," *2016 10th European Conference on Antennas and Propagation (EuCAP)*, Davos, pp. 1-4, 2016.

Spread Spectrum Time Domain Reflectometry and Steepest Descent Inversion to Measure Complex Impedance

Samuel R. Kingston [1], Hunter Ellis [1], Mashad U. Saleh [1], Evan J. Benoit [1], Ayobami Edun [2], Cynthia M. Furse [1,3], Michael A. Scarpulla [1], and Joel B. Harley [2]

[1] Department of Electrical and Computer Engineering
University of Utah, Salt Lake City, UT, 84112, USA
samuel.kingston@utah.edu, hunter.ellis@utah.edu, mashad.saleh@utah.edu, evan.benoit@utah.edu, cynthia.furse@utah.edu, mike.scarpulla@utah.edu

[2] Department of Electrical and Computer Engineering
University of Florida, Gainesville, FL, 32611, USA
aedun@ufl.edu, joel.harley@ufl.edu

[3] LiveWire Innovation, Camarillo, CA, 93012, USA

Abstract ─ In this paper, we present a method for estimating complex impedances using reflectometry and a modified steepest descent inversion algorithm. We simulate spread spectrum time domain reflectometry (SSTDR), which can measure complex impedances on energized systems for an experimental setup with resistive and capacitive loads. A parametric function, which includes both a misfit function and stabilizer function, is created. The misfit function is a least squares estimate of how close the model data matches observed data. The stabilizer function prevents the steepest descent algorithm from becoming unstable and diverging. Steepest descent iteratively identifies the model parameters that minimize the parametric function. We validate the algorithm by correctly identifying the model parameters (capacitance and resistance) associated with simulated SSTDR data, with added 3 dB white Gaussian noise. With the stabilizer function, the steepest descent algorithm estimates of the model parameters are bounded within a specified range. The errors for capacitance (220pF to 820pF) and resistance (50 Ω to 270 Ω) are < 10%, corresponding to a complex impedance magnitude $\left|R + \frac{1}{j\omega C}\right|$ of 53 Ω to 510 Ω.

I. INTRODUCTION

Complex impedance measurements are used in a variety of applications, such as antenna design [1], precision agriculture [2], and estimates of photovoltaic (PV) aging [3]. For antenna design, complex impedance is measured to ensure a good match between the source transmission line and the antenna [4]. For precision agriculture, complex impedance is used as a measure of the moisture content in the soil. In PV systems complex impedance measurements ensure minimal impedance mismatch between the PV panels and charge controllers, for efficient power throughput [5] and the integrity of panels and system [4].

Complex impedance is commonly measured with an inductance-capacitance-resistance (LCR) meter or a vector network analyzer (VNA) [6]–[8]. An LCR meter transmits a small AC voltage signal for a range of frequencies and calculates the complex impedance from the ratio of applied voltage to measured current through the device under test (DUT) [9]. A VNA is similar in that it transmits a small AC voltage and varies frequency, but it calculates the reflection and transmission coefficients at the DUT. From these coefficients and knowledge of the transmission line impedance, the complex impedance is calculated [10].

One of the disadvantages of using an LCR meter or a VNA is that they require the DUT to be disconnected and generally de-energized [9], [10]. PV health monitoring [11] is one example where the system cannot be easily de-energized [12]. In this paper, we propose a new method of measuring complex impedance on energized systems using spread spectrum time domain reflectometry (SSTDR) [13] in conjunction with a steepest descent inversion algorithm.

Reflectometry has been used for detecting and locating electrical faults in transmission lines, aircraft cabling, and PV systems [14], [15]. SSTDR can be used to locate open and short circuit faults on energized systems [13], however there is limited research on using SSTDR to measure complex impedance. In [16], [17] SSTDR is used to measure the impedance of a capacitive load at the end of a transmission line. These methods can

Submitted On: September 14, 2020
Accepted On: January 27, 2021
https://doi.org/10.47037/2020.ACES.J.360211

be adapted to measure inductance, but incorporating resistance for a full complex impedance would significantly increase the complexity of the algorithms. In [16], a dictionary matching approach is implemented. Although effective, this method can be computationally expensive. In [17], a curve fitting approach to identify the shape of the signal is used. This is simple and suitable for loads that are strictly capacitive or inductive, but more complex loads cannot be evaluated with this particular algorithm. In [18], SSTDR was used to evaluate single loads (resistor, capacitor, inductor, PV panel) through visual inspection of the time domain SSTDR response. This paper introduces an inverse method based on steepest descent to measure complex impedance(s) (capacitance and resistance simultaneously), that is both computationally efficient and accurate.

Inversion algorithms are used in radar, acoustics, geophysics, computer vision, and other fields [19]–[21]. The inverse problem consists of extracting useful information from experimental/observed data [21]. Model parameters, which are often found iteratively, describe the observed data and are used to generate predicted data that fit best with the observed data. Steepest descent algorithms are relatively simple, accurate, and computationally efficient [21]. Although steepest descent inversion has a history in geophysics and other fields [22], it has not yet been applied to SSTDR. This paper describes a computationally efficient and accurate method to measure complex impedance using SSTDR and steepest descent.

This paper combines the ability of SSTDR to measure in live systems with an efficient steepest descent inversion algorithm to determine complex impedances from SSTDR responses. We validate this approach by simulating an SSTDR signature with a known complex load impedance (a series connected capacitor and resistor) and add white Gaussian noise to represent experimental data. We demonstrate that our new algorithm accurately estimates impedance from these noisy SSTDR signals. Algorithms used in previous work [16] were able to evaluate capacitance from 278 pF to 409 pF with less than 10% error, and we will show similar results, as well. These algorithms used the shape of the time domain signal for capacitance measurement. However, for complex impedances (including resistance), this time domain analysis is more complicated. In this paper, we will use a steepest descent algorithm in the frequency domain, thus enabling efficient measurement of both capacitance and resistance simultaneously.

II. METHODOLOGY

To measure the complex impedance, we solve an inverse problem using steepest descent [21], [23]. First, we define the inverse problem in terms of the observed data space and the model space. Next, we define the parametric function, which is the function we seek to minimize with a steepest descent algorithm. The parametric function is a combination of the misfit function and a stabilizer function [21]. Through sampling the misfit function, we show that the model space has a unique solution within the bounds of the sampled model space. Finally, we show the steepest descent algorithm using regularization to measure complex impedance. The main purpose of this paper is to demonstrate the methodology. Therefore, we use a relatively simple example of measuring series-connected capacitance and resistance, where the test signal is simulated SSTDR data with added white Gaussian noise to be more representative of experimental data.

A. Setting up the inverse problem

The inverse problem is the solution to the function:

$$\mathbf{d} = \mathrm{A}(\mathbf{m}), \qquad (1)$$

where data **d** is a 4,096 x 1 frequency dependent vector in the observed SSTDR response data space associated with an unknown complex impedance. We have modeled this unknown impedance as a resistor (R) and capacitor (C) connected in series. From (1), **m** is a 2 x 1 vector of the model parameters (R and C). The model space A(**m**) is the function acting on the model parameters **m** to get **d**.

The observed data **d** and model data A(**m**) are SSTDR signatures (converted to the frequency domain) resulting after transmitting an incident 12MHz SSTDR signal, X(ω), through 27.5 m of 10 AWG PV cable (with parameters given in [24]), as shown in Fig. 1. The 27.5 m cable was long enough to separate reflections from the load from those between the SSTDR instrument and the transmission line. We include in the simulation the complex impedance of the SSTDR, $Z_{SSTDR}(\omega)$, the incident simulated signature, X(ω), the transmission line characteristic impedance, Z_0, the load, $R + \frac{1}{j\omega C}$, the reflection coefficient Γ(ω) between Z_0 and the capacitor-resistor load, and the transmission coefficient, T(ω), between Z_{SSTDR} and Z_0. The transmission line characteristics used to model the characteristic impedance, Zo, are defined in [17] using a twin-lead transmission line model for the PV cable.

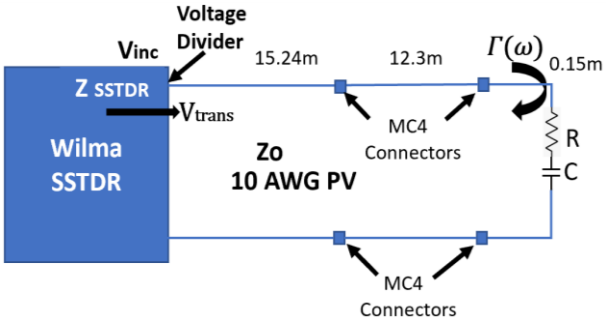

Fig. 1. Experimental setup for measuring SSTDR responses from a capacitive-resistive load.

The observed data, **d,** and the model data in A(**m**) are simulated by the frequency response of a *sinc*-like incident signal, X(ω), multiplied by the reflection coefficient, Γ(ω), and transmission coefficient, T(ω), as:

$$\mathbf{d}_{\boldsymbol{m}=\{R,C\}} \text{ and } \mathrm{A}(\mathbf{m})_{\boldsymbol{m}=\{R,C\}} = \mathrm{X}(\omega)\Gamma(\omega)\mathrm{T}(\omega). \quad (2)$$

From [16] X(ω) is calculated as the Fourier transform of the expected value of the autocorrelation between the incident and reflected SSTDR signals. The reflection coefficient Γ(ω) is calculated as:

$$\Gamma(\omega)_{\boldsymbol{m}=\{R,C\}} = \frac{\left(\mathrm{R} + \frac{1}{j\omega C}\right) - Z_o}{\left(R + \frac{1}{j\omega C}\right) + Z_o}, \quad (3)$$

where R and C represent the resistance and capacitance of the load impedance. The transmission coefficient, T(ω), is calculated as a voltage divider between the impedance of the SSTDR, $Z_{SSTDR}(\omega)$, and the transmission line, Z_0, as:

$$T(\omega) = \frac{Z_{SSTDR}(\omega)}{Z_0 + Z_{SSTDR}(\omega)}, \quad (4)$$

The time domain SSTDR response from (2) for the system shown in Fig. 1 is time-gated [17] to include only the part of the signal where the reflection from the load is seen, and converted to the frequency domain. The propagation through the transmission line is assumed to be ideal (lossless with constant velocity of propagation). Loss and dispersion could be accounted for by adding an additional transfer function with these effects to (2).

For our purpose of testing the algorithm, **d** is a column vector of simulated SSTDR data for a known R and C value, with 3 dB added white Gaussian noise. For a validation test, the known R and C values were chosen to be 200 Ω and 300 pF, respectively. The rows in **d** show the complex energy for each frequency in the bandwidth of the SSTDR signature, **d**. The SSTDR response for a 12 MHz signal covers the frequency band from -24 MHz to +24 MHz, with a frequency spacing of 11.719 kHz, with the highest energy centered at 12MHz [16] and 4096 frequency samples (rows) from -24MHz to +24MHz.

B. Parametric function: Misfit and regularization

We solve for the model parameters of the simulated noisy data, **d,** through a least squares approximation of the parametric function, which is a combination of the misfit function and regularization, similar to [21]. The misfit function is a measure of closeness between the SSTDR responses in the model space, A(**m**), and the simulated noisy SSTDR response, **d**. The misfit function, $\phi_{\mathrm{d}}(\mathbf{m})$, also termed the residual, is calculated for each k^{th} iteration of the steepest descent algorithm as:

$$\phi_{\mathrm{d}}(\mathbf{m}) = \|\mathrm{A}(\mathbf{m}_{\boldsymbol{k}}) - \mathbf{d}\|^2. \quad (5)$$

The least squares minimum best estimate of the model parameters is found when:

$$\phi_{\mathrm{d}}(\mathbf{m}) \leq \eta^2, \quad (6)$$

where η^2 is the noise energy level of the simulated noisy data, **d**. In this example, the observed (measured) data is simulated with added white noise, so that the SNR = 3 dB.

To establish that there is a unique solution for (1) within the bounds of interest for a known load (C = 300 pF, R = 200 Ω), we sampled the parameter space of A**(m)** to get a matrix, **A**, where each column, $\mathbf{a}_i$, in **A** is a simulated SSTDR response from a unique R and C value. We chose the sampled parameter space to be 200 capacitors, logarithmically spaced between 1 pF and 1,000 pF and 80 resistors, linearly spaced between 50 Ω and 500 Ω. It is expected that the unknown RC combination will lie somewhere in this range. **A** has 16,000 columns (200 capacitors x 80 resistors) and 4,096 rows for the complex energy values of each frequency in the SSTDR signature.

The misfit (5) for every SSTDR signature in **A** is plotted in Fig. 3 as a function of the two model parameters, R (horizontal axis) and C (vertical axis), for one test scenario where the observed data, **d,** was simulated using a load C=300pF and R=200Ω. The color shows the misfit for the respective model space signatures. Dark blue represents the minimum of the misfit function, where the simulated model data, A(**m**), closely matches the observed data, **d**.

Regularization was used to make the parametric function more robust and reduce sensitivity to small variations in the data [21]. This enables the steepest descent algorithm to keep model parameters within a specified range (in our case the range of **A)** and enables it to identify the correct model parameters. The regularization was calculated using the stabilization function:

$$\phi_{\mathrm{m}}(\mathbf{m}) = \alpha\|\mathbf{m} - \mathbf{m}_{\mathbf{apr}}\|^2, \quad (7)$$

where α is the estimated regularization factor, described in more detail in the next section. The **m** in (7) is the vector of model parameters (R and C), and $\mathbf{m}_{\mathbf{apr}}$ is the median C=500pF and median R=250Ω in the sampled space of **A**. The medians of both the R and C were chosen to keep the steepest descent estimates within the sampled space.

The algorithm requires an estimated range (max and min) of the model parameters, and there is a tradeoff in robustness vs. efficiency of the algorithm. The broader the range, the more likely the algorithm is to converge to the correct values, but it could take many more iterations. If the range is narrower, the algorithm can converge with fewer iterations, but if the model parameters are outside the range, the correct values would be missed.

Combining the misfit function $\phi_{\mathrm{d}}(\mathbf{m})$ and stabilization function $\phi_{\mathrm{m}}(\mathbf{m})$, the parametric function becomes:

$$\mathbf{P}^{\boldsymbol{\alpha}}(\mathbf{m}, \mathbf{d}) = \phi_{\mathrm{d}}(\mathbf{m}) + \phi_{\mathrm{m}}(\mathbf{m}). \quad (8)$$

We identify the correct model parameters by using steepest descent to iteratively find the minimum solution to (8).

C. Applying a steepest descent algorithm to measure capacitance and resistance

To find the minimum of the parametric function (8), we apply a modified steepest descent algorithm [21]. Steepest descent starts with an initial guess of the model parameters and iteratively identifies the parameters within the model space, A(**m**), that are closest to the model parameters in **d**. The steepest descent algorithm has three steps: Step 1, make an initial guess of the model parameters, $\mathbf{m_0}$. Step 2, from the parameters around this guess, identify the direction within the model space, A(**m**), which results in the greatest slope. Step 3 is to move in this direction to find the next model parameters within A(**m**). Step 4 is to repeat steps 2 and 3 until the model data A(**m**) from the estimated model is within the noise level of the observed data, **d**.

For our case, the initial model parameter guess is an RC combination within the range of the model space, A(**m**). Next, we follow the steepest descent method [21] and define the change of the model parameters for each iteration as:

$$\boldsymbol{\delta m} = -\mathrm{k}^{\alpha}\mathbf{l}^{\boldsymbol{\alpha}}(\mathbf{m}), \tag{9}$$

where the length of a step in the iteration process, k^{α}, is a positive real number. The vector $\mathbf{l}^{\boldsymbol{\alpha}}(\mathbf{m})$ is a column vector defining the direction of steepest descent of the parametric function (8), which is calculated using the Fréchet derivative [21] of C and R. Normalization is applied to $\mathbf{l}^{\boldsymbol{\alpha}}(\mathbf{m})$ to make the step size in the direction of both R and C the same order of magnitude. Specifically, $\mathbf{l}^{\boldsymbol{\alpha}}(\mathbf{m})$ is multiplied by the inverse of the parameter with smaller magnitude, which is C. The steepest descent method is an iterative process of finding each **m** according to:

$$\mathbf{m_{n+1}} = \mathbf{m_n} + \delta\mathrm{m} = \mathbf{m_n} - \mathrm{k}^{\alpha}\mathbf{l}^{\boldsymbol{\alpha}}(\mathbf{m}), \tag{10}$$

where the step size $\mathrm{k}_{\mathrm{n}}^{\alpha}$ is defined by the line search method [16] as:

$$\mathbf{k_n^{\alpha}} = \frac{\|\mathbf{l}^{\boldsymbol{\alpha}}(\mathbf{m})\|^2}{\|\mathbf{F}\mathbf{l}^{\boldsymbol{\alpha}}(\mathbf{m})\|^2 + \|\mathbf{l}^{\boldsymbol{\alpha}}(\mathbf{m})\|^2}, \tag{11}$$

where $\mathbf{F}\mathrm{l}^{\alpha}(\mathbf{m})$ is the Fréchet derivative of the current model parameters, $\mathbf{m_n}$, multiplied by the direction of steepest descent, $\mathbf{l}^{\boldsymbol{\alpha}}(\mathbf{m})$, and α is the regularization factor used to hold $\mathbf{m_n}$ within the bounds of the sampled space.

In the iteration process, the regularization factor, α, starts with a value of zero. The value after the first iteration is determined so that the stabilization function, $\phi_{\mathrm{m}}(\mathbf{m})$, matches $\mathbf{m_1}$ as a ratio to balance the misfit and the stabilizer functions [21] as:

$$\alpha_1 = \frac{\|\mathrm{A}(\mathbf{m_1}) - \mathbf{d}\|^2}{\left\|\mathbf{m_1} - \mathbf{m_{apr}}\right\|^2}. \tag{12}$$

Then for each k^{th} iteration α_{k} is updated according to:

$$\alpha_{\mathrm{k}} = \alpha_1 \mathrm{q}^{\mathrm{k}-1}, \tag{13}$$

where k is the steepest descent loop iteration, and q is a normalizing constant chosen to be 0.5. The iterative process is terminated when the misfit, $\phi_{\mathrm{d}}(\mathbf{m})$, reaches the given noise level, η^2, of the observed data.

In this section, we have shown that there is a unique solution of the inverse problem in (1) within the bounds of the sampled parameter space for measuring complex impedance. This is shown in Fig. 3 for one test case. A steepest descent algorithm with regularization was used to iteratively identify the complex impedance associated with SSTDR signals. However, the algorithm may experience instability when the residual for the current model parameters is close to the residual for neighboring model parameters. As a result, the step size, $\mathbf{k_n^{\alpha}}$, will sometimes overshoot out of the bounds of interest [25]. This can happen when the residuals of differing model parameters are close, which happens if the impedance of the loads are nearly the same. For example, a large capacitance $\left(Z = \frac{1}{j\omega C}\right)$ appears nearly like a short circuit $(Z = 0\ \Omega)$ [16]. How close these are depends on the frequency, *ω*, (for higher *ω*, the impedance of a capacitor is closer to a short circuit). Similar effects are seen for loads that combine capacitance, resistance, and inductance.

To solve the overshoot issue, the algorithm checks if the new estimated model parameters for each iteration are within range. If not, the algorithm implements a random restart [25] by choosing a random RC combination within the bounds of interest. Then the algorithm continues normally. Figure 2 shows a flow chart summarizing the steps to determine the complex impedance.

D. Steepest descent for measuring complex impedance

In this section, we evaluate how effective the steepest descent algorithm is in measuring the complex impedance associated with an observed SSTDR signature. The model parameters (R and C) are found such that the residual of the parametric function (8) is < 1% above the noise level of the simulated noisy SSTDR data. We tested the algorithm for 25 standard resistor values ranging from 51 Ω to ~510 Ω, where R=[51, 56, 62, 68, 75, 82, 91, 100, 110, 120, 130, 150, 160, 180, 200, 220, 240, 270, 300, 330, 360, 390, 430, 470, 510] Ω and 19 standard capacitor values ranging from 1 pF to 1,000 pF, where C=[5, 10, 15, 22, 33, 47, 100, 120, 130, 150, 180, 220, 330, 470, 560, 680, 750, 820, 1,000]pF.

The ranges for R and C were chosen so that the associated SSTDR responses would be distinguishable from one another. and so they would not appear as an open or a short[16]. The resistors and capacitors were connected in series, giving 475 (25x19) total RC combinations. The range for where a f=12 MHz SSTDR signature has highest energy from the load $\left\|R + \frac{1}{j2\pi fC}\right\|$ is from 51.7 to 2,699 Ω.

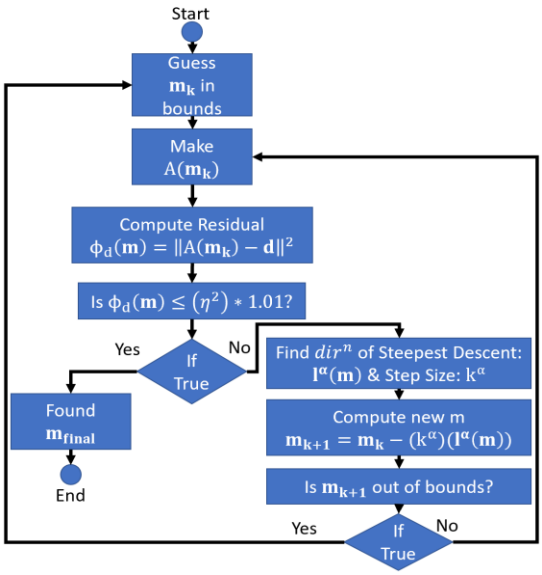

Fig. 2. Flow chart for steepest descent algorithm to measure complex impedance.

Our metric of success is when both model parameters (R and C) are measured with percent error ≤10.5%. Of the 475 different load combinations tested, 200 were successful (42%). Best results (success > 92%) were found when 51 Ω < R < 270 Ω and, simultaneously, 220 pF < C < 820 pF. This successful range corresponds to 53 Ω < $\left\|R + \frac{1}{j\omega C}\right\|$ < 276 Ω. For impedances tested outside of this range, the probability of success was 25%.

Table 1 shows the results for 10 of the 475 RC combinations tested. The results include the known (true) values, the estimated values, the number of iterations to get the final estimations, and the % error for both the R and C estimates. Rows 3 through 9 show RC combinations within the defined range of success where the error is <10.5%. Rows 1, 2, and 10 show results for combinations outside this range, with higher % error. Some tests (e.g., row 1) still provide good estimates, however, success is not ensured. In some cases (e.g., row 2) the algorithm takes the maximum number of iterations (10,000) and still does not converge well.

Table 1: Results of modified steepest descent algorithm

True R (Ω)	True C (pF)	Est. R (Ω)	Est. C (pF)	# Iter.	Error % R	Error % C
51	100	54.4	99	35	6.69	0.07
51	120	202.6	21.8	10,000	297	81.8
51	220	53.7	218	63	5.45	0.87
56	470	55.8	461	5	0.42	2.00
62	560	63.3	557	127	2.12	0.56
120	470	119.9	458	11	0.09	2.62
200	330	204.8	342	21	2.38	3.59
220	820	223.3	795	42	1.48	3.05
270	220	262.6	205	60	2.76	6.82
330	750	330.8	581	185	0.26	22.6

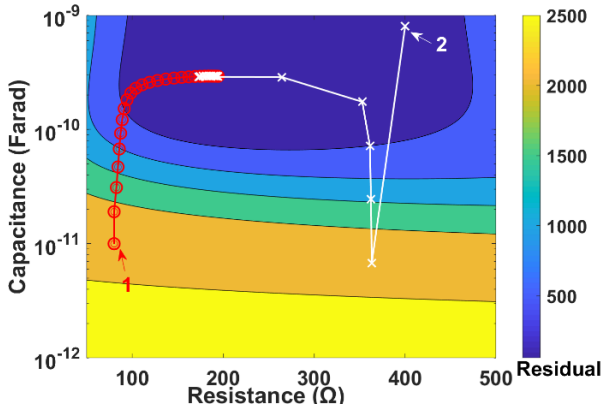

Fig. 3. Misfit as a function of A(**m**) parameters resistance and capacitance for two separate initial guesses.

The initial guess matters, as shown from the two different convergent paths to the correct estimate, shown in Fig. 3. Path 1 starts with the initial guessed model parameters, C=10pF and R=80 Ω, and follows the red circles showing the residuals for each iteration of the steepest descent algorithm. The initial guess has a residual ~ 2,000, as indicated by the color. Through successive iterations, the residual approaches zero, where the simulated model data, A(**m**), matches the observed data, **d**.

Path 2 in Fig. 3 illustrates the need for a random restart modification. It starts with the initial guessed model parameters, C=800pF and R=400 Ω. Note that the resistance value is outside the range of success. Also, the residuals of both the initial model parameters and its neighboring values are close, which causes the step size to overshoot the boundaries of allowable guesses. The algorithm would normally guess a set of model parameters within the bounds of interest (often getting stuck there), but because of the random reset, it jumps to some different random parameters within the range. From the new estimate, path 2 can converge to the minimum and identify the correct model parameters. The final estimated parameters for both paths 1 and 2 are R=199 Ω and C=299 pF for the correct model parameters in **d** that are 200 Ω and 300 pF. Thus, the error for both C and R is < 1%. The number of iterations is dependent on the initial guessed model parameters and the observed data model parameters.

In Fig. 4, we show the convergence of the residuals at each iteration for the two initial guess paths illustrated in Fig. 3. With each progressive iteration in the steepest descent algorithm, the model data is closer to the observed data, and the residual converges to 55, which is below the noise energy level (=59) of the simulated noisy data, **d**. For path 2, marked with black Xs, the first guessed parameter has a relatively low residual. It then jumps to a higher residual because of the new random guess and progresses to lower residuals until it reaches

a value within the noise level. From Figs. 3 and 4, we have shown an example where the steepest descent can correctly identify the model parameters of noisy simulated SSTDR data.

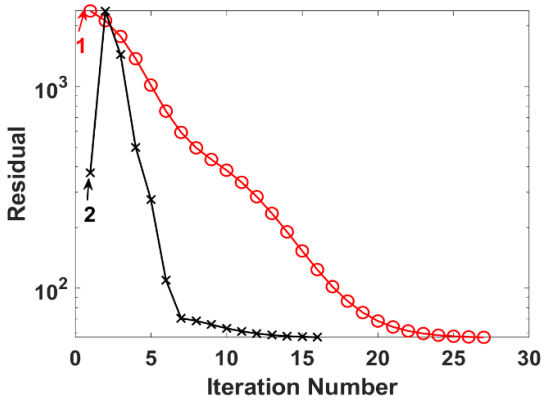

Fig. 4. Convergence of the residual for two different initial guesses. Guess 1 (C=10pF, R=80 Ω) as red circles and guess 2 (C=800pF and R=400 Ω).

E. Steepest descent algorithm complexity

In this section, we discuss the computational complexity of the algorithm and compare it to a similar algorithm. We will estimate complexity by the number of multiplications required per iteration, and the average number of iterations.

For each iteration, the steepest descent algorithm for these examples took 180,256 multiplications. This scales linearly with the number of data points (4,096) in the frequency response. The steps in this algorithm with the largest number of multiplications were calculating the Fréchet derivative (90,130 multiplications) and producing $A(\mathbf{m_k})$ (20,480 multiplications). The number of iterations depends on the initial guess and model parameters, as described in previous sections. We will use an estimate for the average number of iterations (N~88), which was found using the 10% trimmed mean from the tests (e.g., in Table 1) that were within the range of success for both C and R. We used a trimmed mean to remove both the 10% highest and 10% lowest outliers. Note that the mode of the number of iterations was 10, and the median was 46.

From this, when measuring a complex RC impedance within the range of success, the typical number of multiplications is 15.8 million (180,256 multiplications × 88 iterations). For comparison, in [16], an SSTDR response dictionary was used to measure a single parameter (capacitance). If the dictionary were expanded to include combinations of 1,000 C and 1,000 R values, it would contain 1 million (1,000 × 1,000) SSTDR responses (each with 4,096 data points). Measuring both C and R would take ~12.3 billion multiplications (4096 × 3 × 1,000,000), which is significantly greater than for the steepest descent algorithm.

III. CONCLUSION

Using a simple example with a series connected resistor and capacitor, SSTDR and a modified steepest descent algorithm was shown to be an accurate and computationally efficient solution to measure complex impedance. The significance of using SSTDR is that impedances could be measured on energized systems. For a range of RC combination loads where the associated SSTDR response does not appear as an open circuit or short circuit response [16], we were able to measure their impedances with < 10.5% error. The successful estimations for R and C ranged from 50 Ω to 270 Ω and from 220 pF to 820 pF, respectively. This corresponds to complex impedance magnitude 53 Ω < $\left|R + \frac{1}{j\omega C}\right|$ < 276 Ω.

Some of the computational challenges of the algorithm are discussed next. One challenge is that a single load parameter (R or C) can dominate the control of the SSTDR response shape, which can affect the ability to measure the other parameter. For example, the SSTDR response for an RC combination will resemble an open-circuit response if C=1 pF (making the overall impedance large) regardless of what the resistor value is. Another challenge is that the computational complexity is dependent on the initial guess and the number of random restarts required. If the algorithm starts with a poor guess, this will increase the complexity. This idea is illustrated in Figs. 3 and 4, where path 2 takes more iterations to converge than path 1.

ACKNOWLEDGMENTS

This material is based upon work supported by the U.S. Department of Energy's office of Energy Efficiency and Renewable Energy (EERE) under Solar Energy Technologies Office (SETO) agreement number DE-EE0008169 in collaboration with Livewire Innovation and the National Renewable Energy Laboratory. It is also based on ideas and concepts discussed with Dr. Zhdanov, a faculty member of the University of Utah.

DISCLOSURE

Dr. Furse is a co-founder of LiveWire Innovation, Inc. which is commercializing SSTDR technology, and therefore has a financial conflict of interest with this company.

REFERENCES

[1] P. V. Nikitin, K. V. S. Rao, R. Martinez, and S. F. Lam, "Sensitivity and impedance measurements of UHF RFID chips," *IEEE Trans. Microw. Theory Tech.*, vol. 57, no. 5, pp. 1297-1302, 2009.

[2] D. L. Corwin and S. M. Lesch, "Apparent soil electrical conductivity measurements in agriculture," *Comput. Electron. Agric.*, vol. 46, no. 1-3, pp. 11-43, Mar. 2005.

[3] S. P. Bharadwaj, A. E. Ginart, I. N. Ali, P. W. Kalgren, J. R. Celaya, and S. D. Poll, "Solar cells aging estimation based on impedance characterization," *Aerospace Conference*, pp. 1-9, Mar. 2011.
[4] W. Stutzman and G. Thiele, *Antenna Theory and Design*. Wiley Global Education, 2012.
[5] V. Schlosser and A. Ghitas, "Measurement of silicon solar cells AC parameters," *ARSEC*, 2006.
[6] P. A. Cotfas, D. T. Cotfas, P. N. Borza, D. Sera, and R. Teodorescu, "Solar cell capacitance determination based on an RLC resonant circuit," *Energies*, vol. 11, no. 3, Art. no. 3, Mar. 2018.
[7] R. A. Kumar, M. S. Suresh, and J. Nagaraju, "Facility to measure solar cell ac parameters using an impedance spectroscopy technique," *Rev. Sci. Instrum.*, vol. 72, no. 8, pp. 3422-3426, July 2001.
[8] D. Rytting, "ARFTG 50 year network analyzer history," in *2008 71st ARFTG Microwave Measurement Conference*, pp. 1-8, 2008.
[9] IET Labs, Inc., "Precision LCR Meter User and Service Manual," *IET Labs*, 2014.
[10] Anritsu, "Series 37XXXC Vector Network Analyzer Operations Manual," *Anritsu*, 2004.
[11] M. N. Akram and S. Lotfifard, "Modeling and health monitoring of DC side of photovoltaic array," *IEEE Trans. Sustain. Energy*, vol. 6, no. 4, pp. 1245-1253, 2015.
[12] J. Haney and A. Burstein, "PV system operations and maintenance fundamentals," *Next Phase Solar, Inc.*, Aug. 2013.
[13] P. Smith, C. Furse, and J. Gunther, "Analysis of spread spectrum time domain reflectometry for wire fault location," *IEEE Sens. J.*, vol. 5, no. 6, pp. 1469-1478, Dec. 2005.
[14] C. M. Furse, M. Kafal, R. Razzaghi, and Y. Shin, "Fault diagnosis for electrical systems and power networks: A review," *IEEE Sens. J.*, pp. 1-1, 2020.
[15] H. Boudjefdjouf, H. R. E. H. Bouchekara, R. Mehasni, M. K. Smail, A. Orlandi, and F. de Paulis, "Wire fault diagnosis using time-domain reflectometry and backtracking search optimization algorithm," in *31st International Review of Progress in ACES*, pp. 1-2, 2015.
[16] S. R. Kingston, N. K. T. Jayakumar, M. U. Saleh, E. J. Benoit, A. S. Edun, R. Sun, C. Furse, M. Scarpulla, and J. B. Harley, "Measurement of capacitance using spread spectrum time domain reflectometry (SSTDR) and dictionary matching," *IEEE Sens. J.*, pp. 1-1, 2020.
[17] N. K. T. Jayakumar, E. J. Benoit, S. R. Kingston, M. U. Saleh, M. Scarpulla, J. B. Harley, and C. Furse, "Post-processing for improved accuracy and resolution of spread spectrum time domain reflectometry (SSTDR)," *IEEE Sens. Lett.*, vol. 2, no. 3, 2019.
[18] C. Furse, N. K. T. Jayakumar, E. J. Benoit, M. U. Saleh, J. LaCombe, M. Scarpulla, J. B. Harley, S. R. Kingston, B. Waddoups, and C. Deline, "Spread spectrum time domain reflectometry for complex impedances: Application to PV arrays," *IEEE AUTOTESTCON*, pp. 1-4, 2018.
[19] F. Cohen-Tenoudji, B. R. Tittmann, and G. Quentin, "Technique for the inversion of backscattered elastic wave data to extract the geometrical parameters of defects with varying shape," *Appl. Phys. Lett.*, vol. 41, no. 6, pp. 574-576, Sep. 1982.
[20] M. S. Zhdanov, S. Fang, and G. Hursán, "Electromagnetic inversion using quasi-linear approximation," *GEOPHYSICS*, vol. 65, no. 5, pp. 1501-1513, Sep. 2000.
[21] *Inverse Theory and Applications in Geophysics*. 2nd ed., Elsevier, 2015.
[22] M. El-Shenawee, C. Rappaport, D. Jiang, and W. Melsei, "Electromagnetics computations using the MPI parallel implementation of the steepest descent fast multipole method (SDFMM)," *Applied Computational Electromagnetics Society*, vol. 17, no. 2, 2002.
[23] A. A. Goldstein, "On steepest descent," *J. Soc. Ind. Appl. Math. Ser. Control*, vol. 3, no. 1, pp. 147-151, 1965.
[24] M. U. Saleh, C. Deline, S. R. Kingston, N. K. T. Jayakumar, E. J. Benoit, J. B. Harley, C. Furse, and M. Scarpulla, "Detection and localization of disconnections in PV strings using spread-spectrum time-domain reflectometry," *IEEE J. Photovolt.*, vol. 10, no. 1, pp. 236-242, 2020.
[25] R. Jacobs, "Increased rates of convergence through learning rate adaptation," *Neural Netw.*, vol. 1, pp. 295-307, 1988.

Samuel R. Kingston was born in Salt Lake City, Utah, UT, USA in 1991. He received the A.S. degree in Business from Salt Lake Community College, Salt Lake City, in 2011. He received a B.S. degree in Electrical & Computer Engineering from the University of Utah, Salt Lake City, UT, in 2016 and is currently working on a Ph.D. from the University of Utah, Salt Lake City, UT.

From 2017 to current, he has been a Research Assistant with the University of Utah lab working in the algorithms group. He has been working with spread spectrum time domain reflectometry (SSTDR) in being able to detect, localize, and characterize faults within solar panel system. To date, he has written two conference papers and two journal papers for nondestructive health

monitoring. He is currently working on several other journal papers as well, where each one will be a building block in achieving the overall research team goal. His research interests are in signal processing used for health monitoring, renewable energy alternatives, and creating successful startups from conceptual ideas. In 2016, his senior project team received an award for Best Clinic Project where he worked with L3 Communications to develop a way to detect low probability of intercept (LPI) RADAR signals.

Hunter D. Ellis was born in Murray, Utah, UT, USA, in 1997. He is a current M.S. and B.S. student in Electrical Engineering at the University of Utah. He has been a Research Assistant with the University of Utah since 2018. His research interests include Spread Spectrum Time Domain Reflectometry, Photovoltaic, statistical signal processing, semiconductor physics, numerical simulation methods, adaptive filters, and antennas.

Mashad Uddin Saleh (S'17-) received the B.Sc. Engineering degree in Electrical and Electronics Engineering from Bangladesh University of Engineering and Technology, Dhaka, Bangladesh in 2013. He received the M.S. degree in Electrical Engineering from Michigan Technological University, Houghton, MI, USA in 2016. He is currently working towards the Ph.D. degree in Electrical Engineering at the University of Utah, Salt Lake City, UT, USA.

He worked as a Research Assistant during his masters in Michigan Technological University and currently he is working as a Research Assistant at the University of Utah, Salt Lake City, UT. In summer 2018, he worked as a PV Electrical Characterization Intern in National Renewable Energy Laboratory (NREL). His current research interests include reliability, testing, manufacturing, measurements, and characterization of photovoltaic systems.

Evan J. Benoit received a B.S. degree in Nuclear Engineering Technology from Excelsior College in 2015. He received his B.S. and M.S. degrees in Electrical Engineering from the University of Utah in 2019. He is currently pursuing a Ph.D. in Electrical Engineering at the University of Utah.

From 2005 to 2015, he was a Submarine Nuclear Field Electrician's Mate in the US Navy. He began working as a Research Assistant at the University of Utah, Salt Lake City UT during the summer of 2018. His research explores the applicability of spread spectrum time domain reflectometry for identification of complex impedances on transmission lines. Benoit is a member of the Golden Key International Honour Society, the National Society of Leadership and Success, and a student member of IEEE.

Ayobami S. Edun received the B.Eng. degree in Electrical and Electronics Engineering from Federal University of Technology, Akure, Nigeria in 2014. He received the M.S. degree in Electrical and Computer Engineering from University of Florida, Gainesville, FL, USA in 2019. He is currently working towards the Ph.D. degree in Electrical and Computer Engineering at the University of Florida, Gainesville, FL, USA. He currently works as a Research Assistant at the SmartDATA Lab, University of Florida, Gainesville, FL. He has been working with spread spectrum time domain reflectometry (SSTDR) in being able to detect, localize, and characterize faults within solar panel system.

Cynthia M. Furse (M'85–SM'99–F'08) is Professor of Electrical and Computer Engineering at the University of Utah. Furse received her B.S. in Electrical Engineering with a Mathematics minor in 1985, M.S. degree in Electrical Engineering in 1988, and her Ph.D. in Electrical Engineering from the University of Utah in 1994.

She has applied her expertise in electromagnetics to sensing and communication in complex lossy scattering media such as the human body, geophysical prospecting, ionospheric plasma, and aircraft wiring networks. She has taught electromagnetics, wireless communication, computational electromagnetics, microwave engineering, antenna design, and introductory electrical engineering and has been a leader in the development of the flipped classroom.

Furse is a Fellow of the IEEE and the National Academy of Inventors. She is a past AdCom member for the IEEE AP Society and past chair of the IEEE AP Education Committee. She has received numerous teaching and research awards including the 2020 IEEE Chen To Tai Distinguished Educator Award. She is a founder of LiveWire Innovation, Inc., a spin-off company commercializing devices to locate intermittent faults on live wires.

Michael A. Scarpulla (M'05-SM'14) earned the Sc.B. degree from Brown University in 2000 and the Ph.D. from UC Berkeley in 2006, both in Materials Science and Engineering. His Ph.D. work focused on laser processing of ion implanted compound semiconductors, carrier mediated ferromagnetism, and multiband semiconductors. From 2006-2008 he was a Postdoctoral Scholar at UC Santa Barbara working on epitaxial integration of rare-earth pnictides with III-V semiconductors using MBE. Since joining the ECE and MSE faculties at University of Utah in 2008, he has worked in light trapping for photovoltaics, materials processing and characterization of chalcogenide thin film photovoltaics, reflectometry in photovoltaic systems, and defects in wide-bandgap semiconductors. His hobbies include skiing, climbing, and other mountain adventures.

Joel B. Harley (S'05-M'14) received his B.S. degree in Electrical Engineering from Tufts University in Medford, MA, USA. He received his M.S. and Ph.D. degrees in Electrical and Computer Engineering from Carnegie Mellon University in Pittsburgh, PA, USA in 2011 and 2014, respectively.

In 2018, he joined the University of Florida, where he is currently an Assistant Professor in the Department of Electrical and Computer Engineering. Previously, he was an Assistant Professor in the Department of Electrical and Computer Engineering at the University of Utah. His research interests include integrating novel signal processing, machine learning, and data science methods for the analysis of waves and time-series data.

Harley's awards and honors include 2020 IEEE Ultrasonics, Ferroelectrics, and Frequency Control Society Star Ambassador Award, a 2020 and 2018 Air Force Summer Faculty Fellowship, a 2017 Air Force Young Investigator Award, a 2014 Carnegie Mellon A. G. Jordan Award (for academic excellence and exceptional service to the community). He has published more than 90 technical journal and conference papers, including four best student papers. He is a student representative advisor for the IEEE Ultrasonics, Ferroelectrics, and Frequency Control Society, a member of the IEEE Signal Processing Society, and a member of the Acoustical Society of America.

Dual-Mode Filter with High Design Flexibility Using Short-Loaded Resonator

Zhaojun Zhu, Ke Yang, Xiufeng Ren, and Lu Cao

School of Physics
University of Electronic Science and Technology of China, Chengdu, 610054, China
uestc98@163.com, 18729985221@163.com, 17854227863@163.com, cl_stella@163.com

Abstract ─ This work presents a series of independent bandpass filters (BPFs) based on dual-mode resonators (DMRs) with short stub-loaded. BPFs conform to the 802.11n protocol and include three passbands with center frequencies and bandwidths of 2.46 GHz, 3.55 GHz and 5.22 GHz, 130 MHz, 130 MHz and 470 MHz. Insertion loss and reflection loss are 1.5 dB, 1.6 dB and 1.3 dB, 18 dB, 20 dB, 30 dB. The filters are useful in the WLAN/WIMAX applications with compact size. According to the current distributions along the resonator, the feed-lines with high design flexibility arms were introduced in order to supply the needed external coupling for the dual-/tri passbands simultaneously, and achieve good impedance matching in each passband. Finally, by the version 15 of High Frequency Structure Simulator (HFSS), three BPFs with single, dual and triple passbands were designed on the Rogers 5880 substrate with the relative dielectric constant ε_r = 2.2, substrate loss tanδ = 0.002, and the thickness h = 0.508 mm. The BPFs are measured by Agilent 85058E Vector Network Analyzer (VNA). The measured results have good agreement with the simulated ones.

Index Terms ─ Bandpass filter, dual-mode resonator, odd and even-mode theory, tri-band filter.

I. INTRODUCTION

Nowadays, the information age is developing rapidly. Bandpass filter (BPF) plays an important role in microwave circuits, which attracts more attentions of the researchers. Wolff first demonstrated a microstrip dual-mode filter in 1972 [1]. Since then, dual-mode microstrip filters have been widely used in communications systems [2–3]. In the past one decade, various of methods to design the multiband filter have been put forward [4–13]. In [6–8], a tri-band BPF comprises two stepped-impedance resonator (SIRs) with short stub-loaded at the center plane. This method can reduce the overall size of the filter, while always following a larger insertion loss. The tri-band filters [8] which have a wide range of applications for 2.4 GHz, 3.5 GHz, and 5.2 GHz, are designed by using several assembled half-wavelength SIRs without any stub. However, great overall circuit size is inevasible by this way. Furthermore, a tri-band BPF [9] uses a rectangular ring- resonator, its four edges are respectively grounded to form a short stub-loaded, and two opposite sides are added an open stub-loaded. Furthermore, a defected ground structure was adopted to enhance the coupling strength with low insertion loss in [10]. For the above current methods, three major goals need to be achieved, such as compact size, independent control of passband frequencies and low insertion loss.

This letter proposes three folded dual-mode resonator structures based on SIR (DMR 1, DMR 2, and DMR 3). The center frequencies of SIR are prospectively based on even-odd-mode analysis. In addition, several high design flexibility arms structures are introduced to enhance the coupling between resonators and feed-lines. Finally, three BPFs with single, dual, and triple passbands were individually designed, fabricated, and measured.

II. DESIGN OF THE DUAL-MODE RESONATOR

The schematic diagram of the dual-mode resonator (DMR) 1 is shown in Fig. 2 (a), which consists of a half-wavelength resonator and a short-loaded. This DMR is denoted by lengths (L1, L2) and widths (W1) with a short-circuited stub perturbation with length (W2) and width (W3) at the center plane. The even- odd-mode method can be applied to the equivalent circuits because of the symmetrical structure.

Submitted On: September 9, 2020
Accepted On: January 18, 2021

https://doi.org/10.47037/2020.ACES.J.360212

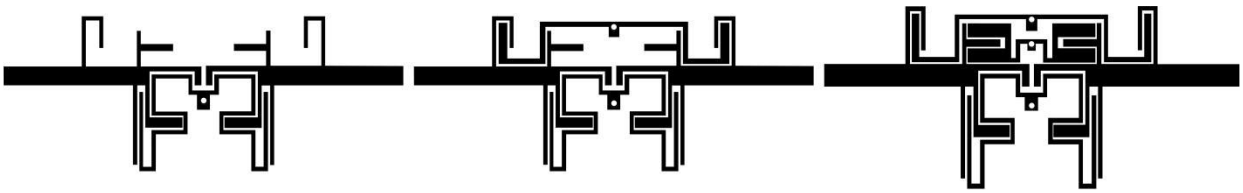

Fig. 1. (a) Schematic diagram of the proposed BPF 1, (b) schematic diagram of the proposed BPF 2, and (c) schematic diagram of the proposed BPF 3.

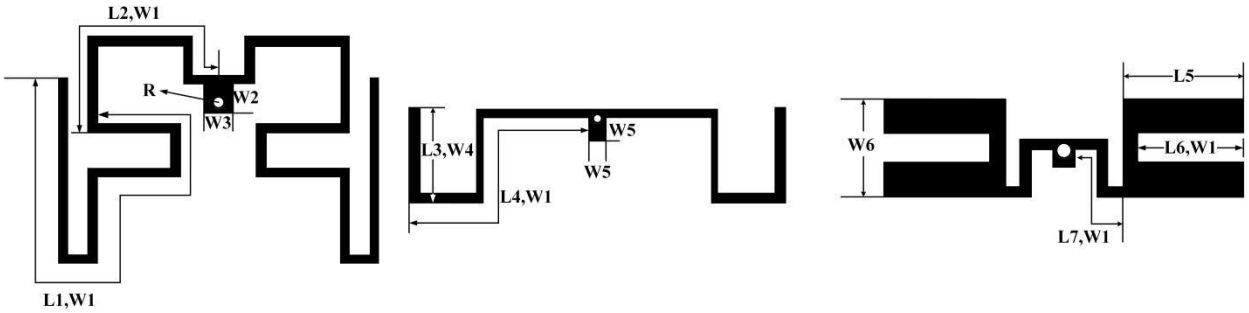

Fig. 2. (a) Schematic diagram of the proposed DMR 1, (b) schematic diagram of the proposed DMR 2, and (c) schematic diagram of the proposed DMR 3.

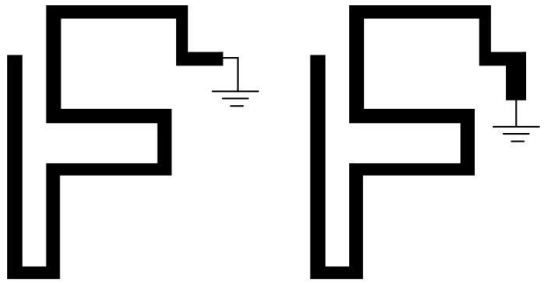

(a) (b)

Fig. 3. DMR analysis using the even-odd-mode method: (a) equivalent circuit in the odd-mode, and (b) equivalent circuit in even-mode.

The commercially available full-wave electromagnetic simulators HFSS were used to characterize the electric field patterns for the dual-mode resonator. HFSS uses the finite element method (FEM) to analyze the electromagnetic characteristics of 3D objects. The basic process of solving the problem by FEM includes three parts, which are the mesh discretization of the object, the solution of the simultaneous matrix equations related the mesh and the postprocessing calculation of the problem.

It can be seen that the whole structure is symmetrical with the center point, so the center point is modeled as the origin point and the mirror operation is applied. The physical excitation of the filter is by the coaxial line with the TEM wave. In order to use the wave-guide port in the simulation code, the port surface must cover more than ninety-five percent of the TEM field. It is assumed that the width of the excitation microstrip is w and the thickness of the dielectric layer is h. The height of the wave port is generally set to 6–10h. When $w > h$, the width of the wave port is set to about 10w; when $w < h$, the width of the wave port is set to about 5w. Finally, the height and width of the wave port of are 10h and 10w in this paper.

According to the standard which is set up by user, HFSS simulation code uses adaptive mesh generation technology. The solution frequency of the meshing is generally set at the center frequency of the filter. After each new mesh subdivision, HFSS will compare the results of the S parameters with the old one. If the error is less than the set criterion, it is shown that the result is convergent and the adaptive process will end. The dimensions are optimized by a full-wave simulation to take all the discontinuities into consideration.

The symmetrical plane can be modeled, as an electric wall (E. W.) with the equivalent circuits in Fig. 3 (a) under odd-mode excitation, while as an magnetic wall (M.W.) under the odd-mode excitation in Fig. 3 (b). Therefore, the odd-mode resonant frequency f_{odd} and even-mode resonant frequency f_{even} can be determined by the L_{odd} and L_{even}, respectively, which can be expressed approximately as:

$$L_{odd} = 2L_1 + 2L_2, \tag{1}$$

$$L_{even} = 2L_1 + 2L_2 + W_2. \tag{2}$$

Then the odd-mode frequency f_{odd} and the even-mode frequency f_{even} can be expressed as:

$$f_{odd} = \frac{c}{L_{odd}\sqrt{\varepsilon_{eff}}}, \quad (3)$$

$$f_{even} = \frac{c}{L_{even}\sqrt{\varepsilon_{eff}}}, \quad (4)$$

where c is the speed of light, and ε_{eff} is the effective dielectric constant of the substrate.

III. DESIGN OF THE PROPOSED FILTERS

The coupling scheme of the single-band filter based on DMR1 and complex feed-lines is shown in Fig. 4.

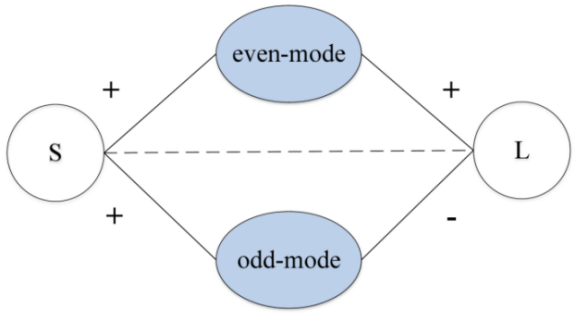

Fig. 4. Coupling structure of the proposed single-band BPF I.

The signal is coupled to two modes at the same time, providing two main paths between the source and load, and there is no coupling between each mode. Two transmission zeros can be created near passband due to the two mainly signals path and source-load coupling (S-L coupling) counteraction. The coupling matrix can be written down as:

$$\begin{bmatrix} 0 & M_{Se} & M_{So} & M_{SL} \\ M_{eS} & M_{ee} & 0 & M_{eL} \\ M_{oS} & 0 & M_{oo} & M_{oL} \\ M_{LS} & M_{Le} & M_{Lo} & 0 \end{bmatrix}.$$

In this coupling matrix, the subscript of e and o refer to the even- mode and odd- mode, separately, while the subscript of S and L refer to the source and the load. Since the proposed single-band filter exhibits symmetry property, the relationship $M_{eS} = M_{eL}$, and $M_{oS} = -M_{oL}$ establishes. The gap between source and load S_o is introduced to provide proper S-L coupling coefficient M_{SL} for generating an additional zero. In order to get coupling matrix, an example is taken of a second order generalized Chebyshev filter with the center frequency of 2.4 GHz, the 3 dB bandwidth of 130 MHz, the return loss of 28 dB and two trans-mission zeros frequencies locate at 1.7 and 2.9 GHz.The corresponding coupling coefficients [14] are:

$$\begin{bmatrix} 0 & 0.79976 & 0.88523 & 0.025 \\ 0.79976 & -1.5551 & 0 & 0.79976 \\ 0.88523 & 0 & 1.5551 & -0.88523 \\ 0.025 & 0.79976 & -0.88523 & 0 \end{bmatrix}.$$

IV. RESULT AND DISCUSSION

In Fig. 2 (a), the length W_2 does not affect the odd-mode resonant frequency, whereas the even-mode is directly depend on the length W_2, to observe the mode splitting, the dual-mode resonators have been simulated with vary loaded size. As shown in Fig. 5 (a), when W_2 increases from 0.4 to 1.2 mm (the others are as L_1 = 15.75 mm, L_2 = 8 mm, W_1 = 0.3 mm, W_3 = 1 mm, R = 0.2 mm), the resonant frequency of the even mode decreases from 2.35 GHz to 2.29 GHz, while that of the odd mode hardly changes. The line lengths L_1 and L_2 affect both the even- and odd-mode resonant frequencies. Figure 5 (b) depicts that the even- and odd-mode resonant frequencies vary with L_1. When L_1 increases from 13.75 mm to 15.75 mm (the others are as L_2 = 8 mm, W_1 = 0.3 mm, W_2 = 0.9 mm, W_3 = 1 mm, R = 0.2 mm), the resonant frequency of the even mode decreases from 2.42 GHz to 2.26 GHz, while that of the odd mode decreases from 2.52 GHz to 2.35 GHz, and it is obvious that two curves are almost parallel lines. From the above two diagrams, it can be seen that desired center frequency can be regulated by changing the length of SIR and the shorted stub.

The structure of the proposed single-band filter I is shown in Fig. 1 (a). It consists of a DMR with the S-L coupling. Since the DMR 1 locates at the down side of the feed lines, another DMR is added to work on 3.5 GHz to get a dual-band filter and make full use of the space of the substrate. Moreover, because of the special of the structure, the two DMRs can be individually designed. Fig. 6 gives the curves about 3 situations: with DMR 1, with DMR 2 and with two DMRs. Figure 1 (b) depicts the layout of the proposed dual-band BPF II. DMR 1 and DMR 2 are distributed over the upper and lower sides of the feed lines, and we can see that DMR 2 is a structure similar to DMR 1. Similarly, DMR 3 (seen in Fig. 1 (c)) can be added into the dual-band BPF, and the tri-band BPF can be gained finally. Thus, the current distributions of the proposed tri-band BPF at the center frequency of each passband are demonstrated in Fig. 7. There is a strong current path for the DMR at its center frequency, while the other DMRs exhibit a weak current distribution. The main reason for the current path is that there is almost no coupling between these DMRs. The three DMRs are independent of each other and do not interfere with each other, so a strong current appears in one DMR at the its center frequency point, while that in other DMRs is weak.

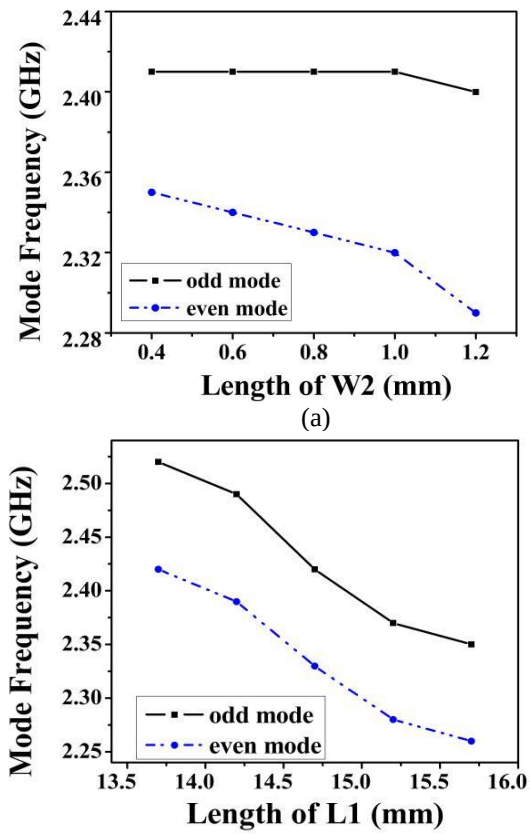

Fig. 5. Variation of even-odd-mode resonant frequency on W_2 (a) and L_1 (b).

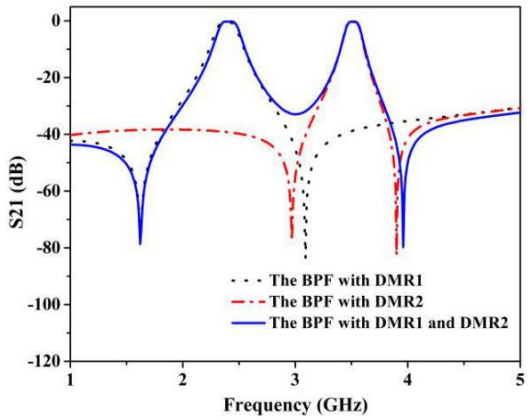

Fig. 6. The simulation of S21 parameter of the dual-band BPF II with DMR 1, DMR 2, DMR 1 and DMR 2.

The geometrical dimensions of proposed filter III are decided as L_1 = 15.75 mm, L_2 = 8 mm, L_3 = 3.3 mm, L_4 = 11.8 mm, L_5 = 3.3 mm, L_6 = 2.9 mm, L_7 = 2.6 mm, W_1 = 0.3 mm, W_2 = 0.9 mm, W_3 = 1 mm, W_4 = 0.5 mm, W_5 = 0.8 mm, W_6 = 2.7 mm, R = 0.2 mm, and the compact sizes are about 0.2×0.13 λ_g.

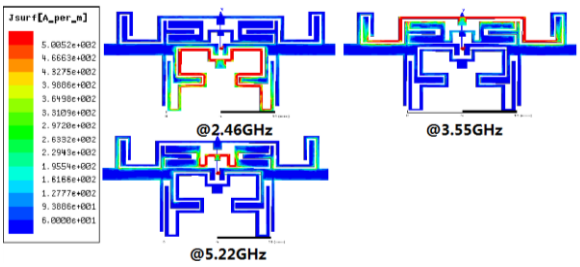

Fig. 7. Current distribution of the proposed tri-band BPF III.

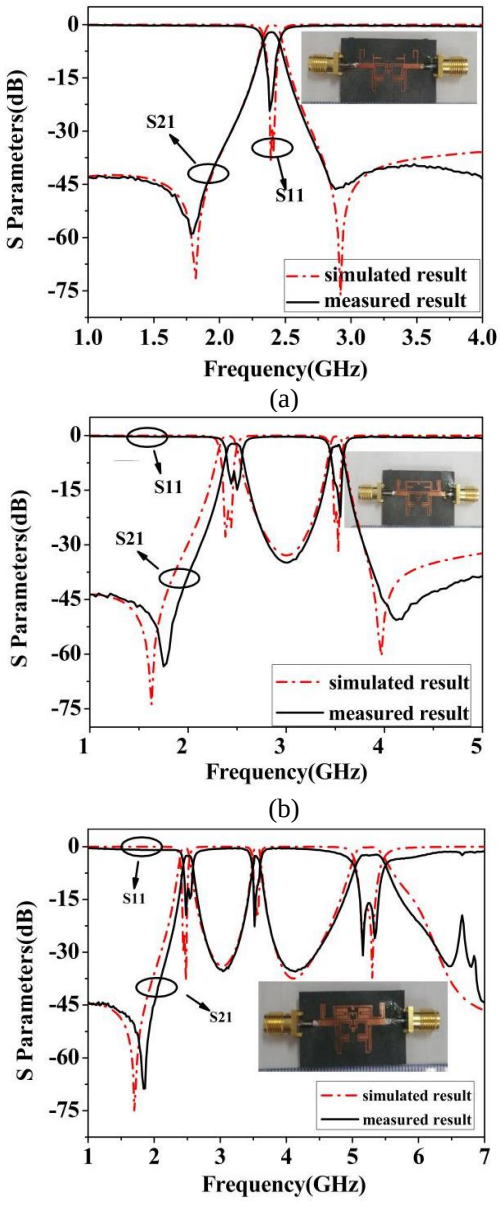

Fig. 8. Simulated and measured results: (a) of the proposed single-band BPF I, (b) of the proposed dual-band BPF II, and (c) of the proposed tri-band BPF III.

Figure 8 depict the results of simulated and measured, the red curves represent the simulated results, while the black curves stand for the measured results. It can be seen the measured results meet the simulated ones very well. Tables 1, 2 and 3 show detailed design specification of BPF I, II, and III. f_0 infers to center frequency of every passband. BW indicates the bandwidth, IL and RL stand for insertion and reflection loss, separately. For the comparison with the previous investigations, Table 4 summarizes some dual-mode BPF performance characteristics. From the Table 4, it can be seen that the presented tri- band BPF shows miniature size with good performances when compared with the previous works.

Table 1: Design specifications of the filter I

Results	f_o/GHz	BW/MHz	IL/dB	RL/dB
Sim.	2.4	130	0.21	35
Mea.	2.4	120	1	21

Table 2: Design specifications of the filter II

Results	Bands	f_o/GHz	BW/MHz	IL/dB	RL/dB
Sim.	Band I	2.4	180	0.2	29
	Band II	3.51	130	0.26	31
Mea.	Band I	2.45	180	1.1	14
	Band II	3.51	130	1.5	20

Table 3: Design specifications of the filter III

Results	Bands	f_o/GHz	BW/MHz	IL/dB	RL/dB
Sim.	Band I	2.4	150	0.3	35
	Band II	3.5	130	0.4	18
	Band III	5.2	470	0.21	35
Mea.	Band I	2.46	130	1.5	18
	Band II	3.55	130	1.6	20
	Band III	5.22	470	1.3	30

Table 4: Comparison between the reference filters and the proposed filter III

References	f_0/GHz	IL/dB	RL/dB	Filter Size ($\lambda g \times \lambda g$)	FBW/%
6	1.57/2.45/5.25	1.5/1.34/0.908	16/16/17	0.182×0.26	8.2/7.3/9.9
7	1.8/2.4/5.8	1.5/0.9/2.9	15/23/18	0.16×0.17	8.9/12.5/5.3
9	1.5/2.45/3.5	1.17/1.02/2.17	19/20/19	0.28×0.11	7.5/5.8/3.6
10	1.8/3.5/5.8	0.88/1.33/1.77	21/15/15	0.108×0.521	7/5/3.5
11	1.52/3.42/5.31	2.6/2.3/5.3	15/35/10	0.36×0.38	5.9/5.8/4
This work	**2.46/3.55/5.22**	**1.5/1.6/1.3**	**18/20/30**	**0.2×0.13**	**5.3/3.7/9**

V. CONCLUSION

In this paper, a kind of folded short-loaded dual-mode resonators are proposed. By controlling length ratios of stepped-impedance resonator and shorted stub, three passbands with two poles can be controlled independently in an appropriate range. Finally, three filters, conforming 802.11n protocol, are designed and fabricated on the Rogers 5880 substrate with the relative dielectric constant ε_r = 2.2, substrate loss tanδ = 0.002, and the thickness h = 0.508 mm. It is shown that the proposed BPFs have the advantages of good performance. The insertion losses of measured are lower than 2 dB, the frequencies can be tuned conveniently and independently. Good agreement can be achieved between measured results and simulated ones. Based on the above analysis, it can be concluded that our design is attractive for multiband wireless communication.

ACKNOWLEDGMENT

This work is supported by Sichuan Science and Technology Program (Grant No.2020YJ0271).

REFERENCES

[1] I. Wolff, "Microstrip bandpass filter using degenerate modes of a microstrip ring resonator," *Electron. Letters*, vol. 8, no. 12, pp. 302-303, June 1972.

[2] B. F. Ganji, M. Samadbeik, A. Ramezani, and A. Mousavi, "Simple configuration low-pass filter with very wide stop band," *Applied Computational Electromagnetics Society Express Journal*, vol. 1, no. 1, pp. 4-7, 2016.

[3] X. Deng, K. D. Xu, Z. Wang, and B. Yan, "Novel microstrip ultra-wideband bandpass filter using radial-stub-loaded structure," *Applied Computational Electromagnetics Society Express Journal*, vol. 1, no. 1, pp. 20-23, 2016.

[4] R. Yin, W. Feng, and W. Che, "High selectivity dual-band bandpass filters using dual-mode resonators," *Applied Computational Electromagnetics Society Journal*, vol. 32, no. 9, pp. 800-805, 2017.

[5] F. Xia, Q. Zhang, and Y. Chen, "Dualband filter using stub-loaded resonators," *2018 International Applied Computational Electromagnetics Society*

Symposium-China (ACES-China), pp. 1-2, 2018.

[6] C.-H. Lee, C.-I. G. Hsu, and H.-K. Jhuang, "Design of a new tri-band microstrip BPF using combined quarter-wavelength SIRs," *IEEE Microwave & Wireless Components Letters*, vol. 16, no. 11, pp. 594-596, 2006.

[7] Q. Li, Y. H. Zhang, X. Feng, and Y. Fan, "Tri-band filter with multiple transmission zeros and controllable bandwidths," *International Journal of Microwave & Wireless Technologies*, vol. 8, no. 1, pp. 9-13, 2016.

[8] F. C. Chen and Q. X. Chu, "Design of compact tri-band bandpass filters using assembled resonators," *IEEE Transactions on Microwave Theory & Techniques*, vol. 57, no. 1, pp. 165-171, 2009.

[9] S. J. Sun, T. Su, K. Deng, B. Wu, and C. H. Liang, "Shorted-ended stepped-impedance dual-resonance resonator and its application to bandpass filters," *IEEE Transactions on Microwave Theory & Techniques*, vol. 61, no. 9, pp. 3209-3215, 2013.

[10] S. Zhang and L. Zhu, "Compact tri-band bandpass filter based on λ/4 resonators with U-folded coupled-line," *IEEE Microwave & Wireless Components Letters*, vol. 23, no. 5, pp. 258-260, 2013.

[11] B. Peng, S. Li, B. Zhang, and S. Wang, "Triband filter with high design flexibility and wide stopband using DGS and shorted stub-loaded resonator," *Microwave and Optical Technology Letters*, vol. 57, no. 5, pp. 1226-1228, 2015.

[12] Z. Zhu, S. Liang, and C. Wei, "Novel pentagonal dual-mode filters with adjustable transmission zeros," *Applied Computational Electromagnetics Society Journal*, vol. 31, no. 10, pp. 1238-1243, 2016.

[13] X. B. Wei, Y. Shi, P. Wang, J. X. Liao, Z. Q. Xu, and B. C. Yang, "Compact dual-band bandpass filter with improved stopband characteristics," *Electronics Letters*, vol. 48, no. 12, pp. 704-705, 2012.

[14] J. S. G. Hong and M. J. Lancaster, *Microstrip Filters for RF/Microwave Applications*. 2nd Edition, John Wiley & Sons, 2001.

Zhaojun Zhu was born in Sichuan, China, in 1978. He received the B.S. degree and the Ph.D. degree in Physical Electronics in University of Electronic Science and Technology of China (UESTC), Chengdu, in 2002 and 2007 respectively. Since 2012, he has been an Associate Professor with the UESTC. His research interests include the design of microwave and millimeter-wave circuits.

Ke Yang was born in Shannxi, China, in1996. He received the B.E. degree in Communication Engineering in Xian University of Science and Technology in 2019, and is working toward the M.A. Eng. degree in UESTC. His research interests include millimeter-wave circuit and phased array wave control algorithm design.

Xiufeng Ren was born in Shandong, China, in1995. She received the B.E. degree in Communication Engineering in China University of Petroleum in 2018, and is working toward the M.A. Eng. degree in UESTC. Her research interests include antenna design and phased array wave control algorithm design.

Lu Cao was born in Jiangxi Province, China, in 1993. She received the B.S. degree in Physics from Gannan Normal University, in 2015, and M.D. degree in UESTC in 2018. Her research interests include the design of microwave and millimeter-wave circuits.

Analysis of EMI from Pantograph-catenary Arc on Speed Sensor Based on the High-speed Train Model

Yutao Tang, Feng Zhu, and Yingying Chen

School of Electrical Engineering
Southwest Jiaotong University, Chengdu, 610031, China
tangyutao@my.swjtu.edu.cn, zhufeng@swjtu.edu.cn, 454621625@qq.com

Abstract ─ There will be the pantograph-catenary arc (PCA) when the pantograph of a high-speed train is separated from the power supply line, and the electromagnetic interference (EMI) caused by the PCA can affect speed sensors of the train. To study the influence of the PCA, firstly, the traction control unit (TCU) speed sensor of the high-speed train is researched. The result shows both overvoltage and electromagnetic radiation (EMR) generated by the PCA can influence the signal of speed sensor. Secondly, the composite model of the train is established. Then, the interference of the PCA on the TCU speed sensor is verified. The results of practical measurements show the PCA causes a maximum overvoltage of 680 V on train body (TB) and increases the magnetic field around TB to a maximum of 58 dBμA/m. This is the reason of sensor malfunction, which is consistent with the theoretical and simulation results. Finally, the methods to reduce the EMI of the PCA are proposed.

Index Terms ─ Electromagnetic Interference (EMI), high-speed train, overvoltage, Pantograph-Catenary Arc (PCA), speed sensor.

I. INTRODUCTION

The high-speed train gets electric energy from the power supply line by the pantograph. But the pantograph needs to be separated from the line after the train stops stably. The pantograph-catenary arc (PCA) will be produced at the moment when the pantograph is separated from the line [1]-[3], and the electromagnetic interference (EMI) of the PCA affects the electronic equipment on the train, such as speed sensor. A typical example is the train doors cannot be opened normally after the train stops at a station in China. According to the analysis results of the door control unit (DCU), there are two ways to close the train doors. Firstly, the driver can send the door closing command to DCU directly to close all the doors. Secondly, the traction control unit (TCU) speed sensors transmit the detected speed to TCU. As long as the speed detected by one of the TCU speed sensors exceeds 5 km/h, all the train doors will be closed automatically [4, 5]. After the train arrives at the station and stops stably, the driver will not issue the directive to close the doors, and the train speed shall be zero. But the fact is the train doors still cannot be opened normally. Therefore, the PCA is likely to interfere with the speed sensor and cause it to malfunction. So, it is necessary to research the EMI caused by the PCA.

Some scholars have used the train model to study the overvoltage on the train bodies (TBs) when the pantograph is separated from the power supply line [6]-[8]. But they did not study the effect of overvoltage on the speed sensors. The electromagnetic radiation (EMR) caused by the PCA of the subway has been measured and analyzed in [9, 10]. But its characteristics are different from those of high-speed trains. In some studies [11, 12], researchers analyzed the working principle of speed sensors and researched the effect of the PCA on it. But they only considered a single influence factor and did not combine the complete train model to study the influence of multiple disturbances.

As an extension of previous works, firstly, the structure and interference modes of the TCU speed sensor on a high-speed train are analyzed. The results show that the sensor signal is impacted by overvoltage and EMR generated by the PCA. Secondly, the structure of the Chinese high-speed train is studied in detail and the composite model is established. The model includes the power supply line, TBs, speed sensors, grounding systems, and PCA. Thirdly, the practical measurements are carried out when the pantograph on the roof of the second TB (02TB) is separated from the power supply line. The results show the maximum value of overvoltage on the 02TB is approximately 680 V, and the magnetic field around the 02TB is nearly 58 dBμA/m. Therefore, the signal of the TCU speed sensor can be affected by the PCA. Finally, the methods of adding protective earthing and nesting magnetic rings are proposed to reduce the EMI caused by the PCA on the TCU speed sensor.

Submitted On: October 4, 2020
Accepted On: December 3, 2020

https://doi.org/10.47037/2020.ACES.J.360213

II. ANALYSIS OF THE STRUCTURE AND INTERFERENCE MODES OF TCU SPEED SENSOR

A. Structure of the high-speed train with TCU speed sensors

The Chinese high-speed train consists of 16 TBs. Besides, there are a pantograph, working earthing, and TCU speed sensor on the 02TB, 07TB, 10TB, and 15TB, respectively [13]. There is one protective earthing between the 08TB and 09TB. The partial structure of the high-speed train is shown in Fig. 1.

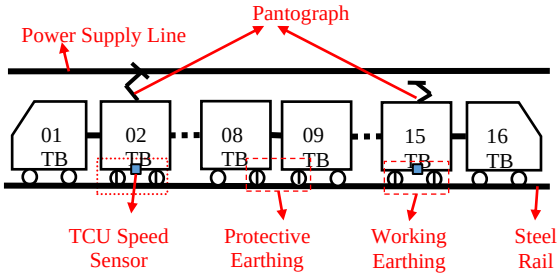

Fig. 1. The partial structure of the high-speed train.

B. Interference of the PCA on TCU speed sensors

The PCA is generated at the moment when the pantograph is separated from the power supply line, which produces EMR and overvoltage on the TBs.

Only one end of the TCU speed sensor cable is connected to the TB as shown in Fig. 2 (a). The overvoltage caused by the PCA creates a parasitic capacitance between the cable shield and the core wire of the sensor as shown in Fig. 2 (b).

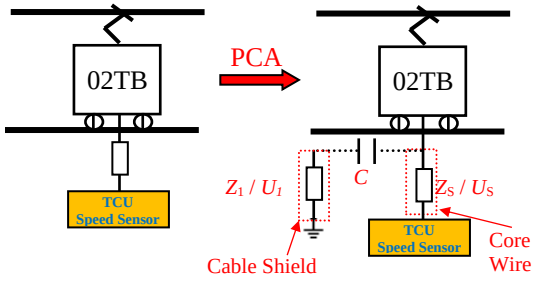

Fig. 2. Connection diagram of TCU speed sensor before and after the pantograph separation.

According to Fig. 2 (b), the inductive voltage generated by the overvoltage on the sensor core wire can be calculated by:

$$U_s = \frac{jwCZ_s}{1+ jwC(Z_1 + Z_s)} U_1, \quad (1)$$

where U_s is the interference voltage, which can impact the signal of the TCU speed sensor. Z_1 and Z_s are the impedance of sensor cable shield and core wire, respectively, U_1 is the overvoltage between the sensor cable shield and the steel rail, and C is the parasitic capacitance generated by the overvoltage [12].

In addition, the EMR from the PCA can also affect the TCU speed sensors. The outer conductor of the sensor cable is made of metal wires. Because there are many small holes, the outer conductor is not completely shielded. The inductive electric field (E) is generated on the surface of the cable because of the EMR. As described in Fig. 3, a part of the inductive electric field (E') will be coupled on the core wire by the tiny holes. Because the $E > E$', the potential difference (U) between the cable shield and core wire can be caused.

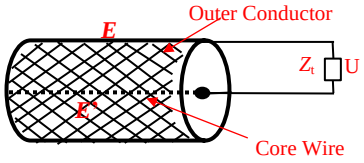

Fig. 3. The diagram of speed sensor cable.

The value of U can be obtained by [14]:

$$U = I \times Z_t \times L_m, \quad (2)$$

where I is the inductive current, Z_t is the transfer impedance per meter cable, and L_m is the effective length of the cable.

Based on the above analysis, the overvoltage and the EMR are two different interference modes of the PCA to TCU speed sensor. They cause the inductive voltage on the core wire and the potential difference between the cable shield and core wire respectively. Besides, they can affect the signal port of the sensor and make it detect the wrong speed signal, which lead to the malfunction of the DCU.

III. COMPOSITE MODEL OF THE HIGH-SPEED TRAIN

A. Structure of the high-speed train model

When the high-speed train is running, the pantograph is connected to the power supply line (25 kV / 50 Hz). The current is transmitted to four traction transformers at 02TB, 07TB, 10TB, and 15TB. In addition, four TCU speed sensors are respectively installed on the wheel shaft end of that TBs.

As shown in Fig. 4, the current flows into the earth by working earthings on the primary side of the transformer. Besides, the high voltage cable, sixteen TBs, and steel rail are also included in the composite model. There is a switch to simulate the separation of the pantograph and the power supply line by opening it. The relevant parameters in the model refer to the equivalent parameters of the Beijing-Tianjin high-speed railway in China as listed in Table 1 [15].

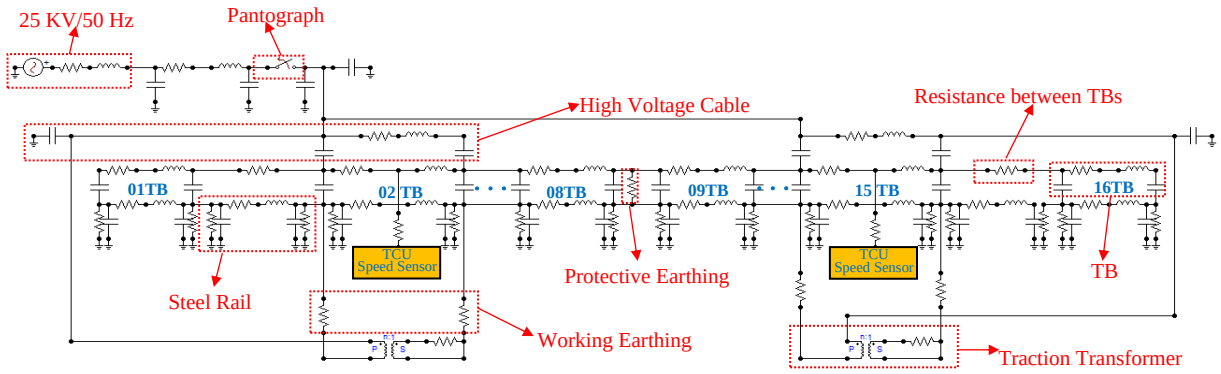

Fig. 4. The diagram of the composite model of the high-speed train.

Table 1: Relevant parameters of the train model

Name	Parameter Name	Parameter Value
TB	Resistance	0.225 mΩ
	Inductance	0.001103375 mH/m
	Capacitance	0.00001007011316 μF/m
	Resistance Between TBs	6.4mΩ
	Length	25 m/TB
Steel Rail	Resistance	0.1367 mΩ/m
	Inductance	0.000429718 mH/m
	Capacitance	0.0000603384 μF/m
	Leakage conductance	0.01 mS/m
Transformer	Equivalent Resistance	2.941 Ω
Protective Earthing	Resistance	0.05 Ω
Working Earthing	Resistance	0.05 Ω

Besides, an arc model will be added to the model to simulate the PCA when the pantograph is separated from the power supply line as described in Fig. 5. The relevant parameters are shown in Table 2.

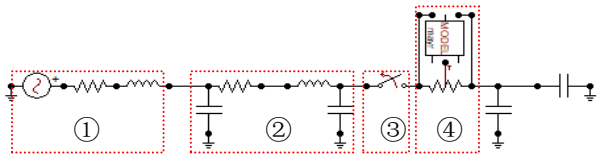

Fig. 5. Model of the PCA generation.

B. Establishment of the PCA model

The current common arc models are Mayr Model, Cassie Model, and Habedank Model [16]. The Habedank Model combines the other two models and makes up for their shortcomings. The mathematical model of Habedank Model is [17]:

$$\begin{cases} \dfrac{dg_C}{dt} = \dfrac{1}{\theta_C}\left(\dfrac{i^2}{u_C \cdot g_C} - g_C\right) \\ \dfrac{dg_M}{dt} = \dfrac{1}{\theta_M}\left(\dfrac{i^2}{P_0} - g_M\right) \\ \dfrac{1}{g} = \dfrac{1}{g_C} - \dfrac{1}{g_M} \end{cases}, \tag{3}$$

where g_C, θ_C, g_M, and θ_M are the conductance and the time constants of Mayr and Cassie Model, respectively. u_C, i, and P_0 are the voltage, current, and dissipative power of arc. P_0 is assumed to be constants in Eq. (3). In fact, it is not constant and needs to be modified to create a more realistic PCA model.

Table 2: Relevant parameters of the model of the PCA generation

No.	Name	Parameter Name	Parameter Value
①	Railway Traction Substations	Voltage	25 KV / 50 Hz
		Resistance	0.165 Ω
		Inductance	10.8 mH
②	High Voltage Cable	Resistance	0.014 mΩ/m
		Inductance	0.000131093 mH/m
		Capacitance	0.00041162 μF/m
③	Pantograph	--	--
④	PCA Model	--	--

The diameter (d) and the convective power (P_k) of the PCA will be changed because of the train speed [18]. P_k of the PCA can be calculated by [19]:

$$P_k' = 0.1464 d (v + 36)^{1.5}, \tag{4}$$

where P_k' is P_k per unit length of the PCA. v is the train speed, which unit is km/h .

The d value is changed by the transverse airflow [20]. The relationship between d and v is:

$$d = 1.5369\sqrt{\frac{i}{v+36}}. \tag{5}$$

P_k' can be derived by Eq. (4) and Eq. (5):

$$P_k' = 0.225\sqrt{i}(v+36). \tag{6}$$

After the train stops, the PCA will be generated at the moment the pantograph is separated from the power supply line. At this moment, the maximum length of the PCA (L_{arc}) is 10 mm and v is 0 km/h. P_k can be obtained by:

$$P_k = 81\sqrt{i}. \tag{7}$$

P_k and the radiation power (P_s) of the PCA account for approximately 80% and 20% of P_0, respectively. So P_0 of the PCA is:

$$P_0 = 101.25\sqrt{i}. \tag{8}$$

According to [21], u_C of the PCA is only related to the length of the arc, and the proportion is a positive constant. u_C of the PCA is calculated by:

$$u_C = 15L_{arc}, \tag{9}$$

where factor 15 is an empirical value when the voltage of the power supply line is 25 KV/50 Hz.

The new PCA model can be derived by Eq. (3) ~ Eq. (9):

$$\begin{cases} \dfrac{dg_C}{dt} = \dfrac{1}{\theta_C}\left(\dfrac{i^2}{150g_C} - g_C\right) \\ \dfrac{dg_M}{dt} = \dfrac{1}{\theta_M}\left(\dfrac{i^{1.5}}{101.25} - g_M\right) \\ \dfrac{1}{g} = \dfrac{1}{g_C} - \dfrac{1}{g_M} \end{cases}. \tag{10}$$

C. Simulation results of the high-speed train model

The simulation results show that the distribution of TB voltage is uniform when the high-speed train is running (the switch is closed). As we can see in Fig. 6, the maximum difference of TB voltage (from the head to the tail of the train, total length is 400 m) is only 0.0036 V, which can be neglected. However, the pantograph will be separated from the power supply line after the train stops (the switch is opened). At this moment, the PCA produces large overvoltage on TB where the pantograph is located. But overvoltage can be discharged by protective grounding. Therefore, the overvoltage on the TBs far away from the pantograph and close to the protective grounding is small (such as 08TB and 09TB). So the distribution of TB voltage is extremely uneven when the pantograph is separated from the line. The maximum TB voltage is nearly 700 V (on the 02TB). But the TB voltage on the 08TB and 09TB is much lower than that on the other TBs, which is only around 50 V as shown in Fig. 7.

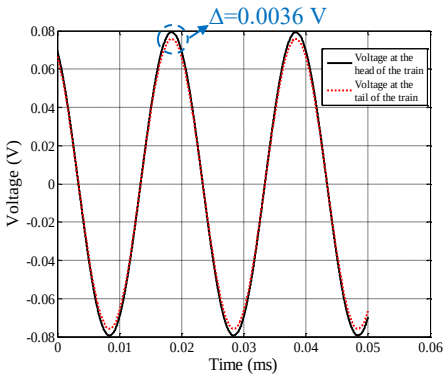

Fig. 6. The TB voltage at the head and tail of the train.

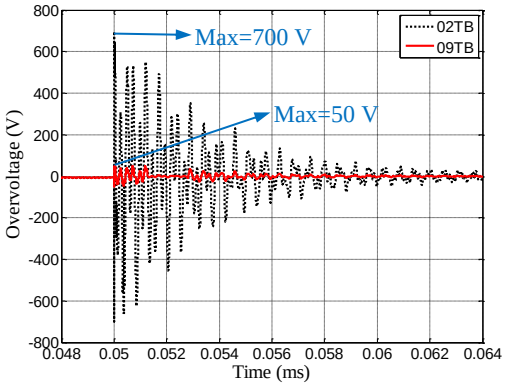

Fig. 7. The overvoltage on 02TB and 09TB.

The train and PCA models are based on the Chinese typical high-speed train and the Beijing-Tianjin high-speed railway in this paper. The potential limitations and several differences need to be noted to extend these models to other cases.

1) There are some differences in structure and related parameters among different types of trains. For example, the trains of Japan and Germany have eight train bodies, while there are only four in Brazil. Moreover, the impedance and position of the grounding system are also different. When the model is applied to other types of trains, the impedance, position, and length of the train bodies and the grounding system should be reset.

2) The characteristics of PCA will be affected by the running environment of trains. The unstable route will aggravate the PCA generation, and the moist or dry air will change the radiation characteristics of the PCA. Therefore, it is necessary to consider the environmental factors in PCA modeling.

3) The model can be used to analyze the EMI on other electrical equipment, like digital encoders, LED display, and temperature sensors. The connection position and electrical structure of the equipment should be

changed accordingly in the model.

IV. MEASUREMENT AND SUPPRESSION OF INTERFERENCE

A. Scenario and results of the measurement

The practical measurements are carried out at a high-speed train station in China. The test items include the TB voltage, magnetic field around the TB, and signal port voltage of the sensor. The pantograph on the 02TB is separated from the power supply line to produce the PCA during the measurement. The relative specifications are listed in Table 3.

Table 3: The specifications of measurement instruments

Instruments		Specifications	
Name	**Model**	**Name**	**Data**
EMI receiver	ESCI-3	Frequency range	9 KHz ~ 3 GHz
		Resolution ratio	0.1 Hz
		Specification	+30 ~ -147 dBm
Loop antenna	HFH2-Z2	Frequency range	9 KHz ~ 30 MHz
Digital multimeter	VC890C	Direct voltage	200 mV ~1000 V
		Alternating voltage	2 ~750 V
Oscilloscope	GDS-2302A	Frequency	500 MHz
		Maximum sampling rate	5 Gsample/s

The 02TB voltage is measured by a digital multimeter as shown in Fig. 8. The results show that the maximum overvoltage on the 02TB is 680 V when the pantograph is separated from the power supply line. It is consistent with the previous simulation results (in Fig. 7).

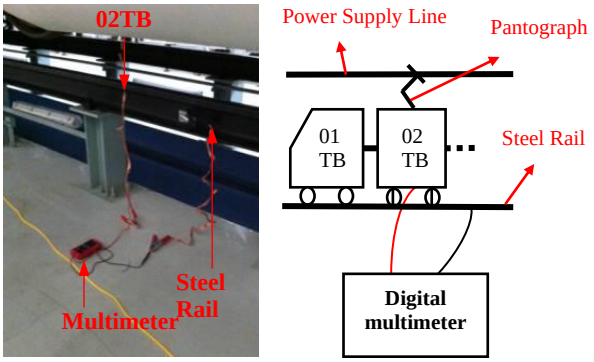

(a) (b)

Fig. 8. Measurement scenario of TB voltage test.

The measurement scenario and results of the magnetic field around the 02TB are shown in Fig. 9 and Fig. 10, respectively. The results show that the magnetic field will increase (up to roughly 58 dBμA/m) because of the PCA.

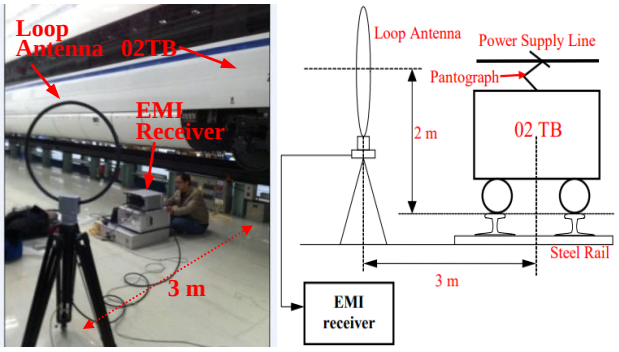

(a) (b)

Fig. 9. Measurement scenario of magnetic field test.

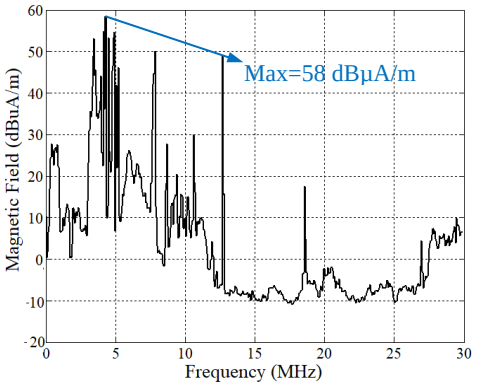

Fig. 10. Measurement results of the magnetic field around the 02TB.

The measurement results show that when the pantograph is separated from the power supply line, the EMI caused by PCA is shown in the following two aspects: Firstly, the interference value of 680 V overvoltage is formed on the TB. Secondly, the magnetic field around the TB is increased, and the strong magnetic field interference is mainly concentrated in 5 MHz and up to 58 dBμA/m. According to the Section II, those two interference modes cause the wrong voltage signal on the TCU speed sensor. The signal port voltage of the sensor is tested by an oscilloscope. In fact, there should not be voltage on the sensor signal port after the train stops. But due to the EMI of PCA, the signal port voltage is approximately 2.6 V when the pantograph is separated as described in Fig. 11. The sensor will be activated if the signal port voltage of speed sensor exceeds 1.5 V. So the EMI of PCA will affect the control of train doors by interfering with TCU speed sensor.

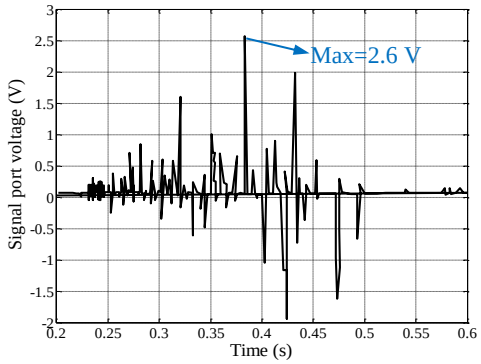

Fig. 11. Signal port voltage of the TCU speed sensor on 02TB.

B. Methods of interference suppression

According to the above research, both the overvoltage and the EMR generated by the PCA can influence the TCU speed sensor.

Firstly, as for the effect from the overvoltage, the interference voltage (U_s) can be restrained by reducing the overvoltage (U_1) as shown in Eq. (1). According to the simulation results in section III, U_1 is greatly reduced by protective earthing. Because the protective earthing is connected to the TBs and the earth, the TB voltage can be discharged by it. But the train has only one protective grounding, which is installed between the 08TB and 09TB (the middle position of the train). A high-speed train is about 400 m, so the overvoltage on the TBs far away from the protective grounding will be very large. Therefore, the new protective earthing can be added on the TBs with higher overvoltage to decrease U_s. Compared with Fig. 11, the signal port voltage of the TCU speed sensor is significantly reduced after the protective earthing is added on the 02TB as shown in Fig. 12.

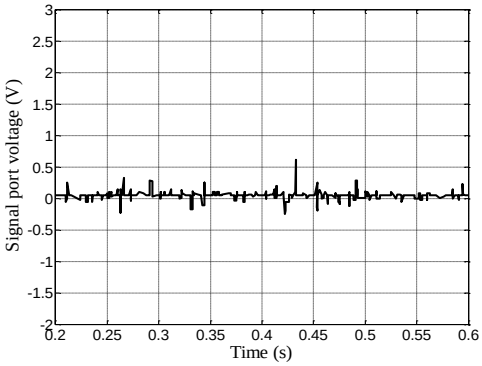

Fig. 12. Signal port voltage of the TCU speed sensor on 02TB after adding a protective earthing.

Secondly, the potential difference (U) between the cable shield and core wire can be reduced to suppress the EMR from the PCA based on Eq. (2). The magnetic rings can absorb the EMR energy and reduce Z_t of cable. Nesting the suitable Ni-Zn ferrite magnetic rings on the cable of the speed sensor can reduce the EMI on the cable. As shown in Fig. 13, the peak of EMI is decreased by about 7 dB after using the magnetic rings. Moreover, the discrete interference is reduced obviously in 10 MHz ~ 30 MHz. The measurement method of the EMI on the speed sensor and the specific selection process of magnetic rings are introduced in detail in another paper of the authors [13].

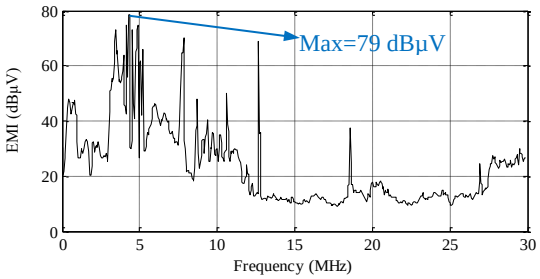

(a) Before nesting the Ni-Zn ferrite magnetic rings

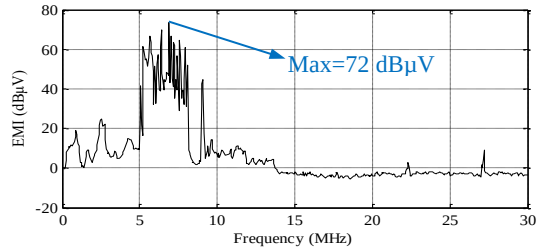

(b) After nesting the Ni-Zn ferrite magnetic rings

Fig. 13. The waveform of EMI on the TCU speed sensor cable.

V. CONCLUSION

The interference of the PCA on the TCU speed sensor of the high-speed train has been measured and analyzed. The conclusions are as follows:

1) The PCA creates the overvoltage (maximum is 680 V) on the TB. Besides, the EMR from the PCA increases the magnetic field to 58 dBμA/m around the TB.

2) The overvoltage can impact the TCU speed sensor signal by the parasitic capacitance between the cable shield and core wire. Also, the EMR can affect the speed sensor by the holes on the sensor cable shield.

3) The overvoltage and EMR caused by the PCA can be effectively suppressed by adding the protective earthing on the train and nesting the Ni-Zn ferrite magnetic rings on the sensor cable respectively.

ACKNOWLEDGMENT

We would like to thank the anonymous reviewers for their insightful comments. This paper is supported

by the National Key R&D Program of China (No. 2018YFC0809500).

REFERENCES

[1] X. Li, F. Zhu, H. Lu, R. Qiu, and Y. Tang, "Longitudinal propagation characteristic of pantograph arcing electromagnetic emission with high-speed train passing the articulated neutral section," *IEEE Transactions on Electromagnetic Compatibility*, vol. 61, no. 2, pp. 319-326, June 2018.

[2] F. Zhu, C. Gao, and Y. Tang, "Influence of pantograph-catenary arc on electromagnetic disturbance of airport terminal omnidirectional beacon," *China Railway Science*, vol. 39, no. 1, pp. 116-121, Jan. 2018.

[3] J. Gou, F. Zhu, J. Zou, J. Ye, H. Li, and Y. Wang, "Research on EMI of instrument landing system on aircraft caused by pantograph arc," *Journal of the China Railway Society*, vol. 40, no. 7, pp. 61-66, July 2018.

[4] K. Huang, Z. G. Liu, F. Zhu, Z. S. Zheng, and Y. Cheng, "Evaluation scheme for EMI of train body voltage fluctuation on the BCU speed sensor measurement," *IEEE Transactions on Instrumentation and Measurement*, vol. 66, no. 5, pp. 1046-1057, May 2017.

[5] F. Zhu, Y. Tang, and C. Gao, "Mechanism and suppression of electromagnetic interference of pantograph-catenary arc to speed sensor of CRH380BL electric multiple unit," *China Railway Science*, vol. 37, no. 6, pp. 69-74, Nov. 2016.

[6] Y. Cheng, Z. Liu, and H. Ke, "Transient analysis of electric arc burning at insulated rail joints in high-speed railway stations based on state-space modeling," *IEEE Transactions on Transportation Electrification*, vol. 3, no. 3, pp. 750-761, Sep. 2017.

[7] Y. Cheng, Z. Liu, H. Ke, and H. Zhou, "Modeling analysis of electric multiple units passing insulated rail joints in high-speed railway station," *IEEE ITEC 2017 Asia-Pacific*, 2017.

[8] F. Fan, "Study on separation between the pantograph and catenary based on improved Habedank arc model," *M.S. Thesis*, Dept. Electr. Eng., Southwest Jiaotong University, Chengdu, China, 2014.

[9] X. Li, F. Zhu, H. Lu, R. Qiu, and Y. Tang, "Longitudinal propagation characteristic of pantograph arcing electromagnetic emission with high-speed train passing the articulated neutral section," *IEEE Trans. IEEE Transactions on Electromagnetic Compatibility*, vol. 61, no. 2, pp. 319-326, June 2018.

[10] X. Li, F. Zhu, R. Qiu, and Y. Tang, "Research on influence of metro pantograph arc on airport navigation system," *Journal of the China Railway Society*, vol. 40, no. 5, pp. 97-102, May 2018.

[11] J. Yang, "EMC experiment and protection method on control vehicle speed and distance measuring equipment of CRH2 HST," *Railway Signaling Commun. Eng*., vol. 7, no. 5, pp. 21-24, Oct. 2010.

[12] J. B. Yang, F. Zhu, J. Li, M. Sha, and D. Q. Yuan, "Electromagnetic interference measurement and analysis of high-speed electric multiple units speed sensor," *Journal of Electronic Measurement and Instrumentation*, vol. 29, no. 3, pp. 433-438, Mar. 2015.

[13] Y. Tang, F. Zhu, H. Lu, and X. Li, "Analysis and suppression of EMI for traction control unit speed sensors of CRH380BL electric multiple unit," *Applied Computational Electromagnetics Society Journal*, vol. 33, no. 5, pp. 553-560, May 2018.

[14] Y. Tang and F. Zhu, "Measurement and suppression of electromagnetic interference to speed sensor of CRH380BL electric multiple unit," *2017 International Applied Computational Electromagnetics Society Symposium*, Sept. 2017.

[15] Y. Wang, Z. Liu, X, Mu, K. Huang, and H. Wang, "An extended Habedank's equation-based EMTP model of pantograph arcing considering pantograph-catenary interactions and train speeds," *IEEE Transactions on Power Delivery*, vol. 31, no. 3, pp. 1186-1194, Jan. 2016.

[16] M. T. Cassieand D. B. Fang, "An improved arc model before current zero based on the combined Mayrand Cassiearc models," *IEEE Transactions on Power Delivery*, vol. 20, no. 1, pp. 138-142, Jan. 2005.

[17] H. Zhou, Z. Liu, Y, Cheng, and K. Huang, "Extended black-box model of pantograph arcing considering varying pantograph detachment distance," *2017 IEEE Transportation Electrification Conference and Expo, Asia-Pacific (ITEC Asia-Pacific)*, Harbin, pp. 1-6, 2017.

[18] X. Chen, B, Cao, Y. Liu, G. Gao, and G. Wu, "Dynamic model of pantograph-catenary arc of train in high speed airflow field," *High Voltage Eng*., vol. 24, no. 11, pp. 3593-3600, Nov. 2016.

[19] X. Yan, W. Chen, and Z. Li, "Simulation for self-extinction behavior of secondary arc in transmission lines," *High Voltage Eng*., vol. 38, no. 9, pp. 2150-2156, 2012.

[20] Y. Liu, G. Chang, and H. Huang, "Mayr's equation-based model for pantograph arc of high-speed railway traction system," *IEEE Transactions on Power Delivery*, vol. 25, no. 3, pp. 2025-2027, Aug. 2010.

[21] T. Zhang, "Characteristic of pantograph arcing for the high-speed train and its influence on traction drive system," *M.S. Thesis*, Dept. Electr. Eng.,

Southwest Jiaotong University, Chengdu, China, 2018.

Yutao Tang was born in Sichuan Province, China, in 1991. She received the B.S. degree in Automation from Southwest Science and Technology University, Mianyang, China, in 2013, and is currently working toward the Ph.D. degree in Electrical Engineering at Southwest Jiaotong University, Chengdu, China.

Her research interests include electromagnetic environment test and evaluation, and electromagnetic compatibility analysis and design.

Feng Zhu was born in Anhui Province, China, in 1963. He received a B.S. degree in Physics from Huaibei Normal University, Huaibei, China, in 1984, an M.S. degree in Physics from Sichuan University, Chengdu, China, in 1987, and the Ph.D. degree in Electromagnetic Theory and Microwave Techniques from Southwest Jiaotong University, Chengdu, in 1997.

He is currently a Professor in the Department of Electrical Engineering, Southwest Jiaotong University. His research interests include electromagnetic environment test and evaluation, electromagnetic compatibility, and numerical electromagnetic methods.

Yingying Chen was born in Shanxi Province, China, in 1996. She received a B.S. degree in Electrical Engineering and Automation from Taiyuan University of Science and Technology in China, in 2018. She is currently pursuing a master's degree in Electrical ngineering at Southwest Jiaotong University, Chengdu, China.

Her research interests include electromagnetic environment testing and evaluation, as well as electromagnetic compatibility analysis and design.

Studying and Analysis of a Novel RK-Sinc Scheme

Min Zhu

School of Electronic and Information Engineering
Jingling Institute of Technology, Nanjing, 211169, China
zomi@jit.edu.cn

Abstract ─ In this paper, a novel high-order method, Runge-Kutta Sinc (RK-Sinc), is proposed. The RK-Sinc scheme employs the strong stability preserving Runge-Kutta (SSP-RK) algorithm to substitute time derivative and the Sinc function to replace spatial derivates. The computational efficiency, numerical dispersion and convergence of the RK-Sinc algorithm are addressed. The proposed method presents the better numerical dispersion and the faster convergence rate both in time and space domain. It is found that the computational memory of the RK-Sinc is more than two times of the FDTD for the same stencil size. Compared with the conventional FDTD, the new scheme provides more accuracy and great potential in computational electromagnetic field.

Index Terms ─ Convergence, dispersion, FDTD, Runge-Kutta, Sinc function, stability.

I. INTRODUCTION

The finite-difference time-domain (FDTD) [1] numerical techniques are widely used today for the analysis of various microwave geometries and for the modeling of electromagnetic wave propagation. However, the method has some significant limitations due to the substantial computer resources required when it involves modeling a complicated problem, which has large stencil size at least 10 cells or more per wavelength. The FDTD has a second order accuracy in spatial-temporal and large significant computational errors. In order to improve the limitations of the FDTD method, lots of methods are proposed, including the HO-FDTD [2-4] and MRTD [5] (Multiresolution Time-Domain). The HO-FDTD is presented by Fang firstly in [2], employing the Taylor series instead of the spatial and temporal derivatives to increasing accuracy. The strong stability Runge-Kutta (SSP-RK) method was first introduced and extended in Refs. [6] and [7]. Compactly supported Nth-order wavelets and *m*th-order *m*th-stage Runge-Kutta are applied in spatial discretization and time integration, respectively.

In this paper, we discuss a new method called RK-Sinc, which is considered has the same convergence level for the time and space domains. The remainder of this paper is organized as follows. In Section II, the basic theory and algorithm of the RK-Sinc method is introduced. The stability, dispersion and convergence of the method are studied in Section III. Computational cost and memory requirements are discussed in Section IV. Numerical example is given in Section V. Conclusions are summarized in Section VI.

Table 1: Coefficients $c(v)$ for the RK-Sinc(2, 2v) method ($0 \le v \le 10$)

v	$c(v)$
1	1.27323954
2	-0.14147106
3	0.05092958
4	-0.02598448
5	0.01570901
6	-0.01052264
7	0.00753396
8	-0.00565884
9	0.00440567
10	-0.00352697

II. THE RK-SINC METHOD

A. High-order Sinc method

Considering an arbitrary function f, using the Sinc function as the basis function to derive one update equation of the high-order Sinc method as follows:

$$E_{i+1/2,j,k}^{x,n+1} = E_{i+1/2,j,k}^{x,n} + \frac{1}{\varepsilon}\sum_{v=1}^{m} c(v)\cdot\left(H_{i+1/2,j+m+1/2,k}^{z,n+1/2}\frac{\Delta t}{\Delta y} - H_{i+1/2,j,k+m+1/2}^{y,n+1/2}\frac{\Delta t}{\Delta z}\right), \quad (1)$$

where $E_{i+1/2,j,k}^{x,n}$, $E_{i+1/2,j,k}^{x,n}$, $H_{i,j+m+1/2,k}^{x,n+1/2}$, $H_{i+1/2,j,k+m+1/2}^{y,n+1/2}$ are electric field and magnetic field coefficients, m, ε, μ, Δt, Δy and Δz are the spatial stencil size, the permittivity, the permeability, the temporal step size, and the spatial step size in the x-, y- and z-direction, respectively. The coefficients $c(v)$ [8] for different spatial stencil sizes are given in Table 1 for the stencil size m is 10.

Submitted On: October 27, 2020
Accepted On: January 18, 2021

https://doi.org/10.47037/2020.ACES.J.360214

B. RK-Sinc method

For simplicity and without loss of generality, in rectangular coordinate system, using the Sinc function to expand the spatial electric and magnetic field components in Maxwell's equation as described in equation (1) and the SSP-RK method to replace the time derivative of the electric field and magnetic field components in the left part of the equation (2), one update equation of the RK-Sinc(2, 2v) which is based on the Sinc function can be written as follows:

$$\frac{\partial E^x_{i+1/2,j,k}(t)}{\partial t}=\frac{1}{\varepsilon}\sum_{v=1}^{m}c(v)\left[\frac{1}{\Delta y}\left(H^z_{i+1/2,j-1/2+v,k}(t)-H^z_{i+1/2,j+1/2-v,k}(t)\right)-\frac{1}{\Delta z}\left(H^y_{i+1/2,j,k-1/2+v}(t)-H^y_{i+1/2,j,k+1/2-v}(t)\right)\right], \tag{2a}$$

$$\frac{\partial E^y_{i,j+1/2,k}(t)}{\partial t}=\frac{1}{\varepsilon}\sum_{v=1}^{m}c(v)\left[\frac{1}{\Delta z}\left(H^x_{i,j+1/2,k-1/2+v}(t)-H^x_{i,j+1/2,k+1/2-v}(t)\right)-\frac{1}{\Delta x}\left(H^z_{i-1/2+v,j+1/2,k}(t)-H^z_{i+1/2-v,j+1/2,k}(t)\right)\right], \tag{2b}$$

$$\frac{\partial E^z_{i,j,k+1/2}(t)}{\partial t}=\frac{1}{\varepsilon}\sum_{v=1}^{m}c(v)\left[\frac{1}{\Delta x}\left(H^y_{i-1/2+v,j,k+1/2}(t)-H^y_{i+1/2-v,j,k+1/2}(t)\right)-\frac{1}{\Delta y}\left(H^x_{i,j-1/2+v,k+1/2}(t)-H^x_{i,j+1/2-v,k+1/2}(t)\right)\right], \tag{2c}$$

$$\frac{\partial H^x_{i,j+1/2,k+1/2}(t)}{\partial t}=\frac{1}{\mu}\sum_{v=1}^{m}c(v)\left[\frac{1}{\Delta z}\left(E^y_{i,j+1/2,k+v}(t)-E^y_{i,j+1/2,k+1-v}(t)\right)-\frac{1}{\Delta y}\left(E^z_{i,j+v,k+1/2}(t)-E^z_{i,j+1-v,k+1/2}(t)\right)\right], \tag{2d}$$

$$\frac{\partial H^y_{i+1/2,j,k+1/2}(t)}{\partial t}=\frac{1}{\mu}\sum_{v=1}^{m}c(v)\left[\frac{1}{\Delta x}\left(E^z_{i+v,j,k+1/2}(t)-E^z_{i-v+1,j,k+1/2}(t)\right)-\frac{1}{\Delta z}\left(E^x_{i+1/2,j,k+v}(t)-E^x_{i+1/2,j,k-v+1}(t)\right)\right], \tag{2e}$$

$$\frac{\partial H^z_{i+1/2,j+1/2,k}(t)}{\partial t}=\frac{1}{\mu}\sum_{v=1}^{m}c(v)\left[\frac{1}{\Delta y}\left(E^x_{i+1/2,j+v,k}(t)-E^x_{i+1/2,j-v+1,k}(t)\right)-\frac{1}{\Delta x}\left(E^y_{i+v,j+1/2,k}(t)-E^y_{i-v+1,j,k+1/2}(t)\right)\right]. \tag{2f}$$

III. NUMERICAL PROPERTIES

In this section, the stability, dispersion and convergence of the RK-Sinc method are discussed.

A. Stability

Refer to the Yee's FDTD stability relation [1] and using the Fourier transforms to the Eq. (2) [9], and considering uniform spatial step size ($\Delta x = \Delta y = \Delta z = \Delta$), the general form of the stability condition for the Sinc (2, 2v) can be derived as:

$$\Delta t \le \frac{\Delta}{\mathrm{c}\left(\sum_{v=1}^{m}|c(v)|\right)\sqrt{d}}, \tag{3}$$

where c is the speed of light in free space, d is the spatial dimension.

According to [10], the stability of the RK-Sinc method can be derived as:

$$\Delta t \le \frac{L\Delta}{\mathrm{c}\left(2\sum_{v=1}^{m}|c(v)|\right)\sqrt{d}}, \tag{4}$$

$$s=\frac{\mathrm{c}\Delta t}{\Delta}\le\frac{L}{\sqrt{d}\,2\sum_{v=1}^{m}|c(v)|}=s_{\max}, \tag{5}$$

where L is a constant dependent on the order p of SSP-RK, and can be derived as $\sqrt{3}$ and $2\sqrt{2}$ [6],[11] for the RK_3-Sinc and RK_4-Sinc, respectively.

The maximum stability factor $S_{\max}$ is listed in Table 2. It is show that the RK_4-Sinc is stricter than the RK_3-Sinc.

Table 2: The maximum CFL number for the RK-Sinc method

	RK_3-Sinc	**RK_4-Sinc**
S_{max}	0.3317	0.5353

B. Dispersion

Defining the stability factor s = (cΔt) /Δ=0.25, the number of cells per wavelength $N = \lambda_c$ /Δ, u is the ratio of the theoretic wavelength λ_c to the numerical wavelength λ_n, and V_n is the numerical phase velocity. With the wave propagation angle θ = 90° and Φ = 0°, Figs. 1-3 show the dispersion errors V_n /c versus N for the FDTD and RK-Sinc methods in 3D case.

Figure 1 shows that the RK-Sinc method presented the better dispersion characteristics at the same spatial stencil size. Figure 2 shows the dispersion errors versus wave propagation angle Φ for different methods with θ = 90° and $\Delta x = \Delta y = \Delta z = \lambda$ /5. The FDTD method for different stencil size all presents lower dispersion errors. From Fig. 3, we can see that the RK_4-Sinc is a little fluctuation to that of the RK_3-Sinc method, the RK_4-Sinc has the better dispersion error.

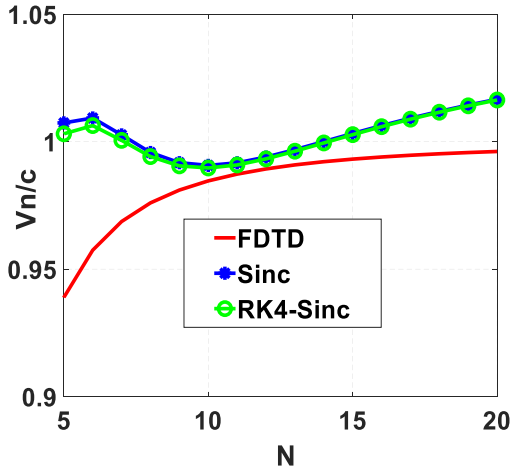

Fig. 1. Dispersion errors of the different methods.

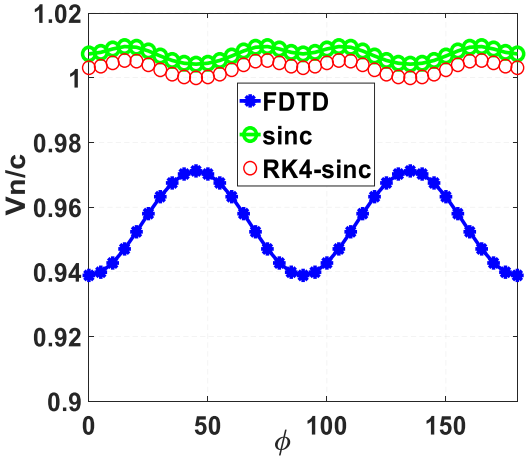

Fig. 2. Dispersion errors versus Φ of the different methods.

C. Convergence

Similar to the RK-MRTD (Runge-Kutta Multiresolution Time-Domain) method in [12], the convergence relation of the RKp-Sinc(2, 2v) can be written as:

$$\text{RK-Sinc-error} \le C_t \Delta t^p + C_x \Delta x^v . \tag{6}$$

When $v > p$ and $\Delta t = s\Delta/c$ ($s \le 1$), it can be simplified as:

$$\text{RK-Sinc-error} \le C_t \Delta t^p + C_v \Delta t^v \le C_p \Delta t^p , \tag{7}$$

where C_t, C_x, C_v and C_p are coefficients.

The convergence properties of the FDTD, RK3-Sinc and RK4-Sinc are described in Fig. 4 and it can be easily found that the order is 2, 2.2 and 3.6 respectively, the δ is uniform spatial step size ($\Delta x = \Delta y = \Delta z = \delta$). The results demonstrate that the RK-Sinc has the faster convergence rate than the FDTD method at the same stencil size.

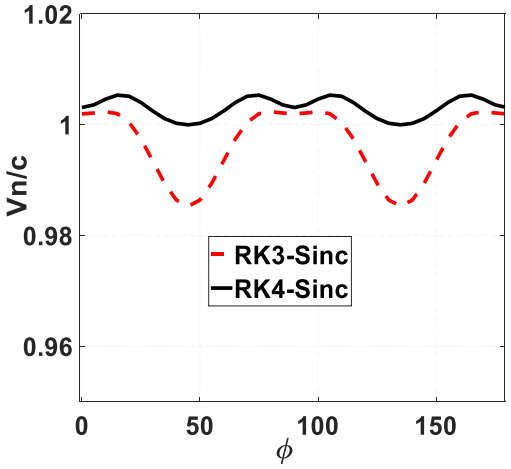

Fig. 3. Dispersion errors versus Φ of the RK-Sinc method.

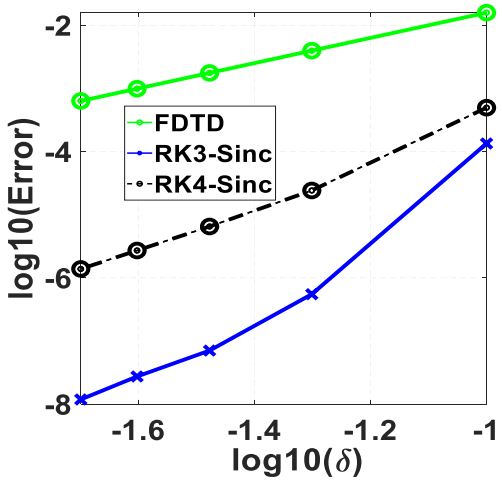

Fig. 4. Convergence of the FDTD, RK$_3$-Sinc and RK$_4$-Sinc methods.

D. Computational cost and memory requirements

According to the RK-MRTD method in 3D case [12-14], at each time step for FDTD method only E and H fields at a final time need to be stored, while the memory requirements of the RK-Sinc is more than two times of the FDTD for the same mesh size in [11]. The cost of the FDTD can be written as Cost $_{\text{FDTD}}$ = 2 $(M_1)^3 \times 2$. It is obviously that the RK$_p$-Sinc needs largely more than p times computational cost than the FDTD method for the same mesh size.

In 3D case, for a single time step, the computational cost of the high order Sinc(2, 2v) method can be written as follows:

$$\text{Cost}_{\text{Sinc}} = 2 (M_1)^3 \times 2v, \tag{8}$$

where M_1 is the number of cells in a single direction, 2m is the size of the stencil.

According to [12], the cost of the RK-Sinc can be written as follows:

$$\text{Cost}_{\text{RK}p\text{-Sinc}} = 2\,(M_2)^3 \times p \times (2v+1), \tag{9}$$

where M_2 is the number of cells in a single direction.

If the computational domain is unit size, Δx_1 and Δx_2 are the cell sizes of the Sinc(2, 2v) and RK$_p$-Sinc(2, 2m) methods, then $M_1 = 1/\Delta x_1$, $M_2 = 1/\Delta x_2$; if Δt_1 and Δt_2 are the maximal stable time step for the Sinc(2, 2v) and RK$_p$-Sinc(2, 2v) methods, and Δt_2 chosen as $2\Delta t_1/p$. If the total computational time is 1, then the cost of the two methods as follows:

$$\text{Cost}_{\text{Sinc}} = 2(M_1)^3 \times 2v \times \frac{1}{\Delta t_1}, \tag{10}$$

$$\begin{aligned}\text{Cost}_{\text{RK-Sinc}} &= 2\left(M_2\right)^3 \times p \times \left(2v+1\right) \times \frac{1}{\Delta t_2} \\ &= \left(M_2\right)^3 \times p^2 \times \left(2v+1\right) \times \frac{1}{\Delta t_1}.\end{aligned} \tag{11}$$

IV. NUMERICAL EXAMPLE

In this section, the RK-Sinc is applied to solve a dielectric material slab in one dimension. The thickness of the slab is 8mm, the relative permittivity of the slab is 3.8. The spatial step size is Δx, and the total computational domain is discretized as $\Delta x = \lambda/5$, which λ is the wavelength in the media and corresponds to the concerned maximum frequency $f_{\max}$=10GHz.

The analytical solution is the Mie series solution and the reflection coefficients of the FDTD and RK$_4$-Sinc are shown in Fig. 5. From the Fig. 5, we can see that the RK$_4$-Sinc is the better than FDTD method. Figure 6 describes the errors between the methods and the analytical solution, we can obtain that the RK$_4$-Sinc has the better dispersion error than FDTD Scheme.

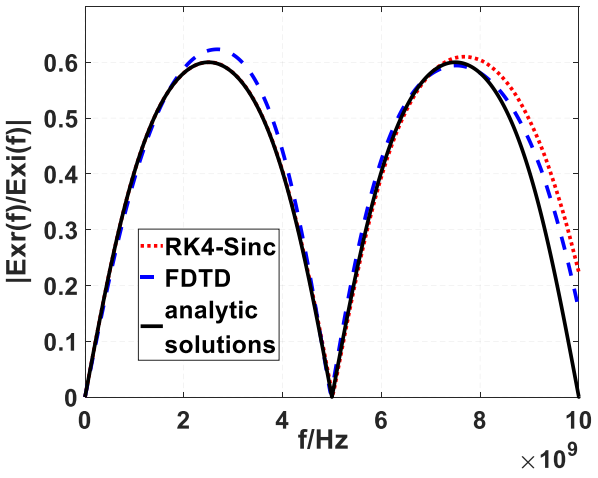

Fig. 5. Magnitude of reflection coefficients for RK$_4$-Sinc FDTD method and analytic solution.

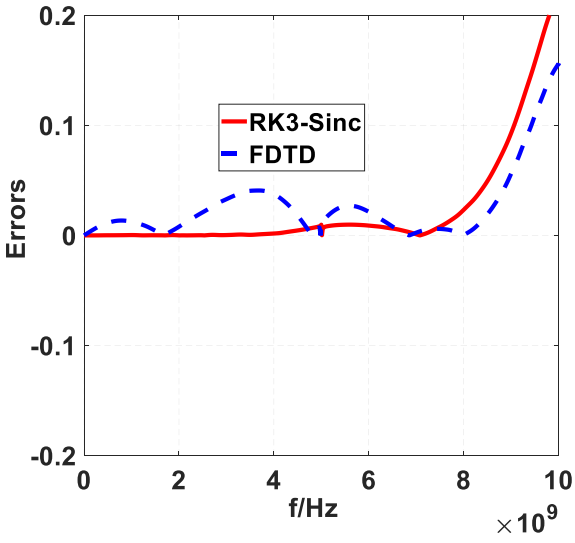

Fig. 6. Errors of the FDTD and RK$_4$-Sinc method.

VI. CONCLUSION

In this paper, a novel method RK-Sinc based on the SSP-RK and the Sinc function has been presented. The characteristic including stability, dispersion and convergence is analyzed and discussed. It can be easily found that the RK-Sinc method has the better dispersion and the faster convergence rate than FDTD method with the same spatial and temporal stencil size. The computational cost and memory requirements are studied and show that the RK$_p$-Sinc needs largely more memory requirements and computational cost of the FDTD for the same mesh size. The dielectric material slab example shows that the RK-Sinc is more accuracy than FDTD method. Therefore, the RK-Sinc scheme can reduce the numerical dispersion and has a fast convergence rata, we can draw a conclusion that the new method is more accurate and efficient, and has well potential applications in some certain computational electromagnetic filed.

ACKNOWLEDGMENT

The work was also supported by This work is supported by the High-Level Talent Foundation of Jinling Institute of Technology (Grant No. jit-b-201716).

REFERENCES

[1] K. S. Yee, “Numerical solution of initial boundary value problems involving Maxwell's equation in isotropic media,” *IEEE Trans. Antennas Propagat.*, vol. AP-14, no. 3, pp. 302-307, May 1966.

[2] J. Fang, “Time domain finite difference computation for Maxwell’s equation,” *Ph.D. dissertation*, Univ. of California at Berkeley, Berkeley, CA, 1989.

[3] C. W. Manry, S. L. Broschat, and J. B. Schneider, "High-order FDTD methods for large problems," *Applied Computational Electromagnetics Society Journal*, vol. 10, no. 2, pp. 17-29, 1995.

[4] D. W. Zingg, "Comparison of the high-accuracy finite difference methods for linear wave propagation," *SIAM J. Sci. Comput.*, vol. 22, no. 2, pp. 476-502, 2000.

[5] M. Krumpholz and L. P. B. Katehi, "MRTD: New time-domain schemes based on multiresolution analysis," *IEEE Trans. Microw. Theory Tech*., vol. 44, pp. 555-571, Apr. 1996.

[6] S. Gottlieb, C.-W. Shu, and E. Tadmor, "Strong stability-preserving high-order time discretization methods," *SIAM Rev*., vol. 43, no. 1, pp. 89-112, 2001.

[7] M. H. Chen, B. Cockburn, and F. Reitich, "High-order RKDG methods for computational electromagnetics," *J. Sci. Comput*., vol. 22/23, no. 1-3, 205-226, June 2005.

[8] J. Z. Zhang and Z. Z. Chen, "A higher-order FDTD using Sinc expansion function," *2000 IEEE MTT-S International*, pp. 113-116, 2000.

[9] E. M. Tentzeris, R. L. Robertson, J. F. Harvey, and L. P. B. Katehi, "Stability and dispersion analysis of battle-Lemarie-based MRTD schemes," *IEEE Trans. Microw. Theory Tech*., vol. 47, no. 7, pp. 1004-1013, July 1999.

[10] M. Fujii and W. J. R. Hoefer, "Dispersion of time-domain wavelet Galerkin method based on Daubechies compactly supported scaling functions with three and four vanishing moments," *IEEE Microwave Guided Wave Lett*., vol. 10, no. 7, pp. 1752-1760, July 2002.

[11] X. Chen and Q. S. Cao, "Analysis of characteristics of two-dimensional Runge-Kutta multiresolution time-domain scheme," *Progress in Electromagnetics Research M*, vol. 13, pp. 217-227, 2010.

[12] Q. S. Cao, R. Kanapady, and F. Reitich, "High-order Runge-Kutta multiresolution time-domain methods for computational electromagnetics," *IEEE Trans. Microw. Theory Tech.*, vol. 54, no. 8, pp. 3316-3326, Aug. 2006.

[13] M. Zhu and Q. Cao, "Studying and analysis of the characteristic of the high-order and MRTD and RK-MRTD scheme," *Applied Computational Electromagnetics Society Journal*, vol. 28, no. 5, pp. 380-389, May 2013.

[14] M. Zhu and Q. S. Cao, "Analysis for three-dimensional curved objects by Runge-Kutta high order time-domain method," *Applied Computational Electromagnetics Society Journal*, vol. 30, no. 1, pp. 86-92, Jan. 2015.

Design and Analysis of a Novel Hybrid Excitation Flux Reversal Machine

Xianming Deng, Zhen Jia, and Xiaohan Zhao

Jiangsu Province Laboratory of Mining Electric and Automation, China University of Mining and Technology
Xuzhou, 221116, China
xmdengcumt@126.com, TS19130046A31@cumt.edu.cn

Abstract ─ A novel hybrid excitation flux reversal machine (HEFRM) is developed. The machine has a simple reluctance rotor and a stator, which has both an ac armature winding and a dc field winding. The core on the surface of the pole arc at the centerline of the stator pole and the core on the outer surface of the stator yoke each have a slot along the rotating axis, where the field windings are placed. A permanent magnet (PM) with opposite polarity is placed respectively on each side of a slot in the same stator pole. In this paper, the working principle of the new HEFRM is introduced, the influence of magnetic pole parameters and armature parameters on motor performance are also analyzed, and genetic algorithm (GA) is used for multi-objective optimization of the torque characteristics. Finally, the HEFRM prototype is built, and its theoretical correctness is verified by the finite element analysis (FEA).

Index Terms ─ FEA, flux-reverse machine, GA, hybrid excitation, multi-objective optimization.

I. INTRODUCTION

Flux-reverse machine (FRM) is a new type of machine, in which rare-earth PMs are added to the stator or the surface of pole shoes of a switched reluctance machine (SRM). Because of its high power density, small rotational inertia, compact structure, easy to install, and other performance advantages, the application prospects are very broad, it can be used in automotive power generation, power tools, industrial drive, and other fields [1-4]. Since the end of the last century, the single-phase and three-phase FRM has been proposed [5], and many new types of FRM have been developed as a result of extensive research on the structure of the FRM, such as double stator flux reversal machine [6], flux reversal linear machine [7-9], Halbach permanent magnet flux reversal machine [10] and hybrid excitation flux reversal machine [11].

HEFRM has two different magnetomotive force sources, the air gap main magnetic field is established by permanent magnets and the electric excitation plays an auxiliary role. Thus, the PM machine can be combined with the electric excitation machine organically [12-14]. When operating as a motor, the speed range of the motor is extended; when operating as a generator, the output voltage can be adjusted to improve the quality of the power supply. The HEFRMs are promising candidates for many areas especially for direct-drive systems requiring a wide speed range. Thus, it is of high research value and practical significance.

In this paper, a new type of hybrid excitation flux reversal permanent magnet machine is proposed. Meanwhile, the FEA is used to analyze its performance, and achieve its modulation of the air-gap magnetic field. By comparison, it is verified that it can achieve a wider speed range and better overload capability.

II. STRUCTURE AND WORKING PRINCIPLE

The basic structure of the traditional flux reversal machine is shown in Fig. 1. It consists of four basic parts: the armature winding, the permanent magnet, the field winding, and the rotor as a magnetic flux modulator. The PM magnetomotive force (MMF) of the traditional flux reversal machine is basically unchanged during operation. In vector control, to run the machine above the base speed, the only way is to adjust the direct axis current to attenuate the magnetic field for flux weakening speed regulation. However, the torque performance of the machine will inevitably be wakened. Therefore, to better achieve magnetic field regulation, a novel hybrid excitation flux reversal machine is proposed in this paper, as shown in Fig. 1 (a).

Compared with the traditional flux reversal machine, in the structure of the HEFRM, along the rotating axis, there is a field winding slot not only on the core of the pole arc surface at the centerline of the stator pole, but also on the core of the outer surface of the stator yoke. The DC field winding is in the form of concentrated winding, which is alternately wound in the field winding slot, as shown in Fig. 1. The structure of the power winding is the same as that of a normal winding. The power winding is placed in the stator slot, which is orthogonal to the field winding in space. A PMs is placed on both sides of each stator pole shoe of the machine. Each PM is opposite in polarity to a PM on the same

Submitted On: August 22, 2020
Accepted On: January 18, 2021

https://doi.org/10.47037/2020.ACES.J.360215

tooth and identical in polarity to a PM on an adjacent tooth. For the application of the new structure, the HEFRM and the traditional flux reversal machine have the same arrangement of PMs and the same number of pole pairs. So, the structure and operating principle of the two machines are very similar, which greatly simplifies the theoretical analysis and design of the new machine.

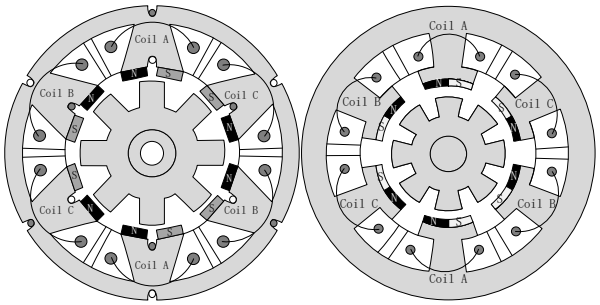

Fig. 1. (a) Basic structure diagram of hybrid excitation flux reversal permanent magnet machine, and (b) basic structure diagram of traditional flux reversal permanent magnet machine.

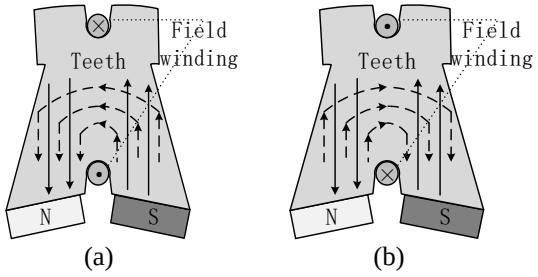

Fig. 2. Flux linkage of a stator tooth: (a) turn on the flux enhancement current, and (b) turn on the flux weakening current.

In general, the field winding is connected with demagnetization current to conduct flux weakening speed regulation. As shown in Fig. 2 (b), after the flux weakening current is applied, the magnetic field of the field winding forms a loop through the stator teeth. This loop is connected in series with the permanent magnet magnetic circuit. When the flux of the field winding passes through the permanent magnet, which is in danger of demagnetization if not properly controlled. As shown in Fig. 2 (a), if demagnetization of a PM occurs, the current opposite to demagnetization can be applied, in that PM can be magnetized to improve system reliability. Since the field winding is spatially orthogonal to the power winding, the two are decoupled. As shown in the Fig. 3, when the power winding is applied a sinusoidal voltage, the induced electromotive force of the field winding on the same tooth is very weak. Without considering the effect of armature current on excitation current, this characteristic makes it possible to simplify the control strategy in weak magnetic control. Moreover, the field winding is placed in a special slot instead of in the stator slot. This design makes the field winding does not occupy the stator slot area with the armature winding. It also does not weaken the electrical load and synchronous reactance of the armature windings by increasing the field winding. Therefore, the design of the machine can be further simplified.

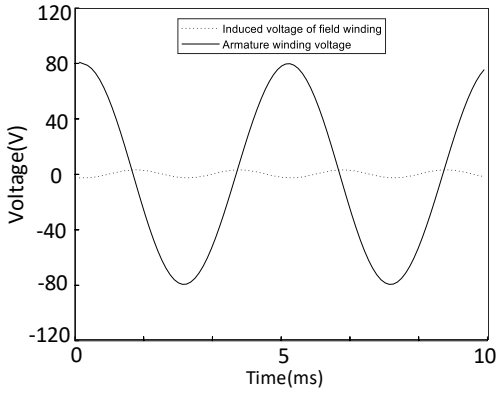

Fig. 3. Induced electromotive force of field winding when armature winding is electrified.

The working principle of HEFRM is similar to that of traditional flux reversal machine, which belongs to the family of flux modulation machines. Magnetic flux modulation machine armature winding pole number P_a and magnetic field rotation angular velocity Ω_a meet the requirements:

$$\begin{cases} P_a = |P_e - P_m| \\ \Omega_a = (P_e\Omega_e - P_m\Omega_m)/(P_e - P_m) \end{cases}, \quad (1)$$

where Ω_e and Ω_m are MMF of the permanent magnet and the angular velocity of the rotor, P_e and P_m are the numbers of poles of PM and the period number of flux modulator, in FRM $P_m = Z_r/2$, Z_r is the number of rotor slots. To place the three-phase winding, the number of stator slots and the number of armature winding poles shall be satisfied:

$$Z_s = 3kP_a, k = 1,2,3\cdots. \quad (2)$$

From the above analysis, the commonly used pole slot combinations of HEFRM are shown in Table 1.

Table 1: Pole slot combinations of HEFRM

Z_s	Z_r	2	4	5	7	8	10	11
6	P_a	1	1	2	2	1	1	2
	SPP	1	1	0.5	0.5	1	1	0.5
	GR	2	4	2.5	3.5	8	10	5.5
12	P_a	4	2	1	1	2	4	5
	SPP	0.5	1	2	2	1	0.5	0.4
	GR	0.5	2	5	7	4	2.5	2.2

PS: SPP is the number of slots per pole per phase, GR is gear ratio (Ratio of rotor slot number Z_r to winding pole number P_a).

Taking 6-stator-slot / 8-rotor-slot HEFRM as an example, the distribution of the magnetic force line of HEFRM is shown in Fig. 3. As can be seen from this figure, whether the PMs are excited individually or the field windings are excited individually, when the rotor rotates a rotor slot distance, the flux linkage of the A-phase windings are reversed. Therefore, the operation principle of HEFRM is the same as that of traditional FRM. Due to the use of hybrid excitation, the working flux density of the PM B_m is determined by the joint action of the residual magnetic field of the PM B_r and applied magnetic field exerted on the PM by the excitation coil and the armature winding together H_m:

$$B_m = B_r + \mu_0\mu_{rm}H_m \,, \tag{3}$$

where μ_{rm} is the relative permeability of PM. The external MMF is equal to the magnetic pressure drop of the air gap and PM. Ignoring the magnetic pressure drop of the core, the MMF of the whole magnetic circuit can be expressed as:

$$H_m l_m + H_g l_g = N_{dc}I_{dc} + N_{ac}I_{ac} \,, \tag{4}$$

where NI is the MMF of the external field winding, l_m and l_g is the thickness of PM and the length of air gap, respectively. H_g is the air gap magnetic field strength. In the air gap, the flux density of magnetic field strength can be expressed as:

$$B_g = \mu_0 H_g \,. \tag{5}$$

Besides, both air gap flux φ_g and permanent magnetic flux φ_m can be expressed as the multiplication of flux density and cross-sectional area:

$$\begin{cases} \varphi_g = B_g A_g \\ \varphi_m = B_m A_m \end{cases}, \tag{6}$$

introducing the magnetic flux leakage coefficient k,

$$\varphi_g = \frac{\varphi_m}{k} \,. \tag{7}$$

Substituting (4) - (7) into (3) can be obtained:

$$B_m = \frac{1}{1+\mu_{rm}\frac{A_m l_g}{A_g l_m K}}\left[B_r + \mu_0\mu_{rm}\frac{N_{dc}I_{dc}+N_{ac}I_{ac}}{l_m}\right] . \tag{8}$$

From the above equation, it can be seen that the operating magnetic density of a permanent magnet can be increased or decreased by changing the direction of the incoming excitation current. Due to the slotting of the rotor, the air gap length of the machine is not fixed but varies periodically with the circumferential position angle θ_s and the rotor position angle θ. The air gap flux density $\mathrm{B}(\theta_s, \theta)$ can be expressed as the product of the MMF $F_m(\theta_s)$ and the air gap permeability function $\Lambda(\theta, \theta_s)$:

$$\mathrm{B}(\theta_s, \theta) = F_m(\theta_s)\Lambda(\theta, \theta_s) \,. \tag{9}$$

The distribution of the magnetic field lines of the machine is shown in Fig. 4.

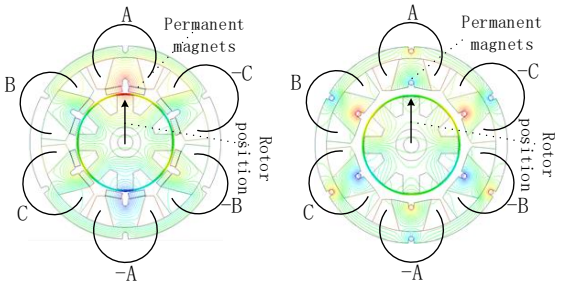

(a) (b)

Fig. 4. Distribution of magnetic field lines under different excitation modes: (a) separate excitation of permanent magnet, and (b) the field winding is separately excited.

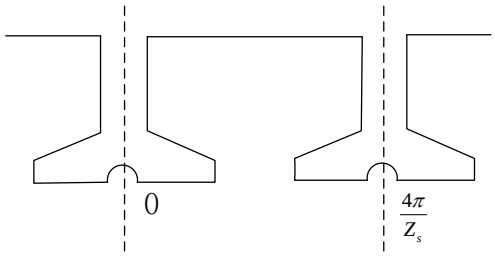

Fig. 5. Distribution of magnetic force lines in different rotor positions.

The structure and PM arrangement of HEFRM are shown in Fig. 6. and the stator slot centerline at position 0, as shown in Fig. 5, the MMF $F_m(\theta_s)$ is an odd function with period $\mathrm{T} = 4\pi/Z_s$:

$$F_m(\theta_s) = \sum_{n=1,3,5\cdots}^{\infty} F_n sin\left(\frac{nZ_s\theta_s}{2}\right) , \tag{10}$$

where

$$\begin{cases} F_n = \frac{8F_c}{n\pi} sin\left(\frac{n\pi}{2}\right) cos\left(\frac{n\pi(1+S_0+S_1)}{4}\right) sin\left(\frac{n\pi(1-S_0+S_1)}{4}\right), \\ F_c = B_m l_m/\mu_0\mu_{rm} \end{cases} \tag{11}$$

where S_0 is the ratio of stator slot opening width to stator slot spacing; S_1 is the ratio of stator slot opening width

to stator slot width. The slotting diagram of stator and rotor is shown in Fig. 6.

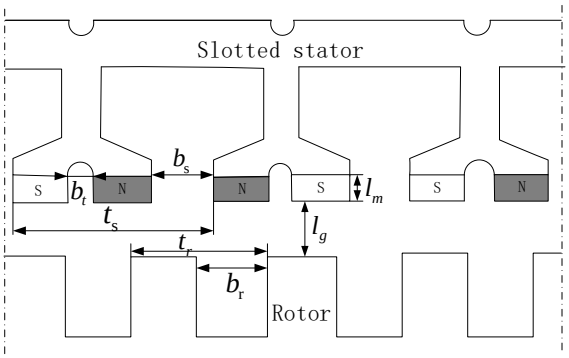

Fig. 6. Slotting diagram of stator and rotor.

As shown in Fig. 5, HEFRM is a typical double salient structure, whose air-gap permeance $\Lambda(\theta,\theta_s)$ can be expressed as the product of the air gap relative permeance $G_r(\theta,\theta_s)$ when the stator is not slotted but the rotor is and the air gap relative permeance $G_s(\theta_s)$ when the stator is slotted but the rotor is not slotted:

$$\Lambda(\theta,\theta_s)=\frac{\mu_0}{l_g}G_r(\theta,\theta_s)G_s(\theta_s), \tag{12}$$

where $G_r(\theta,\theta_s)$ is the air gap relative permeance when the stator is not slotted but the rotor is slotted, and it can be expressed as:

$$G_r(\theta,\theta_s)=\frac{l_m(\theta)}{l_m(\theta)+l_g(\theta,\theta_s)}, \tag{13}$$

where $l_m(\theta)$ and $l_g(\theta,\theta_s)$ respectively represent the distribution of magnetizing direction length and effective air gap length of permanent magnet along circumferential direction when the stator is not slotted and the rotor is slotted. After Fourier decomposition, we can get:

$$G_r(\theta,\theta_s)=G_{r0}+\sum_{i=1,2\cdots}G_{ri}cos[iZ_r(\theta_s-\theta)]. \tag{14}$$

Similarly, $G_s(\theta_s)$ can be expressed as:

$$G_s(\theta_s)=G_{s0}+\sum_{m=1,2\cdots}^{\infty}G_{sm}\cos\left(mZ_s\theta_s\right). \tag{15}$$

To sum up, (9) is rewritten as follows:

$$\mathrm{B}(\theta_s,\theta)=\sum_{\substack{n=1,3,5\cdots\\ i=0,1,2\\ m=0,1,2}}G_{ri}G_{sm}\,F_n sin\left(\frac{nZ_s\theta_s}{2}\right)\cdot$$

$$cos\big(iZ_r\,(\theta_s-\theta)\big)cos(mZ_s\theta_s). \tag{16}$$

Combining (8), (10), (11), and (16), it can be seen that by changing the magnitude and direction of the excitation current, the magnitude of the working magnetic density of the PM can be changed, thus the distribution of MMF of the PM can be changed. Through the modulation of the rotor, a rotating magnetic field can be generated, which directly changes the value of the air gap rotating magnetic field. However, it should be noted that changing the excitation current only changes the amplitude of each harmonic of the air-gap field, and does not introduce new harmonics. The process is shown in Fig. 7.

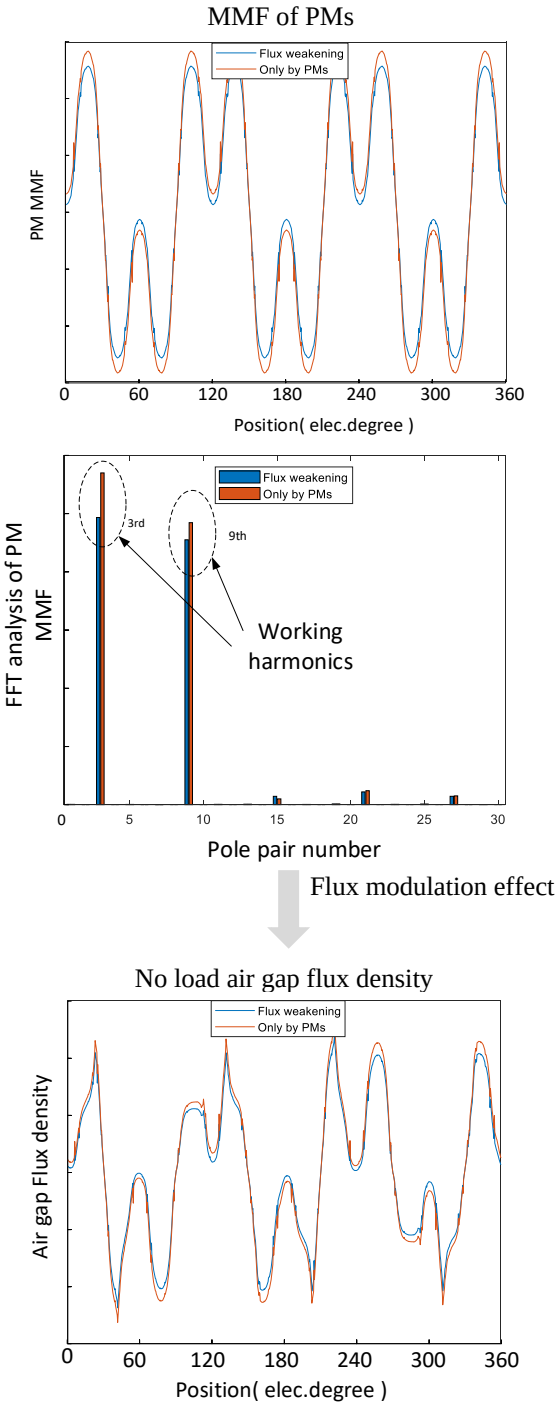

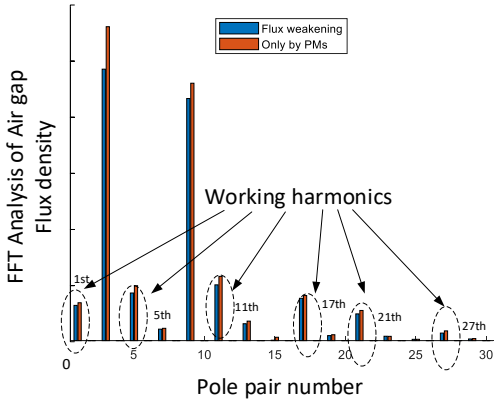

Fig. 7. Comparison of PM MMF and air gap flux density when PM acting alone and flux weakening.

In the analysis of back electromotive force (EMF), to analyze the harmonics of the EMF, the theory of winding function can be applied. The winding function of a three-phase winding is expressed as:

$$\begin{cases} N_a(\theta_s) = \sum_{j=1,3,5\cdots} N_j cos(jP_s\theta_s) \\ N_b(\theta_s) = \sum_{j=1,3,5\cdots} N_j cos\left(jP_s\theta_s - \frac{2}{3}\pi j\right) \\ N_c(\theta_s) = \sum_{j=1,3,5\cdots} N_j cos\left(jP_s\theta_s + \frac{2}{3}\pi j\right) \\ N_j = \frac{2}{j\pi}\frac{N_s}{P_s}K_{wj} \end{cases}, \quad (17)$$

where N_j is the peak value of the jth harmonic of the winding function, N_s is the number of turns in series of each phase, K_{wj} is the winding factor of the jth harmonic and P_s is the pole number of armature winding. The EMF expression of phase A winding can be obtained:

$$e_a(t) = -\frac{d}{dt}\left[r_g l_{stk}\int_0^{2\pi} \mathrm{B}(\theta_s,\theta)N_a(\theta_s)\,d\theta_s\right]\pi\Omega_m \cdot$$

$$r_g l_{stk} Z_r \frac{\mu_0}{l_g}\sum_{\substack{i=\frac{v}{Z_r} \\ j,n,m=1,3,5\cdots}} iG_{ri}G_{sm}F_n N_j cos(iZ_r\theta)\,, \quad (18)$$

where r_g is the radius of the stator inner circle, l_{stk} is the stack length, rotor position angle $\theta = \Omega_m t$, $\mathrm{v} = \frac{(n\pm 2m)Z_s}{2} \pm jP_s$. The comparison of back EMF is shown in Fig. 8.

III. TORQUE PERFORMANCE OPTIMIZATIN DESIGN

Torque density and torque ripple are important performance indexes of FRM. The torque ripple of flux reversal machine is divided into cogging torque caused by stator PMs and rotor harmonic permeance, and torque ripple caused by stator back EMF harmonic and winding current.

In PM machine, cogging torque is inherent. Cogging torque is generated by the harmonic of MMF under the action of higher harmonic of air gap permeance. It is defined as the negative derivative of the magnetic field energy w to the stator-rotor relative position angle θ, when the machine is not energized. It can be expressed as:

$$T_{cog} = -\frac{\partial w}{\partial \theta}, \quad (19)$$

where the magnetic field energy W can be approximately equal to the air gap magnetic field energy W_{gap}:

$$W_{gap} = \frac{1}{2\mu_0}\int_V B(\theta_s,\theta)^2 dV$$

$$= \frac{(R_2^2-R_1^2)l_{stk}}{2\mu_0}\int_0^{2\pi} B(\theta_s,\theta)^2 d\theta_s\,, \quad (20)$$

where R_1 and R_2 are the rotor outer diameter and stator inner diameter respectively. Combined with (16), it can be written as:

$$T_{cog} = \frac{\pi Z_r(R_2^2-R_1^2)l_{stk}}{4l_g}\sum_{i_1\pm i_2=N_p}^{\infty}(i_1 \pm$$

$$i_2)G_{ri_1}G_{ri_2}G_{sm_1}G_{sm_2}F_{n_1}F_{n_2}sin\left(N_p Z_r\theta\right), \quad (21)$$

where

$$N_p = \frac{(n_1\pm n_2\pm m_1\pm m_2)Z_s}{2Z_r}. \quad (22)$$

It can be seen from (21) that the cogging torque is related to the magnetic pole parameters, armature parameters and the number of pole slots of stator and rotor. It can be seen from (22) that not all permeability harmonics will affect cogging torque, and the cogging torque can be reduced by reducing the amplitude of the magnetic pole parameter $F_{n_1}F_{n_2}$ and the armature parameter $\mathrm{G}_{ri_1}\mathrm{G}_{ri_2}G_{sm_1}G_{sm_2}$.

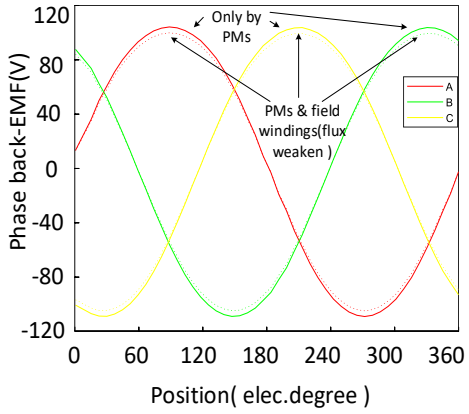

Fig. 8. Comparison of phase back-EMF when PM acting alone and flux weakening.

According to the principle of electromechanical energy conversion, the output torque of three-phase flux reversal machine T_e can be written as:

$$T_e = [e_a(t)i_a(t) + e_b(t)i_b(t) + e_c(t)i_c(t)]/\Omega_m, \quad (23)$$

where $e(t)$ and $i(t)$ are three-phase back EMF and phase current respectively. Combining (17) and (18), (23) can be rewritten as:

$$T_e = \frac{3}{2} i\pi r_g l_{stk} Z_r I_s \frac{\mu_0}{l_g} \cdot \sum_{\substack{i=\frac{v}{Z_r} \\ j,n,m=1,3,5\cdots}} iG_{ri}G_{sm}F_n N_j cos[(i \pm 1)Z_r\theta], \quad (24)$$

where I_s is the peak value of rated current. Take $i, m = 1$, then T_e is equal to the average torque T_{avg}; take $i, m \neq 1$, then T_e is equal to the torque ripple T_r. It can be seen from (24) that, similar to cogging torque, the output torque and torque ripple can also be adjusted by modifying the magnetic pole parameter F_n and armature parameters $G_{ri}G_{sm}$.

Both torque density and torque ripple are affected by the parameters of the magnetic pole and armature. Consequently, in this section, we will use the genetic algorithm combined with the finite element algorithm to design a multi-objective optimization of this machine. From the analysis in the first section, it has been seen that the MMF generated by the field winding only affects the amplitude of the PM working MMF and air gap flux density, and does not change its harmonic content. Therefore, the number of slots for the stator and rotor can be selected in the same way as for the conventional flux reversal machine. In this section, 6-rotor-slot / 8-stator-slot is selected as an example. Its pole ratio is large, and the electromagnetic torque is also relatively large.

A. Design optimization procedure

To optimize the design of the proposed HEFRM, according to the basic structure and working principle of the machine presented in Section II, a prototype has been designed and simulate by FEA. The FEA parameters are shown in Table 2.

For the output torque of the machine, we want greater torque density and smaller torque ripple. Therefore, The objective functions fixed for this optimization are:

-Maximize the average torque of the machine output (T_{avg}),

-Minimize machine torque ripple ($T_{cog} + T_r$).

From the analysis in Section II, the magnetic pole and armature parameters of the machine can be changed by changing stator-rotor slot opening ratio and stator tooth slot opening ratio. Therefore, the optimization parameters are:

-Rotor slot opening ratio (S_2),

-Stator slot opening ratio (S_0),

-Stator tooth slot opening ratio (S_1).

Due to the requirements of mechanical strength and the space for placing the windings. The constraints of the optimization parameters are shown in Table 3.

Table 2: FEA parameters

Parameter	Value	Parameter	Value
Phase number	3	Stator outer diameter	100mm
Rotor slot number	8	Rotor outer diameter	50mm
Stator slot number	6	Air gap length	1mm
Stack length	80mm	PM thickness	3mm
Turns per AC coil	160	PM remanence	1.15T
Turn ratio of dc to ac winding	0.5	Rated speed	1500rpm
Stator tooth slot opening ratio	0.22	Rated frequency	200Hz
Stator slot opening ratio	0.35	Rated ac winding current	5A
Rotor slot opening ratio	0.45	Maximal dc winding current	5A

PS: The rotor slot opening ratio S_2 is defined as $S_2 = b_r/t_r$, where b_r is the rotor slot width and t_r is the rotor slot pitch.

Table 3: Constraints of the optimization parameters

Optimization Parameters	Minimum	Maximum
Rotor slot opening ratio (S_2)	0.4	0.6
Stator slot opening ratio (S_0)	0.2	0.5
Stator tooth slot opening ratio (S_1)	0.2	0.4

Setting the above conditions, the optimization engine uses multi-objective genetic algorithm, the population size is set to 10 times the number of optimization parameters, that is 30, and the maximum number of generations is 65.

B. Optimization results

The optimization of this machine using the multi-objective genetic algorithm took 30 hours, with a total of 1840 model iterations. The Pareto-optimal front of the average torque verse torque ripple of the machine output is obtained, as shown in Fig. 9.

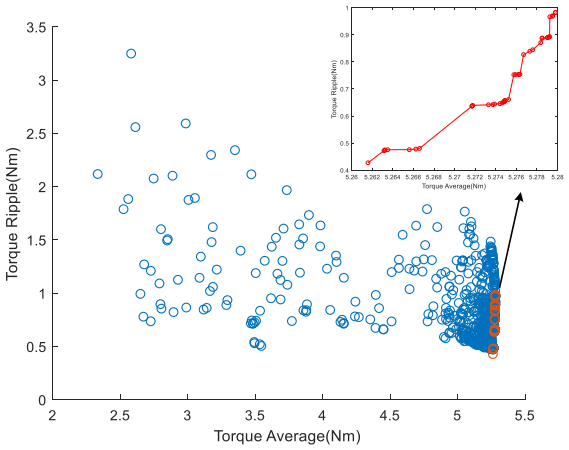

Fig. 9. Pareto-optimal front.

The comparison of optimized parameter values before and after optimization is shown in Table 4, and the comparison of output torque before and after optimization is shown in Fig. 10. As can be seen in Fig. 10, the optimized machine has a larger average torque and smaller torque ripple.

Table 4: Constraints of the optimization parameters

Optimization Parameters	Initial Value	Optimization Values
Rotor slot opening ratio (S_2)	0.45	0.58
Stator slot opening ratio (S_0)	0.35	0.27
Stator tooth slot opening ratio (S_1)	0.22	0.2

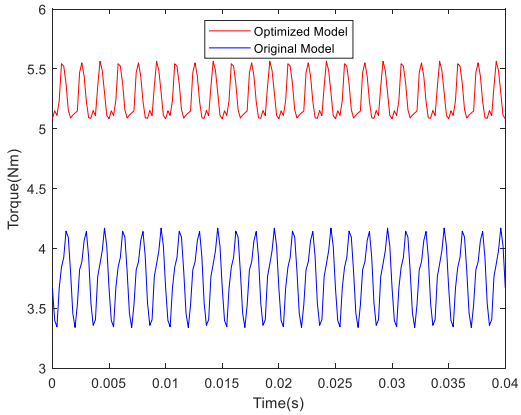

Fig. 10. Comparison of output torque before and after optimization.

The optimization algorithm is based on the results of 2D FEA, considering that the machine contains different active magnetic circuits. We also performed 3D FEA to evaluate the end effect. The open-circuit end effect coefficient E_{eopen} and the on-load end effect coefficient E_{eload} [15] are defined respectively:

$$\begin{cases} E_{eopen} = \dfrac{E_{3-D}}{E_{2-D}} \times 100\% \\ E_{eload} = \dfrac{T_{avg3-D}}{T_{avg2-D}} \times 100\% \end{cases}, \tag{25}$$

where E_{eopen} can be defined as the ratio of back EMF E_{3-D} from 3D FEA and the back EMF E_{2-D} from 2D FEA. E_{eload} can be defined as the ratio of the average torque T_{avg3-D} from the 3D FEA and the average torque T_{avg2-D} from the 2D FEA. The result is shown in Fig. 11.

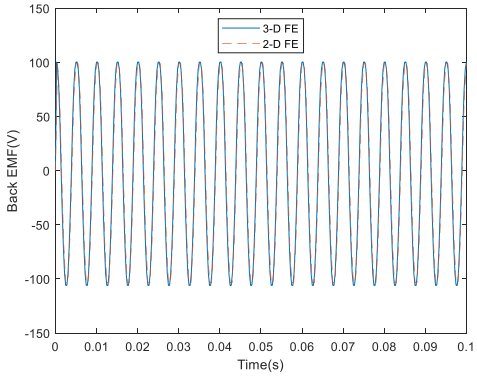

(a) Output torque

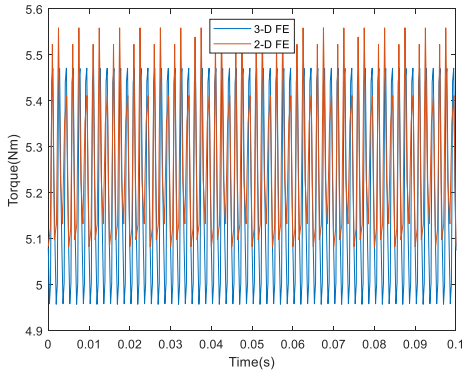

(b) Back EMF

Fig. 11. Comparison between 3D FEA and 2D FEA.

Table 5: End effect coefficient

Project	2D FEA	3D FEA
Average output torque	5.2633Nm	5.1966Nm
E_{eload}	98.7%	
Back EMF amplitude	98.9564V	100.3322V
E_{eopen}	101.4%	

From Table 5, we can see that the end effect coefficients are small. Therefore, we can consider that the optimal model parameters of the machine obtained from 2D FEA are reasonable.

IV. PERFORMANCE ANALYSIS

To analyze the performance of the HEFRM, the machine parameters are shown in Table 6, and its output characteristics are tested.

Table 6: Parameters of HEFRM

Parameter	Value	Parameter	Value
Phase number	3	Stator outer diameter	100mm
Rotor slot number	8	Rotor outer diameter	50mm
Stator slot number	6	Air gap length	1mm
Stack length	80mm	PM thickness	3mm
Turns per AC coil	160	PM remanence	1.15T
Turn ratio of dc to ac winding	0.5	Rated speed	1500rpm
Rated phase voltage	220V	Rated load	5Nm
Stator tooth slot opening ratio	0.2	Rated frequency	200Hz
Stator slot opening ratio	0.27	Rated ac winding current	5A

Under the given rated voltage, the electric field winding is connected with the flux enhancement current. The machine starts with rated load, and its dynamic response is shown in Fig. 12.

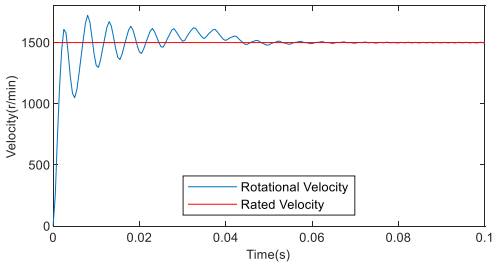

(a) Machine speed response

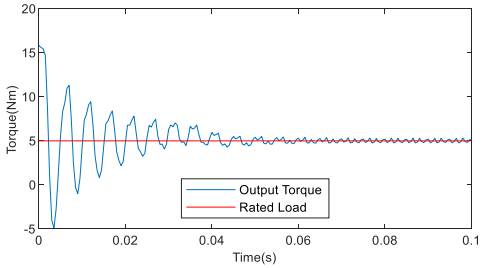

(b) Machine torque response

Fig. 12. Dynamic characteristics of machine.

From Fig. 12, it can be seen that the machine reaches steady state after 0.08 seconds. The machine efficiency is shown in Table 7.

Table 7: Rated efficiency of machine in machine state

Input Electromagnetic Power	1153.8W
Copper loss	92.6W
Core loss	43W
Machine efficiency	88.25%

When the control strategy of $i_d = 0$ is adopted. The angle between the phase current and the back EMF is kept at 0° by changing the excitation current without increasing the d-axis current component. Under the above conditions, Fig. 13 analyzes the relationship between voltage, output torque and speed, and the coupling relationship between field winding and power winding. As can be seen from Fig. 13 (a), when the excitation current is $-5A$(flux enhancing), the rated voltage can be reached as soon as possible. This is because the excitation current assists magnetism. Therefore, before reaching the rated speed, the output limit of the inverter voltage will be reached first. If the speed continues to increase, the main flux must be weakened by increasing the stator d-axis current. When the excitation current is 5A (flux weakening), the electric limit is reached when the rated speed is exceeded. This shows that with $i_d = 0$, the speed range can be increased just by adjusting the excitation current. As can be seen from Fig. 13 (b), when the excitation current is $-5A$ (flux enhancing), the output torque is 18% and 55% higher than the output torque when the excitation current is 0A and 5A, respectively. This shows that within a certain speed range, the overload capability of the machine can be greatly increased just by adjusting the excitation current.

The torque angle characteristic curve of HEFRM is shown in Fig. 14, and the corresponding torque angle is 90° when the control strategy of $i_d = 0$ is adopted. When the phase voltage of the machine is below the rated voltage, the torque angle can be kept at 90° for speed regulation. If the speed continues to increase, because the voltage output limit of the inverter has been reached, the voltage cannot continue to rise. The current angle is no longer zero, that is $i_d \neq 0$. The torque angle starts to increase and the output torque starts to decrease. At this time, the current angle is no longer zero, that is, $i_d \neq 0$, the torque angle begins to increase and the output torque begins to decrease. From the figure, it can be seen that in the process of increasing the torque angle, the torque output capacity can be improved by increasing the flux enhancement current, that is, the machine has higher overload capacity. From Fig. 15, it can be seen that under the condition of keeping the rated voltage unchanged, applying flux weakening current can significantly increase

the speed range of HEFRM compared to excitation with PMs separately.

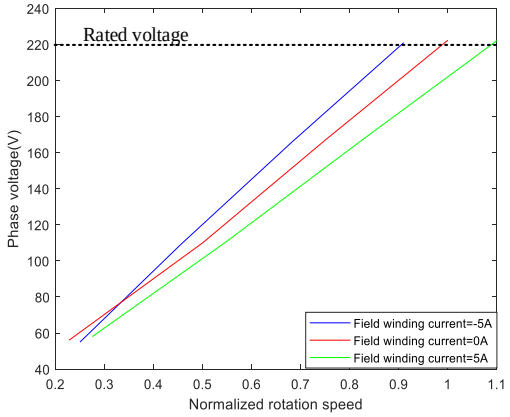

(a) Relationship between phase voltage and speed

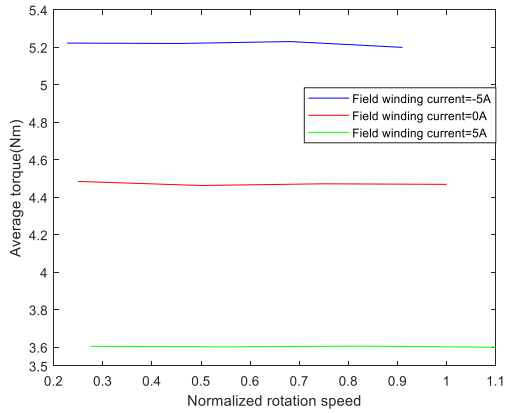

(b) Relationship between output torque and speed

Fig. 13. Comparison of relations under different excitation current .

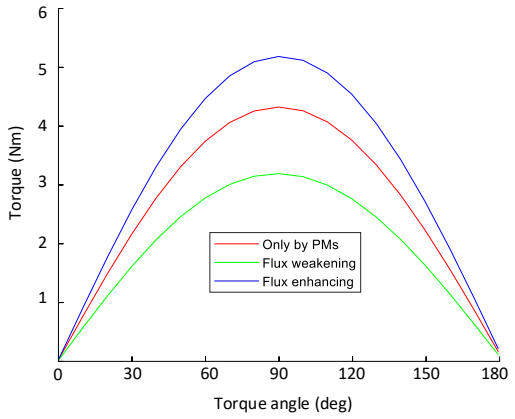

Fig. 14. Torque angle characteristic curve.

Figure 16 shows the comparison between the induced voltage the rated voltage of the field winding under different excitation currents. It can be seen that due to the new structure of the machine, the induced voltage of the field winding is almost zero when the flux enhancement and flux weakening currents are applied. This brings great convenience to the control of the field winding current.

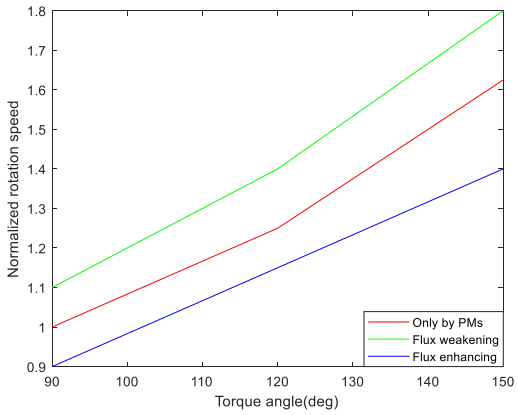

Fig. 15. Torque angle speed relationship (rated voltage).

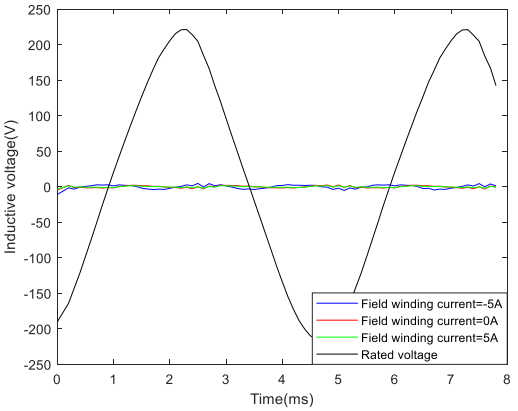

Fig. 16. Relationship between induced voltage and rated voltage of field winding.

V. CONCLUSION

This paper presents a novel hybrid excitation flux reversal machine. Compared with the traditional flux reversal machine, this structure has three advantages. First, the DC field winding is not placed in the stator slot, thus it will not occupy the stator slot area with the armature winding. Second, the DC field winding is decoupled from the armature winding, which is convenient to the control of the excitation current. Third, reasonable design of slot opening ratio of stator tooth slot can reduce torque ripple. When the genetic algorithm is applied for multi-objective optimization of the machine, we found that the optimal torque performance is obtained with stator tooth slot opening ratio of 0.2, stator slot opening ratio of 0.27, and rotor slot opening ratio of 0.58. Finally, under the control strategy of $i_d = 0$, it is

validated that a wider speed range and better overload capability can be achieved just by adjusting the excitation current.

ACKNOWLEDGMENT

This work was supported by the Natural Science Foundation of Jiangsu Province Grant No. BK20190634.

REFERENCES

[1] C. X. Wang, I. Boldea, and S. A. Nasar, "Characterization of three phase flux reversal machine as an automotive generator," [J]. *IEEE Transactions on Energy Conversion*, vol. 16, no. 1, pp. 74-80, Mar. 2001.

[2] V. Prakht, V. Dmitrievskii, V. Klimarev, and D. Askerov, "High speed flux reversal motor for power tool," [C]. *2016 6th International Electric Drives Production Conference (EDPC), IEEE*, pp. 306-311, Feb. 2017.

[3] W. Hua, X. Zhu, and Z. Wu, "Influence of coil pitch and stator-slot/rotor-pole combination on back EMF harmonics in flux-reversal permanent magnet machines," [J]. *IEEE Transactions on Energy Conversion*, vol. 33, no. 3, pp. 1330-1341, Jan. 2018.

[4] H. Yang, H. Lin, Z. Q. Zhu, H. Wang, S. Fang, and Y. Huang, "A novel flux-reversal hybrid magnet memory machine," [C]. *2017 IEEE Energy Conversion Congress and Exposition (ECCE), IEEE*, pp. 5853-5860, Nov. 2017.

[5] R. P. Deodhar, S. Andersson, I. Boldea, and T. J. Miller, "The flux-reversal machine: A new brushless doubly-salient permanent-magnet machine," *IEEE Transactions on Industry Applications*, vol. 33, no. 4, pp. 925-934, Aug. 1997.

[6] Z. Z. Wu and Z. Q. Zhu, "Partitioned stator flux reversal machine with consequent-pole PM stator," [J]. *IEEE Transactions on Energy Conversion*, vol. 30, no. 4, pp. 1472-1482, July 2015.

[7] C. Shi, R. Qu, B. Kou, D. Li, Y. Gao, and Y. Zhou, "A novel HTS flux-reversal linear permanent magnet machine with a lower number of mover teeth and higher thrust density," [J]. *IEEE Transactions on Applied Superconductivity*, vol. 28, no. 3, pp. 1-5, Jan. 2018.

[8] W. Li, K. T. Chau, T. W. Ching, and C. Liu, "A phase-decoupled flux-reversal linear generator for low-speed oscillatory energy conversion using impedance matching strategy," [J]. *IEEE Transactions on Industrial Electronics*, (99), 1-1, Jan. 2018.

[9] L. Xu, G. Liu, W. Zhao, J. Ji, and Z. Ling, "Analysis of new modular linear flux reversal permanent magnet motors," [J]. *IEEE Transactions on Magnetics*, vol. 51, no. 11, pp. 1-4, Nov. 2015.

[10] K. Xie, D. Li, R. Qu, and Y. Gao, "A novel permanent magnet vernier machine with Halbach array magnets in stator slot opening," [J]. *IEEE Transactions on Magnetics*, vol. 53, no. 6, pp. 1-5, June 2017.

[11] Y. Gao, D. Li, R. Qu, X. Fan, J. Li, and H. Ding, "A novel hybrid excitation flux reversal machine for electric vehicle propulsion," [J]. *IEEE Transactions on Vehicular Technology*, vol. 67, no. 1, pp. 171-182, Sep. 2017.

[12] D. Li, Y. Gao, R. Qu, J. Li, Y. Huo, and H. Ding, "Design and analysis of a flux reversal machine with evenly distributed permanent magnets," [J]. *IEEE Transactions on Industry Applications*, vol. 54, no. 1, pp. 172-183, Sep. 2017.

[13] Y. Gao, R. Qu, J. Li, J. Li, J. Li, and L. Wu, "Power factor of three-phase flux reversal machines," [C]. *2015 IEEE International Magnetics Conference (INTERMAG). IEEE*, 1-1, July 2015.

[14] M. Lin, G. Yang, and N. Li, "Overview of hybrid permanent magnet memory machine systems and their key technologies," Proceedings of the CSEE, vol. 38, no. 4, pp. 1187-1202, Feb. 2018. (in Chinese).

[15] Z. Z. Wu and Z. Q. Zhu, "Comparative analysis of end effect in partitioned stator flux reversal machines having surface-mounted and consequent pole permanent magnets," [J]. *IEEE Transactions on Magnetics*, vol. 52, no. 7, pp. 1-4, July 2016.

Xianming Deng was born in Sichuan, China. He received his B.S., M.S., and Ph.D. in Electrical Engineering from China University of Mining and Technology, Jiangsu, China. He is currently a Professor in the School of Electrical and Power Engineering of China University of Mining and Technology. His current research fields include power electronics and motor drive.

Zhen Jia was born in Xinjiang, China. He received his B.S. in Electrical Engineering from Chongqing University, Chongqing, China. He is currently receiving a Master education at China University of Mining and Technology. His current research interests include power electronics and motor drive.

Xiaohan Zhao was born in Shandong, China. She received her B.S. in Electrical Engineering from Shandong University of Technology, Shandong, China. She is currently receiving a Master education at China University of Mining and Technology. Her current research interests include power electronics and motor drive.